Loughborough University

Department of Materials

AN INVESTIGATION OF CADMIUM, HARD CHROMIUM AND THEIR POSSIBLE REPLACEMENT COATINGS FOR AEROSAPCE APPLICATIONS

by

Han Jiang

Project Supervisor: Dr. Geoffrey Wilcox
Industrial Supervisor: Mr. Andrew Bastow
Mr. David Collins

AIRBUS

(Han Jiang, 2013)

Abstract

High velocity oxygen fuel (HVOF) thermally sprayed WC/Co/Cr coating is considered as an electroplated hard Cr (EHC) coating replacement and Al-based coatings including electrodeposited Al (EDAl), flame sprayed Al (FSAl) and SermeTel 962 are considered as electrodeposited Cd (EC) coating replacements. This is due to the environmental issues surrounding the continued use of the latter two systems. All these coatings were characterised in terms of composition, morphology, microstructure, porosity and corrosion resistance (electrochemical linear polarisation resistance). Surface analytical techniques used included scanning electron microscopy (SEM), energy dispersive X-ray spectroscopy (EDX), X-ray photoelectron spectroscopy (XPS) and focused ion beam scanning electron microscopy (FIBSEM). The feasibility of these coatings to replace EHC and EC coatings has also been identified. When used in-service the hard and the sacrificial coating replacements can be in physical contact making galvanic compatibility of direct importance. In the study, a zero resistance ammeter technique (ZRA) was used to identify the severity and mechanism of galvanic corrosion between these replacement coatings quantitatively. The SermeTel 962 coating presented the best corrosion resistance and barrier protection properties. It also provided the best galvanic compatibility with the HVOF WC/Cr/Co coatings of all the replacement coating systems examined.

Severe local corrosion was observed on the HVOF WC/Cr/Co coating during the galvanic corrosion testing due to Al_2O_3 trapped on the interface of the coating and substrate from previous grit blasting pre-treatment. The corrosion behaviour and mechanisms of HVOF WC/Cr/Co coatings has been studied by electrochemical methods, including potentiodynamic and potentiostatic tests. The effects of Al_2O_3 on the corrosion of the coatings have also been identified. The metallic binder in the coating presented anodic corrosion behaviour during galvanic corrosion and its corrosion rate was also accelerated by electrical connection to Al_2O_3 or immersion in

electrolytes containing Al_2O_3.

An Al_2O_3 film was also considered by Airbus as a final treatment for the HVOF WC/Cr/Co coating to improve its galvanic compatibility with sacrificial coatings due to its low conductivity. Electrolytic deposition and sol-gel deposition were considered to apply the Al_2O_3 film. Electrolytic deposition was suggested to be effective to deposit Al_2O_3 on a steel substrate, but not on the HVOF WC/Cr/Co coating. Sol-gel deposition produced dense and uniform Al_2O_3 film on both steel and HVOF WC/Cr/Co coatings with appropriate pre-treatment.

In addition, electrodeposited Mn-Cu coating has been investigated as a promising replacement for EC coatings. In this study, the electrodeposition processes of Mn-Cu coatings on mild steel has been investigated and optimised by electrochemical methods, such as cathodic polarisation test and galvanostatic deposition. The coatings were also characterised by SEM/EDX, X-ray diffraction (XRD) and linear polarisation resistance (LPR). A dense and uniform Mn-Cu coating containing more than 90 at.% Mn was produced by an optimised process using a modified sulphate based bath.

Keywords:

Galvanic corrosion, SermeTel 962, HVOF WC/Cr/Co coating, Al_2O_3, electrodeposited Mn-Cu coating

Acknowledgements

I would like to take this opportunity to thank many people for their assistance and understanding for the duration of this project.

Firstly, I would like to register my sincere thanks to my supervisor Dr G.D. Wilcox for his continuous support, encouragement with patience and guidance throughout the project. Secondly, I would like to acknowledge Mr A.J. Bastow and Mr D.J. Collins for being my industrial supervisor and Airbus for supplying a truly fascinating project for me to undertake.

I also would like to thank the staff in Department of Materials for assistance and advice; in particular Mr J. Bates, Dr G. West, Dr Z. Zhou and Dr K. Yendall for their valuable technical input; Mr D. Insley, Mr M. Callender and Mr M. Kemp for the realization of my corrosion tester design. Additionally, I also want to appreciate my colleagues with whom I have shared a laboratory over the last year, for their interest, support and discussions.

Finally, but certainly not least, I would like to give thanks to: my parents, Longjian Jiang and Lihua Zhang, for a lifetime of love and support; my wife, Qi Zhang, for always standing by my side throughout my life time.

Abbreviations

ABP	Airbus process
AIPS	Airbus process specification
AMS	Aerospace material specification
APS	Atmospheric plasma spraying
ASTM	American standards for testing materials
BS	British Standard
CP	Cold press
EBC	Environmental barrier coating
EC	Electrodeposited cadmium
EDAl	Electrodeposited aluminium
EDX	Energy dispersive X-ray spectroscopy
EEC	European Economic Community
EHC	Electroplated hard chromium
EIS	Electrochemical impedance spectroscopy
EN	Electroless nickel
FEGSEM	Field emission gun scanning electron microscopy
FSAl	Flame sprayed aluminium
FIBSEM	Focused ion beam scanning electron microscopy
GCA	Galvanic corrosion assembly
HVOF	High velocity oxygen fuel
IBAD	Ion beam assisted deposition
IVD	Ion vapour deposition
LPR	Linear polarisation resistance
MAO	Microarc oxidation
OCP	Open circuit potential
PVD	Physical vapour deposition
SCE	Saturated calomel electrode
SEM	Scanning electron microscopy
SIMS	Static ion mass spectroscopy
SVET	Scanning vibrating electrode technique
TEM	Transmission electron microscopy
TS	Thermal spray
XPS	X-ray photoelectron spectroscopy
XRD	X-ray diffraction
ZRA	Zero resistance ammeter

Symbols

at.%	Atomic percent
Al	Aluminium
Al_2O_3	Alumina
$Al_2(NO_3)_3$	Aluminium nitrate
$Al_2(SO_4)_3$	Aluminium sulphate
cm	Centimetre
C	Carbon
$CaCl_2$	Calcium chloride
Cd	Cadmium
CdO_2	Cadmium oxide
$CdCl_2$	Cadmium chloride
Co	Cobalt
Cr	Chromium
Cu	Copper
$CuSO_4$	Copper sulphate
E_{corr}	Free corrosion potential
Fe	Iron
$FeCl_3$	Ferric chloride
h	Hour
H	Hydrogen
HNO_3	Nitric acid
H_3PO_4	Phosphoric acid
H_2SO_4	Sulphuric acid
I_{corr}	Corrosion current
KCl	Potassium chloride
$KMnO_4$	Potassium permanganate
L	Litre
m	Metre
M	Mole per litre
Mg	Magnesium
min	Minute
Mn	Manganese
MnO_4	Manganese oxide
$MnSO_4$	Manganese sulphate
mM	Millimole per litre
mm	Millimetre
mV	Millivolt
mA	Milliampere
NaCl	Sodium chloride

NH_3	Ammonia
NH_4Cl	Ammonium chloride
NH_4F	Ammonium fluoride
NH_4NO_3	Ammonium nitrate
$(NH_4)_2SO_4$	Ammonium sulphate
Ni	Nickel
O	Oxygen
OH	Hydroxyl
℃	Celsius degree
P	Phosphorus
R_p	Linear polarisation resistance
s	Second
Si	Silicon
Sn	Tin
V	Volt
µ	Micro-
Ω	Ohm
W	Tungsten
WC	Tungsten carbide
wt.%	Weight percent
Y	Yttrium
Zn	Zinc
ZnO	Zinc oxide
Zr	Zirconium

CHAPTER 1: INTRODUCTION

1.1 Background

EHC and EC coatings are utilised in the aerospace industry for improving surface mechanical properties and corrosion resistance respectively. They are also utilised in areas where they are in physical contact for example on aircraft landing gear (Figure 1). However, due to the high toxicity of the coating processes and the actual materials themselves, alternative more environmentally friendly coatings, are being investigated to examine the feasibility of wholesale replacement of EHC and EC coatings. Airbus, as project drivers suggested HVOF WC/Co/Cr as a replacement for EHC coatings while Al-based coatings, including EDAl, FSAl and SermeTel 962 (Al/P/Cr) coatings as alternatives for EC. However, in previous investigations, Airbus found that in some cases, where these replacement coatings were applied to the same part and were in contact, galvanic bimetallic corrosion arose, in particular on the anodic sacrificial coatings. Al-based coatings usually present anodic corrosion behaviour during galvanic corrosion. In this way, Al phases may be transformed into Al_2O_3 corrosion products, which reduce the sacrificial protection property of coatings significantly. Therefore, it is necessary to identify the galvanic corrosion resistance of Al-based coatings as replacements for sacrificial EC coating.

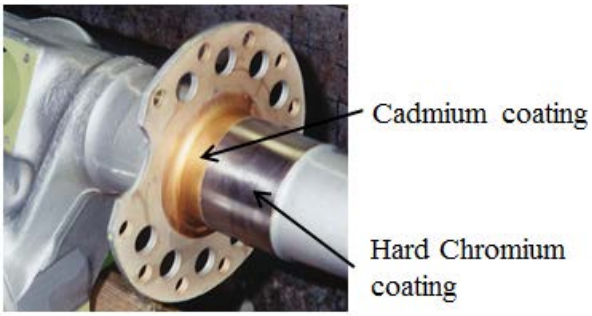

Figure 1. A landing gear component with EC and EHC coatings in physical contact[1]

As an EHC coating replacement, thermal spray coatings applied by HVOF process are

used in a diverse range of engineering applications to improve wear resistance. HVOF coatings have also been reported to present good bond strength, low residual stresses and low porosity[2]. In galvanic corrosion systems suggested by Airbus, HVOF WC/Cr/Co coating was expected to act as a cathode in contact with various sacrificial coatings. However, the active metallic binder (Co-Cr) of HVOF WC/Cr/Co coating could present some significant negative effects on the corrosion behaviour of the coating.

It has also been suggested by Airbus that an Al_2O_3 layer may be applied on a HVOF WC/Cr/Co coating as an insulating treatment to improve its galvanic corrosion resistance. Electrolytic deposition and sol-gel deposition have been considered to be simple, easy to adopt and require low processing temperatures. These two methods are also appropriate to apply the Al_2O_3 layer due to their low level of damage to the substrate compared to traditional thermal spray processes.

In addition to the Al-based coatings, Mn alloy coatings also appear quite promising since they are sufficiently active to provide sacrificial protection to steel components. A significant problem with Mn-based coatings is a phase transformation from an as-deposited ductile γ-phase to a brittle α-phase after few weeks at ambient temperature[3, 4, 5]. In this aspect, Cu has been suggested to be capable of stabilising the ductile γ-phase of Mn[6]. Airbus also proposed electrodeposited Mn-Cu coating as an EC replacement. Therefore, a further investigation into electrodeposition of a Mn-Cu coating and an examination of its performance was undertaken.

1.2 Research Objectives

According to the requirement of Airbus (project sponsor), the first aim of this programme was to investigate the severity of galvanic corrosion in HVOF (WC/Cr/Co)/Al-based coating couples by quantitative electrochemical methods. The replacement coating systems were also compared with original EHC and EC coatings

under similar circumstances to identify the feasibility of the replacement coatings. Both the original and replacement coatings were characterised in terms of composition, morphology, microstructure, porosity and corrosion resistance (LPR). A ZRA technique was used for monitoring the electrode potential of the sacrificial coating and the galvanic current of the couple over a period of 15 days in 3.5 wt.% NaCl to quantify the level of galvanic activity. All the coatings were characterised after the galvanic corrosion experiments to observe changes in the morphology and composition of the coating surfaces. SEM, EDX, XPS and FIBSEM), XRD and TEM were used for this characterisation.

The second aim was to identify the corrosion resistance and mechanism of HVOF WC/Cr/Co coatings in a neutral solution. Electrochemical methods, including anodic polarisation and potentiostatic tests, were utilised to indicate the anodic corrosion behaviour of the coating. The HVOF WC/Cr/Co coatings were characterised by SEM/EDX after the electrochemical investigations. During the galvanic corrosion of the HVOF WC/Cr/Co coating coupled with the sacrificial coatings, it was occasionally found that Al_2O_3 particles trapped at the interface of the coating and substrate caused a severe local corrosion of the coating. Therefore, the effects of Al_2O_3 particles on the corrosion of HVOF WC/Cr/Co coatings were also investigated by electrochemical analysis and immersion tests.

The third aim of the programme was to identify the feasibility of electrolytic deposition and sol-gel deposition to apply an Al_2O_3 layer on HVOF WC/Cr/Co coating. The electrolytic deposition of Al_2O_3 was investigated by cathodic polarisation test and galvanostatic deposition. All the Al_2O_3 layers were characterised by SEM/EDX.

The last experimental aim was to investigate and optimise the electroplating processes for Mn-Cu to produce a dense and uniform deposit with high Mn content. The optimisation of the electroplating bath was carried out by identifying its cathodic

behaviour with different chemical constituents and concentrations. The electroplating parameters including current density, time and agitation were adjusted following galvanostatic deposition. All the coatings were characterised in terms of morphology and composition (SEM/EDX). The coatings produced from an optimised process were also identified for general corrosion resistance (LPR), crystalline structure (XRD) and corrosion behaviour in a glycol-based aircraft de-icing fluid (immersion test).

CHAPTER 2: LITERATURE REVIEW

2.1 Effects of Electroplated Coating Systems on the Environment

Metal finishing operations such as electroplating and conversion coating are widely applied in the aerospace industry. Metal finishing operations onto metal and non-metal substrates are recognised as an essential step in the manufacture of many components by improving mechanical properties, lengthening component life, and reducing manufacturing and maintenance costs. EC and EHC coatings have been widely accepted to provide high corrosion and wear resistance respectively for more than 60 years. However, with the increasing concern over the toxicity and carcinogenicity of Cd and Cr ions, electroplating processes (especially Cr and Cd) are recognised as a major source of environmental pollution. Electrolytic Cd and Cr plating processes produce environmental hazards in many ways. Air emissions and skin contact from electroplating solutions results in direct human exposure, which is carcinogenicity. Large volumes of toxic waste are produced, including waste rinse water, spent electroplating solutions, spent acids and bases used in cleaning and pre-treatment. Additionally, during repair and maintenance operations of Cd and Cr electroplated military equipment, prior to rebuilding, all the old coatings must be removed by anodic caustic or acid stripping, which produces a toxic waste stream. Due to the toxicity and carcinogenicity of Cd and Cr, before disposing of spent solutions and contaminated water, all toxic materials must be removed by precipitation and evaporation and shipped to a toxic waste dump. So electroplated Cd and Cr have to be applied under severe scrutiny and regulation, thus increasing costs and potentially chemical risks.

2.2 Cd

Cd is a soft, ductile and bluish-white metal found in group 12 of the Periodic Table. It is

chemically similar to Zn which is also in the same periodic group. It prefers the +2 oxidation state in most of its compounds (as Zn does) and exhibits a low melting point compared to transition metals. It is one of the rarer elements in the earth's crust at an average concentration of between 0.1 and 0.5 ppm.

Cd was originally discovered as an impurity in zinc carbonate. In nature, it occurs as a minor component in most Zn ores in a Zn/Cd ratio of approximately 100:1 and therefore Cd is a byproduct from the smelting and refining of Zn ores. Cd was used for a long time as a pigment and as a corrosion resistant coating on steel and its compounds were used to stabilize plastic. Until recently, it was an important metal with widespread use throughout industry in a broad range of products and applications such as Ni-Cd batteries, TV tubes, Cd telluride solar panels, a metallic alloying element and as a catalyst. Environmental concerns have limited many of these uses.

2.2.1 Toxicity of Cd

As a pollutant, Cd can be released into the environment from fossil fuel combustion, phosphate fertilizers, natural sources, iron and steel production, cement production, nonferrous metal production and electroplating. Smelting and refining of metallic ores, electroplating and the manufacture or reprocessing of Cd containing alloys are thought to be the main sources of Cd emissions. The most dangerous form of occupational exposure to Cd is inhalation of fine dust and fumes, or ingestion of highly soluble Cd compounds, which can result initially in metal fume fever but may progress to chemical pneumonitis, pulmonary edema and death[7]. Moreover, during the 1960's there was increasing concern that Cd might be related to cancer of the prostate and lung. The studies of the controlled laboratory tests on rats, mice and hamsters[8] indicated that occupational exposure to Cd in some form (possibly as the oxide) increased the incidence of prostate and respiratory tract cancers, whilst cumulative exposure was linked to lung cancer.

With the increasing concern for the toxicity and carcinogenicity of Cd, a publication was issued by Her Majesty's Inspectorate of Pollution[9], in which maximum airborne releases of Cd were set at 0.05 mg/m^3 for processes involving the use of Cd or any of its compounds. For minimising aquatic releases of Cd, several methods have been proposed, such as ion exchange on zeolites, adsorption on activated charcoal, binding by immobilised algae and cathodic reduction[10]. An electrochemical treatment by fibrous carbon electrodes was reported as a complementary method to the already existing ones[10]. This method can reduced Cd concentration efficiently from several tens of ppm to a ppb level.

2.2.2 EC Coatings

EC coatings are usually electroplated from alkaline cyanide solutions at temperatures in the range of 15~30 ℃. Stringent controls are necessary for the use of cyanide baths due to their high toxicity, which is an obvious drawback of the process. Additionally, the coated steel can undergo hydrogen embrittlement due to H_2 evolution during the electroplating process, which results in the need for subsequent heat-treatment. Acidic fluoroborate electroplating solutions can also be used to prevent the build-up of internal stresses within steel components. Post-treatments such as etching, passivation and brightening can be carried out as necessary.

During the electroplating process, Cd may be released into the environment through a number of ways. The most likely of these ways are releases from the drag-out tank, which is used to rinse the coated steel to remove any residual electrolyte. It is possible that Cd can be released from the post-treatment of the coatings and addition of Cd compounds to the electroplating solution for adjustment of compositional levels. According to Her Majesty's Inspectorate of Pollution[9], it is important to minimise Cd emissions, such as recycling or re-using waste and contaminated water, and treatment of wash water by electrolytic recovery, ion exchange or membrane processes.

2.2.2.1 Advantages

Cd electroplating is currently widely applied in the aerospace industry for corrosion protection of airframe components and fasteners made from steel. EC coatings offer excellent barrier protection, which can be further improved by chromate passivation.

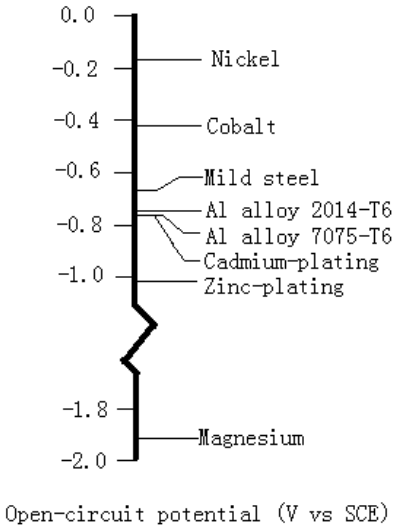

Figure 2. Open-circuit potential of various metals and alloys in quiescent 600 mM NaCl solution at 25 ℃[11]

Figure 2 shows that Cd has good sacrificial properties, with a more negative open-circuit potential (OCP) than that of steel and a similar value to Al and its alloys. Therefore Cd can provide good sacrificial protection to steels and reduce the risk of damage to Al alloys through galvanic corrosion. The high inherent lubricity of EC coatings also makes them important for protecting fasteners because only moderate torque values are needed to obtain the required bolt clamping loads, even without the use of lubricants. Additionally, Cd produces less voluminous corrosion products than Zn, which is beneficial in overcoming the problem of seizure commonly associated with Zn coated fasteners. In this way, EC coatings may be able to remain intact after repeated tightening and untightening of fasteners. Cd is also easily soldered and compatible with most types of solder without the use of aggressive fluxes[12]. It can be easily painted and damaged coatings can also be repaired effectively by means of brush electroplating.

2.2.2.2 Disadvantages

Despite all of the excellent properties, due to its high toxicity, current legislation dictates that Cd must be reduced to minimal levels, and there have been attempts to ban the metal entirely in some countries. In an EEC commission directive[13], it stated that the use of Cd should be banned on equipment and machinery for use in the food industry, agriculture, household goods, general engineering and many other applications. Moreover, the discharge levels of waste and effluent of Cd from industrial processes have fallen over the last 30 years and are currently extremely low. Therefore several treatments become necessary to remove all traces of Cd before discharge, making Cd a relatively expensive metal to electrodeposit. Additionally, Cd has excellent corrosion performance in marine atmospheres, but in sulphurous industrial atmospheres its corrosion resistance is lower.

2.2.3 Replacements for EC Coatings

A great deal of work has been carried out to find suitable replacements for EC coatings. The alternatives are mainly based on Zn alloy electrodeposits, Al-based coatings and composite coatings consisting of metallic particles in an inorganic matrix.

2.2.3.1 Zn Alloys Coatings

Electrodeposited Zn coatings are an obvious choice to replace EC coatings on steels, due to their sacrificial protection because they are more electrochemically negative than steels. However, as mentioned previously, voluminous corrosion products from Zn can cause the seizure of threaded fasteners. Zn's electrochemical negativity can easily lead to galvanic corrosion between Zn coatings and underlying substrates when the Zn coating is damaged in some way, which reduces the overall level of protection

due to accelerated sacrificial dissolution. One way to alleviate this is to alloy more noble metals, (such as Co, Ni and Sn) with the Zn in an electrodeposited alloy coating.

2.2.3.1.1 Zn-Ni Coatings

Zn-Ni can be deposited from either acidic or alkaline solutions, which are typically based around sulphate and chloride salts, without the addition of cyanides[14]. A dual anode system is employed to replenish spent ions in an acid solution. They tend to deposit high Ni concentrations of 8-15 wt.%, but the coatings are non-uniform due to poor current density distribution. Alkaline solutions were developed to obtain more uniform alloy compositions, and give deposits containing 5-9 wt.% Ni. As well as dual anode systems, some alkaline processes use a single Zn anode and Ni ions need periodic replenishment by the addition of a concentrate.

Corrosion protection properties of Zn-Ni alloy coatings depend on the Ni content. It was noted that alloy coatings containing 13 % or less Ni protected steel in a sacrificial manner, but with an increase in a Ni content to more than 15 % this is lost, the coating became more noble offering only barrier protection to the steel[14]. The 12 wt.% Ni alloy coatings are of particular interest as a potential replacement for Cd, since their electrochemical potential is similar to that of Al and Cd[15]. A potential problem with these alloy coatings is that chromate passivation treatments of Zn-Ni alloy coatings are necessary to suppress the dezincification process and improve its corrosion resistance[14]. Moreover, some new regulations[16] limit the usage of Ni or some of its compound due to possible environmental problems caused by them.

2.2.3.1.2 Zn-Co coatings

Zn-Co alloys were reported as deposited from acidic chloride electrolytes with additions of KCl, H_3BO_3 and NH_4Cl. These electrolytes can give deposits with a wide

range of Co contents from 0.7 to 32 wt.%[17]. The deposits with a Co content less than 1 wt.% presented angular grains. The morphology of the deposits transformed into nodular dense grains with increase in Co content and it was noted to be a homogeneous and featureless nano-crystalline structure as the Co content reached 32 wt.%. It was reported that Zn-Co alloys with >30 wt.% Co showed higher corrosion resistance than other alloys with low Co content[17].

A ternary Zn-Ni-Co (6.9 wt.% Ni, 3.9 wt.% Co) coating was electrodeposited by Eliaz et al. from an acid bath of chloride salts, sulphanilic acid and gelatin[18]. From their potentiodynamic polarisation scans and electrochemical impedance spectroscopy analysis, the corrosion resistance of the Zn-Co-Ni coating proved to be approximately 10 times higher than that of the Zn-Ni (9.2 wt.% Ni) coating and 7 times higher than that of Zn-Co (9.7 wt.% Co) coating[18]. It was suggested that the co-deposition of Co and Ni resulted in a change in the phase content, the crystal orientation and a finer grain size, which improved corrosion resistance compared to the binary Zn-Ni and Zn-Co coatings. However, as a similar problem with Ni, the future use of Co alloy coatings is uncertain due to limitation of environmental regulations.

2.2.3.2 Al Based Coatings

Al based coatings have attracted more and more attention as an EC coating replacement during the last decades due to its excellent corrosion resistance. Similar galvanic potentials permit their application on Al alloys to eliminate galvanic corrosion in aerospace application. Moreover, Al based coatings are easily anodised and the oxide layers shows good mechanical properties and decorative appearance[19]. Al coatings can be produced by a number of methods, including electrodeposition, vapour deposition, sputtering and metal spraying.

2.2.3.2.1 Electroplated Al Coatings

Electrodeposition of Al is not carried out from conventional aqueous electrolytes, but from non-aqueous electrolytes, and in an inert nitrogen atmosphere due to the high activity and negative reduction potential of Al. The coatings obtained are very dense and exhibit good substrate adhesion. Chang et al.[20] reported that a dense, continuous, and adherent Al layer was electrodeposited on a Mg alloy from an aluminium chloride ($AlCl_3$)-1-ethyl-3-methylimidazolium chloride (EMIC) ionic liquid.

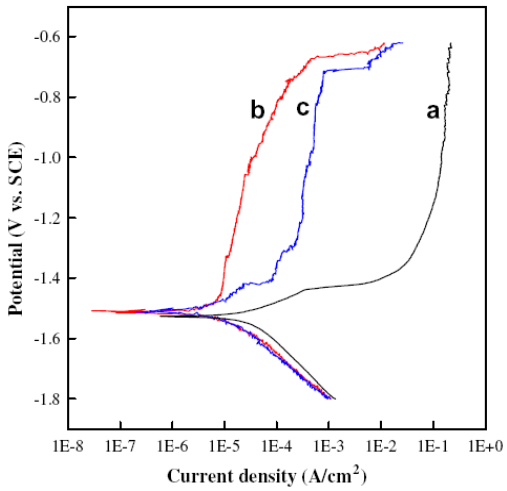

Figure 3. Potentiodynamic polarization curves of (a) bare Mg alloy, (b) -0.2 V Al-deposited sample, (c) -0.4 V Al-deposited sample. The measurement was performed in 3.5 wt.% NaCl solution[20]

From Figure 3, compared to the value for the bare Mg alloy, the LPR, R_P, of the -0.2 V Al-coated sample was much higher, which indicated that the Al coating led to an improvement in corrosion resistance. The authors also pointed out that a high deposition rate would bring about a 'loose structure' and small cracks within the Al layer and consequently cause a reduction in its protective capability.

Al coatings applied by electrodeposition from ionic liquids have been demonstrated to effectively enhance the corrosion resistance of steel substrate materials due to the sacrificial protection of the Al and its ability to form a stable oxide film on its surface[20]. In the early 1950s, it was proposed that Al can be deposited from room temperature molten salts based on $AlCl_3$[21]. In commercial applications, electroplating of Al is based

on organic solvents such as alkylaluminium compounds in toluene at 100 ℃ and $AlCl_3$ and $LiAlH_4$ in tetrahydrofurane[19]. However, these processes are not regarded as environmentally compliant because the AlR_3 compounds are self-combustible and explosive. Therefore, electrodeposition of Al from $AlCl_3$ based ionic liquids has been of increasing interest since the 1980s. These liquids allow the deposition of Al in a non-flammable environment.

Bardi et al. have successfully electrodeposited Al on P90 Al-Li alloys from a chloroaluminate ionic liquid (1-butyl-3-methyl imidazolium heptachloroaluminate $[BMIm]Al_2Cl_7$) to improve their corrosion resistance[22]. It was found that due to the high activity of Al-Li, if exposed to air, the alloy rapidly formed an alternating layer containing $Al_2O_3/Al(OH)_3$ and lithium carbonate. This was thick enough to prevent the homogeneous electrodeposition of Al, the latter growing only as islands scattered on the surface, leaving the main part of the sample uncoated (Figure 4A). Polishing the samples inside a glove box, where water and oxygen contents were below 5 ppm, prevented oxidation and contamination and allowed the electrodeposition of a dense, homogeneous and well adhering Al layer (Figure 4B).

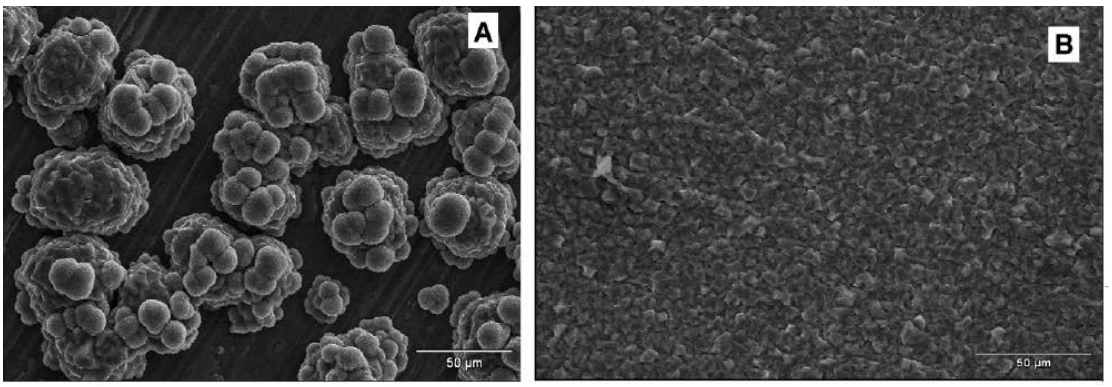

Figure 4. SEM micrograph of electrodeposited Al produced from $[BMIm]Al_2Cl_7$ at room temperature on (A) untreated Al-Li alloy (B) polished Al-Li alloy without oxidation[22]

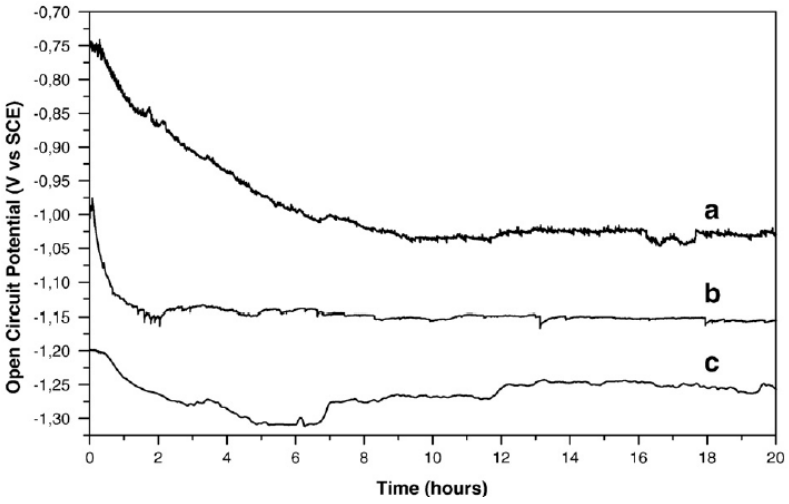

Figure 5. OCP curves as a function of time of (a) pure Al, (b) Al-electroplated Al-Li alloy and (c) bare Al-Li alloy in aerated 3.5 wt.% NaCl at room temperature[22]

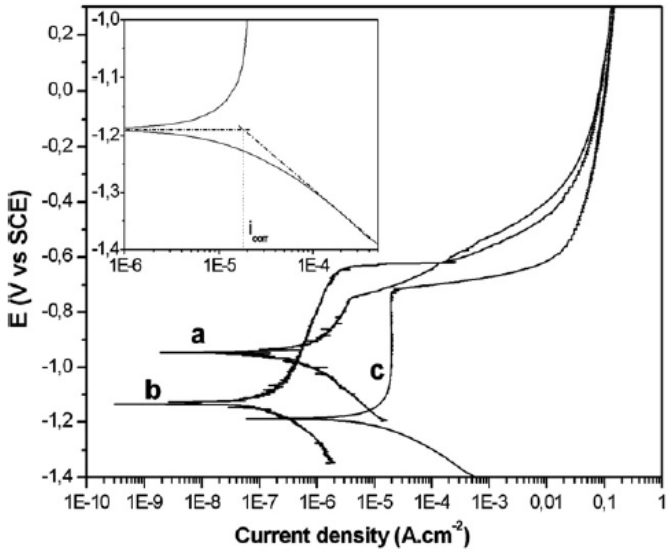

Figure 6. Potentiodynamic anodic polarization curves (scan rate 0.3 mV/s) of pure Al (a), Al-electroplated Li-Al (b) and bare Li-Al (c) samples. The curves are recorded in aerated 3.5 wt.% NaCl solutions at room temperature. The inset shows the evaluation of I_{corr} for the bare P90 sample[22]

The OCP curves of pure Al, Li-Al alloy and Al-electroplated Li-Al in 3.5 wt.% NaCl were characterised by an initial period of time where the potential shifted towards more negative values[22] (Figure 5). For Al, other authors have suggested this to be a result of the degradation of the surface Al_2O_3 layer via the formation of nanopores and the adsorption of Cl^-[23, 24]. The potentiodynamic anodic polarisation curve of the Al coating presented a wide passive region extending from close to the corrosion potential (E_{corr}) to approximately -0.7 V, followed by a sudden increase of the current,

due to the breaking down of the passive Al_2O_3 layer and the start of pitting corrosion (Figure 6). Al-electroplated Al-Li alloys presented a much lower corrosion current density compared to bare Al-Li alloy.

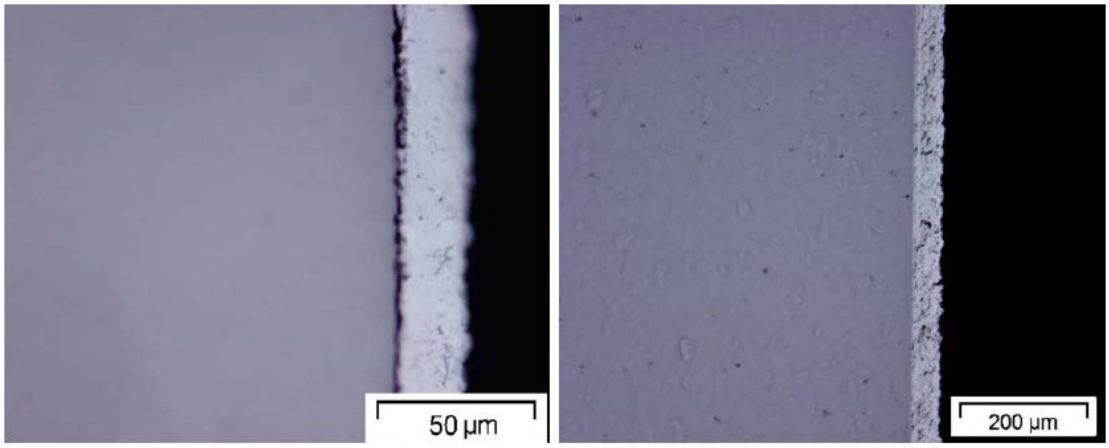

Figure 7. (a) Optical cross-section of 20 µm thick Al coating on steel obtained galvanostatically at 20 mA/cm^2 for 2 h. (b) Optical microscopy cross-section of 40 µm thick Al produced at 20mA/cm^2 on mild steel with significant adherence improvement due to in-situ electrochemical etching. The electroplating bath was based on [EMIm]Cl/$AlCl_3$ (40/60 mol.%).[25]

Liu et al. employed the Lewis acidic 1-ethyl-3-methylimidazolium chloride [EMIm]Cl/$AlCl_3$ (40/60 mol.%) ionic liquid for the electrodeposition of Al onto mild steels[25]. It was found that the pre-treatment of the substrates had significant effects on the coating adhesion. The Al coating deposited on the conventionally pre-treated mild steel surface looked uniform in thickness, but presented poor adhesion to the steel surface (Figure 7 (a))[25]. Poor adhesion may have resulted from a thin iron oxide layer forming after the last pre-treatment step. The oxide layers chemically dissolve during aqueous electrodeposition through the use of acidic solvents. However, the oxide layer does not dissolve in ionic liquids, which subsequently prevents adherent deposition of Al. For removal of the pre-formed iron oxide layer, in-situ electrochemical etching was employed on the mild steel surface at 20 mA/cm^2 for 4 h[25]. It is obvious that the uniform Al coating was well adhered to the in-situ electrochemical etched mild steel substrate without any observable crevices between substrate and coating (Figure 7 (b)). During the in-situ electrochemical etching, iron ions were formed prior to the

deposition of the Al on the mild steel. It was presumed that at the initial stage of deposition of Al, subsequently Fe ions close to the surface resulted in an Al-Fe codeposit at the interface, which produced strong adhesion between the mild steel surface and the deposited Al.

2.2.3.2.2 Flame Sprayed Al Coatings

It has been reported that thermally sprayed Al coatings have a high potential for surface modification of Mg alloys and are promising materials in the automotive industry due to their lightweight[26]. The corrosion resistance of Mg-Al alloys was improved by a thermally sprayed Al coating due to the formation of Al rich oxides and networks of β-phase ($Mg_{17}Al_{12}$)[27]. In general, thermally sprayed Al coatings are quite uniform in thickness and there is no phase transformation with respect to the original powder during the thermal spraying process. The interfacial reaction of Al coatings with the substrate can be controlled by post-coating heat treatments and the high level porosity of the coating can also be reduced by post-treatment methods, such as cold-pressing[27]. Pardo et al.[26] investigated the corrosion behaviour of thermally sprayed Al on commercial Mg-Al (AZ31, AZ80 and AZ91D) alloys and the effect of a cold-pressing post-treatment (CP) on the morphology and corrosion performance of the coatings. SEM secondary electron micrographs of cross-sections of the Al thermal sprayed (Al-TS) coatings (Figure 8), indicated a very rough surface with interconnecting pores randomly distributed within the layer. Poor bonding was also evident at the substrate/coating interface. The sand blasting pre-treatment also resulted in a rough substrate/coating interface. The CP post-treatment for Al-TS coatings produced smoother and more homogeneous surfaces. Figures 8 (b) and 9 (b) also reveal the absence of cracks and pores within the coating and at the substrate/coating interface. Cold-pressing was therefore effective in reducing the porosity and improving the bonding of the coating to the substrate.

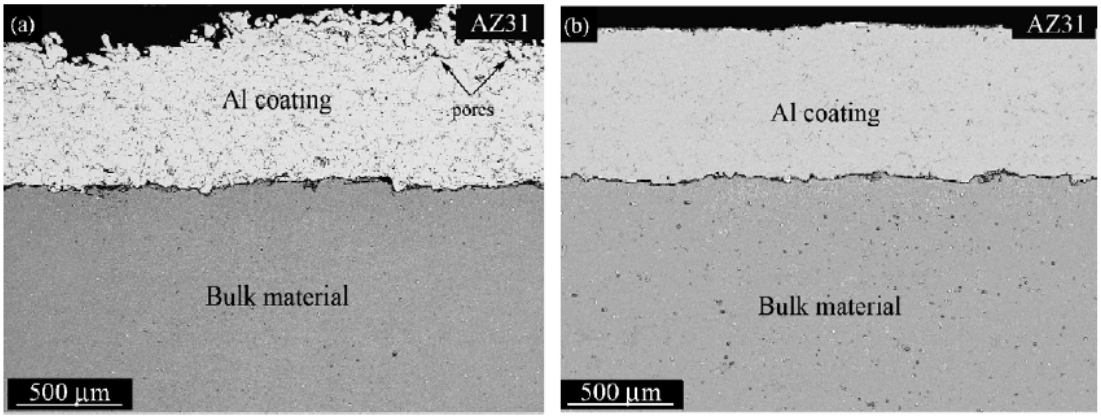

Figure 8. Backscattered scanning electron micrographs of the cross-sections of (a) Al-TS and (b) Al-TS+CP coatings on a Mg-Al alloy substrate[26]

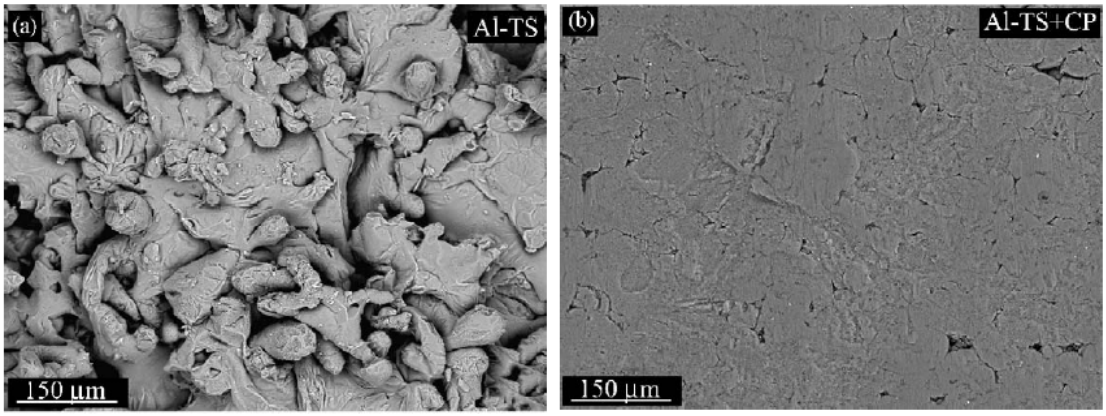

Figure 9. Scanning electron micrographs of the surface morphology of Al-coatings on a AZ31 Mg-Al alloy: (a) Al-TS and (b) Al-TS+CP coatings[26]

In the corrosion behaviour investigation of the Al-TS coatings, they exhibited mass gain during the immersion test in 3.5 wt.% NaCl solution. It was suggested that the interconnecting pores in these coatings facilitated the penetration of chloride ions with subsequent corrosion attack and formation of Al corrosion products. So it was thought that an inferior corrosion protection was provided by the Al-TS coatings. The CP coatings revealed significantly lower values of mass gain and improved corrosion performance due to the elimination of interconnecting pores within the layers. The Al-TS+CP coatings presented lower corrosion rates (1.5×10^{-2} mg $\cdot$ cm$^{-2} \cdot$ h^{-1}) than the Al-TS coatings ($> 6.0 \times 10^{-2}$ mg $\cdot$ cm$^{-2} \cdot$ h^{-1})[26]. Anodic and cyclic polarization curves of Al-TS, Al-TS+CP and Mg alloys in 3.5 wt.% NaCl solution showed that the corrosion current density of Al-TS coatings were similar or even higher than untreated

AZ80 and AZ91D alloys (Figure 10). This could be caused by the galvanic acceleration of the corrosion of Mg of the alloy substrates due to penetration of the electrolyte through the interconnecting pores in the Al-TS coatings.

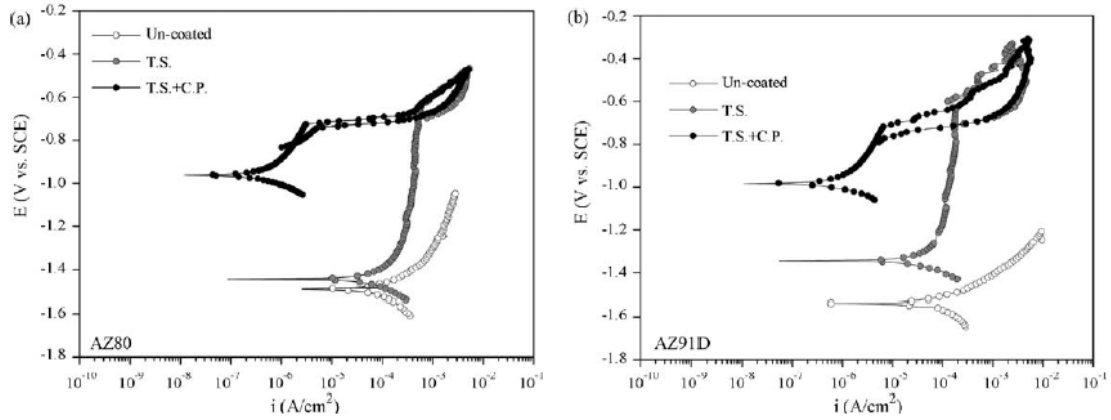

Figure 10. Anodic and cyclic polarization curves in 3.5 wt.% NaCl solution for 7 days (a) AZ80 Mn-Al alloy with Al-TS coatings and (b) AZ91D Mn-Al alloy with Al-TS coatings[26]

The R_p values of Al-TS+CP coatings were higher than those of untreated substrates and Al-TS coatings by one to three orders of magnitude as shown in Table 1. Increase of R_p with immersion time was suggested to result from the nucleation and growth of a slightly protective layer of Al-rich corrosion products over the coating surface that offered additional electrochemical resistance.

Table 1. Variation of R_p for Mg and Mg alloys with Al-TS coatings as a function of the immersion time in 3.5 wt.% NaCl solution[27]

Material		R_p (kΩ*cm^2)			
		1 h	1 day	3 days	7 days
Mg (99%)	Un-coated	0.02	0.03	-	-
	TS	0.22	0.21	0.14	-
	TS + CP	16.3	26.4	108	110
AZ31	Un-coated	0.35	0.32	0.24	0.11
	TS	0.17	0.21	0.19	0.28
	TS + CP	16.3	64.8	119	120
AZ80	Un-coated	5.30	2.96	2.12	0.30
	TS	0.18	0.24	0.34	0.38
	TS + CP	14.0	53.4	60.2	90.0
AZ91	Un-coated	1.30	0.88	0.31	0.16
	TS	0.18	0.29	0.41	0.52
	TS + CP	15.0	50.1	72.8	92.0

2.2.3.2.3 Physical Vapour Deposited (PVD) Al Coatings

PVD of Al is utilised in the aerospace industry. An improved PVD process called ion vapour deposition (IVD) has also been developed for applying Al[28]. Coatings produced by these methods offer good substrate adhesion but tend to be porous due to their columnar grain structure, so the coatings do not perform well in salt fog or immersion tests. Peening with glass beads has been used to seal these pores and provide a denser coating, which helps to improve corrosion resistance. IVD Al coatings and EC coatings were said to have similar OCP[28]. So IVD Al coatings usually provide good sacrificial protection to steel substrates. Additionally, due to the non-electrochemical process of IVD, no H_2 was introduced into the coating or substrate during the coating process. IVD Al coatings also provided better oxidation and sulphidation resistance than Cd[28], so they can be used at higher temperatures.

2.2.3.3 Metal-Inorganic Composite Coatings

Metal-inorganic composites are also suggested to be suitable alternatives to electrodeposited cadmium. Metal-inorganic composite coatings consist of a sacrificial

metal in an inorganic matrix in flake or powder form. The matrix is usually based around a phosphate and chromate slurry. The coatings are usually applied by dip-spin or dip-drain procedures and then baked to consolidate the structure.

The SermeTel 962 coating consisting of densely packed Al particles in a chromate/phosphate inorganic binder was investigated by Robinson and Figueroa[29]. The coating was cured at 315 ℃ to give a total thickness of 70 μm.The micrograph shown in Figure 11 indicates that the SermeTel 1140/962 coatings contained pores, mostly at the coating/substrate interface. These pores are thought to have formed during the drying of the inorganic binder in the curing process. The results of a $KMnO_4$ porosity test revealed that the SermeTel 1140/962 appeared to be relatively free of through-thickness coating defects (Figure 12). So these pores were mostly closed, rather than interconnecting.

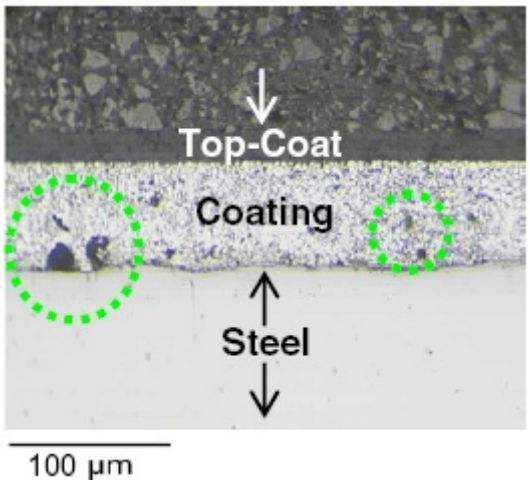

Figure 11. Cross-section through a SermeTel 1140/962 coating showing pores (circles indicate major discontinuities in the coating)[29]

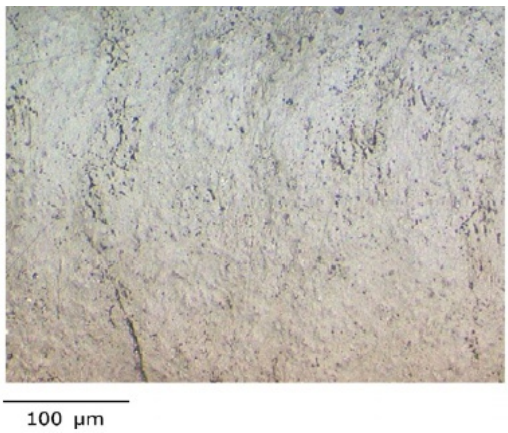

Figure 12. Micrograph of the surface appearance of SermeTel 1140/962 coating after 3.5 h immersion in dilute $KMnO_4$ solutions[29]

A modified polyurethane top-coat was applied to enhance the corrosion resistance and barrier properties of the coating. Figure 13 shows open-circuit trends for Cd and SermeTel 1140/462 coatings in 3.5 wt.% NaCl solution. The OCP of the Cd maintained an almost constant value in the range -750 to -725 mV (SCE) and the surface appeared unaffected. The potential of the SermeTel 962 was in the range -800 to -725 mV (SCE) and slightly more active than the Cd for the first 900 hours of the test, it then became progressively more noble, ending at -650 mV (SCE), which was close to the potential value of freely corroding steel. So the SermeTel 962 coating was no longer sufficiently active to provide sacrificial corrosion protection to the substrate at this point. So it can be suggested that Cd coatings presented better corrosion resistance in a long-term application than SermeTel 962 coatings.

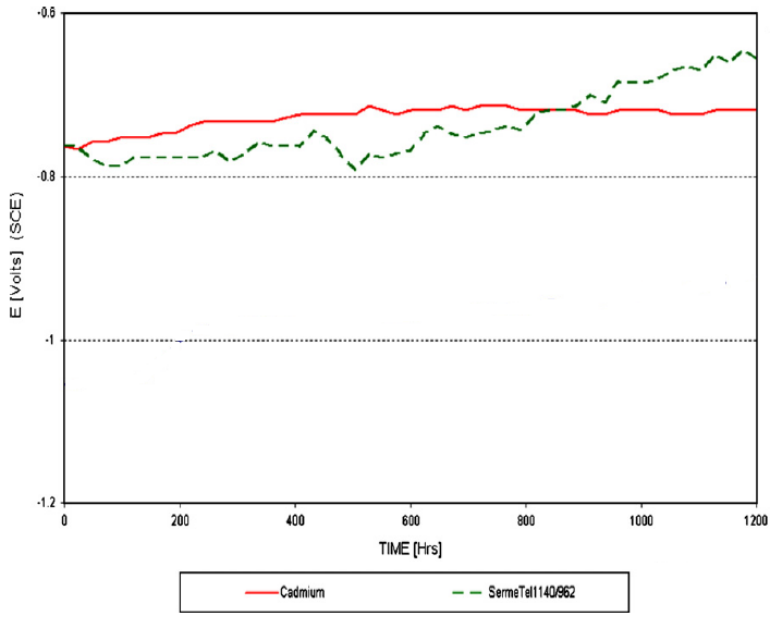

Figure 13. Comparison of the OCP of Cd and SermeTel 1140/962 coatings during 1200 h immersion in 3.5 wt.% NaCl[29]

2.3 Cr

Cr is a grey, lustrous, hard metal with a high melting point. It has been regarded as an important metal due to its high corrosion resistance and hardness. Steel could be made highly resistant to corrosion and discoloration by adding Cr to form the so-called stainless steels. Electroplated Cr is currently the highest-volume use of the metal. Cr is the 21st most abundant element in the Earth's crust with an average concentration of 100 ppm[30]. Cr exhibits a wide range of possible oxidation states. The most common are +3 and +6, with +3 being the most stable. The relation between Cr (III) and Cr (VI) strongly depends on pH and the oxidative properties of the location. Cr is easily passivated by oxygen in air, forming a thin protective oxide surface layer, which is dense and prevents the diffusion of oxygen into the underlying material. Cr is widely used as an alloying element for steel, electroplating and passivation processes to increase corrosion resistance and hardness. It was also widely applied in dyes and pigments for aesthetic purposes due to its colourful compounds. Hexavalent Cr is toxic and carcinogenic, so the use of Cr from hexavalent sources is severely controlled.

2.3.1 Toxicity of Cr

Trivalent Cr compounds and Cr metal are not regarded as serious health hazards, however, the high toxicity and carcinogenic properties of hexavalent Cr have been known for a long time. Several in-vitro studies indicated that high concentrations in cells can also lead to DNA damage[31]. The acute toxicity of hexavalent Cr is due to its strong oxidation properties. It damages kidneys, the liver and blood cells through oxidation reactions after it reaches the blood stream. Chromate dust is also known for its carcinogenity.

2.3.2 EHC Coatings

Cr coatings are often used for their aesthetic qualities or engineering properties depending on thickness. Thin Cr coatings (< 1 μm) are used for decorative purposes, whilst thick ones are employed to improve wear and abrasion resistance. EHC, also known as industrial Cr electroplating, is used to reduce friction, increase wear and corrosion resistance. It has a high hardness of at least 1000 HV and higher thickness than the decorative treatment with a thickness typically ranging from 75 to 250 μm[32]. The Cr electroplating process generally consists of three different stages: degreasing and manual cleaning to remove all residual traces of dirt and impurities on the substrate; various pre-treatments depending on the substrate to increase adhesion of the coating; placement into the Cr electroplating bath, which typically consists of Cr trioxide and sulphuric acid at an operating temperature of 45 to 60 ℃; application of a electroplating current of 1.55-3.10 $\times 10^3$ A/m^2, under which the component is left for the required time to attain thickness[6].

2.3.2.1 Advantages

Compared to HVOF Cr3C2-25%NiCr (~0.25 dry against brass) and WC-12%Co coatings (~0.27 dry against brass), EHC coatings take advantage of the low coefficient

of friction (~0.20 dry against brass)[33]. Moreover, it can be lower than any other metal after micro-finishing when used against steel, iron, brass, bronze or Al alloys, so Cr electroplating is used as a bearing surface. EHC coatings are also a very good option for long lasting wear resistant surfaces because they are much harder than casehardened steel[32]. Cr coatings also provide protection from the environment through a barrier mechanism due to their inert properties. They resist most organic and inorganic compounds and acids, except hydrochloric acid.

2.3.2.2 Disadvantages

EHC coatings tend to be microporous or microcracked, which offers little protection to the substrate material in aggressive environments[34]. EHC does not have a levelling effect, so surface defects and roughness are amplified[32]. The hardness and microcrack density of EHCs vary as a function of the bath composition, current density, bath agitation, and temperature. So EHC coatings usually incorporate corrosion resistant under coatings, such as nickel to provide good corrosion resistance. The fatigue strength of D2 steel was reported to decrease due to EHC[12], so the design of hard Cr electroplated components, which are subjected to dynamic loads, must consider this negative influence to guarantee safety during operation. Shot peening was used to induce a compressive residual stress by surface plastic deformation to produce an increase in fatigue strength of structures subjected to constant and variable amplitude loading[35]. Moreover, health and environmental issues from problems of Cr electroplating increase costs and have resulted in a search to identify possible alternatives.

2.3.3 Replacements for EHC Coatings

Some of the EHC alternatives proposed incorporate an undercoating or consist of layered structures to provide good corrosion resistance. These alternative coating

systems are expected to match the Cr performance and gain some improvement as well. All alternative coatings discussed here include electrodeposited, electroless and thermal sprayed coating systems.

2.3.3.1 Cr Based Coatings

A Ni "barrier" layer followed by a electrodeposited Cr(III) coating was investigated and compared to EHC[36]. Its corrosion resistance was comparable to EHC coatings when evaluated using the ASTM B 117 Salt Fog Test[37] or the CASS Test (ASTM B 368, Copper Accelerated Salt Spray)[38] and better than EHC when subjected to the Corrodkote Test (ASTM B 380)[39]. Pulsed current electroplating was applied to obtain better, thicker, trivalent Cr coatings for functional applications[34]. However, when the coatings received a surface pre-treatment to reduce porosity and close microcracks, the corrosion performance was improved but still could not meet the 96-hour arbitrary exposure set for EHC.

A cathodic arc sputtering process was also suggested to deposit thin, dense Cr films[40]. In an immersion test carried out over a period of 24 hours in 4 wt.% NaCl solution, this type of coating performed as well as the traditional EHC coating.

A proprietary, laser-alloying technique[41] or a more traditional, co-diffusion technique[42] have been used to diffuse Cr with Ni or Si into the surfaces of substrate metals to improve their corrosion resistance. Laser melting was used to produce alloyed layers on substrates of Al and 7175 high resistance Al alloy with injection of Cr powder. The size of the Cr powder particles has a significant effect on the alloy layers. The laser-alloyed layer presented a considerable amount of porosity and was chemically and structurally heterogeneous, which was suggested to be caused by entrapped H_2 bubbles[41]. The H_2 is presumed to result from two ways. One is the decomposition of water adsorbed at the materials' surface, the other is from the decomposition of water vapour released during the calcinations of $Al(OH)_3$, which

forms when Al alloy substrates are exposed to a humid atmosphere. Remelting by laser was used after alloying, this eliminated porosity and refined the microstructure and produced homogeneous alloyed layers. Laser-alloyed layers present very high hardness when compared to the untreated material. Laser alloying increased the hardness from 50 to about 155 HV for Al and from 155 to about 300 HV for 7175 alloy substrates. Laser alloying also improves the pitting corrosion resistance of Al and its 7175 alloy depending on the Cr content in the laser-alloyed layers. The pitting potential of Al shifted to positive direction after laser-Cr-alloying (Figure 14 (a)). As Figure 14 (b) shows, the pitting potential of 7175 Al alloy increased from -730 mV to -620 mV, -380 mV and -270 mV for Cr concentrations of 5 wt.%, 10 wt.% and 12 wt.% respectively, which was suggested to result from the formation of CrOOH and Cr_2O_3, which enhanced the passive film formed. This passive film was believed to be less soluble in an acid environment than the untreated Al, which contained only Al oxide, so a higher potential was needed to nucleate and propagate the pits. So these Cr-containing diffusion coatings were also said to provide excellent resistance to high-temperature oxidation, sulphidation, and halide attack[29].

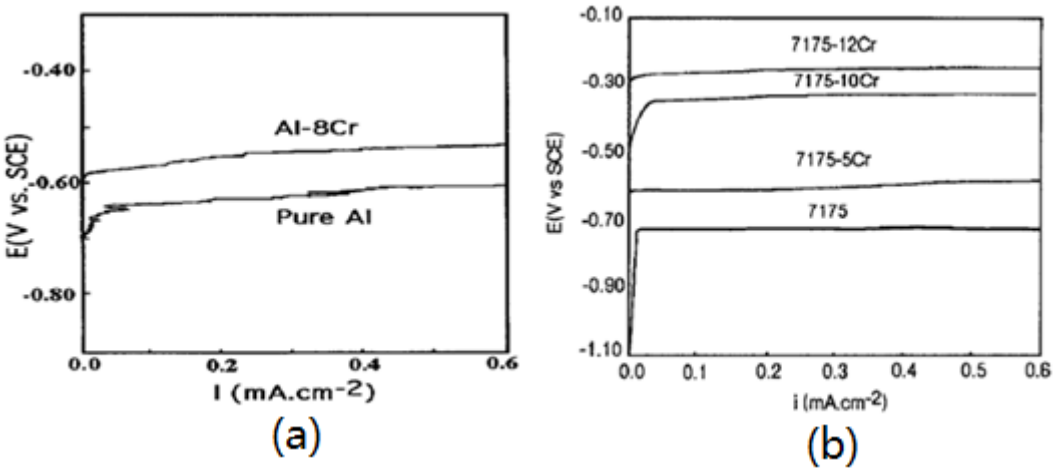

Figure 14. Anodic polarization curves for laser-Cr-alloyed (a) Al and (b) 7175 Al alloy[41]

2.3.3.2 Co Based Coatings

Co based alloy coatings are considered as alternatives for EHC coatings due to their promising mechanical properties and improved corrosion resistance. Some properties

were described in Brooman's report [34]. In high temperature application tests, electrodeposited Co-W coating cracked at 500 ℃ and peeled at 600 ℃, while the Cr-coated specimen continued to adhere well to the substrates at 600 ℃. The hardness of the Co-W coating was about 1.4 to 1.5 times less than the EHC coated specimen. However, in potentiodynamic polarization and electrochemical impedance spectroscopy (EIS) tests, Co-W coated specimens with heat treatment at 500 ℃, exhibited corrosion rates that were 1.6 to 2.0 times less than the EHC coatings, which may result from the surface oxide layer formed during annealing. Hyeong et al.[43] suggested that the presence of a small amount of P in the Co-W coatings significantly improve the hardness and protection against aggressive environments. It was reported that the microhardness of the as-deposited EHC coating was higher than that of the as-deposited Co-W-P coating. However, with an increase in annealing temperature, the microhardness of Co-W-P coating was improved significantly and became much higher than that of the EHC coating. Co-W-P coatings also presented a more noble corrosion potential than EHC coatings, which implied a superior corrosion protection property from the EHC coating on plain carbon steel. Increasing the annealing temperature was also suggested to improve the polarisation resistance of Co-W-P coatings[43]. However, Co's future is uncertain due to increased environmental scrutiny and its high cost may also limit its application in the future.

2.3.3.3 Ni Based Coatings

Despite all environmental concerns, Ni and Ni alloy coatings deposited by electrolytic or electroless techniques are still regarded as EHC alternatives. They are hardenable and provide good corrosion resistance, especially in alkaline environments. Like Cr, protection is provided by the formation of a physical barrier between the substrate and the environment.

Electroless Ni (EN) coatings containing P (usually 8 to 10 wt.%) can provide desirable

properties[44]. The coatings with low P content are harder, but less corrosion resistance than those with high P content. Brandl and Gendig[45] compared the corrosion resistance of EN and EHC coatings as a barrier layer in multilayer coatings. The multilayer coatings were comprised of the barrier layer, EN or EHC coatings, on a tool steel followed by a hard coating, TiN or CrN, deposited by a physical vapour deposition technique. It was found that the EN layers showed better corrosion resistance than the EHC coatings subjected to deaerated, 1 M H_2SO_4 solution at 25 ℃. This was attributed to corrosion via the microcracks in the latter coatings.

Some electrodeposited Ni-Mo and Ni-W alloys have also been suggested as alternatives for EHC[46]. The hardness and corrosion resistance of the coatings was dependent upon the composition, deposition system and subsequent heat treatments used. A Ni-35%W alloy coating showed good corrosion resistance and high hardness as a replacement for EHC. OCP measured for this and other alternatives for EHC showed that Ni-W was anodic with respect to Cr, unlike unalloyed Ni (Figure 15)[47]. Minor alloying additions, such as boron or hard particles such as SiC can be used to modify hardness and wear properties of Ni-W alloy coatings.

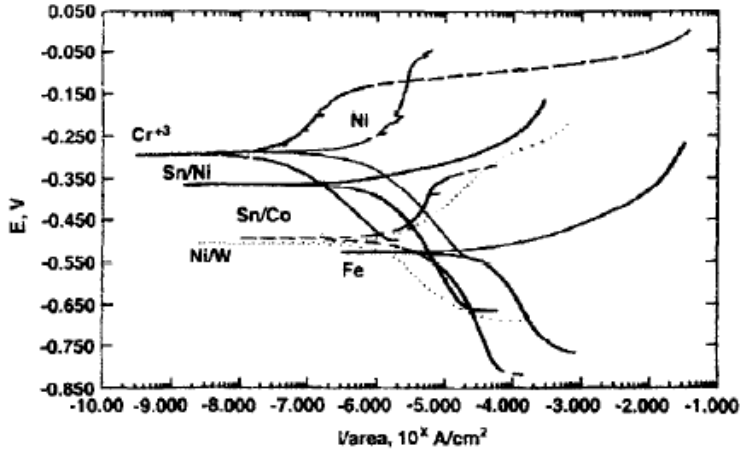

Figure 15. Polarization (Tafel) plots for selected EHC replacement alloys[47]

2.3.3.4 Inorganic Coatings

Protective SiO_2-based coatings applied to Al and brass substrates have been

investigated as alternatives to EHC coatings[48]. Plasma-enhanced chemical vapour deposition was used to deposit and modify SiO_2-based coatings, which were hard and showed good corrosion resistance, especially in salt fog exposure (Table 2).

Table 2. Corrosion-related properties of plasma-enhanced chemical vapour deposited inorganic (SiO_2) polymercoatings[48]

Test[a]	Results for Aluminum Substrates	Results for Brass Substrates
Salt fog—ASTM B 117	>2,000 hours	>1,000 hours
CASS—ASTM B 368	120 hours	120 hours
Boil water—ASTM D 870	1 hour	1 hour
Chemical resistance—ASTM D 4652	Pass	Pass
Ultraviolet exposure—ASTM G 53	>2,000 hours	>3,000 hours
Filiform attack—Metroline	140 hours	140 hours
Humidity—ANSI/BHMA A 156	>1,000 hours	>1,000 hours

Several coatings applied by a dry deposition technology, HVOF method, are also considered as potential replacements for EHC[49]. The HVOF coating technique has been widely applied in the commercial and military aircraft sectors and the general defence industry. The HVOF process is a thermal spray technique. During this process, fuel gas and oxygen are pre-mixed, and then fed at high pressure into a combustion chamber, where they burn to produce a hot, high-pressure gas stream. The coating powder particles are injected directly into this combustion region of the gun under automatic control. The HVOF process can deposit a dense, uniform coating, typically with less than 1% porosity, an oxide content of less than 1% and bond strength in excess of 80 MPa[50]. The main HVOF produced coatings are WC or WC-Co coatings and coatings also containing mixtures of Ni, Cr, Fe and Si. In general, addition of small amounts of Cr into the coatings improves corrosion resistance. Due to reduced worker exposure, though the small amounts of Cr contained in the coatings, the Cr is metallic as opposed to hexavalent and compliance with environmental regulations is easier to attain. Some results for salt fog testing of HVOF coatings were summarised by Brooman[49] (Table 3). It should be noted that the corrosion performance can vary as a function of deposition equipment, coating powder, deposition parameters, presentation of inclusions, porosity, and surface finish as shown in Table 3. In the corrosion resistance test (neutral slat fog ASTM B 117[37]), WC coatings applied by several HVOF techniques to AISI 4130 steel presented a better corrosion resistance than EHC coatings.

Table 3. Corrosion resistance of some hard EHC alternative coatings applied by the HVOF technique[49]

Composition	Thickness, μm	Substrate	ASTM B 117 Results[a]
WC	100–150	4130 Steel	Better than EHC (>200 hours)
WC-Co	100–200	Steels	Comparable to or better than EHC
WC-Co-Cr	100–200	Steels	Excellent (>750 hours)
WC-Co/Ni-Cr-Mo	400	Steel	No evidence or corrosion
Ni-Cr-Mo	400	Steel	No evidence of corrosion
Ni-Cr-Si-B	—	Steels	Excellent (>750 hours)
Ni-W-Cr-Si-B	—	Steel	Comparable to EHC
Fe-Cr-Mo	400	Steel	Fair—"corrosion scale" present
Fe-Cr-Ni	—	Steel	Comparable to EHC
Cr_3C_2/Ni-Cr	—	Steels	Better than EHC (~390 hours)

Table 4. Results of the neutral salt spray test over 24, 48 and 72 h of HVOF WC and EHC coatings on AISI 4340 steels[51]

Salt Spray test				
Testing time	Tungsten carbide (100μm)	Electroplated Hard Chromium coating		
		16 μm	36μm	49μm
24h	30%	90%	70%	50%
48h	50%	100%	100%	100%
72h	100%	100%	100%	100%

Nascimento et al.[51] compared several HVOF coatings to EHC on AISI 4340 steels in terms of corrosion resistance, fatigue strength and wear performance. Both HVOF WC coatings and EHC coatings decreased the fatigue strength of AISI 4340 and this decrease of the fatigue strength was higher with EHC than with WC coated specimens. In the wear weight loss tests, the HVOF WC coatings showed better results than the EHC coatings. Both HVOF WC coatings and EHC were fully corroded after 72 h of the salt spray test, however, WC coatings showed higher salt spray corrosion resistance than the EHC coatings (Table 4), which may result from their different thicknesses. Moreover, the HVOF deposition process is faster than conventional Cr electroplating and due to no H_2 evolution during HVOF processes, the time and cost required for embrittlement-relief treatment is eliminated. As shown in Table 5, HVOF WC coatings also presented higher hardness values than EHC[50]. Due to their ability to provide improved wear, impact and fatigue resistance and equal or better corrosion resistance, HVOF WC coatings have been considered as alternatives to EHC coatings in many demanding applications.

Table 5. Coating characteristics and performance results of a HVOF WC coating and a electroplated hard chromium coating[50]

Property	HVOF tungsten carbide coating	Hard chromium plate
Macrohardness, HRC	>70	60 – 70
Microhardness, DPH 300	>1050	750 – 850
Bond strength, MPa (psi)	>80 (10,000)*	~41 (6,000)
Porosity	<1%	Inherently cracked
Coating thickness, mm (in.)	>0.08 (0.003)	< 0.13 (0.005)
Surface finish, Ra	<4	<4
Corrosion test (ASTM B117), hours	720	55
Surface temperature limits, °C (°F)	550 (1025)	400 (750)

HVOF applied coatings are utilised to protect the surface of components used in highly erosive environments. The HVOF process employs low temperature and supersonic speeds of particles to avoid overheating of the substrate and makes the deposition possible on materials with relatively low melting temperatures. Moreover, Schwetzke and Kreye[52] proposed that HVOF thermal spraying was one of the better methods for the deposition of WC-CoCr and CrC-NiCr feedstock powders, due to the high velocities and lower temperatures experienced by the powder particles resulting in less decomposition of the carbides during spraying. Therefore, these result in higher quality, more wear-resistant coatings, with higher levels of retained reinforcing material and less porosity. The microstructures of WC-CoCr and CrC-NiCr coatings were investigated by Picas et al.[53]. The coating microstructures consisted of a metallic binder of Co-Cr and Ni-Cr and dispersed carbide phases WC and CrC (bright and dark particles, respectively, Figures 16 (a and b) and 17 (a and b). The coatings exhibited a typical splat pattern-like structure, which was suggested to result from the collapse of the droplets on the substrate. During the HVOF spraying process, the powder particles are accelerated and heated as they travel through the flame. Except for the carbide, the external part of the particles melts and the coating forms by the piling up of the impacting droplets which are flattened by the acceleration forces and then rapidly cooled.

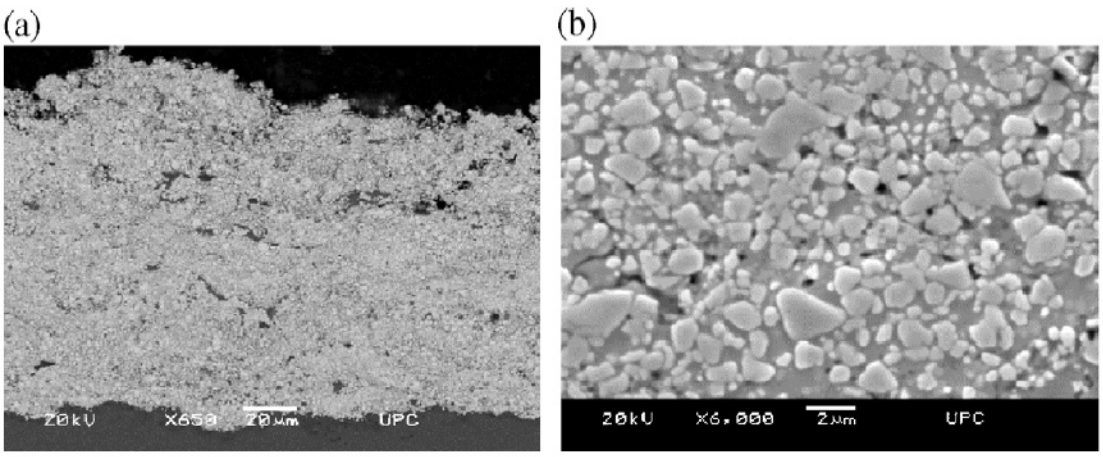

Figure 16. SEM micrographs showing (a) the cross-section of HVOF $WC_{86}Co_{10}Cr_4$ coating on a steel substrate and (b) microstructural detail of the coating[53].

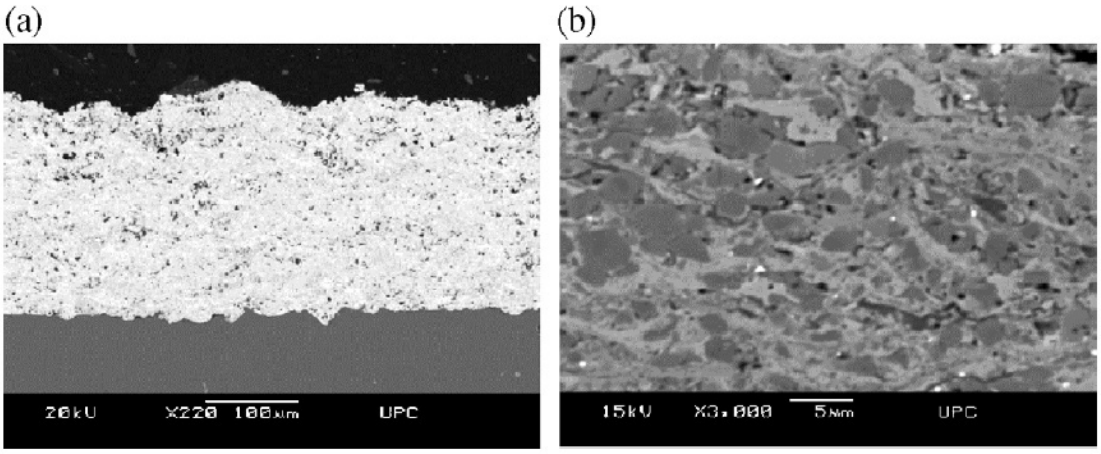

Figure 17. SEM micrographs showing the cross-sections of (a) $CrC_{75}NiCr_{25}$ coating on an Al substrate and (b) microstructural detail of the coating[53].

2.4 Deposition of Al_2O_3 Coatings

Al_2O_3 coatings can be considered to provide further barrier protection to substrates (e.g. steels and Al alloys), which is expect to eliminate galvanic corrosion due to its low conductivity. They also show some promising mechanical properties. Several methods have been reported for applying Al_2O_3 coatings, including the sol-gel process, microarc oxidation, ion beam assisted deposition, electrochemical deposition and thermal spraying.

2.4.1 Sol-gel Al_2O_3 Coatings

SiC is widely applied as a high-temperature structural ceramic due to its high thermal conductivity and low thermal expansion coefficient. However, corrosion of SiC at high temperatures limits its application. In this environment, silica scale (SiO_2) on the surface of the SiC reacts with water vapour and forms volatile silicon hydroxide ($Si(OH)_4$), which results in further corrosion. An Al_2O_3 coating was suggested as an "Environmental Barrier Coatings (EBC)" to increase the corrosion resistance of SiC. The sol-gel method is the economical way to develop the desired performance of the EBC system. A Sol-gel alumina EBC for SiC grit was investigated by Kim et al.[54]. It was found that the SiC surface in water is negatively charged at 3.5<pH<5.5 and boehmite sol clusters are positively charged, thus the coating forms by electrostatic interaction of the two. During the investigation, alumina sol was prepared using boehmite. SiC particles were pre-oxidised at 1100 ℃ for 10 h in air to form the SiO_2 scale. Pre-treatment of the SiC surface by NH_4OH was proposed to modify the deposition of the Al_2O_3 sol layer by generating substantial hydroxylation of the natural silica coating on the SiC through the following reaction:

$$SiO_2 + 2NH_4OH \rightarrow Si(OH)_4 + 2NH_3(g) \qquad \text{Equation (1)}$$

It was found that NH_4OH treatment of pre-oxidised SiC grit induced the negatively charged surface by the formation of –OH bonds and thus fast gelation and uniform coating of the positively charged boehmite sol. After surface pre-treatment, SiC grits were exposed to an Al_2O_3 sol through dipping or stirring in the sol at room temperature. Coated SiC grit were centrifuged to remove excess alumina sol, dried and heat treated at 1450 ℃ for 2 h in air. The cross-sections of coated SiC grits show that the dip-coating provided more uniform and thicker coatings than the stirred coating method as shown in Figure 18.

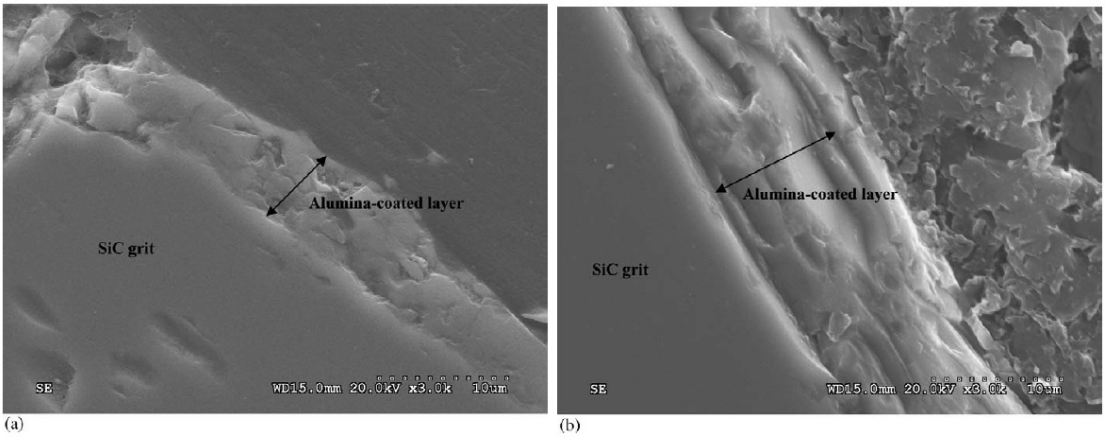

Figure 18. Cross-sections of Al_2O_3 (a) stir-coated and (b) dip-coated SiC[54]

Moreover, during the heat treatment of such films, it was believed that boehmite decomposed to Al_2O_3, which partially reacted with the silica present on the SiC surface to form mullite ($3Al_2O_3 \cdot 2SiO_2$) at the interface. The strongly bonded mullite interface played a significant role in maintaining the integrity of the Al_2O_3 coating and SiC substrate. Oxidation of coated SiC was also investigated at 1200 ℃ in air, for 24-72 h. About 4 times lower weight gain was observed for the coated SiC as compared to the as-received SiC, with no significant differences between the coating techniques (Figure 19).

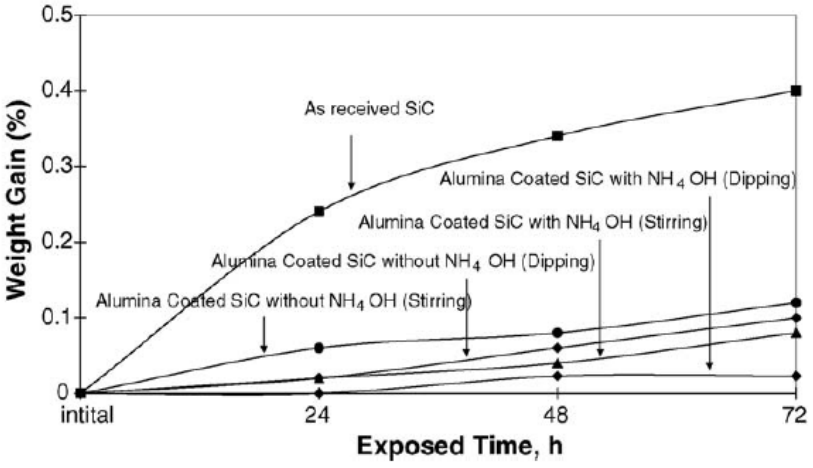

Figure 19. Weight gain due to oxidation for as-received and coated SiC at 1200 ℃[54]

2.4.2 Microarc Oxidation (MAO) Al_2O_3 Coatings

Microarc oxidation (MAO) is proposed as a novel and unique technique for depositing

thick, dense and ultra-hard ceramic coatings on Al and Al-alloy substrates[55]. The MAO coatings have exhibited superior mechanical properties when compared to anodic oxide coatings and have higher adhesive strengths than plasma sprayed ceramic coatings. Sundararajan and Krishna[55] investigated thick Al_2O_3 coatings synthesized on Al-alloy substrates by MAO. An alkali-silicate solution was used as an electrolyte, and the coating deposition was carried out at a constant current density of 0.3 A/cm^2 using a 50 Hz frequency alternating current-high voltage power supply source. During the formation of the MAO coatings, firstly, a number of discrete discharge channels formed in the oxide layer as a result of a loss in its dielectric stability in a region of low conductivity. The material in the channel is heated up to temperatures of 10^4 K by generated electron avalanches. Due to the strong electric field, the anionic components are drawn into the channel. Concurrently, aluminium and alloying elements were melted out of the substrate, enter the channel and were oxidised. Oxidised Al was ejected from the channel onto the coating surface in contact with the electrolyte and thus increased the coating thickness. Finally, the discharged channel cooled and the reaction products were deposited onto its walls. During the solidification of Al_2O_3 droplets, γ-Al_2O_3 was formed due to the very high cooling rate experienced by the oxide layer being ejected from the channels, which immediately contacted the electrolyte. From the XRD spectra of the 'as deposited' surface layers of the MAO coatings processed for 1, 3, 5, 10, 20 and 30 min, respectively, it can be seen that these are comprised of mainly the γ-Al_2O_3 phase with a small proportion of α-Al_2O_3 (Figure 20). However, the underlying layers of the alumina coatings remained heated due to the low thermal conductivity of alumina, which resulted in the further transformation of the initially formed γ-Al_2O_3 to the much harder α-Al_2O_3. Therefore, α-Al_2O_3 content increased with increasing depth from the coating surface towards the coating substrate interface and the hardness of the coatings increased with increasing thickness as shown in Figure 21.

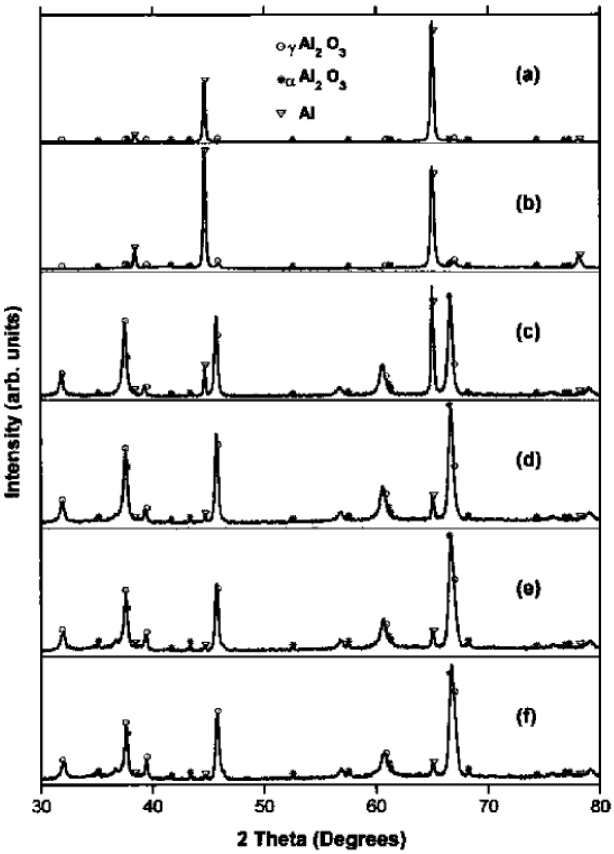

Figure 20. XRD spectra of MAO coatings processed for (a) 1; (b) 3; (c) 5; (d) 10; (e) 20 and (f) 30 min[55]

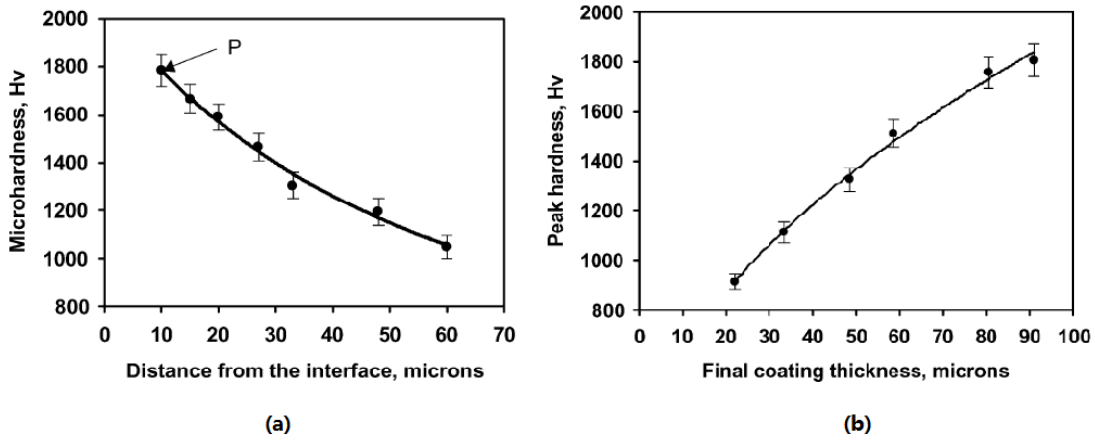

Figure 21. (a) Influence of final coating thickness on peak hardness measured at 10 μm distance from the interface between Al_2O_3 coating and Al-alloy substrate. (b) Variation in microhardness of MAO coating as a function of the distance from the interface between Al_2O_3 coating and Al-alloy substrate[55]

2.4.3 Ion Beam Assisted Deposited (IBAD) Al_2O_3 Coatings

Ion beam assisted deposition (IBAD) has been developed as a deposition technique for

applying Al_2O_3 coating and has distinct advantages[56], such as better coating adhesion and less porosity. Jiaming and Weijiang[57] investigated IBAD Al_2O_3 coatings with different thickness. Al_2O_3 coatings were formed by evaporating pure Al (99.9 %) in an O_2 atmosphere with a deposition rate of 0.4 nm/s. An IBAD facility[58] used in the study irradiated a sample with 10 keV Ar ions at an incidence angle of 45 ° and a beam current density of 20 $\mu A/cm^2$. O_2 pressure in the chamber during the deposition dominated the O concentration in the coating. 1.2×10^{-2} mbar of O_2 pressure, deposited transparent and colorless alumina coatings. From the Rutherford Backscattering Spectrometry (RBS) spectrum of the coating, it was observed that the relative concentrations of Al, O and Ar were in a ratio of about 2:3:0.2. Moreover, through comparison of the auger electron peak of Al, O and the Al-Al_2O_3 mixture, it can be seen that only one Al Auger electron peak for Al_2O_3 was found in the coating, which indicated that all the Al atoms were in the form of Al_2O_3 (Figure 22). No significant difference between the XRD spectrum of the Si substrate and that with an IBAD alumina coatings indicated that the latter are amorphous.

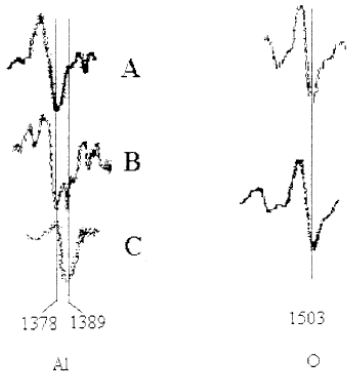

A) Auger electron peak in coating's surface and after sputtering
B) Auger electron peak of Al-Al_2O_3 mixing material
C) Auger electron peak of pure Aluminium

Figure 22. Auger electron spectrum of Al in ion beam assisted deposited Al_2O_3 coating[57]

From Figure 23, it was shown that the corrosion resistance of IBAD Al_2O_3 coatings increased with increase in coating thickness. The high thickness resulted in less micropores in vacancies between the adjacent grains during the deposition of the Al_2O_3. However, there were some micropores near large defects, whose dimensions were

much larger than the thickness of the coating. Increased coating thickness did not eliminate these micropores significantly. Therefore, corrosion resistance increased greatly as the coating thickness reached 1500 nm.

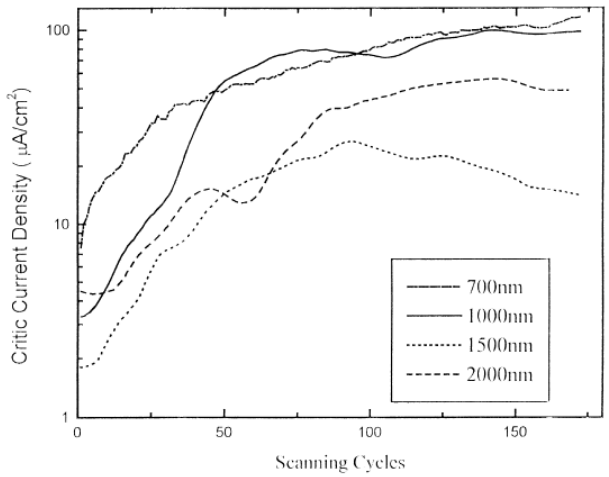

Figure 23. Electrochemical measurement results of CK45 steel samples with Al_2O_3 coatings of different thickness in acetic aqueous buffer solution of pH 5.6[57].

From Figure 24, it can be seen that the presence of the coatings improved microhardness and this increased with increase in thickness. Under a load of 98 mN, the microhardness of the sample with a 2 μm thick Al_2O_3 coating was about 3 times that of the uncoated steel.

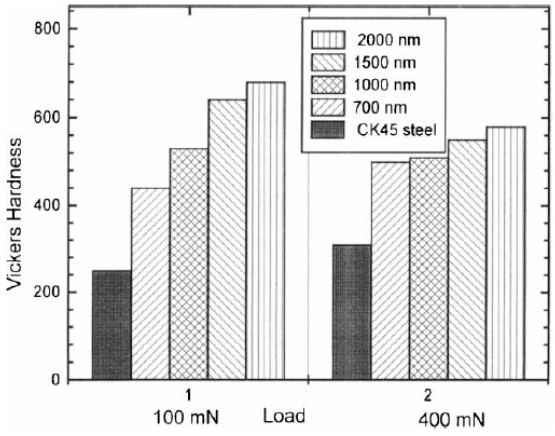

Figure 24. Microhardness of samples with Al_2O_3 coatings measured under loads of 98 and 392 mN by a Vickers' indentor[57]

2.4.4 Electrochemically Deposited Al_2O_3 Coatings

Electrochemical deposition methods present several advantages over alternative coating techniques for applying Al_2O_3 coatings. For example, the thickness and morphology of the deposit can be controlled by the electrochemical process parameters, and relatively uniform deposits can be obtainable on complex shapes. Moreover, the deposition rate for electrochemical processes is higher than that for most other methods[59]. Lgamri et al.[60] applied Al_2O_3 coatings on steels by electrochemical methods. Addition of Y to Al_2O_3 coatings was suggested to improve oxidation resistance and adhesion of the coatings. The steel substrates were chemically pre-treated in an aqueous solution of H_2SO_4 with suitable accelerator and inhibitor, such as thiosulphates and propargyl alcohol, to form a functional conversion coating on the steel substrate surface. That conversion coating was very rough and had pores and cavities with a range of dimensions, which facilitated the electrolytic deposition of Al_2O_3 and increased adhesion of the deposit. The condition of deposition of Al_2O_3 is shown in Table 6.

Table 6. Conditions for the Al_2O_3 and Al_2O_3/Y deposits on a low-carbon steel containing 0.2 % carbon[60]

Current density (I)	-100 mA cm^{-2}
Temperature	13 °C
$[Al_2(SO_4)_3 \cdot 14\ H_2O]$	1 M
YCl_3	0.15 M
pH	3
Treatment time	15 min

The porous conversion coating acted as cathode and formation of OH^- may occur at the bottom of the pores with a resulting rise in local pH, which promoted precipitation in the pores and at the surface of oxide or hydroxide compounds with varying degrees of hydration. The deposit was then cleaned with tetrahydrofuran, washed with distilled water and then dried in air at room temperature. From Figure 25, it can be seen that the electrolytically deposited Al_2O_3 coating presented a homogeneous morphology with the superficial micro cracks, whose width was of the order of 1 μm.

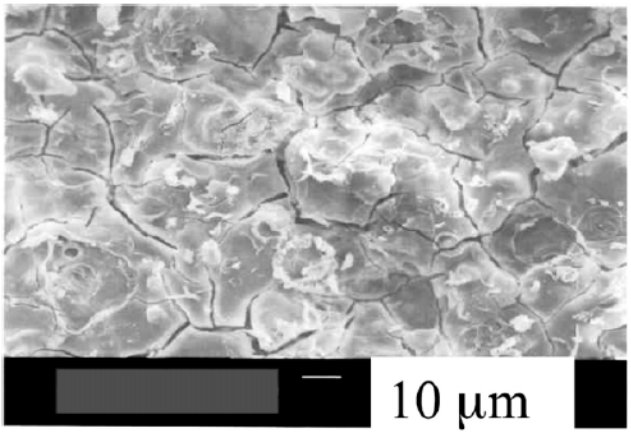

Figure 25. SEM secondary electron micrograph of electrolytically deposited Al_2O_3 coating from $Al_2(SO_4)_3$ bath on a steel substrate[60]

Oxidation behaviour of electrolytically deposited Al_2O_3 coatings at high temperature was investigated by comparison of the oxidation curves of uncoated and coated steel. Figure 26 shows the isothermal variation as a function of time for weight changes per unit area for the oxidation tests performed at 750 ℃ in air. The uncoated steel oxidised rapidly in the first few minutes of heating and became slower after 20 min. Loss of mass implied that an iron oxide layer flaked off at the end of the 2 h heating period. For steel with an Al_2O_3 deposit, the oxidation curve revealed a parabolic behaviour. After 1 h of heating, the oxidation rate became almost static through the formation at the surface of the substrate of a thick and very adhesive layer of Al_2O_3, which gave protection through 11 h of thermal treatment without further scaling. The Al_2O_3 deposit after heat-treatment was also analysed by SIMS (Figure 27). It was found that the presence of the Al in the surface and in depth. Moreover, the Al content decreased slightly then increased with depth, which implied effective diffusion in the conversion layer and, by consequence, good adhesion of this deposit. Even after 3000 s of analysis, the Al was also detected, which meant that the Al distributed toward the interfacing lays down a conversion layer-steel substrate.

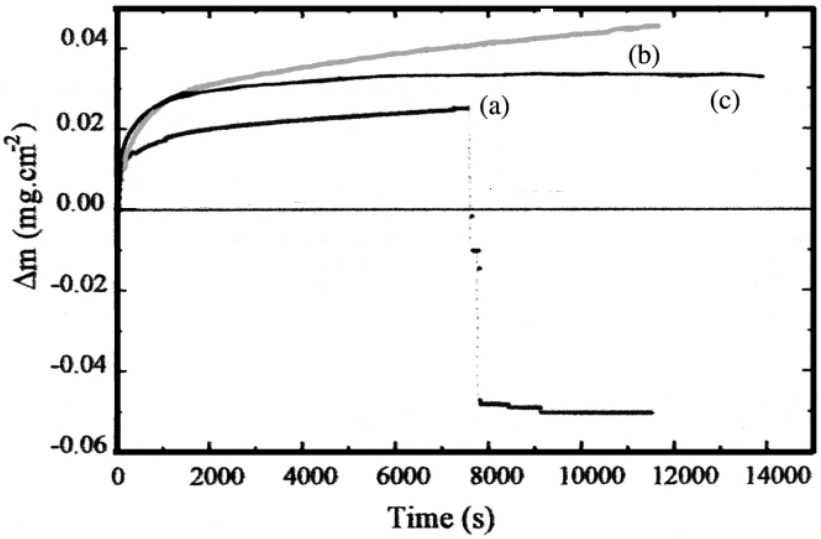

Figure 26.Weight gain of steel against thermal treatment time in air at 750 ℃. (a) Uncoated steel; (b) steel with conversion treatment and (c) steel with Al_2O_3 deposit[60]

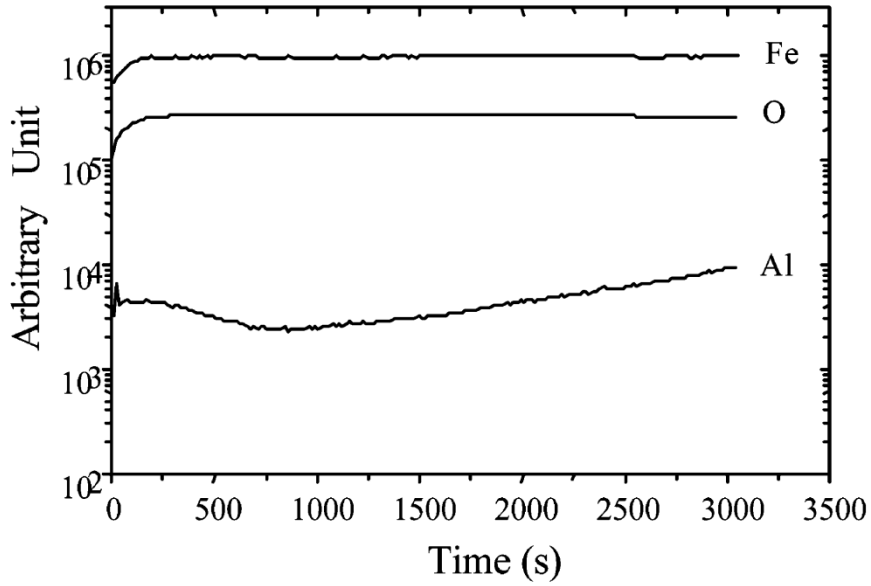

Figure 27. Distribution profiles of the elements on the steel coated with Al_2O_3 coatings after heat treatment at 750 ℃ in air, against bombardment time applied by SIMS, using IMS300 Cameca analyser[60]

2.4.5 Thermal Sprayed Al_2O_3 Coatings

2.4.5.1 Thermal Spray Al_2O_3 Coatings from Nanostructured Ceramic Agglomerated Powders

Nanostructured materials have been extended to coating processes using the thermal

spray technique due to their superior wear resistance when compared to conventional thermal spray coatings. Nanostructured particles smaller than 100 nm, cannot be thermally sprayed by the regular powder feeders currently being employed in thermal spray. The tiny nanoparticles clog the hoses and fittings and the high levels of carrier gas flow for injecting individual nanoparticle would tend to destabilize the thermal spray jet. Low individual nanoparticles inertia during spraying also makes the deposition process very inefficient. It was reported that nanoparticles can be agglomerated via spray-drying and then sintered into microscopic particles to be sprayed using regular powder feeders[61]. For spraying nanoparticles, it is important to control the degree of melting for achieving good adhesion and cohesion, and keeping the nanostructural character of the powder particles. In such a way, the initial nanostructure of the feedstock can be embedded in the coating microstructure. Therefore, the coating microstructure consists of semi-molten particles that are spread throughout the coating and fully molten particles that act as a binder maintaining coating integrity[62]. This coating structured was described as a 'bimodal microstructure', as shown schematically in Figure 28.

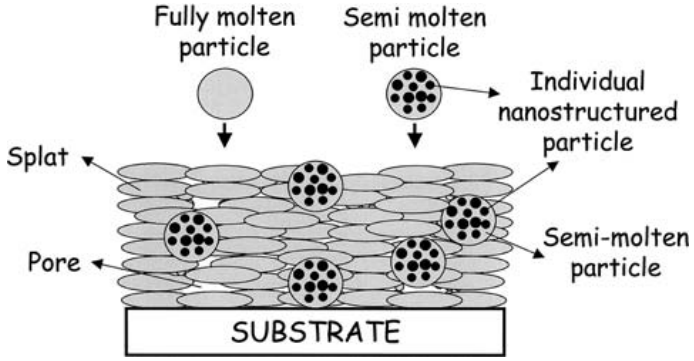

Figure 28. Typical schematic (cross-section) of the bimodal microstructure of thermal spray coatings formed by fully molten and semi-molten nanostructured agglomerated particles[62]

The semi-molten particles (nanozones) in the coating can present a dense or porous structure. Dense nanozones form when the molten part of a semi-molten particle, fully or almost fully, infiltrate into the capillaries of the agglomerates during thermal spraying[61]. Turunen et al.[63] applied thermal sprayed Al_2O_3 coatings by HVOF spraying

of normal and nanostructure Al_2O_3 powders. The addition of Ni into Al_2O_3 coatings was also investigated. The condition and powders used for the investigation are shown in Tables 7 and 8.

Table 7. Spray powders for the alumina deposition by HVOF on grit blasted carbon steel plates[63]

Powder	Material code	Manufacturer and method	Agglomerate size [μm]	Crystal size	Phase structure
Al-1110	ref-Al_2O_3	Praxair, fused and crushed	5–22	Conventional	alpha
Boehmite	*n*-Al_2O_3	VTT, agglomerated and sintered	2–25	Nano range	alpha
Boehmite	*n*-Al_2O_3–2% Ni	VTT, agglomerated and sintered	4–23	Nano range	theta
Boehmite	*n*-Al_2O_3 –5% Ni	VTT, agglomerated and sintered	2–26	Nano range	theta

Table 8. Diagnostic data for different condition of HVOF thermal spray of alumina conditions on grit blasted carbon steel plates[63]

Spray condition	Ratio H_2/O_2	Total flow [l/min]	Standoff [mm]	T [°C]	v [m/s]
A	2.85	1050	150	2050±5	1025±25
B	2.85	1050	200	1989±6	874±69
C	2.48	1050	150	2040±3	1073±34
D	2.00	1050	150	1990±4	1014±7
E	2.85	890	150	2027±5	1003±14

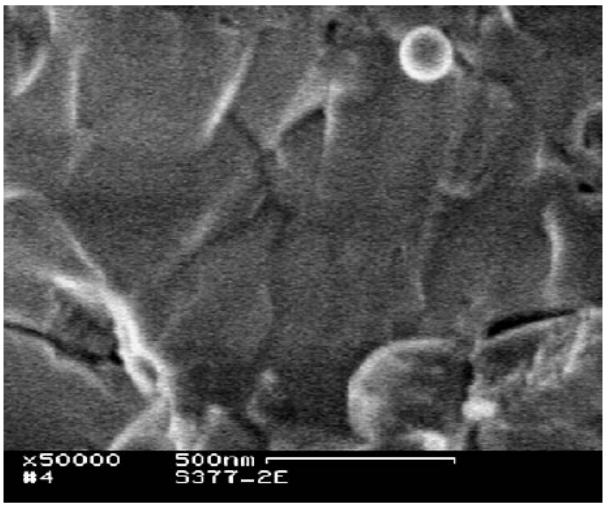

Figure 29. SEM micrograph of a fracture surface of nano-Al_2O_3 HVOF coating[63]

A high resolution SEM secondary electron micrograph of the fracture surface of nano-Al_2O_3 sprayed by condition D (Table 8) is shown in Figure 29. Al_2O_3 grains with dimensions in the range of hundreds of nanometers were observed. The 'nanozones' resulted from a significant high particle velocity from the HVOF process in spite of

extensive melting of the powder. Mechanical properties of the coatings were investigated by abrasive wear resistance tests, hardness measurements, and by measuring cracks formed around the Vickers hardness indentations. Comparisons between pure nano-Al_2O_3 coatings and the reference coatings showed that the hardness was higher for the nano- Al_2O_3 coatings (Figure 30). This was suggested to result from the refinement of the coating microstructure through the use of nanocrystalline feedstock. By using spray condition D (Table 8), the coatings presented high hardness and good wear resistance due to good inter-lamellar adhesion. Dense 'nanozones' showed high hardness and wear resistance because they exhibited more uniform microstructures. Moreover, a crack arresting effect of 'nanozones' spread throughout the coatings' microstructure was suggested to be important for improved wear resistance. Using nanostructured powders was also proposed to result in a better splat-to-splat contact, which tended to impede crack propagation.

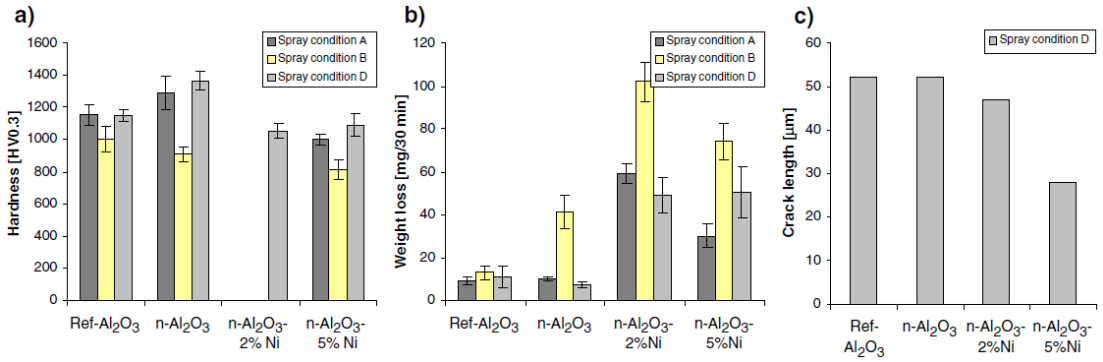

Figure 30. (a) Vickers hardness (HV 0.3), (b) weight loss in rubber wheel abrasion test, and (c) cumulative length of horizontal cracks around a Vickers indentation of Al_2O_3 coatings sprayed from different conditions[63]

2.4.5.2 Suspension Thermal Sprayed Al_2O_3 Coatings

In addition to thermal spray nanostructured Al_2O_3 coatings from agglomerated powders, a method, so-called suspension thermal spraying, was developed to produce nanostructured Al_2O_3 coating. In this technique, a liquid suspension of fine particles with diameters ranging from several nanometers to a few micrometers was used as the material feedstock[64]. A higher ratio of the initial nanostructure particles was retained.

Toma et al.[64] produced Al_2O_3 ceramic coatings by atmospheric plasma spraying (APS) and HVOF with aqueous and alcoholic suspensions of nano- and sub- micrometer-sized powders. Al_2O_3 powders with 400 nm average particle size were added into distilled water or ethanol to produce a suspension with 20-25 wt.% powder. The pH of the suspensions was adjusted to obtain stable suspensions. During spraying, ultrasonically and magnetically stirred agitation were used to break up the agglomerates and to avoid reagglomeration of the particles as shown in Figure 31. Suspension spraying was adapted to the APS and HVOF processes (Figure 31). The conditions and spraying parameters are summarized in Table 12.

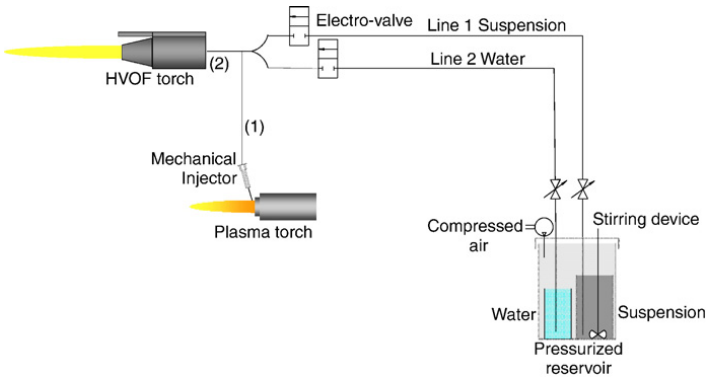

Figure 31. Implementation of liquid injection in the APS (1) and HVOF (2) systems[64]

Table 9. Suspension plasma spraying parameters for applying alumina coatings[64]

Suspension	Sample symbol	Ar (slpm)	H_2 (slpm)	He (slpm)	Current (A)	Voltage (V)	Spray distance (mm)
Al_2O_3/H_2O	AW1	40	10	–	650	84	70
	AW2						60
Al_2O_3/EtOH	AA1	40	6	–	500	74	50
	AA2		4	10	500	72	
	AA3		–	25	750	67	

The microstructures of the suspension-sprayed coatings depended on the suspension properties and spraying parameters. The microstructures of the coatings mentioned in Table 9 were shown in Figures 32 and 33. From Figure 32 (a), it can be seen that Al_2O_3 coatings applied by mechanical injection of aqueous Al_2O_3 suspension into Ar-H_2 plasma presented a porous coating characterised by a bimodal microstructure, which consisted of unmelted and partially melted nanoparticles embedded in the structures of fully melted particles. Figure 32 (b) implied that a smaller spray distance resulted in a

denser bimodal microstructure. The position of the plasma jet which the droplets passed through dominated the melting state of the droplets. The regions with the high plasma temperature which the primary drops pass through, resulted in full melting of the particles, while the external zones of the plasma jet presented limited thermal and kinetic transfers between the plasma and the resultant particles.

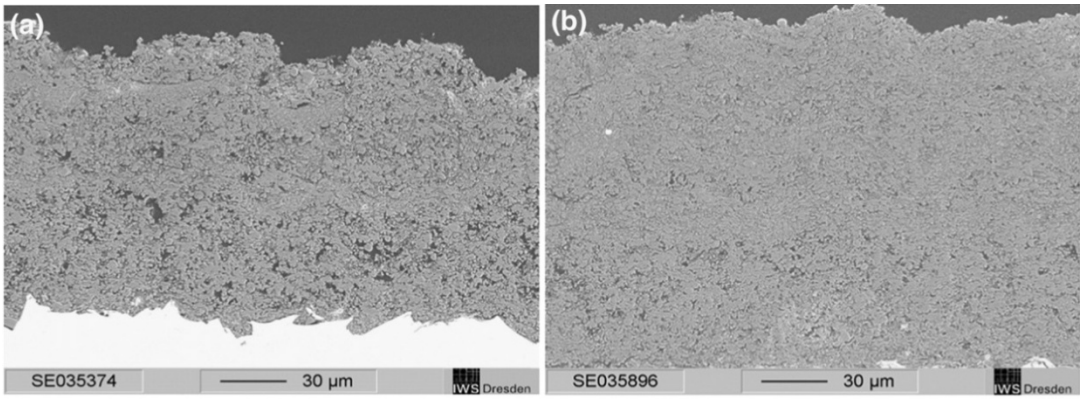

Figure 32. Microstructures of Al_2O_3 aqueous suspension plasma-sprayed coatings: (a) AW1 and (b) AW2[64]

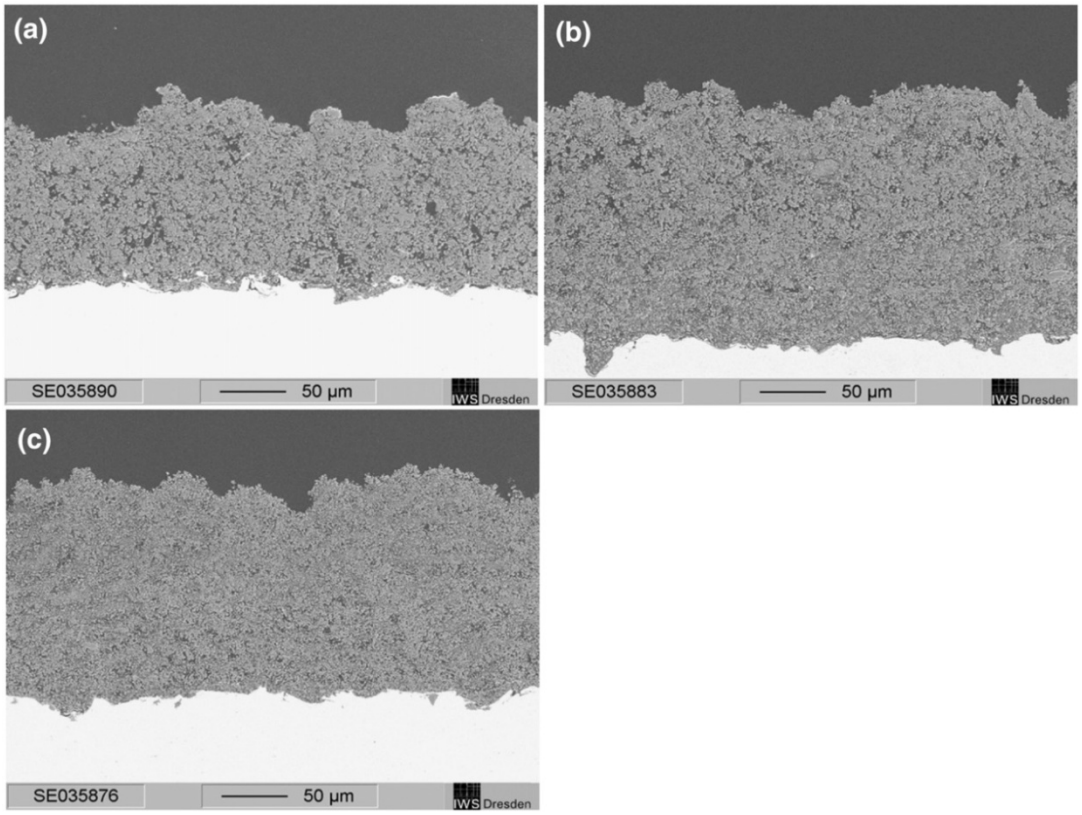

Figure 33. SEM micrographs of Al_2O_3 alcoholic suspension plasma-sprayed coatings: (a) AA1; (b) AA2 and (c) AA3[64]

The microstructures of Al_2O_3 alcoholic suspension plasma-sprayed coatings by different plasma gas mixtures are shown in Figure 33. Spraying with Ar-H_2 plasma resulted in porous deposits with splat-like structured fully melted particles and some spherical agglomerated nanoparticles. Spraying in Ar-He and Ar-He-H_2 plasma jets resulted in a less porous coating with a higher proportion of agglomerated nanoparticles. Arc instabilities in the plasma torch for Ar-H_2 plasma produced voltage fluctuations and resulted in a continuous variation of the length, position and velocity of the plasma jet. The liquid droplets penetrated either at the edge or close to the jet axis depending on the voltage fluctuations. Reduced drop penetration resulted in particles impacting the substrate in a partially melted state and caused porosity in the microstructure. The use of helium reduced the arc fluctuations and the droplets penetrated more uniformly into the core of the plasma jet. The HVOF suspension technique was used to prepare thick Al_2O_3 coatings (> 200 μm). The microstructures of Al_2O_3 deposits resulting from the spraying of aqueous suspensions in an HVOF flame produced impacting of melted and partially melted particles as well as agglomerated nanoparticles. A porous coating microstructure was observed, which was less porous than the coating from plasma spraying (Figure 34).

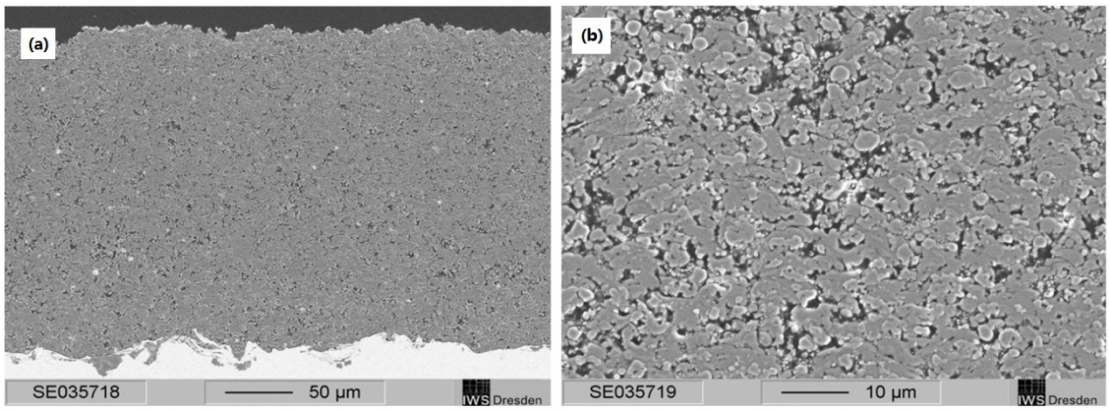

Figure 34. Cross-sectional micrographs of HVOF aqueous suspension-sprayed Al_2O_3 coatings at two different magnifications[64]

2.5 Electroplating System of Mn and its Alloys

As one of the candidates for EC coating replacement, electroplated Mn-based coatings

are considered due to their promising sacrificial protection and mechanical properties[3]. Pure Mn coatings are not utilised because of their high reactivity, which makes them corrode quickly. Mn also presents a brittle phase at room temperature. Mn displays four metallurgical phases, named α-, β-, γ- and δ-Mn[65]. The transformations between these solid Mn phases are expressed as:

$$\alpha \overset{700℃}{\Longleftrightarrow} \beta \overset{1079℃}{\Longleftrightarrow} \gamma \overset{1143℃}{\Longleftrightarrow} \delta$$

Mn in its α-phase shows the highest hardness (583 Knoop Hardness number (KHN)) but is too brittle to utilise practically, whilst γ-Mn is observed with a hardness of 350 KNH and good ductility. γ-Mn can be produced by electroplating[3, 4, 5], but the as-deposited γ-Mn coatings were reported to recrystallise and transform to α-phase at room temperature. For lowering the reactivity, it is suggested that manganese can be alloyed with some more noble metals, such as Zn[14, 66, 67], Sn[68, 69], Ni[70,71] and Fe[72]. Co-deposition with Cu[6, 72, 74, 75] was reported to stabilise ductile γ-Mn phase at room temperature. In addition to continuous current electroplating, pulsed current electroplating can be applied to Mn-based electrodeposition[76, 77] as well. Moreover, Mn-based coatings were also suggested to electroplate from non-aqueous ionic liquids other than aqueous systems[78].

2.5.1 Pure Mn Electroplating

A lot of electrochemical investigations of pure Mn deposition have been carried out to offer useful guidelines for Mn -based alloy electrodeposition. Since 1930, industrial Mn electrowinning has been applied, and pure Mn has been electrodeposited from both sulphate and chloride solutions[4]. Gong et al.[3] produced Mn deposits in different morphologies and microstructures at various current densities and pH values from $MnSO_4$ baths on stainless steel 304 plates. It was found that at low current densities (30~100 mA/cm^2), the deposits displayed silvery matte, compact and uniform traits, with a regularly shaped polycrystalline microstructure (named Type I). As the current densities increased to above 100 mA/cm^2, black shiny deposits with a cellular

microstructure formed (named Type II). The manganese coatings deposited at low current densities were observed as γ-phase with approximately hardness of 147 KHN. With increasing current density, the deposits tended to be amorphous rather than polycrystalline. It was also noted that a phase transformation from γ-phase to α-phase occurred in Type I deposits due to the recrystallisation of γ-phase at room temperature. The chemical distributions in these two types of Mn deposits were also obtained by XPS (Figure 35). It was noted that Mn oxides/hydroxides formed on the surface of the Mn coating. This was attributed to the high reactivity of Mn in an ambient environment. For Type II deposits, the Mn exhibited as oxides/hydroxides rather than metal. It was suggested that Mn is electrodeposited in the forms of oxides/hydroxides at high current densities[3].

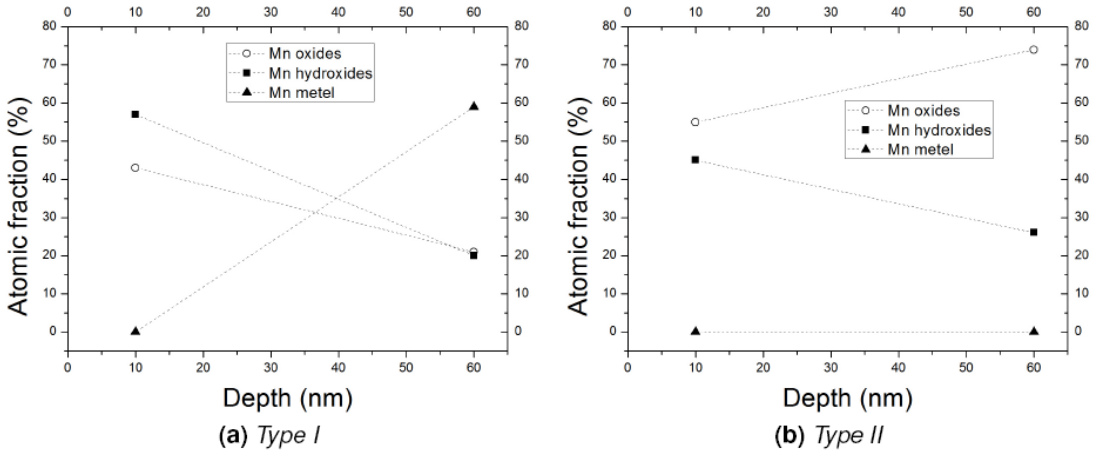

Figure 35. XPS depth profiling of both Type I and Type II Mn electrodeposits[3]

The corrosion resistance of the two types of coatings was also compared. From Figure 36 (a), in a Na_2SO_4 / H_3BO_3 system, both the coatings had corrosion potentials (E_{corr}) of -1.6 V. Type I Mn coatings were observed to dissolve from the substrate during the immersion tests, which resulted in an abrupt change in E_{corr} to -0.8 V. For Type II Mn coatings, E_{corr} increased gradually towards -1.2 V, which still gave sacrificial protection to the substrate. It was implied that the corrosion resistance of the amorphous coatings (Type II) was higher than that of the crystalline ones (Type I) in Na_2SO_4 / H_3BO_3 systems. In a NaCl system, both the coatings presented good corrosion resistance. From

SEM/EDX observations of the coatings after corrosion tests, a layer with an apparent composition of MnO_2 formed on the coating surfaces. It was suggested that such oxide films could slow the corrosion kinetics being a passive film[4].

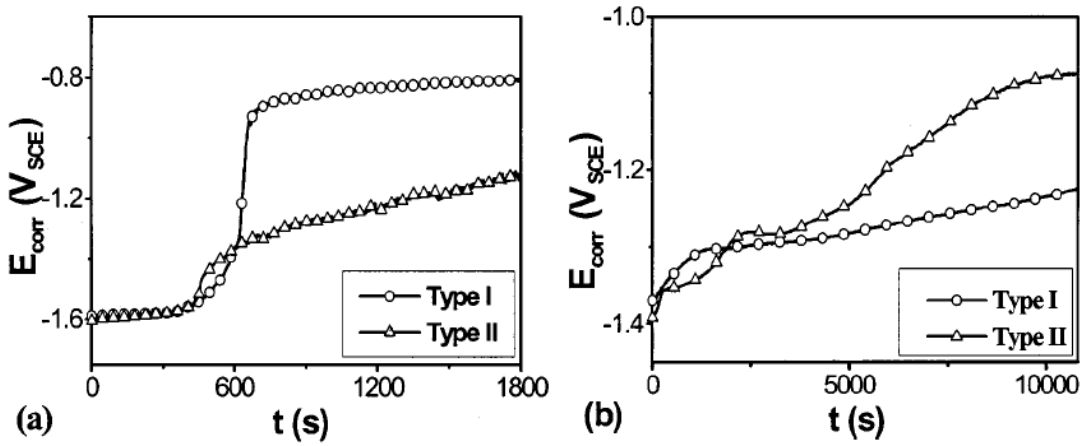

Figure 36. E_{corr} vs. time plots for electroplated manganese immersed in (a) 0.5 M Na_2SO_4 + 0.5 M H_3BO_3 at pH 3.0 and (b) 2.5 % NaCl at pH 3.0[4]

2.5.2 Mn-Zn Alloy Electroplating

Mn-Zn alloys can be electroplated from citrate-based, sulphate-based[14] and chloride-based baths[77]. Non-aqueous ionic liquids have also been utilised to apply Mn-Zn coatings[78]. In all the systems, the sulphate-citrate formulations are the most widely applied electrolytes for producing Mn-Zn alloys with high Mn content (up to approximately 60 wt.%). However, their low cathode current efficiencies and possible Mn citrate precipitates during deposition limit their application[14]. Crystal structures of Mn-Zn alloys have been investigated by Tsuchiya et al.[79]. It was found that five phases were formed in the electrodeposited Mn-Zn alloy coatings with Mn content from 0.01 to 100 wt.%, these were η-phase, Γ-phase, ε-phase, γ-Mn and α-Mn. From Figure 37, it can be summarised that the single ε-phase presents at around 20 wt.% or less Mn. The ε-phase and γ-Mn co-exist in the coating with 20~50 wt.% Mn. Above 50 wt.% Mn, the γ-Mn is the predominant phase. It was also found that γ-Mn would be transformed to α-Mn after heating above 250 ℃, which could be attributed to the recrystallisation of the γ-Mn.

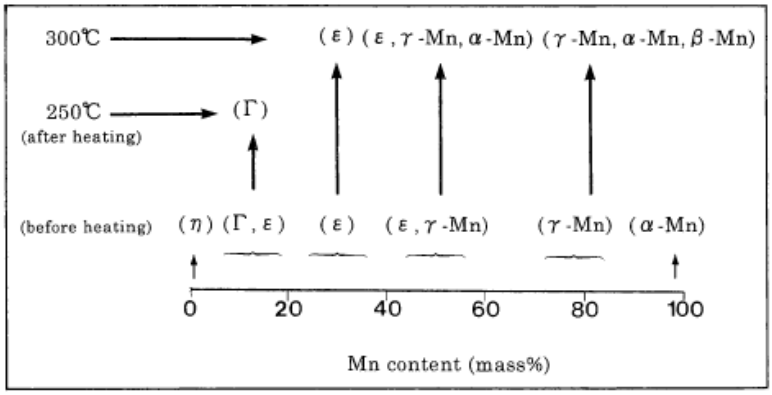

Figure 37. Schematic diagram for changes of alloy phases in electrodeposited Zn-Mn alloys by heating[79]

The corrosion resistance of Mn-Zn alloy coatings with low Mn content (~6 wt.%) electrodeposited from chloride-based solution with NH_4SCN additives were investigated by Diaz-Arista et al.[73] and Oritz et al.[66]. With increasing Mn content, the passivation current density and corrosion rate of the Mn-Zn coatings decreased. It was attributed to the formation of MnO, $Mn_{0.98}O_2$, and Mn_5O_8 during the corrosion tests. These Mn oxides promote the formation of a compact and stable passivation layer, which improves the protective capacity of Mn-Zn coatings.

2.5.3 Mn-Sn Alloy Electroplating

Mn-Sn electroplating was utilised from alkaline tartrate solutions in the 1950s[6]. The Mn-Sn coatings were claimed to have 55 wt.% Mn but of poor coating quality and low cathodic current efficiency. In a recent study, Gong and Zangari[80] produced Mn-Sn coatings from simple ammonium sulphate solutions. At a high current density of 400 mA/cm^2, a bright, glossy and compact Mn-Sn coating was produced with tiny fibrous crystallites. A high Mn content above 98 wt.% was obtained. At a low current density, a heterogeneous Mn-Sn coating was observed with high Sn and O content, but some additions, such as tartrate, ethylene diaminetetraacetic acid (EDTA) and gluconate were suggested to improve the coatings appearance and microstructure. The coatings with a high percentage of intermetallic $Mn_{1.77}Sn$ phase was said to be a good

sacrificial protection for steels.

Mn-Sn electrodeposition was further studied by Chen and Wilcox[68, 69] and the sulphate-based bath formulation was modified and optimised by adding boric acid and Tween 20. With the optimised electrolyte composition and electroplating condition, Mn-Sn alloy coatings with manganese content of 0~40 wt.% can be produced. The corresponding cathode current efficiency (CCE) was within the range of 50~70 %, which is much higher than that of Gong and Zangari's system[80]. Moreover, a much lower current density (10 mA/cm^2) was applied to produce a compact and uniform Mn-Sn coating, which mainly consisted of fine-grained $MnSn_2$. During corrosion tests in NaCl solutions, Mn-Sn coatings with about 30 wt.% Mn presented the highest corrosion resistance, which was as good a sacrificial coatings as chromate passivated Zn-Ni alloy coatings and far outperformed unpassivated pure Zn or Zn-Ni coatings. That good corrosion performance is attributed to the formation of stable Mn oxide/hydroxides during corrosion, which could provide a further physical barrier from corrosion mediums. However, the spontaneous growth of Sn whiskers on Mn-Sn deposits observed by Chen et al.[81] may limit the application of Mn-Sn coatings on electronic components.

2.5.4 Mn-Cu Alloy Electroplating

2.5.4.1 Continuous Current Electroplating of Mn-Cu

As mentioned previously, most Mn alloy coatings suffer from the problem of phase transformation from ductile γ-Mn to brittle α-Mn at room temperature. However, co-deposition of Cu with Mn was found to eliminate this problem and improve its mechanical properties for fastener application. It can also ennoble Mn coatings and improve their corrosion resistance. Early Mn-Cu coatings were electroplated from neutral (pH 7.2~7.4) sulphate-based electrolytes with NH_4^+ at high current densities

(110~330 mA/cm^2). The as-deposited coatings presented good appearance with approximately 97 wt.% Mn, but a low cathodic current efficiency (~37 %) was observed[6]. The effects of current density and electrolyte formulation on the mechanical properties and corrosion resistance of electrodeposited Mn-Cu coatings have been reported in several papers[6, 73, 74,75].

2.5.4.1.1 Effect of Current Density

Current density has a significant effect on both the morphology and composition of Mn-Cu coatings[73]. At current densities less than 100 mA/cm^2, coatings were dark, rough and discontinuous with less than 7 at.% Mn, 60~80 at.% Cu and 15~40 at.% O. At current densities from 100 to 330 mA/cm^2, the Mn content of coatings increased with increasing current density. The compact and uniform Mn-Cu coatings were observed and the highest Mn content reached more than 96 at.%. Stablised γ-Mn phase was observed to predominate in the coatings at room temperature with no oxygen. Compared to pure Mn electrodeposits[4], a smaller grain size was evident in the Mn-Cu coatings. At high current densities over 400 mA/cm^2, uniform, glossy and bright coatings with high Mn content (~96 at.%) were obtained, which were proven to be amorphous.

2.5.4.1.2 Effect of Cu Ion Concentration

The concentration of Cu^{2+} in electrolytes affected Mn-Cu electroplating through two mechanisms[73]. On the one hand, the optimal current density ranges for producing crystalline (Type I) and amorphous (Type II) Mn-Cu coating were strongly dependent on Cu^{2+} concentration. As Cu^{2+} concentration increased, the current density range, where porous coatings were produced, was widened and the current density necessary for obtaining Type I and II Mn-Cu coatings increased. On the other hand, the Cu content in Mn-Cu coatings was in direct proportion to the Cu ion concentration of electrolytes.

2.5.4.1.3 Mechanical Properties

As an alternative for the replacements of EC coatings, electrodeposited Mn-Cu coatings display both a promising low friction coefficient and good ductility. Mechanical properties of Mn-Cu coatings were compared with that of EC and pure Mn coatings by Gong et al.[74]. The mechanical properties were characterised by friction coefficient, nanohardness (H) and reduced modulus (E_r). Moreover, a value of H/E_r was utilised, which is the resistance to plastic penetration. This value was suggested as a better measurement of the materials' ability to withstand plastic damage than hardness or reduced modulus alone[82]. Table 10 shows that both Type I and II Mn-Cu coatings have lower in friction coefficients than EC coatings. Crystalline Mn-Cu coatings display rougher morphologies than amorphous ones, which results from the regular-shaped crystalline structures[73]. Compared to pure Mn coatings, co-deposition of Cu decreased both the hardness and reduced modulus of Mn-Cu coatings. Mn-Cu coatings present much lower reduced modulus than EC coatings, however, in terms of the value of H/E_r, both Type I and II Mn-Cu coatings show good mechanical properties for the replacement for EC.

Table 10. Friction coefficient, nanohardness and reduced modulus of electrodeposited cadmium (ECD), crystalline Mn-Cu (Type I), amorphous Mn-Cu (Type II), crystalline Mn (Type I) and amorphous Mn (Type II) coatings[74]

Parameters	ECD Cd	Mn-Cu		Mn	
		Type I	Type II	Type I	Type II
Friction coefficient	0.8	0.7	0.5	-	0.5
Nanohardness H (GPa)	0.3	0.1	0.5	0.4	4
Reduced modulus E_r (GPa)	151.9	10.5	32.9	31.3	95.3
H/E_r^2 ($\times 10^{-4}$)	0.13	9.1	4.6	4.1	4.4

2.5.4.1.4 Corrosion Resistance Properties

Gong et al.[74] investigated the corrosion resistance of Mn-Cu coatings. Through potentiodynamic scans, the corrosion resistance of pure Mn, pure Cu and Mn-Cu

coatings was characterised by corrosion potential (E_{corr}) and corrosion current density (I_{corr}) as shown in Table 11. The E_{corr} of pure Mn was about -1.35 V_{SCE} and the I_{corr} were 120 and 40 $\mu A/cm^2$ for crystalline and amorphous Mn coatings respectively. Pure copper coatings exhibited an E_{corr} of about -0.37 V_{SCE} and a I_{corr} of about 29.4 $\mu A/cm^2$. The E_{corr} of Mn-Cu coatings was approximately -1.23 V_{SCE}, which was attributed to the co-deposition of Cu ennobling the Mn coating. Moreover, the I_{corr} of amorphous and crystalline Mn-Cu coatings were 140 and 431 $\mu A/cm^2$ respectively, which were higher than that for pure Mn and Cu coatings. This was suggested to result from galvanic coupling between Mn and Cu according to the mixed-potential theory[83]. It was also noted that co-deposition of copper widens the passive region and lowers the passive current density of Mn-Cu coatings, which results in good barrier protection properties during corrosion. With increasing Cu content, the E_{corr} of Mn-Cu coatings shifted in the positive direction and the coatings became easier to passivate.

Table 11. The corrosion resistance of electrodeposited Mn, Cu and Mn-Cu coatings[74]

Property	Mn (crystalline)	Mn (amorphous)	Cu	Mn-Cu (crystalline)	Mn-Cu (amorphous)
E_{corr} (V_{SCE})	-1.35	-1.35	-0.37	-1.23	-1.23
I_{corr} ($\mu A/cm^2$)	120	40	29.4	431	140

2.5.4.2 Pulsed Current Electroplating

Pulse electroplating was initially used to produce Cu and Au coatings. It can modify the quality of electrodeposits and now it is widely utilised for many other metal and alloy coatings[84]. Compared to conventional direct current electroplating, pulse electroplating applies current for a period followed by a relaxation time with no current passing[77]. More parameters other than current density can be controlled in pulse electroplating, including peak current density, current 'on' time, current 'off' time, duty cycle and pulse frequency. A high peak current density is necessary to reach a corresponding direct current density, so pulse electroplating usually causes a high nucleation rate and produces deposits with a finer grain size[84]. Moreover, it was reported that pulse

electroplating can also improve current distribution and mass transportation during processes, which may result in increased brightness, reduced porosity and low impurities[85]. A relevant study was reported by Mangolini et al.[76, 77] to compare continuous current electroplated Mn-Cu coatings with pulsed current electroplated ones from similar sulphate-based solutions. Compact and uniform Mn-Cu coatings with >95 wt.% Mn were produced by pulse electroplating. The mechanical properties and corrosion resistance of the coatings were as good as those of the continuous current electroplated ones. Pulse electroplating was noted to improve the surface appearances and brightness of Mn-Cu coatings. It was also noted that pulse electroplating produced coatings with larger average grain size of the coatings than continuous electroplating. It was explained to be attributed to enhanced hydrogen content desorption during the relaxation time, which caused lattices to expand.

2.5.4.3 Non-Aqueous Ionic Liquid Electroplating of Mn-Cu

Electroplating from aqueous solution is one of the most widely applied surface finishing processes. However, with more and more novel metal and alloy coatings, which have quite negative electrode potentials, proposed to be deposited by electroplating, low cathodic current efficiency and narrow potential windows of aqueous electroplating systems limit their commercial applicability.

Electroplating from non-aqueous ionic liquid electrolytes is proposed to eliminate these two major problems. Non-aqueous ionic liquid electrolytes are solely composed of ions with low melting points below 100 ℃. Due to absence of water in ionic liquid electrolytes, H_2 evolution is significantly inhibited, which can usually bring a high cathodic current efficiency. The wide potential windows of ionic liquid electrolytes allow them to produce more active metal and alloy coatings. As mentioned previously, several studies about electroplating Al from non-aqueous ionic liquid electrolytes have been undertaken. Electroplating pure Mn and its alloys from ionic liquids has also been

investigated. Pure Mn was produced from a room-temperature ionic liquid butylmethylpyrrolidiniumbis- ((trifluoromethyl)sulfony) imide (BuMePy-TFSI) by Deng et al.[86]. A Mn-Zn alloy coating was successfully electroplated from tri-1-butylmethylammonium bis((trifluoromethane)sulfonyl)imide ($Bu_3MeN^+Tf_2N^-$) with good surface appearance and corrosion resistance[87]. In these two ionic liquid systems, Mn and Zn ions were introduced by anodic dissolution due to insolubility of corresponding metal salts in the ionic liquids. A different ionic liquid system (urea/choline chloride) was proposed to produce Mn-Zn coatings with good adhesion to the steel substrates and containing 22 wt.% Mn by Chung et al.[77]. The concentrations of Mn and Zn ions are easy to control by adding Mn and Zn chlorides due to their good solubility in 2:1 urea/choline chloride.

Mn-Cu coatings were reported to be electroplated on tungsten substrates from a N-butyl-N-methylpyrrolidiniumbis(trifluoromethylsulfonyl)imide (BMP-TFSI) ionic liquid system[88]. Anodic dissolution of corresponding metal electrodes was utilised to introduce Mn^{2+} and Cu^+ into the ionic liquids. Different deposition potentials and compositional ratio of [Cu(I)/Mn(II)] were applied to produce Mn-Cu coatings. During electroplating, the reduction rate of Cu was controlled by diffusion due to its more positive reduction potential. Because of the high activity of Mn, its reduction rate was predominated by the applied potential and concentration of Mn^{2+}. Therefore, the more negative applied potential and higher concentration of Mn^{2+} in the ionic liquids, the higher the Mn content presented in the corresponding coatings. All the coatings exhibited amorphous structures and good adherence to the substrates. Decreasing grain size was observed in the coatings with increasing Mn content. In terms of corrosion resistance, the Mn-Cu coatings displayed passivation behaviour during electrochemical corrosion tests in NaCl solution. Oxide films formed on the Mn-Cu coatings during corrosion tests, which inhibited the continuous dissolution of the coatings. Compared to corresponding pure Mn and Cu coatings, the Mn-Cu co-deposits exhibited higher corrosion resistance.

2.6 Galvanic Corrosion

The free corrosion potential of a metal is an electrode potential attained by that metal immersed in an electrically conducting liquid. This potential is determined by the equilibrium between the anodic and cathodic reactions occurring on its surface. Galvanic corrosion occurs when two metals with significantly different potentials are in electrical contact in an electrically conducting electrolyte. Due to the different potentials of the two metals in the electrolyte, a current flows from the anodic (more electronegative) metal to the cathodic (more electropositive) metal in order to equalise the potentials. In this way, an oxidation reaction occurs at the anode and the anode metal dissolves into metal ions and produces the galvanic corrosion (Figure 38). Electrochemical reduction reactions occur at the cathode for electrical balance, this could be the reduction of dissolved O_2 or H^+.

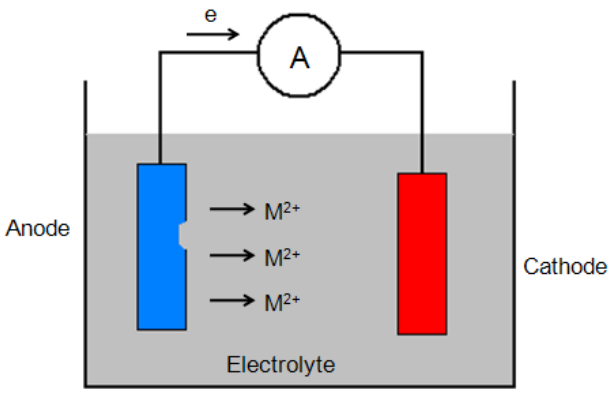

Figure 38. Schematic diagram of galvanic corrosion in a galvanic couple

There are four basic requirements necessary to cause galvanic corrosion. These are as follows[89]:

1) An electrolyte bridging two metals
2) An electrical connection between two metals
3) Sufficient difference in potential between two metals
4) A sustained cathodic reaction on the cathode metal.

2.6.1 Factors Affecting Galvanic Corrosion

There are many factors that affect galvanic corrosion, including electrode potential,

cathodic efficiency, anode/cathode area ratio, and the nature of the electrolyte.

2.6.1.1 Electrode Potential

As mentioned previously, a sufficient difference in potentials between the two metals is necessary to provide the driving force for a significant galvanic current. However, the magnitude of the potential difference alone does not indicate the amount of galvanic corrosion, which also depends on the kinetics of reaction on the electrodes in the couple. A change in the kinetics of the anodic or cathodic reaction or a change in the nature of the reaction can cause a change in potential, which can result in polarity changes for some galvanic couples. Potential changes can be caused by complex ions, changes in pH, temperature and intense aeration. For example, the potential of the most electropositive alloys decreases with temperature in seawater due to the absence of a biofilm, which forms in natural seawater at ambient temperature[90]. This biofilm, which forms over a period of a few days to a few weeks catalyses the cathodic reduction of dissolved O_2 and increases the potential of the metals. However, the addition of small quantities of Cl or raising the temperature can prevent the formation of biofilms. Moreover, in deaerated seawater, the potential of the high-alloy stainless steels, such as 6 % Mo austenitic stainless steels and super duplex stainless steels, become more electronegative with decrease in the dissolved O_2 content. Temperature changes were found to affect potentials sufficiently to cause polarity reversals between some metals. At temperatures above 60 ℃, iron becomes anodic to Zn, which results in corrosion of galvanized steel in hot water systems[89].

2.6.1.2 Electrode Efficiency

Due to varying kinetics of reactions on metals, the rate of the anodic or cathodic reaction is not the same for all metals when they form part of a galvanic couple. Electrode efficiency is defined as the rate of the reaction at the metal (anode or cathode)

surface. In galvanic corrosion, the efficiency of the cathodic reaction usually has more significance than that for the anodic reaction[89]. The galvanic current caused by the two coupled metals is accompanied by a shift in the potential of the anodic member to a more electropositive value and in the potential of the cathodic member to a more electronegative value, this is called polarisation. In neutral electrolytes, the cathode is almost always polarised much more than the anode because of the fact that a small area of sacrificial anode will effectively provide protection to a relatively large cathodic area. The extent of the polarisation determines how effective any particular metal may be as a cathode to drive the corrosion of the anode.

2.6.1.3 Area Ratio

The ratio of the exposed areas of the anode and cathode of a galvanic couple plays an important role in the severity of the subsequent of galvanic corrosion. The larger the cathode compared with the anode, the more O reduction, or other cathodic reaction, can occur and the greater the galvanic current. This results in more corrosion at the anode. Under static or slowly flowing conditions, the galvanic corrosion current is often dependent on the rate of diffusion of dissolved O_2 to the cathode. So the severity of galvanic corrosion is proportional to the cathode surface area. So for a constant area of cathode, the corrosion current is constant but the current density increases as the anode area decreases. Therefore, under immersed conditions in a highly conductive electrolyte, extremely small anodic areas may exist at discontinuities, such as cracks or pores in cathodic coatings. In this case, it is necessary to specify a thickness of adequate integrity to apply protection when immersed in highly conducting electrolytes.

2.6.1.4 Environments

2.6.1.4.1 Electrolyte

The electrolyte has a major influence on galvanic corrosion due to its composition, pH

and electrical conductivity, which affect both the intensity and the distribution of corrosion. In an electrolyte of low conductivity, corrosion is confined to an area near the junction between two metals. So the total amount of corrosion may be low, but it is likely to be highly localised and therefore, may be intense. In highly conducting electrolytes, corrosion will be more widespread than in a less conducting one.

In common with local cell corrosion, galvanic corrosion is also sensitive to the constituents in the electrolyte that affect stability of the corroded metal ions. The presence of bicarbonate, silicate and sulphate enhances the formation of insoluble and adherent corrosion products. In some cases insoluble corrosion products from the anodic metal can deposit upon and induce crevice corrosion of the cathodic metal of a couple.

2.6.1.4.2 Aeration and Flow Rate

The majority of practical situations involving galvanic corrosion arise in aqueous solutions under conditions in which the cathodic reaction is the reduction of dissolved O_2. Galvanic corrosion is, therefore, partly dependent upon the rate at which O_2 can diffuse to the cathodic surface from the bulk electrolyte. In flowing, aerated electrolyte the oxide film formed on the cathodic surface is likely to thicken, thus diminishing the galvanic corrosion of the coupled metal. In neutral electrolytes complete deaeration will, in many instances, suppress galvanic corrosion. However, under such anaerobic conditions, cathodic depolarisation and corrosion can occur if an alternative reaction to the reduction of dissolved O_2 is available, such as metal ion reduction and deposition.

2.6.2 Monitoring of Galvanic Corrosion

The corrosion rate of a galvanic couple can be estimated by several techniques, such as overlaying the polarization curves of the individual components of a galvanic couple using the mixed potential theory, and also the zero resistance ammeter (ZRA)

technique. Moreover, the scanning vibrating electrode technique (SVET) and the immersion technique can also be used to calculate the maximum corrosion rate of a galvanic couple as discussed in the following sections.

2.6.2.1 Zero Resistance Ammeter (ZRA) Technique

ZRA is a current to voltage converter that produces a voltage output proportional to the current flowing between it and input terminals while imposing a 'zero' voltage drop to the external circuit. ZRA is typically used to measure the galvanic coupling current between two dissimilar electrodes. Jia et al.[91] applied a galvanic corrosion assembly (GCA) with ZRA to investigate the effects of area ratio of anode/cathode, solution film thickness and distance between anode and cathode, on the galvanic corrosion of magnesium alloy and mild steel. As Figure 39 shows, the GCA consisted of some metal plates with different area. In this manner, the galvanic currents of the couples with different area ratios and distances apart can be measured by a ZRA through connecting or disconnecting some of the metal plates.

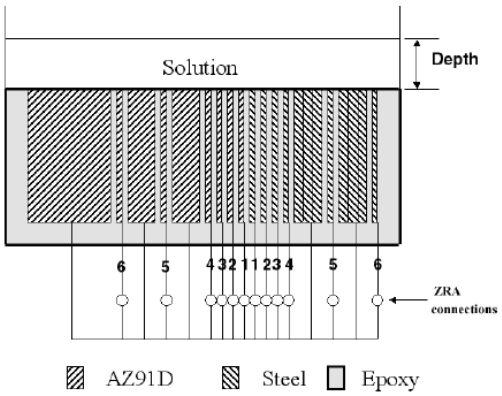

Figure 39. Multi-electrode Mg-steel galvanic corrosion assembly (GCA) for the study of galvanic corrosion[91]

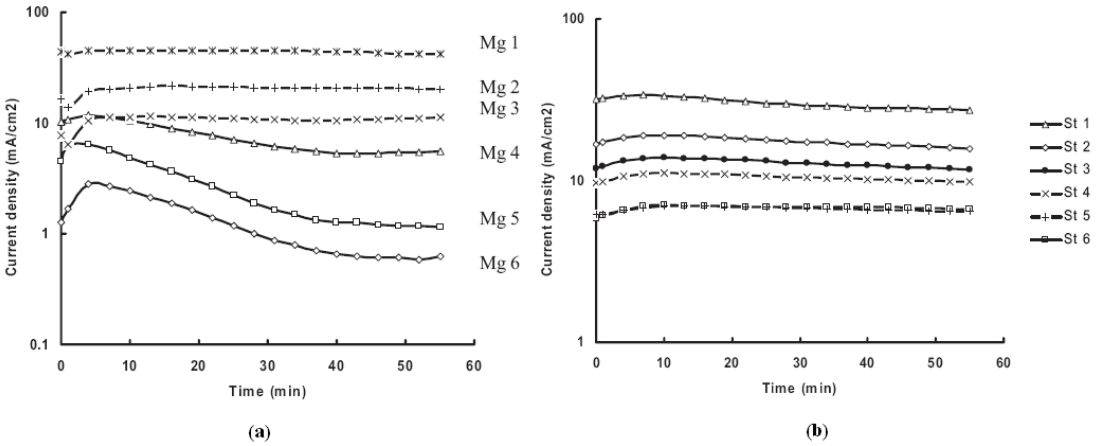

Figure 40. (a) Galvanic current density at AZ91D Mg alloy electrodes (designated Mg 1 to Mg 6) in 5 % NaCl solution. (b) Galvanic current density at steel electrodes (designated St 1 to St 6) in 5 % NaCl solution[91].

Figure 40 shows the measurement of galvanic current using the GCA illustrated in Figure 39 for electrodes of AZ91D (magnesium alloy) and steel in 5 wt.% NaCl solution. The initial decrease of the galvanic current for electrodes Mg4 and Mg6 was suggested as a result of the corrosion product deposit contributing some protection on electrodes. Moreover, the effects of area ratio of anode to cathode, solution film thickness and distance between anode and cathode were also investigated. It was suggested that the galvanic current of the AZ91D electrodes increased with decrease in area ratio of anode to cathode as expected. The increase of solution film thickness also increased the galvanic current of each electrode because the thicker solution films reduced the solution resistance against the current flow. The increase of the insulating distance between the AZ91D electrodes and mild steel electrodes led to less galvanic corrosion attack both locally and in total.

2.6.2.2 Scanning Vibrating Electrode Technique (SVET)

SVET is an AC technique which measures the localized current in an electrolyte above a sample by virtue of the IR drop in the electrolyte. Deshpande[92] used SVET to investigate the corrosion behaviour of two galvanic couples, AE44 (Mg Alloy) – mild steel and AE44 – AA6063 (Al alloy) in a 1.6 wt.% NaCl solution. In the experiments,

the two dissimilar metals were ground at the edges, held tightly using a vice and wrapped with tape and then hot mounted to achieve a very good electrical contact with each other. Two scan rates were used to indicate effect of the scan rate on the SVET results as Table 12 shows. A typical SVET output is shown in Figures 41 (a) and 42 (a), which is represented in terms of the potential difference. The current density was calculated from the SVET output[93] as:

$$j = -\sigma \frac{\Delta E}{A} \qquad \text{Equation (2)}$$

Where j is the current density in A/m^2, σ is the conductivity of the electrolyte solution in S/m, ΔE is the potential difference across the vibration amplitude in V, and A is the vibration amplitude in m.

The corrosion rate, C_R, was calculated from the current density using Faraday's law[94] as follows:

$$C_R = \frac{M}{zF\rho} j \qquad \text{Equation (3)}$$

Where M is the atomic mass of the corroding series, z is the number of electrons, F is the Faraday constant and ρ is the density of the corroding metal.

Table 12. The parameters used in SVET experiments by Deshpande with faster and slower scans for AE44-mild steel and AE44-AA6063 couples[92]

Galvanic couple	AE44 – mild steel faster scan	AE44 – AA6063 faster scan	AE44 – mild steel slower scan	AE44 – AA6063 slower scan
X scan width (μm)	18,000	18,000	18,000	18,000
Y scan width (μm)	1000	1000	1000	1000
X μm per point	100	100	100	500
Y μm per point	50	50	500	500
Scan rate (μm s^{-1})	2000	500	33.33	166.67
Full scale sensitivity (mV)	4	1.6	4	1.6
Output time constant (s)	1	1	1	1

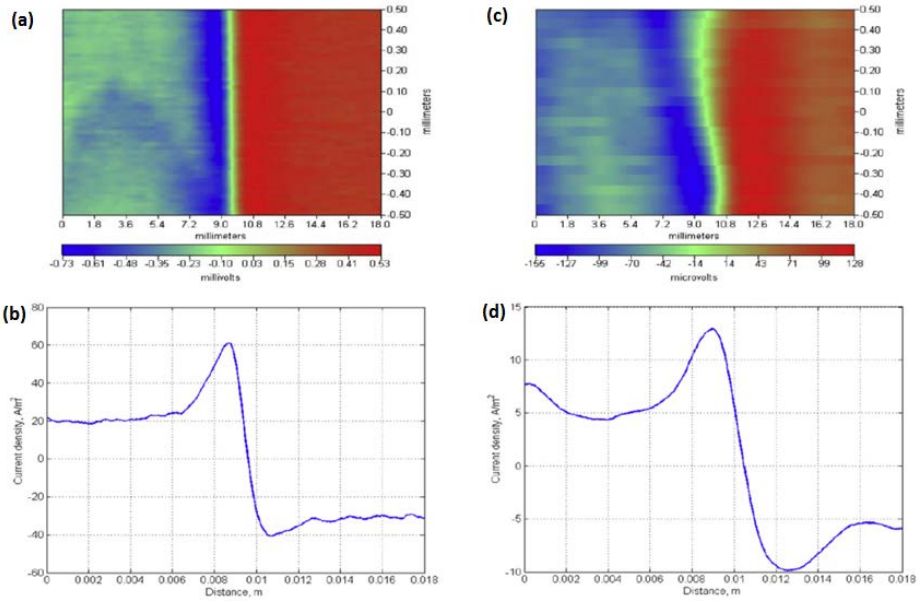

Figure 41. (a) The SVET area scan for the potential difference obtained using the faster scan parameters for AE44 – mild steel couple. (b) The current density variation with distance from the junction of the same couple. (c) The SVET area scan for the potential difference obtained using the faster scan parameters for AE44 – AA6063 couple. (d) The current density variation with distance from the junction of the same couple[92].

From Figures 41 (a) and (c), the potential difference in the scanning area can be seen and that half of the galvanic couple shows negative potential difference and the other half shows a positive potential difference. Both the anodic and the cathodic peak current densities in the vicinity of the junction of the galvanic couple were captured from the potential difference with distance from the galvanic couple junction (Figures 41 (b) and (d)).

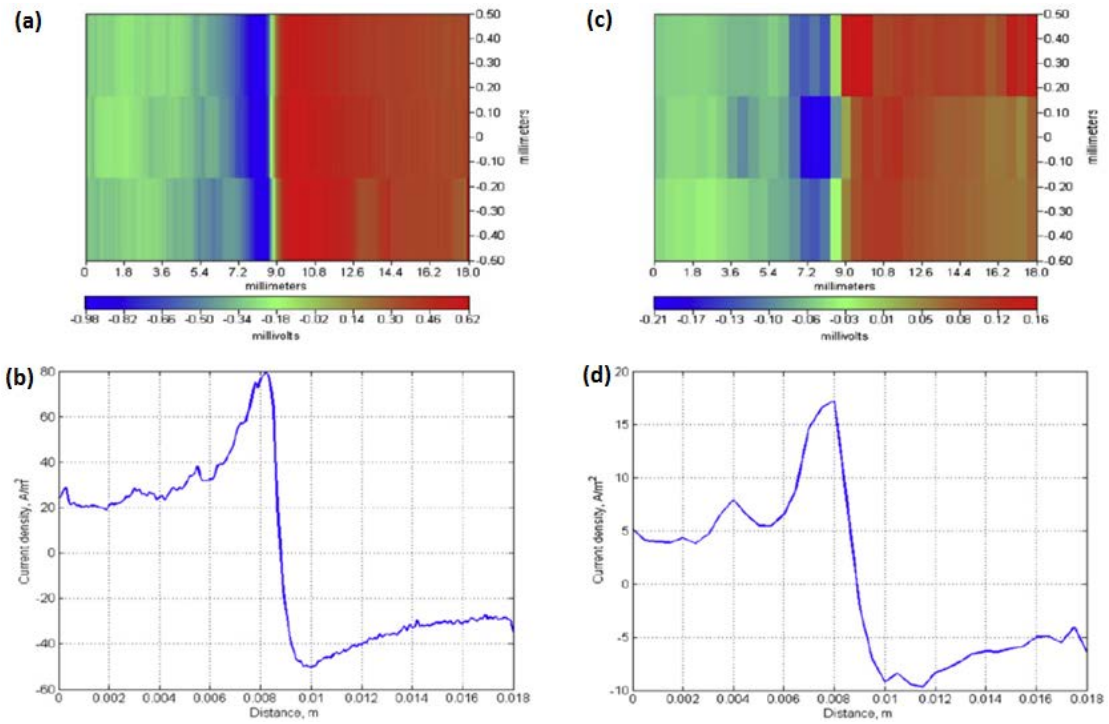

Figure 42. (a) The SVET area scan for the potential difference obtained using the slower scan parameters for AE44 – mild steel couple. (b) The current density variation with distance from the junction of the same couple(c) The SVET area scan for the potential difference obtained using the slower scan parameters for AE44 – AA6063 couple. (d) The current density variation with distance from the junction of the same couple[92].

It was noted that in the faster scan rate, the current density at both of the anodic and cathodic region peaks were captured at around 3 mm away from the junction. It was suggested that this resulted from the data acquisition time being far smaller than the output time constant. Deshpande[57] suggested that the data acquisition time needed to be three times the output time constant in order to receive 95% of signal, and it needed to be five times the output time constant to receive 99% of signal, which spatially resolved the current density variation. Figures 42 shows that in the slower scan rate, both the anodic and the cathodic peak current densities are captured within 1 mm of the distance from the junction. So in the SVET experiments, spatial variation of current density can be captured for both galvanic couples by varying the probe scan rate and thereby controlling the date acquisition time. In the system studied, AE44 was anodic or preferentially corroded to both mild steel and AA6063. Hence, only the anodic component of the galvanic couple was considered to calculate the corrosion rate. As

Figures 41 and 42 shows, the value of the current density is maximum at the junction of the couple and decreases with the distance away from the junction due to IR drop. The SVET was used to estimate the maximum corrosion rate at the junction of the couple by calculation from the peak potential difference. As Table 13 shows, AE44 coupled with mild steel corroded approximately 5 times faster than coupled with AA6063.

Table 13. The maximum corrosion rate estimated from the SVET experiments for AE44-mild steel and AE44-AA6063 couples[92]

Galvanic couple	Peak SVET output (mV)	Anodic peak current density ($A\,m^{-2}$)	The maximum corrosion rate	
			$nm\,s^{-1}$	$mm\,y^{-1}$
AE44 – mild steel	98	81.7	6.24	197
AE44 – AA6063	21	17.5	1.34	42

2.6.2.3 Immersion Experiments

In an immersion experiment, a ground galvanic couple is prepared and hot mounted, then freely suspended in an electrolyte. After immersion for 3 days, the sample is scrubbed to remove the entire corrosion product from the metal surface. Then the couple is observed in cross-section by a high resolution digital camera to measure the maximum pit depth formed at its junction. This is another method to estimate the galvanic corrosion rate.

In addition to applying the SVET for galvanic corrosion investigation, Deshpande[92] also used immersion experiments to estimate the maximum corrosion rate of the AE44-mild steel and AE44-AA6063 couples. Photographs of the cross-sectional view of the AE44-mild steel and AE44-AA6063 couples after 3 days of immersion test are shown in Figure 43. It can be seen that in both couples, a maximum pit depth was formed at their junctions. The maximum pit depth formed at the junction was used to estimate the maximum corrosion rate as shown in Table 14.

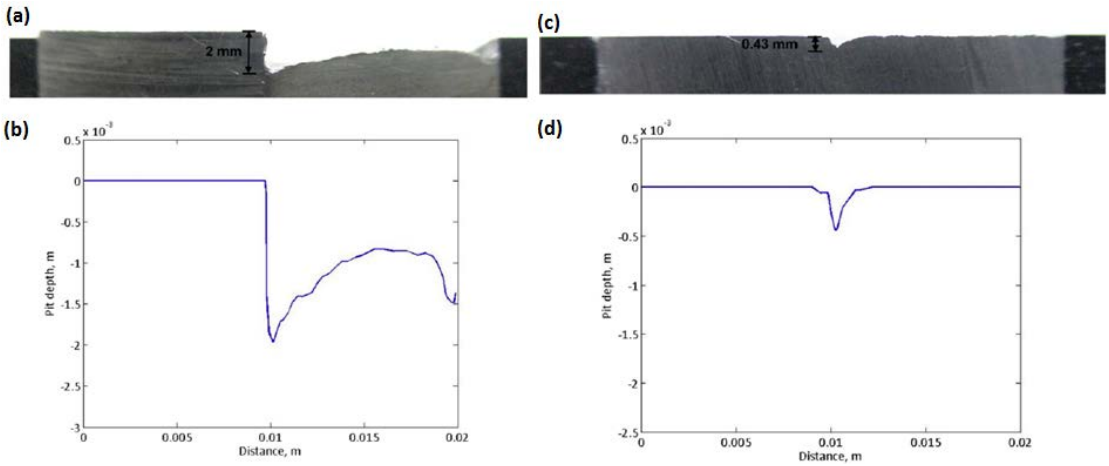

Figure 43. (a) A photograph of the cross-sectional view of an AE44 – mild steel couple after 3 days of immersion in the 1.6 wt.% NaCl solution. (b) The surface profile of the same couple obtained using a secondary electron micrograph digitization technique. (c) A photograph of the cross-sectional view of an AE44 – AA6063 couple after 3 days of immersion in the electrolyte solution. (d) The surface profile of the same couple obtained using a secondary electron micrograph digitization technique[92].

Table 14. The maximum corrosion rate estimated from the immersion experiments for AE44 – mild steel and AE44 – AA6063 couples[92].

Galvanic couple	Maximum pit depth in mm after 3 days of immersion	The maximum corrosion rate	
		$nm\ s^{-1}$	$mm\ y^{-1}$
AE44 – mild steel	2	7.72	243
AE44 – AA6063	0.43	1.66	52

Compared to the results from the SVET (Table 13), it was found that the maximum corrosion rates of AE44 coupled to mild steel and AA6063 obtained from the immersion tests were comparable in magnitude, with the value obtained from the immersion test being about 20% higher than that from the SVET test. Deshpande[92] suggested that this over-prediction from the immersion technique could be attributed to the exposure time of the galvanic couple to the electrolyte solution, which caused a change in the pH of the electrolyte. The pH increased significantly in the immersion test after the exposure time of 3 days. The distance between the probe and surface could also cause under-prediction of the corrosion rates using the SVET technique.

2.7 Summary

From the literature review, it can be seen that EC coatings are currently still applied as sacrificial coatings in the aerospace industry due to their excellent barrier protection, good galvanic compatibility with Al alloys and high inherent lubricity. However, the high toxicity of the coating and its electroplating process has been realised and that limits their application. From the literature review, it can be seen that a lot of possible replacements for EC coatings have been proposed. The replacement coatings include mainly Zn alloys and Al-based coatings. As EC replacements, Zn is normally co-deposited with more noble metals, such as Ni and Co. Both electroplated Zn-Ni and Zn-Ni-Co alloy coatings exhibit comparable corrosion resistance to the EC coating, however, the possible environmental problems caused by Ni and Co make their feasibility as EC coating replacements, long term, in doubt. For Al-based coatings, their good corrosion resistance and barrier protection make them well regarded as EC replacements. In the literature review, it can be noted that there are a lot of studies about Al-based coatings produced by electroplating (organic electrolyte), flame spraying and PVD, which exhibit good sacrificial and barrier protection properties. However, few reports address a comparison of EC and Al-based coatings in terms of morphology, composition, barrier protection and corrosion resistance, in essence, for assessing the feasibility of Al-based coatings as EC coating replacements. In this thesis, the assessment of Al-based coatings as EC replacements has been addressed by a laboratory based comparison.

From the literature review, it can be seen that EHC coatings have a similar problem to EC coatings, so the high toxicity of their electroplating process limits their future application though EHC coatings themselves exhibit high hardness, barrier protection and a low coefficient of friction. Many studies have been carried out to find their replacements. Currently, trivalent Cr-based, Co alloy, Ni alloy and inorganic coatings (HVOF WC/Cr/Co coatings) are mainly regarded as possible EHC replacements due

to their similar mechanical properties, particularly in hardness. Due to the environmental concerns, the future of Co alloy and Ni alloy coatings as EHC replacements is still uncertain. Therefore, many researchers suggest the feasibility of HVOF WC/Cr/Co coatings as EHC replacements due to their comparable hardness. However, as a composite coating, there are few investigations studying the corrosion resistance of HVOF WC/Cr/Co coatings by electrochemical methods. In this Ph.D. thesis, the corrosion resistance and corrosion mechanism for HVOF WC/Cr/Co coatings were investigated and addressed by electrochemical methods.

Sacrificial coatings and hard coatings have a high possibility of being in physical contact in aerospace applications, particularly on landing gear. Therefore, the galvanic compatibility of sacrificial and hard coatings is important in this application. From the literature review, few studies were noted reporting this type of investigation. In this thesis, the compatibility of EC/EHC coatings and their replacements has been investigated and the severity of possible galvanic corrosion between them was also addressed.

In order to improve the galvanic compatibility of HVOF WC/Cr/Co coatings with sacrificial coatings, an insulating and hard layer was considered for application on the surface of HVOF WC/Cr/Co coated steels. Al_2O_3 coatings are reported to have a barrier protection property. The low conductivity of Al_2O_3 coatings allows them to improve the electrochemical properties of substrates, such as galvanic corrosion resistance. Few investigations are apparent investigating the feasibility of the deposition of Al_2O_3 coatings on HVOF WC/Cr/Co coated steels to improve galvanic corrosion resistance. In this thesis, methods to deposit Al_2O_3 coatings on coated steels have been investigated and their feasibility as a treatment has been addressed.

In addition to Zn alloy and Al-based coatings, from the literature review, it is also noted that the possibility of electroplated Mn alloy coatings as EC replacements has been studied and reported due to their good mechanical and sacrificial protection

properties. Of the Mn alloy coatings, Mn-Cu is of particular interest because the co-deposition of Cu with Mn can stabilise the ductile γ-Mn phase. Several studies have been carried to investigate the electroplating of Mn-Cu coatings, however, few investigations are reported about the electroplating mechanism following changes in in electrolyte composition. The latter has been investigated in this work by electrochemical methods and the optimisation of the electroplating process was addressed.

CHAPTER 3: EXPERIMENTAL PROCEDURES

In this project, according to the requirements of Airbus, the feasibility of EC and EHC coatings replacements was investigated. The first part of the experimental programme was to identify the galvanic compatibilities of the sacrificial and hard coatings qualitatively and quantitatively by monitoring their electrode potential and galvanic current during galvanic corrosion. All the replacement coating systems were also compared with EC and EHC coatings in terms of morphology, composition, corrosion resistance, and porosity to identify the feasibility. The second part of the experimental programme was to investigate the corrosion of HVOF WC/Cr/Co coatings as EHC replacements further by electrochemical methods. In order to improve the galvanic compatibilities of HVOF WC/Cr/Co coatings with the sacrificial coatings, Airbus suggested applying an Al_2O_3 coating on a HVOF WC/Cr/Co coating. Therefore, the third part of the experimental programme was to apply Al_2O_3 coatings on HVOF WC/Cr/Co coatings by the electrochemical method and the sol-gel method due to their low damage to underlying HVOF WC/Cr/Co coating. The last part of the experimental programme was to investigate the electrodeposition of Mn-Cu coatings as a potential sacrificial replacement coating according the requirements of Airbus.

3.1 Galvanic Corrosion between EC and EHC, and Their Replacements

Airbus suggested Al-based coatings, including EDAl, FSAl and SermeTel 962, as replacements of EC coating and HVOF WC/Cr/Co coating as replacement for EHC coating. In the galvanic corrosion investigations, all the coatings were applied to 300M high strength steels obtained from Airbus. The substrate and coatings investigated were as followings:

Table 15. The composition of 300M high strength steel (AMS 6419F[95]) used in the investigations

Element	C	Mn	Si	P	S	Cr	Ni	Mo	V	Cu
Min (wt.%)	0.40	0.60	1.45	-	-	0.70	1.65	0.30	0.05	-
Max (wt. %)	0.45	0.90	1.80	0.01	0.10	0.95	2.00	0.50	0.10	0.35
Note: The balance is Fe										

Table 16. The specification of the coatings used in this project

Sacrificial Coating	**Hard Coating**	**Specification**	**Thickness (µm)**	**Suppplier**
EC	-	AIPS 02-04-002[96]	~12	Poeton
SermeTel 962	-	PCS-2550[97]	~32	Sermetel
EDAl	-	MIL-DTL-83488 D[98]	~35	Alumi-Plate
FSAl	-	AIPS 02-03-004[99]	~425	Sultzer
	EHC	ABP 1-4042[100]	~105	Poeton
-	HVOF (WC/Co/Cr) 10%Co 4%Cr	MD PCS2560[101]	~170	Delore Stellite

In order to investigate the feasibility of the replacements for EC and EHC coatings, all the coatings were characterised in terms of morphology, composition and corrosion resistance. Techniques included optical microscopy, XPS, SEM and FIBSEM were used for the morphology and compositional characterisation of the coatings. Free corrosion potential, LPR, and porosity of the coatings were measured electrochemically to identify the corrosion resistance of the coating systems. The galvanic compatibility between the sacrificial and the hard coatings was also investigated by monitoring the galvanic current and electrode potential of the galvanic couples.

3.1.1 Morphology and Compositional Characterisation

3.1.1.1 Sample Preparation for Cross-section Characterisation

Cross-sections of coatings were mounted in phenolic hot mounting resin with carbon

filler at a standard size (30 mm diameter) for polishing. After mounting, the cross-section of the sample was ground and polished in an automatic grinding/polishing system (TegraSystem, including TegraForce-5 and TegraDoser-5, Struers). By altering the grinding/polishing discs from the coarsest to the finest grade, the cross-section was polished gradually to achieve a 1 μm surface finish. In order to ensure the 1 μm surface finish of the specimens and to remove residual surface damages caused by prior polishing, a twenty-minute final chemo-mechanical polishing with colloidal silica suspension (OPS, Struers) was applied to samples using a MD-Chem. polishing cloth (Struers). The polished specimens were rinsed than then cleaned with methanol immediately after polishing to avoid as less contamination as possible on the specimen cross-sections.

3.1.1.2 Optical Microscopy

A Reichert MEF-3 microscope was used to observe the samples for the initial phase of characterisation. Bright field illumination was used for the observation.

3.1.1.3 Field Emission Gun Scanning Electron Microscopy (FEGSEM)

A LEO 1530VP FEGSEM equipped with energy dispersive X-ray spectroscopy (EDX) was used to observe surface morphology and general elemental composition of all the coatings. The analysis was performed on both the surface and cross-sections of the coated steel samples before and after corrosion investigations. The latter included galvanic corrosion tests, linear polarisation resistance tests and porosity tests. Secondary electron secondary electron micrographs were obtained with a primary beam operating energy of 20 kV and a working distance of 10~15 mm between the electron beam aperture and sample surface. In some cases, samples were gold sputter coated in order to improve conductivity.

3.1.1.4 Focused Ion Beam Scanning Electron Microscopy (FIBSEM)

A Fei Nova 600 Nanolab dual beam focused ion beam scanning electron microscopy (FIBSEM) was used for site-specific analysis particularly sectioning and imaging of feature areas of galvanic couples. The feature areas were ablated by a focused gallium ion beam to observe cross-sections for further identification of the effects of galvanic corrosion on composition and morphology of the coatings.

FIBSEM was also used to prepare TEM samples of the features observed on the surface of coatings after galvanic corrosion. For TEM preparation, a thin Pt layer (10 μm long and 2 μm wide) was initially deposited on the surface of the selected feature area for protection. Then the materials on both sides of the Pt coated area were milled out using the gallium ion beam. A U-shaped cut was then performed on the thin film sample and a small ligament left connected to the bulk sample. After that, a micromanipulator was inserted near to the end of the thin film, which was not connected to the bulk sample. Pt was deposited at the connected area between the micromanipulator tip and the sample to bond them together. The thin film sample was detached from the bulk sample by removing the small ligament using the ion beam. Following this, the thin film sample was lifted and then welded to a TEM grid by Pt deposition. After that, a final thinning of the sample was performed on both sides of the thin film sample to reduce the thickness to less than 150 nm.

3.1.1.5 Transmission Electron Microscopy (TEM)

A JEOL FX2000 transmission electron microscopy (TEM) equipped with Oxford Instruments Inca energy dispersive X-ray spectroscopy (EDX) was utilised for further analysis of the TEM samples prepared by FIBSEM. Both microstructure and composition of the features were identified.

3.1.1.6 X-ray Photoelectron Spectroscopy (XPS)

In this project, an EDAl coating with Cr passivation treatment and a SermeTel 962 coating containing chromate inorganic binder were observed by XPS (VG ESCALAB Mk I) to identify the chemical state of Cr. Pass energy of 85 eV was used and the Al Kα X-rays source anode voltage was set at 8 kV with a filament current of 20 mA. XPS spectra of two samples (1 cm^2) were obtained by irradiating with a beam of X-rays while simultaneously measuring the kinetic energy and number of electrons that escape from the initial 5 to 10 nm of the samples being analysed. The obtained XPS spectra were analysed by software, XPSPEAK41, to confirm and identify the presence of trivalent and hexavalent Cr in these two samples.

3.1.2 Corrosion Resistance Characterisation

3.1.2.1 Free Corrosion Potential Investigations

The free corrosion potentials of the electroplated cadmium, EHC and HVOF WC/Cr/Co coatings were measured. An EG&G potentiostat/galvanostat model 263A controlled with PowerSuite software was employed to monitor open-circuit potential (OCP) with time. The electrochemical experiments were conducted in an electrochemical cell consisting of a sample and a reference electrode (saturated calomel electrode (SCE) terminating with a salt-bridge ((saturated KCl) and probe). Both sides of the sample were masked off with chemically resistant tape (3M polyester tape 8403) and only a 1 cm^2 area of coating surface remained uncovered on one side. The samples were immersed directly into the electrolyte of 3.5 wt.% NaCl solution and their OCP was monitored for 30 min.

3.1.2.2 Galvanic Corrosion Investigation

Galvanic corrosion tests were carried out in accordance with ASTM G71[102]. An ACM Instruments Dynamic Zero Resistance Ammeter (ZRA), model Dynamic 8, was used to measure the galvanic corrosion current between both EHC and HVOF WC/Cr/Co and electroplated cadmium coatings. The electrode potential of the sacrificial coatings was monitored using an ACM instruments BOB 8. Logging was carried out for 15 days with the initial data sampling rate being every 10 s to include any possible early transient effects. This was then reduced to every 30 min after the first 75 h, in order to keep the total number of data points to a minimum for effective data manipulation.

Test samples (4 samples for each coating) were disc shaped, 3 mm thick and 5 cm in diameter. A special cell was constructed and utilised for galvanic corrosion trials as shown in Figures 44 and 45. The cell consisted of two rectangular end plates, a three-way hollow column and two bolted joints. The cell was designed to allow stability of electrodes during long-term galvanic corrosion measurements. Atmospheric electromagnetic noise interference was minimised through the use of a Faraday cage. Figure 46 shows a schematic of the equipment and the connections made for a single cell.

The coated substrates were positioned at both ends of the three-way hollow column and then tightened via two bolted joints. The cell was then filled with 3.5 wt.% NaCl solution. A reference electrode (SCE) terminating with a salt-bridge and probe was introduced into the cell as also shown in Figure 46. The sample with hard coatings (EHC and HVOF WC/Cr/Co) was connected to a common ground on both of the monitoring electronic instruments. Usage of the cell gave a 1:1 area ratio for the samples on test. The two pieces of equipment were intended to be used manually; however, their outputs were connected to a personal computer for ease of data acquisition via a Pico ADC-24 data logger.

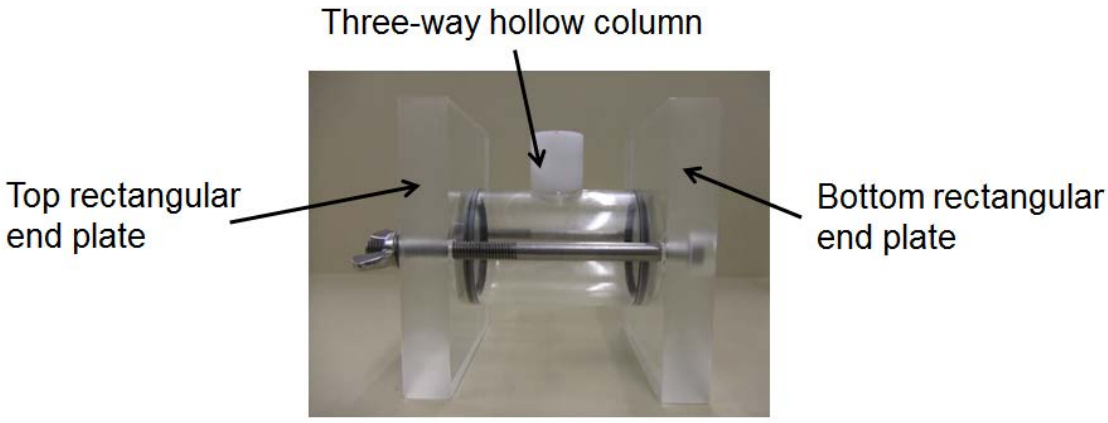

Figure 44. Photograph of galvanic cell apparatus

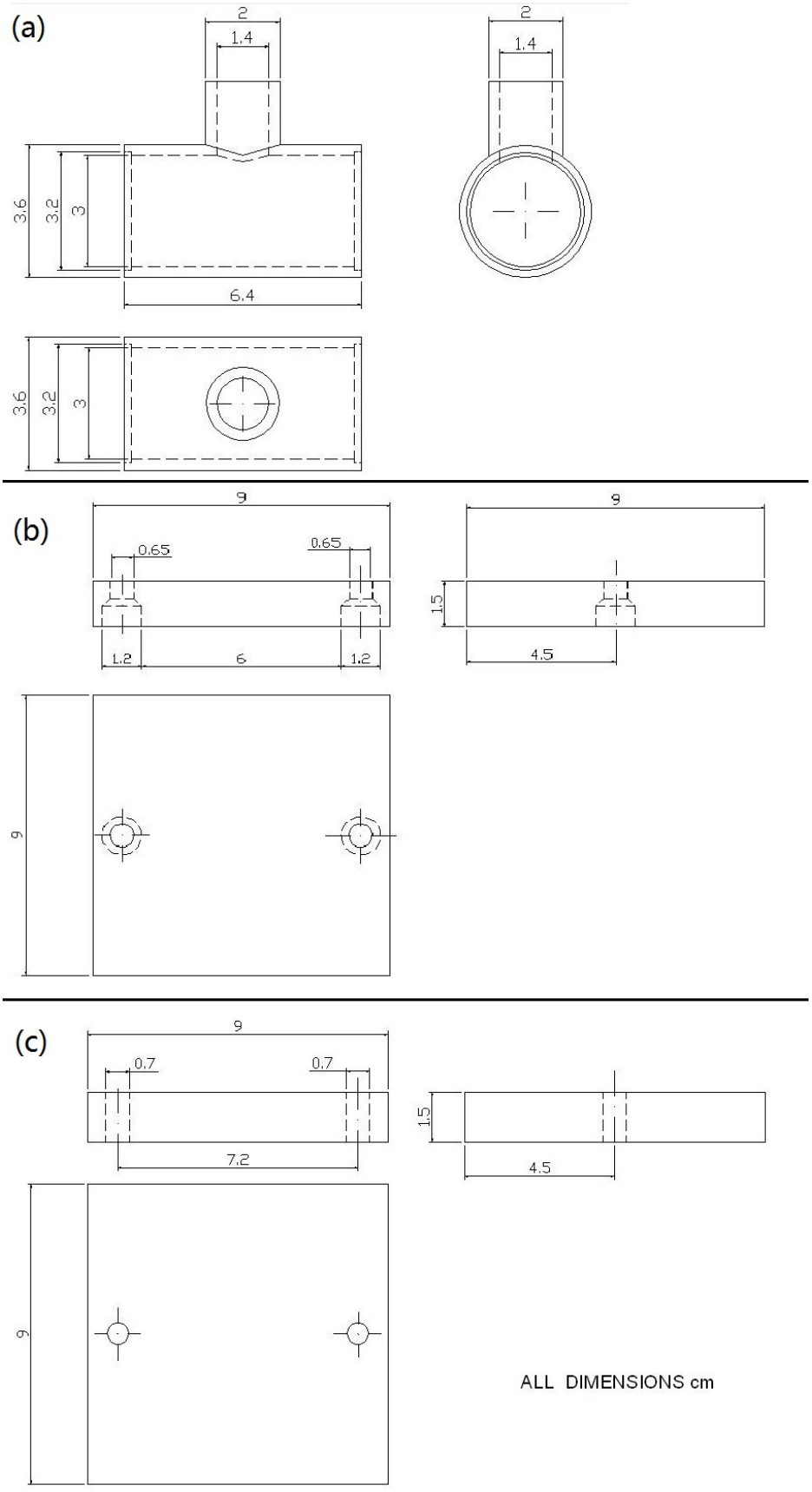

Figure 45. Design of cell apparatus for galvanic corrosion tests (a) a three-way hollow column (b) bottom rectangular end plate (c) top rectangular end plate

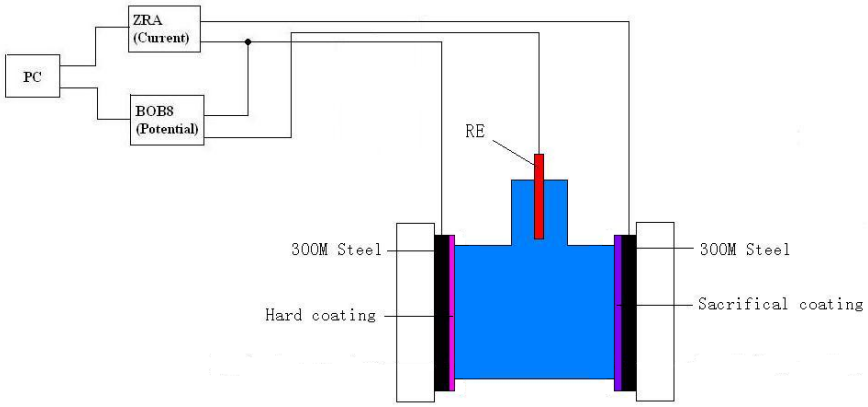

Figure 46. Schematic of the galvanic corrosion monitoring equipment format

3.1.2.3 Linear Polarisation Resistance (LPR) Measurement

The linear polarisation resistance values of the sacrificial coatings were measured. An EG&G potentiostat/galvanostat model 263A controlled with PowerSuite software was employed to perform linear polarization measurements. The electrochemical experiments were conducted in a three-electrode electrochemical cell. The counter electrode was a platinum coated titanium mesh electrode (4 cm^2) and the reference was SCE terminating with a salt-bridge probe. A new NaCl electrolyte was used for each LPR measurement to avoid contamination of the bath. The potential scans were carried out from $\pm$0.25 V vs. OCP of the samples with a 10 mV/min scan rate. All the samples were immersed in the 3.5 wt.% NaCl solution at 20 ℃ for 30 min to obtain a stable open circuit potential for the LPR plots. Potential vs. current density was plotted within a potential range $\pm$20 mV around the free corrosion potential (E_{corr}) to determine the polarisation resistance by graphical interpretation. The gradient of a line drawn for the data slope was taken as the polarisation resistance value.

3.1.2.4 Porosity Test

The presence of flaws, in the form of pores and cracks in sacrificial coatings, may result in the steel substrate being exposed to corrosive conditions, leading perhaps to reduced corrosion protection. The barrier properties of the coatings were studied by means of

the $KMnO_4$ porosity test, as described in the British Standard EN ISO 10308:1997[103]. The specimens were immersed in a dilute solution of $KMnO_4$ (0.15 g/L) for 3.5 h. They were then rinsed with water, dried and observed by SEM/EDX. Any discontinuities in the coating were made visible by brown/black deposits of MnO_2, which formed on the coating surface by a reaction between the permanganate solution and the exposed area of underlying steel substrates. The content of Mn and O in the coatings after the porosity tests was measured to assess their porosity.

3.2 Corrosion of HVOF WC/Cr/Co Coating

It was found that Al_2O_3 particles remained at the interface of the steel substrate and the HVOF WC/Cr/Co coatings causing severe local corrosion of the HVOF WC/Cr/Co coatings surrounding them. In these investigations, corrosion between Al_2O_3 particles and the HVOF WC/Cr/Co coating was investigated by immersion tests and electrochemical methods.

3.2.1 Grit Blasting Treatment

For investigating the effects of Al_2O_3 particles on the corrosion of HVOF WC/Cr/Co coatings, grit blasting treatment was used to introduce Al_2O_3 particles into the surface of the HVOF WC/Cr/Co coatings. Guyson Safti grit Brown #120 Al_2O_3 particles with 105 μm diameter were applied using a Guyson blast cleaning cabinet (Model 300/20 AD). A HVOF WC/Cr/Co coating was lightly grit blasted at a distance of 20 cm away from the blast nozzle. The resultant HVOF WC/Cr/Co coating presented a bright surface. The blasted coating was then rinsed with deionized water and methanol, and dried. Al_2O_3 particles were observed to be entrapped in the surface of the grit blasted HVOF WC/Cr/Co coatings using optical microscopy.

3.2.2 Immersion Test

3.2.2.1 Immersion Tests in Different Electrolytes

In order to investigate the effect of Al_2O_3 on the corrosion of HVOF WC/Cr/Co coatings, NaCl solutions with addition of Al_2O_3 powders were utilised for immersion tests HVOF WC/Cr/Co coatings. Due to low solubility of Al_2O_3 in NaCl solution, a steric dispersant was also added into immersion electrolyte to keep Al_2O_3 powders dispersing in the solution during immersion tests. Through the comparison of the morphology and composition of HVOF WC/Cr/Co coating after immersion in the electrolyte with and without Al_2O_3, the effects of Al_2O_3 on the corrosion of HVOF WC/Cr/Co coatings could be identified.

The HVOF WC/Cr/Co coated steel was cut into small pieces of surface area 1 cm^2. The cross section and reverse of the samples were then covered with chemically resistant tape. Four electrolytes were produced for the immersion test. They were (1) 3.5 wt. % NaCl solution; (2) 3.5 wt. % NaCl solution with 20 wt. % Al_2O_3 particles (500~800 nm); (3) 3.5 wt. % NaCl solution with 1 wt. % Al_2O_3 particles (500~800 nm); and (4) 3.5 wt. % NaCl solution with 20 wt. % Al_2O_3 particles (500~800 nm) and 1.5 wt. % steric dispersant. The samples were observed after 7 days of immersion in the four electrolytes to investigate the effects of the Al_2O_3 particles on the corrosion of the HVOF WC/Cr/Co coatings.

3.2.2.2 Immersion Test of the Grit Blasted HVOF WC/Cr/Co Coatings

Al_2O_3 particles were trapped on the surface of the HVOF WC/Cr/Co coatings by grit blasting. The immersion tests were carried out in the cell as shown in Figure 47. A grit blasted sample was fixed at one end of the cell and tightened by two bolts. The

electrolyte was then poured into the pipe. In this way, only the surface of the coating was immersed in the electrolyte. The coatings treated by different grit blasting techniques were observed after 7 days of immersion to investigate the effect of the trapped Al_2O_3 particles on the local corrosion of the HVOF WC/Cr/Co coatings.

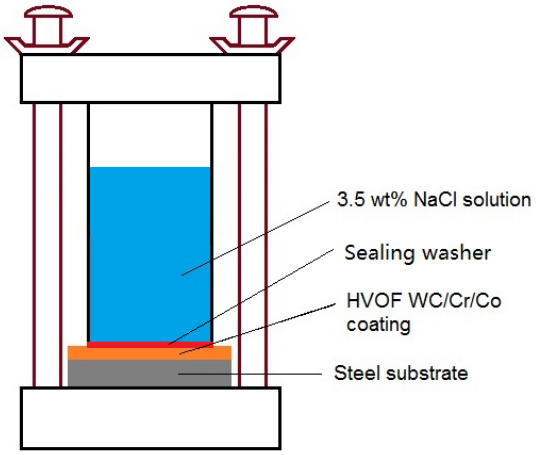

Figure 47. A schematic of the cell used for testing immersion the Al_2O_3 grit blasted HVOF WC/Cr/Co coatings

3.2.3 Anodic Polarisation Test

An EG&G potentiostatic/ galvanostatic model 263A controlled with PowerSuite software was employed to perform anodic polarisation tests. The electrochemical experiments were conducted in a three-electrode electrochemical cell. The counter electrode was a platinum mesh immersed directly in the electrolyte of 3.5 wt.% NaCl solution. The reference electrode was SCE terminating with a salt-bridge probe. The potential scans were carried out from 0 V to +2.0 V overpotential with a 10 mV/min scan rate. Anodic polarisation tests of HVOF WC/Cr/Co coatings were also carried out in 3.5 wt.% NaCl solution with 1 wt.% Al_2O_3 particles present.

3.2.4 Potentiostatic Test

Two noteworthy points were observed in the anodic polarisation curves of Section 3.2.3 at the potentials of 250 and 700 mV. Therefore, two potentiostatic tests of HVOF WC/Cr/Co coatings were performed at 250 and 700 mV respectively over a period of

100 min. The HVOF WC/Cr/Co coatings were then observed by SEM/EDX to identify the possible corrosion of the HVOF WC/Cr/Co coatings.

3.3 Investigation of the Deposition of Al_2O_3 Coatings

To improve the galvanic corrosion resistance of HVOF WC/Cr/Co coatings, an insulating layer was applied onto the HVOF WC/Cr/Co coatings. An Al_2O_3 film was investigated for this purpose due to its low conductivity and high hardness. Electrochemical deposition and sol-gel deposition were investigated as application methods due to their low level of damage to substrates. The two methods have been reported to apply Al_2O_3 on mild steel substrates[60, 104]. Therefore, all the investigations started on steel substrates and were subsequently carried out onto HVOF WC/Cr/Co coatings.

3.3.1 Electrochemical Deposition of Al_2O_3 Coatings

3.3.1.1 Pre-treatment of the Steel Substrates Prior to Al_2O_3 Film Formation

Deposits were prepared on mild steel panels (Brent Europe Ltd). Substrates were prepared in the form of $1\ \text{mm} \times 20\ \text{mm} \times 10\ \text{mm}$ specimens. Samples were degreased with acetone in an ultrasonic bath for 10 min, washed with distilled water and then dried by hot air.

A chemical pre-treatment was necessary to produce a porous and rough surface, named ‘conversion coating’, prior to the Al_2O_3 film to improve the adhesion to the substrate. Al^{3+} was suggested to react easily with OH^- at the bottom of the pores of the conversion coating to produce a mixture of Al_2O_3 and $Al(OH)_3$ during deposition process[60]. The porous conversion coatings on steels can be obtained by chemical treatment in acidic baths containing additives with chalcogenides such as thiosulphates.

Corrosion inhibitors such as propargyl alcohols are also necessary to control film growth. The conversion coating was suggested to act as a bond between substrates and Al_2O_3 films and facilitate the interfacial reactions[105].

In this study, the preparation of the conversion coatings consisted of two steps: firstly the steel panel was immersed in 20 wt.% H_2SO_4 solution for 10 s and then further immersed in H_2SO_4 solution with thiosulphates and propargyl alcohol, to control the growth of the coating and to obtain properties such as microporosity with the resulting high surface area. Conditions of the pre-treatment are presented in Table 16.

Table 17. Conditions for the conversion treatment

Sulphuric acid concentration	2.04 M
Sodium Thiosulphate concentration	6×10^{-3} M
Propargyl alcohol concentration	2×10^{-2} M
Temperature	60 ℃
Treatment time	15 min

3.3.1.2 Preparation of Al_2O_3 Deposits

The electrochemical deposition of Al_2O_3 compounds was performed in aqueous solution using a platinum electrode as the anode and SCE as the reference electrode. Deposits containing hydrated alumina ($Al_2O_3 \cdot xH_2O$) and aluminium hydroxide ($Al(OH)_3$), named semi-alumina, were produced cathodically, and according to a process which involves both electrochemical and chemical reactions. In this study, depositions of semi-alumina from $Al_2(SO_4)_3$ and $Al(NO_3)_3$ solutions were investigated. After electrochemical deposition, semi-alumina deposits on substrates were dehydrated into Al_2O_3 films. Dehydration of the semi-alumina was carried out in air at 20 ℃ for 1 day. Some samples were heat treated at 150 ℃ for 2 h for dehydration. YCl_3 was also added to $Al_2(SO_4)_3$ solutions to investigate the modification of Al_2O_3 deposits because the addition of Y was reported to improve adhesion and morphology of Al_2O_3 films[66]. The experimental variables of the deposition process from $Al_2(SO_4)_3$

solution and $Al(NO_3)_3$ solution are shown in Tables 17 and 18 respectively.

Table 18. Conditions for the Al_2O_3 and Al_2O_3/Y deposits from $Al_2(SO_4)_3$ solution ('√' = used parameter)

Sample	Current density (mA/cm^2)		Stirring	Time		Electrolyte	
	30	100		15	30	$Al_2(SO_4)_3$ 1 M	$Al_2(SO_4)_3$ 1 M YCl_3 0.15 M
1		√		√		√	
2		√	√	√		√	
3	√			√		√	
4		√			√	√	
5		√		√			√

Table 19. Conditions for forming Al_2O_3 deposits from $Al(NO_3)_3$ solution

Cathodic current density	30, 60 and 100 mA/cm^2
$Al(NO_3)_3 \cdot 9H_2O$	0.1 M
NH_4NO_3	0.1 M
Temperature	20 ℃
Time	5 and 15 min

3.3.2 Sol-gel Deposition of Al_2O_3 Coatings

The sol-gel deposition of Al_2O_3 was investigated initially with a steel substrate. Further investigation was carried out with a HOVF WC/Cr/Co coated steel substrate.

3.3.2.1 Pre-treatment of Steels and HVOF WC/Cr/Co Coatings for Sol-gel Deposition of Al_2O_3

Mild steel and HVOF WC/Cr/Co coated steel (1×3 cm) were used as substrate materials. The samples were grit blasted with Al_2O_3 particles of 105 μm diameter. After grit blasting, the samples were degreased with acetone and preserved in desiccators. Some of the grit blasted samples and as-received samples were chemically

pre-treated by a Zn phosphating treatment. The parameters for the phosphating treatment are shown in Table 19.

Table 20. The parameters used in the zinc phosphating treatment for steel and for HVOF WC/Cr/Co coatings

	Composition (g/L)	**Temperature (℃)**	**Immersion Time (min)**
ZnO	20	65	20
H_3PO_4	16		
$CaCl_2$	12		
$FeCl_3$	1		
NH_4F	1		

3.3.2.2 Preparation of Sol-gel Al_2O_3 Deposits

An Al_2O_3 sol was produced by adding Al isopropoxide to deionized water in a molar ratio of 1:100. HNO_3 (1 M) was used to adjust the pH of the mixture to 4. The mixture was stirred subsequently at 85 ℃ until it turned to a clear sol. The sol was then evaporated to the desired concentration of 1 M. Mild steel and HVOF WC/Cr/Co coated samples with different pre-treatments (as mentioned in Section 3.3.2.1) were immersed in the alumina sol for 10 s and withdrawn. The samples were air-dried at 20 ℃. The air-dried coated samples were then heat-treated in a muffle furnace at 400 ℃ for 1 h.

3.4 Investigation of the Electroplating of Mn-Cu Coatings

Electroplating of Mn-Cu on mild steel was investigated as a replacement for EC coatings due to its good sacrificial protection properties and mechanical properties.

3.4.1 Preparation of Substrates

Mild steel plates with an effective surface area of 3 cm^2 (1.0×3.0 cm) were employed as the substrate in the project. A series of pre-treatment processes were operated for samples prior to electroplating. Initially, substrates were mechanically polished using different grade of SiC papers from 240 grit up to 800 grit. For degreasing, the substrates were firstly ultrasonically cleaned with acetone and then cathodically treated with an alkaline solution containing 25 g/L Na_2CO_3, 25 g/L NaOH, and 50 g/L Na_3PO_4 at 40-50 ℃. Finally the substrates were pickled in a 32 % HCl (S.G. 1.16) for 15 s just prior to electroplating. After each step, the substrates were rinsed in deionised water and then acetone, and finally dried.

3.4.2 Cathodic Polarisation of Mn-Cu Electroplating

In order to identify the effects of Mn^{2+}, Cu^{2+}, NH_4^+ and Tween 20 (a surfactant) on the electroplating of Mn-Cu coatings, the cathodic potentiodynamic behaviour of steel substrates in the electrolytes with different compositions (Table 20) was investigated with a scan rate of 10 mV/min a potential range from 0 to -2.5 V vs. OCP. A three-electrode cell system was utilised for the experiments at 20 ℃. The anode was a platinized titanium mesh (2 cm × 4 cm), and the reference electrode saturated calomel. Electrochemical experiments were made using a Schlumberger SI 1286 potentiostat, controlled by CorrWare software.

Table 21. The formulation of electrolytes used to investigate the cathodic polarisation of mild steel

Electrolytes	1	2	3	4	5	6	7	8	9
$MnSO_4$ (0.59 M)	√	√	√	√	√	√			
$CuSO_4$ (5 mM)	√	√	√				√	√	√
$(NH_4)_2SO_4$ (1 M)	√	√		√				√	
Tween 20 (5 ml/L)	√				√				√

3.4.3 Continuous Current Electroplating of Mn-Cu Coatings

Electrodeposited Mn-Cu coatings were prepared using baths No. 1, No. 2 and No. 3 as detailed in Table 20. Electroplating was conducted in a 2 L glass beaker with 1 L of the electrolyte. The electroplating system was set up in a similar format to the previously mentioned (Section 3.1.2.3) in cathodic polarisation experiments and carried out at 20 ℃. All the chemicals used were laboratory reagent grade from Fisher Scientific UK, Ltd. The pH value of the bath was measured and adjusted to the desired range with 35 % $(NH_4)_2SO_4$ (S.G. 0.88) and > 95% H_2SO_4 (S.G. 1.83). Two pH value ranges were applied for electroplating at 2.4-2.6 and 6.4-6.6. The coating was deposited using a range of current densities from 0.1 to 0.5 A/cm^2 to produce a nominal film thickness of 10 μm. Confirmation of the film thickness was made on coated panels using a Fischer Dual scope MP4C with EGAB 1.3 magnetic induction probe. A longer electroplating time of 10 min was also applied to investigate thicker Mn-Cu coatings (up to ~27 μm). A magnetic stirrer paddle (64 × 9.5 × 9.5 mm) operating at about 60 rpm, was also investigated to identify the effects of agitation on electroplating of Mn-Cu coatings. After electroplating, the samples were rinsed with deionized water followed by acetone and hot air dried.

3.4.4 Immersion Test in an Aircraft Fluid

According the requirement of Airbus, fluid immersion tests in accordance with ISO 2812-1[106] were conducted to establish whether the Mn-Cu coating was likely to degrade on prolonged contact with some commonly used aircraft chemical. Triplicate test panels were fully immersed in Konsin (Glycol-based Runway De-icing Fluid (RDF)) from Univar at 70 ℃ for 336 h.

Following immersion the test panels were evaluated for coating removal and appearance, after wiping 5 times along the length of the panel with a soft napped cloth. An observation by SEM/EDX was conducted to identify corrosion products.

3.5 Quality Control of Procedure

To obtain accurate, reproducible and reliable data, it was necessary to consider the important issues associated to good experimental practice. This included:

- Repetition: All the electrochemical tests were repeated at least two times to ensure that the data produced is reproducible. All the compositional characterisation tests (EDX) were carried out at least three times to ensure that the data produced is representative.
- Consistency: All the experimental were carried out by using relevant standards or in the same procedures to ensure the consistency of experimental practices.

These issues were all adhered and thus the data produced in this project is reproducible and representative.

CHAPTER 4: RESULTS

4.1 Galvanic Corrosion between EC and EHC, and their Replacements

In this section, all the coatings, including hard coatings (EHC and HVOF WC/Cr/Co coatings) and sacrificial coatings (EC, FSAl, EDAl and SermeTel 962 (Al-based composite) coatings) are characterised in terms of morphology, composition, porosity and corrosion resistance. EC and EHC coatings are compared with their alternatives to identify their feasibility as replacement coatings. Galvanic compatibility and the corrosion mechanisms between the hard and sacrificial coatings are also shown and discussed.

4.1.1 Morphology and Composition of All the As-received Coatings

4.1.1.1 EC Coating

Figure 48 shows the surface of the EC coating. It can be seen that it has an irregular and rough relief. According to the AIPS 02-04-002 specification[96], a post-treatment passivation was performed on the EC coating, as the presence of Cr on the surface from EDX measurements (Table 21) indicates. From the coating cross-section (Figure 49), a relatively open and heterogeneous structured coating with a thickness of about 12 μm was observed. Some cracks were evident on the surface of the coating and some of these spread out into the top area of the coating. Gaps were also observed at the interface between the steel substrate and EC coating. Trapped Si in the coating from the silica polishing preparation also suggested some porosity in the coating.

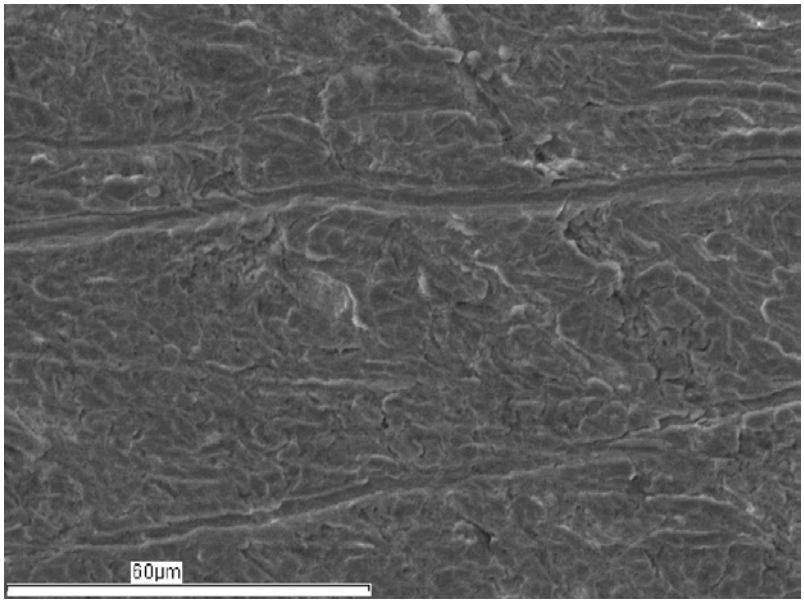

Figure 48. SEM secondary electron micrograph of the ‘as received’ surface of a EC coating on 300M steel substrate

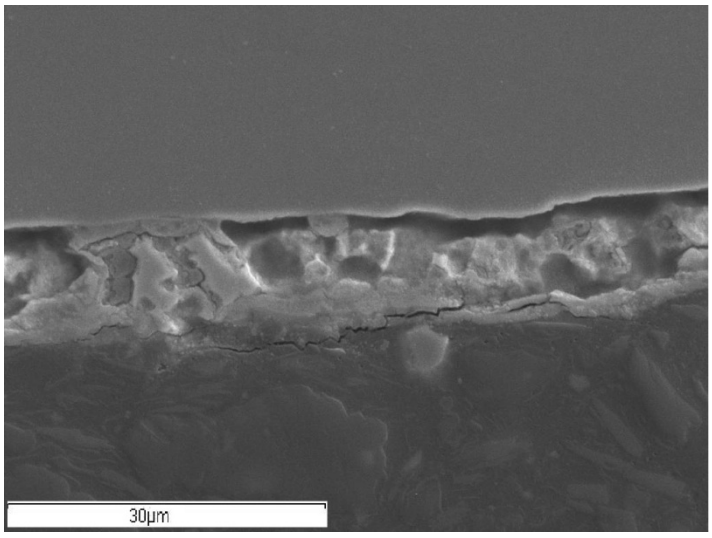

Figure 49. SEM secondary electron micrograph of the cross-section of the ‘as received’ EC coating on 300M steel substrate

Table 22. General compositional analysis of the EC coating from EDX measurements

Element (at.%)	Cd	Cr	Si	O
Surface	83.2	16.8	-	-
Cross section	16.9	-	6.6	76.5

4.1.1.2 EHC Coating

As-received EHC coatings were ground to obtain a smoother surface according to ABP 1-4042[100] as shown in Figure 50 prior to receipt. The hard coating composition was

found to be 100% Cr from EDX data. From the cross-section, a dense, homogeneous EHC coating with a thickness of approximately 105 µm was observed and good adhesion to the substrate was also evident, as shown in Figure 51.

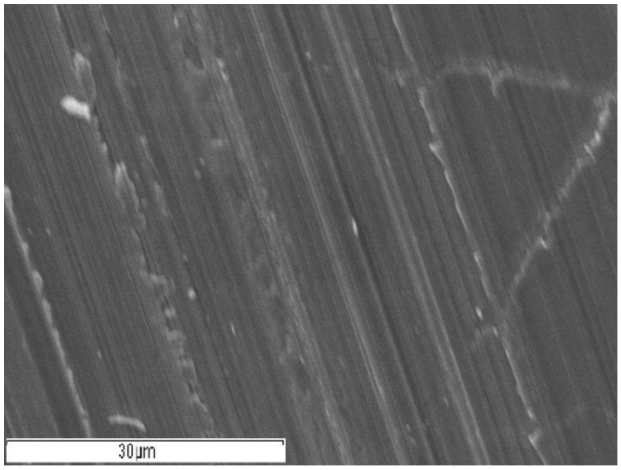

Figure 50. SEM secondary electron micrograph of the ground surface of an EHC coating on 300M steel

However, some cracks were also observed. Small cracks with an average length of approximate ~5 µm were dispersed throughout the whole coating and some longer cracks can also be observed to traverse the whole coating ending at the interface between the coating and the substrate.

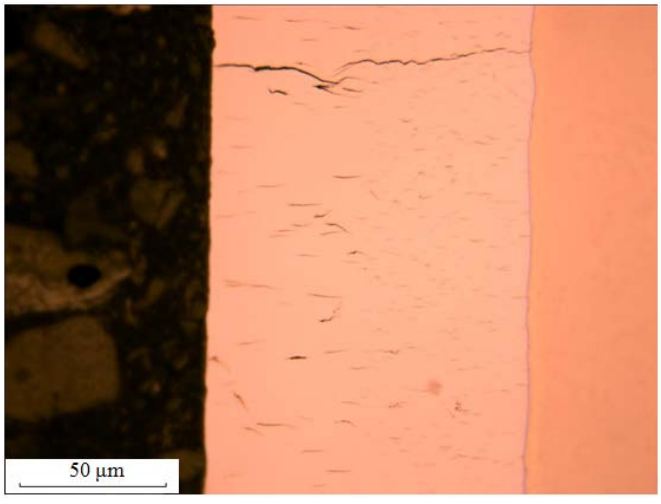

Figure 51. Optical micrograph of the cross-section of the ground EHC coating on 300M steel

4.1.1.3 HVOF WC/Cr/Co Coating

The HVOF WC/Cr/Co coating exhibited a rough and open structured surface, where

WC phases (area 1 in Figure 52 (a)) were observed to be dispersed in the metallic Co-Cr binder (area 2 in Figure 52 (a)). A lot of pores between the WC phases were also observed to expose the underlying binder. In these spaces, oxidation of the metallic binder was observed by the presence of O. From the cross-section of the HVOF WC/Cr/Co coating, two phases, namely the WC particles and Co-Cr metallic binder were identified by EDX (Figure 52 (b)). In the coating, WC particles with a range of sizes were dispersed in the metallic Co-Cr binder. In general, the coatings exhibited a dense and uniform microstructure with some pores. From the EDX measurements in the table of Figure 52, only W and C were detected in the particle phases in the coating and a mixture of W, C, Cr and Co were observed in the binder area of the coating.

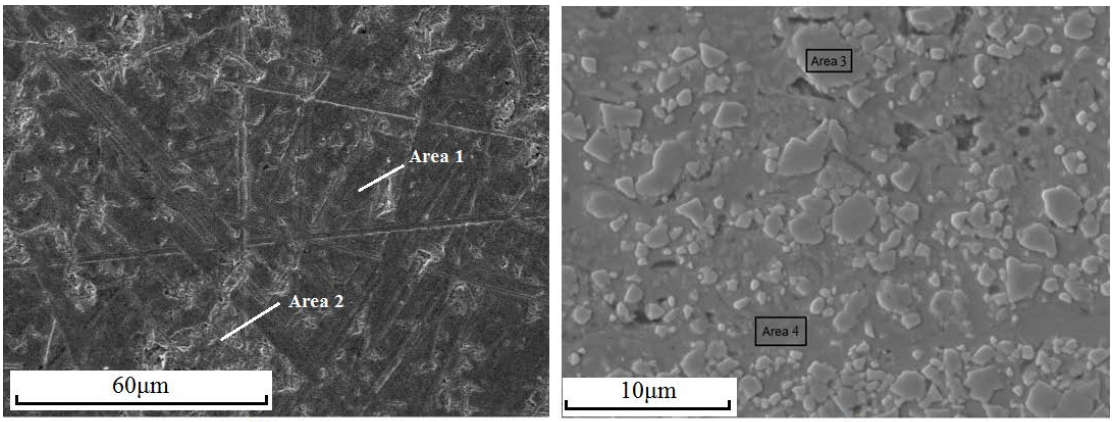

Element (at.%)	C	W	Cr	Co	O
Area 1	42.9	36.8	5.1	15.2	-
Area 2	-	55.0	7.1	17.0	20.9
Area 3	60.3	39.7	-	-	-
Area 4	39.6	31.8	6.9	21.7	-

Figure 52. SEM secondary electron micrographs of the (a) surface and (b) cross-section of an HVOF WC/Cr/Co coating on 300M steel substrate with general compositional analysis of surface (WC phase (area 1) and binder (area 2)) and cross-section (particle (area 2) and binder (area 4)) from EDX measurements

4.1.1.4 FSAl Coating

Figure 53 shows that the surface of the FSAl coating exhibited a splash pattern-like structure, which probably resulted from the collapse of the molten coating droplets on

the substrate. EDX data (table of Figure 53) show that Al-Si alloy particles were thought to be used in the production of the coatings.

From the secondary electron micrograph of the cross-section of the FSAl coating, some interconnecting pores were observed (Figure 54). The pores in the coatings were investigated by EDX and a composition map was obtained (Figure 55), where green represents the Al signal, blue is Si and red O. From Figure 55, in addition to Si detected in the coatings from Al-Si alloy particles, a significant increase of the Si content was observed in the pores of coatings, which was suggested to be an impurity produced during polishing with the colloidal silica suspension and trapped in the pores of the coating. The pores in the coatings also showed a high level of oxidation. The interface between the steel substrate and the coating is shown in Figure 56. A phase different from both the coating and the substrate was observed at the interface. EDX results illustrate that the phase consists of elements of both the aluminium coating and the steel substrate. The high percentage of C detected is suggested to result from the precipitation of carbides from the steel substrate. Other alloying elements from the steel also precipitated at the interface.

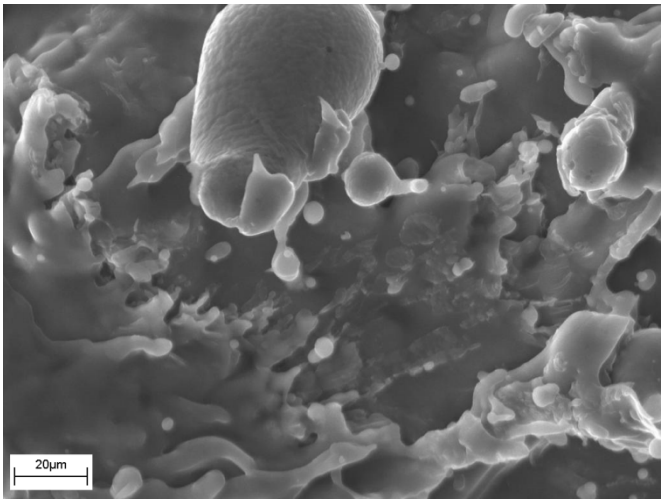

Element (at.%)	Al	Si
Surface	95.9	4.1

Figure 53. SEM secondary electron micrograph of the ‘as received’ surface of FSAl coating. The general composition measured by EDX is given below

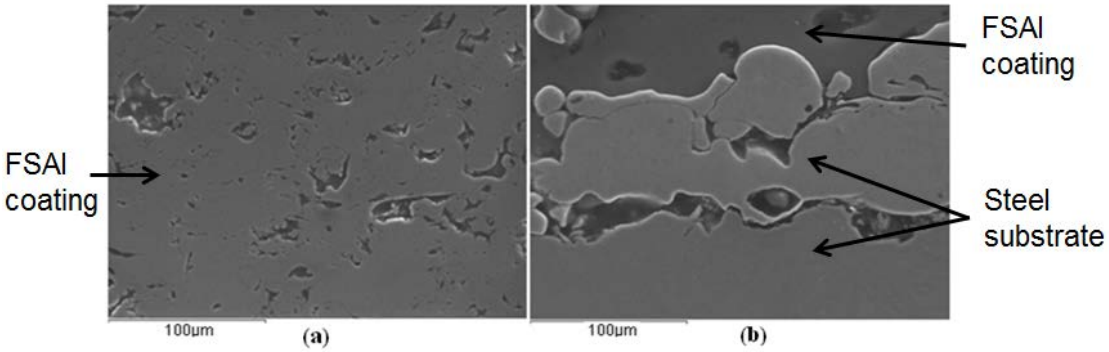

Figure 54. SEM secondary electron micrographs of the cross-section of (a) the FSAl coating and (b) the interface between the coating and the steel substrate

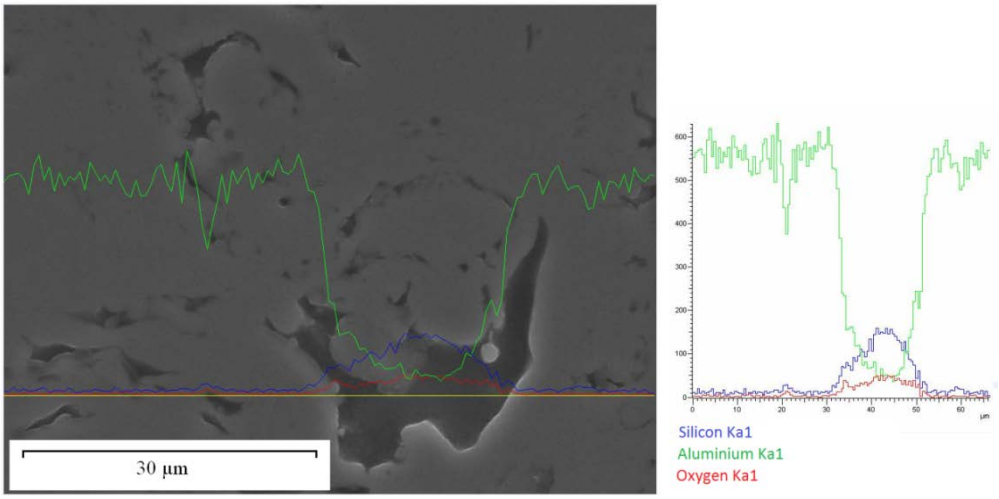

Figure 55. Line scans of a pore in the cross-section of the FSAl coating by EDX

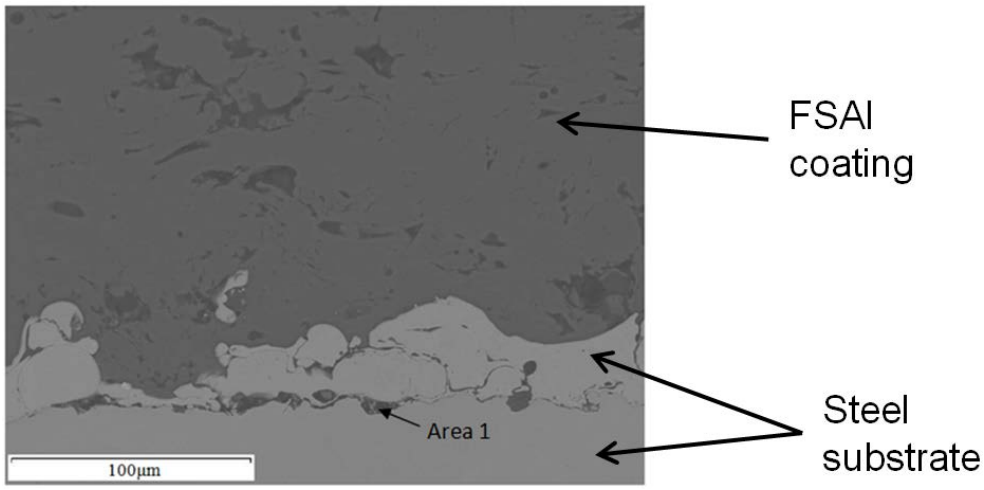

Element (at.%)	C	O	Al	Si	Fe	Ni	Sn
Area 1	64.8	24.9	0.3	0.7	3.2	6.0	0.1

Figure 56. SEM secondary electron micrograph and compositional analysis of the cross-section of the interface between the flame sprayed aluminium coating and the steel substrate using EDX

4.1.1.5 EDAl Coating

The EDAl coating was post-treated with a trivalent-Cr-based passivation. As shown in Figure 57, cracks were observed on the surface of the Cr conversion coating. The trivalent Cr conversion coating appeared to consist of Zr and Cr as evidenced by the EDX data (Figure 57). From the optical micrograph of the cross-sectioned EDAl coating (Figure 58), adhesion to the substrate appeared to be good and there was a marked absence of cracking or pores in the coating. From the SEM secondary electron micrograph, it can be seen that the EDAl coating was dense and homogeneous. Only Al was observed by EDX in the coating cross-sections (Figure 58).

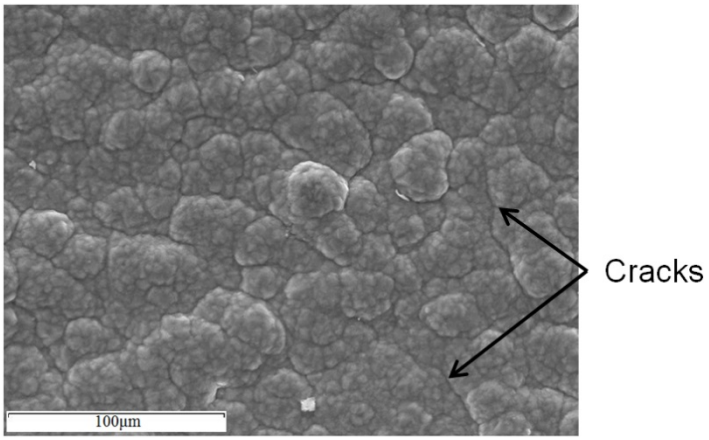

Element (at.%)	O	Al	Cr	Zr
Surface	11.2	87.9	0.5	0.4

Figure 57. SEM secondary electron micrograph of the surface of an EDAl coating together with the general composition below measured by EDX

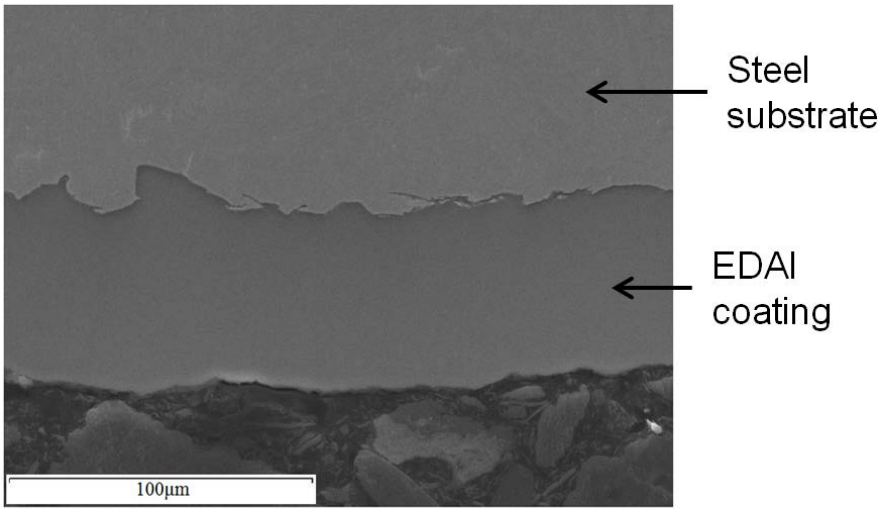

Figure 58. SEM secondary electron micrograph of the cross-section of an EDAl coating

4.1.1.6 SermeTel 962 Coating

A SermeTel 962 coating consists of Al particles in a phosphate/chromate binder sprayed onto the substrate and then cured at 315 ℃[97]. The SermeTel 962 coating can be post-treated by lightly abrading usually with abrasive grit or glass beads in a suction or pressure blast cabinet at very low air pressure to increase electrical conductivity[97].

The surface of the as-deposited coatings presented as packed particles, which were dispersed in the binder (Figure 59). Some pores seemed to be present between the Al particles. However, from the EDX data, the phosphate and chromate binder was presented in these pores and a high content of Al and O were also detected, which implied a good diffusion between the particles and binder. Therefore, a low porosity of the SermeTel coating was expected. Figure 60 illustrates a cross-section of the SermeTel coating. Connections between Al particles were observed in the phosphate and chromate binder and some discrete pores were dispersed in the coating. The absence of Si, which was easily trapped in the pores of the coatings from polishing, also implied a low porosity of the SermeTel coatings (Figure 60).

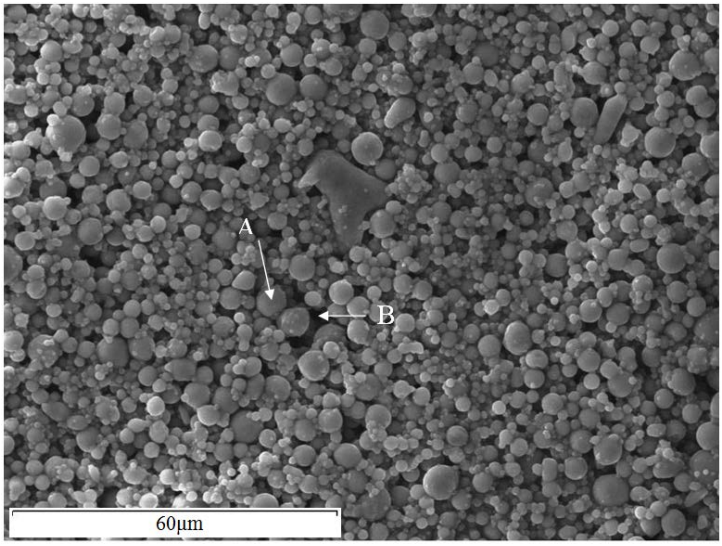

Element (at.%)	O	Al	Mg	P	Cr
A (Particle)	5.0	95.0	-	-	-
B (Binder)	4.9	88.5	2.1	3.0	1.5

Figure 59. SEM secondary electron micrograph of the surface of an as-deposited SermeTel 962 coating with composition of the particle (A) and the binder (B) below measured by EDX

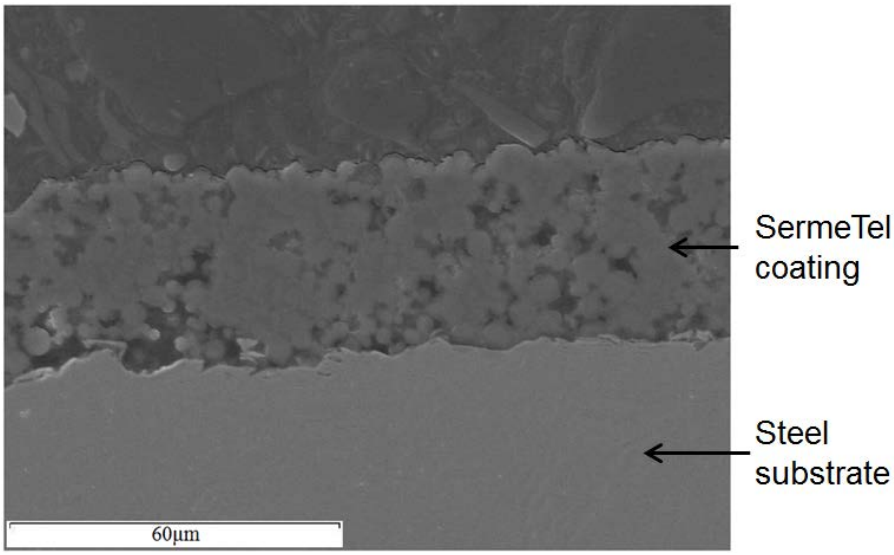

Element (at.%)	O	Al	P	Cr
Cross section	37.2	51.8	9.0	2.0

Figure 60. SEM secondary electron micrograph of the cross-section of an as-deposited SermeTel 962 coating with general composition below measured by EDX

Figure 61 shows that cured Al particles on the surface of the post treated SermeTel 962 coatings were abraded and deformed, appearing to increase contact with each other. This presumably increased the electrical conductivity[97]. The post treatments were only applied on the surface of the coating, therefore there was no significant difference in

the morphology and compositional data portrayed in the cross-section of the treated coating expected. However, compared to the as-deposited coatings (Figure 60), Al particles were dispersed more discretely and more interconnected pores presented in the treated coatings (Figure 62). Moreover, Si, arising from polishing, was detected in the pores of the coating. The appearance of Si in the binder suggested marked porosity. It was thought that during the abrasion treatment, the porosity of the surface increased due to the loss of binder between the Al particles.

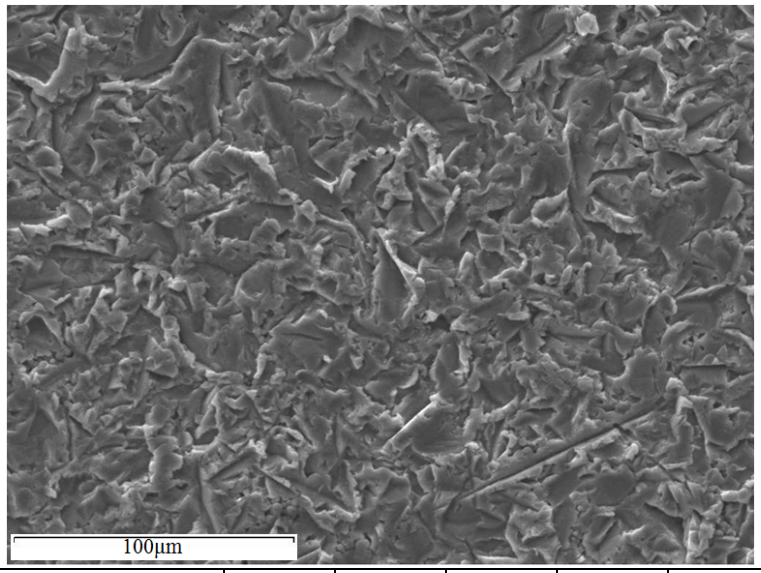

Element (at.%)	O	Mg	Al	P	Cr
Surface	21.7	1.6	72.5	3.4	0.8

Figure 61. SEM secondary electron micrograph of the surface of a post-treated SermeTel 962 coating together with general composition below measured by EDX

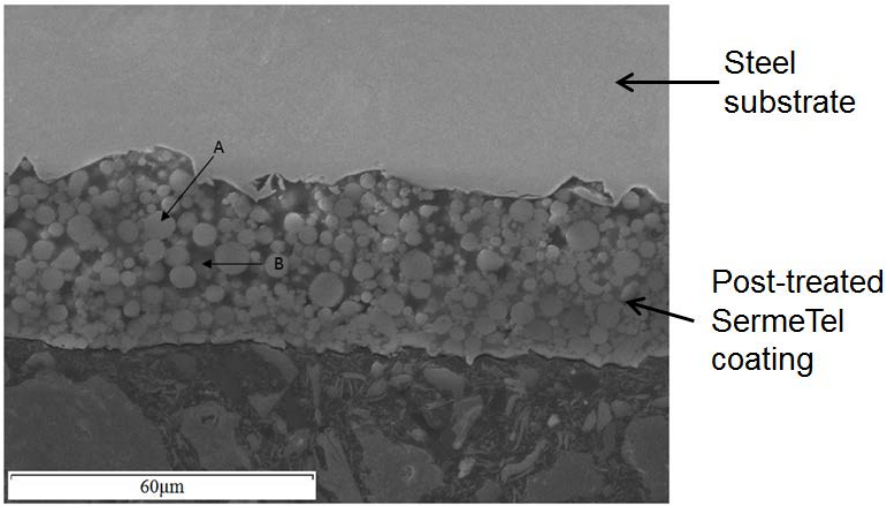

Element (at.%)	O	Al	Si	P	Cr
A (Particle)	3.2	96.8	-	-	-
B (Binder)	49.6	30.4	18.8	0.8	0.4

Figure 62. SEM secondary electron micrograph of the cross-section of a post-treated SermeTel 962 coating together with the composition of a particle (A) and the binder (B) below measured by EDX

4.1.2 Linear Polarisation Resistance Corrosion Experiments

The corrosion resistance of the sacrificial coatings were identified by LPR tests and shown in Figure 63. From the polarisation curves, it was found that the EC coating had the most negative E_{corr} which suggested it might be the best sacrificial protection for the steel substrate. For the 'alternative' coatings, EDAl had the lowest open circuit potential. The SermeTel 962 coating had a higher OCP, however, after a post-treatment of light abrasion, it decreased significantly. The FSAl coating presented a higher potential than the pure Al coating due to the inclusion of the alloying element, Si.

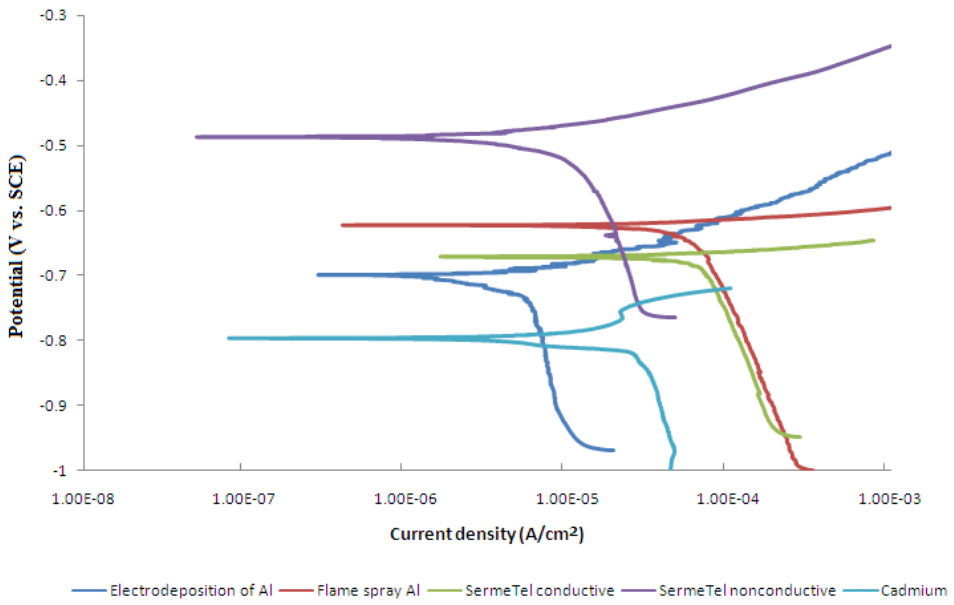

Figure 63. Linear polarization curves for the sacrificial coatings in 3.5 wt.% NaCl solution

Table 23. Experimental data for the sacrificial coatings under polarisation in 3.5wt. % NaCl solution

	EDAl	SermeTel nonconductive	Cd	FS Al	SermeTel conductive
E_{corr} (mV vs. SCE):	-699	-487	-796	-621	-672
I_{corr} ($\mu A/cm^2$):	5.36	9.99	26.1	62.8	72.6
R_p ($\Omega \cdot cm^2$)	6510	2990	1570	256	175

LPR (R_p) are used to identify the corrosion resistance of the sacrificial coatings. The higher R_p presents, the better corrosion resistance a sacrificial coating has. According to the methods outlined in reference[107], the corrosion current was calculated from the intersection of extrapolated lines from both the cathodic and anodic polarisation curves and a horizontal line from the E_{corr}. The potential range for the polarisation curve extrapolation is beyond ± 70 mV overpotential[107]. In the polarisation curves, where the potential is below ± 20 mV vs. E_{corr}, the potential had a linear relation with current[107]. The slope of this line is the LPR value R_p, is:

$$R_p = \Delta E / \Delta I = \beta_a \cdot \beta_c / \left[2.3 I_{corr} \left(\beta_a + \beta_c\right)\right] \qquad \text{Equation (4)}$$

Where R_P is LPR, β_a and β_c are the Tafel slopes for the anode and cathode reactions, I_{corr} is corrosion current. The equation implies that LPR has an inverse relation to the corrosion current. Table 22 shows that the trends of the LPR and corrosion current matched each other well. The EDAl coating presented a dense and homogenous structure without any noticeable defects and this was thought to result in the highest LPR (Table 22). The SermeTel coating, without post-treatment, presented a low corrosion current and a high LPR value. As-deposited SermeTel coatings have a microstructure of discrete Al particles bound by a phosphate/chromate binder, which resulted in low electrical conductivity. Additionally, addition of Cr to the coating was also suggested to improve its corrosion resistance. The LPR of the EC coating was lower than the EDAl coating and untreated SermeTel 962 coatings due to, perhaps, its much lower E_{corr}. In contrast, the FSAl coating and post-treated SermeTel coating did not exhibit a high LPR. High porosity and the heterogeneous structure of the FSAl resulted in the low LPR. The light abrasion treatment of the SermeTel 962 coating increased its electrical conductivity, which probably reduced its LPR significantly.

The coatings were also observed by SEM after the LPR tests. The EC coating had a lower LPR than the EDAl and untreated SermeTel 962 coating. As shown in Figure 64, a significant increase in the O content on the surface of the EC coating was observed after the LPR test. As mentioned in the characterisation of the EC coating, Cd was easily oxidised. During the LPR test, oxide corrosion products were observed and cracking in these deposits was also evident.

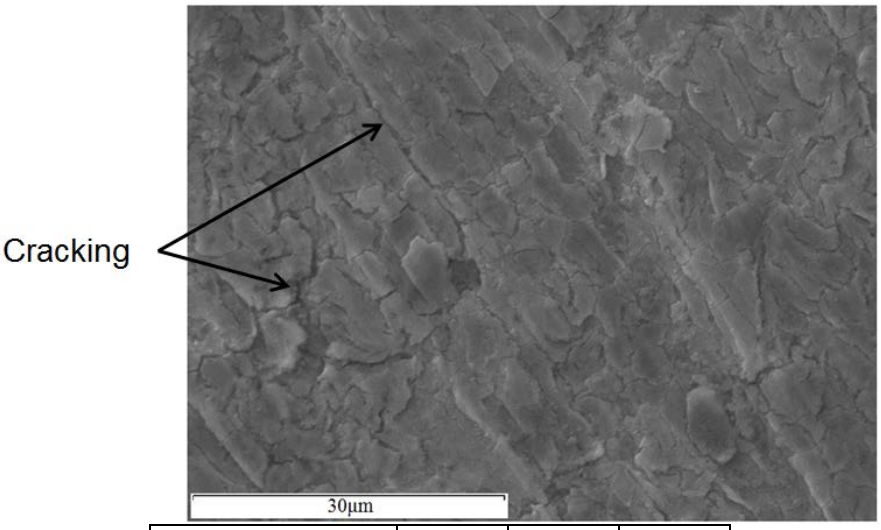

Element (at.%)	O	Cd	Cr
Surface	80.1	17.0	2.9

Figure 64. SEM secondary electron micrograph of the surface of the EC coating after LPR testing with general composition below measured by EDX

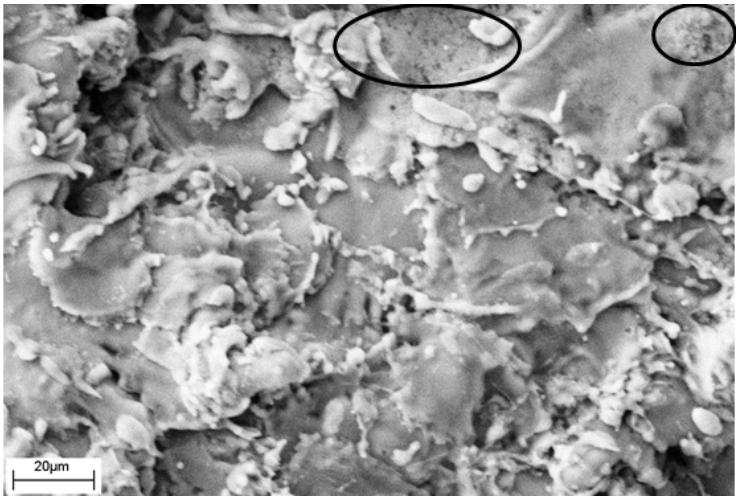

Element (at.%)	Al	Si
Surface	95.4	4.6

Figure 65. SEM secondary electron micrograph of the surface of the FSAl coating after LPR testing with general composition below measured by EDX

For the FSAl coating, no corrosion products were observed on the surface and there was also no significant difference in the composition of the surface of the coating after the LPR tests (Figure 65). However, compared to the as-received coating (Figure 53), there was a clear morphological change in the surface of the coating (circled area in Figure 65), which was more porous, perhaps, as a result of the effects of corrosion.

From Figure 66, there was no significant difference observed with respect to the morphology and composition of the surface of the EDAl coating after the LPR tests. However, it can be seen that some pitting-like attacks presented (circled area in Figure 66) on the surface of the EDAl coating after the LPR test. EDX data from the pitted area showed the underlying EDAl coating by the presence of 100 at.% Al.

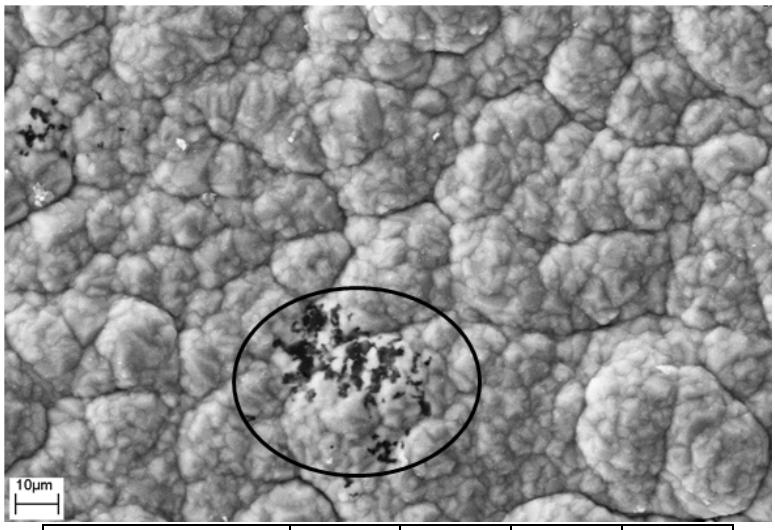

Element (at.%)	Al	O	Cr	Zr
General surface	84.8	14.2	0.6	0.4
Black dot	100.0	-	-	-

Figure 66. SEM secondary electron micrograph of the surface of the EDAl coating after LPR testing with general composition below measured by EDX

The untreated SermeTel 962 coating also had a high LPR. After the test, there was no significant difference observed in the morphology of the coating (Figure 67). In terms of composition of the coating after the LPR test, the O content increased slightly, which implies the slight oxidation of the Al particles in the coating.

From the observation of the post-treated SermeTel 962 coating after the LPR test, some areas of the conductive SermeTel coating presented serious corrosion (area B in Figure 68) and the corrosion of the Al exposed the binder, where EDX analysis showed a higher level of P and Cr. Oxide corrosion products were also observed on the corroded area. Some areas remained with a similar composition and morphology as the coating before the LPR test (area A in Figure 68).

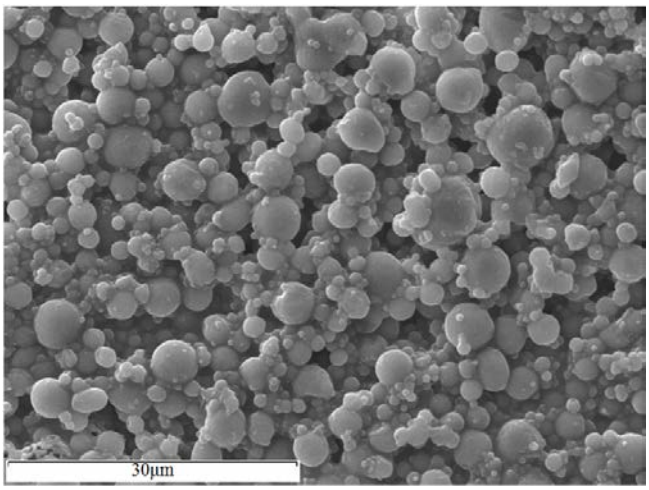

Element (at.%)	O	Al	Mg	P	Cr
Surface	15.8	78.5	1.6	3.0	1.1

Figure 67. SEM secondary electron micrograph of the surface of the untreated SermeTel 962 coating after LPR testing with general composition below measured by EDX

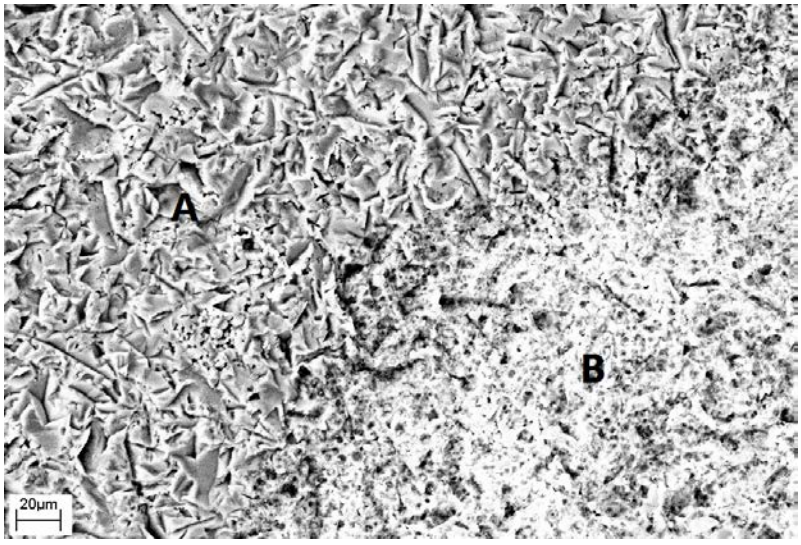

Element (at.%)	O	Al	Mg	P	Cr
Area A	-	93.9	2.3	3.8	-
Area B	38.0	47.6	3.5	8.5	2.4

Figure 68. SEM secondary electron micrograph of the surface of the post-treated SermeTel 962 coating after LPR testing: (A) general area (B) corroded area. Compositions measured by EDX in table below.

4.1.3 Porosity Tests

The sacrificial coatings were immersed in a $KMnO_4$ solution (0.15 g/L) for assess

their porosity. The sacrificial coatings were analysed by SEM and EDX after porosity testing. The porosity was revealed by measurement of the Mn content in the coating due to the formation of MnO_2, which resulted from the reaction of the $KMnO_4$ with the underlying steel exposed by any discontinues in the coating. The reaction producing the MnO_2 is as follows:

$$3Fe + 2MnO_4^- + 8H^+ \rightarrow 3Fe^{2+} + 2MnO_2 + 4H_2O^{2-} \quad \text{Equation (5)}$$

As noted previously, the passivation treatment for the EC coating protected it from significant oxidation. After the porosity test (Figure 69), a significant increase in the O content was observed, but there was no Mn detected on the surface of the EC coating. It was assumed that any discontinuities in the passivation coating caused the oxidation of the exposed Cd and subsequent formation of the oxide films, where cracks had formed. This resulted in the increase in the O content on the surface of the EC coating. The formation of the oxide film may increase the barrier properties of the coating, which prevented the penetration of the $KMnO_4$ solution to the steel substrate. This resulted in the absence of Mn on the surface of the EC coating after the porosity test.

Some interconnecting pores were observed on the FSAl coating when viewed using the SEM, which implied it may have significant porosity. Figure 70 shows morphology and composition of the surface of the coating after the porosity testing. The surface of the FSAl coating was significantly affected by its immersion in the $KMnO_4$ solution. High porosity resulted in a high formation level of MnO_2 on the surface as evidenced by the high percentage of Mn and O on the surface. It can be suggested that FSAl coating offers relatively poor barrier protection to the substrate.

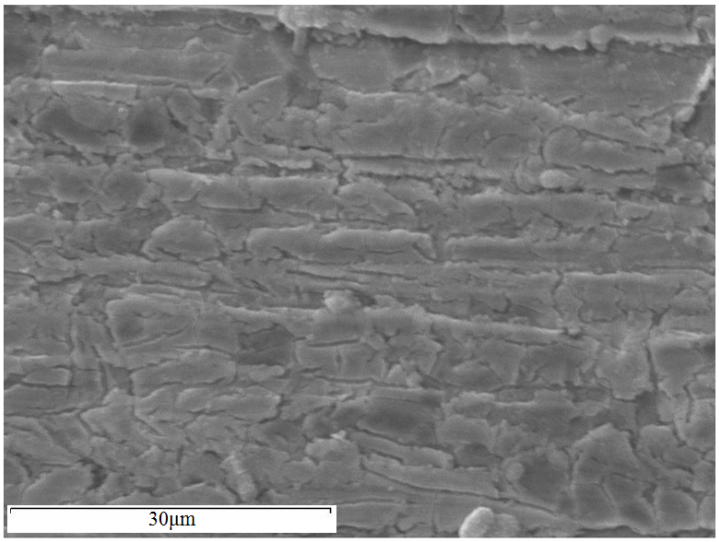

Element (at.%)	O	Cd	Cr
Surface	80.4	16.3	3.3

Figure 69. SEM secondary electron micrograph of the surface of the EC coating after porosity testing together with an elemental compositional analysis using EDX below

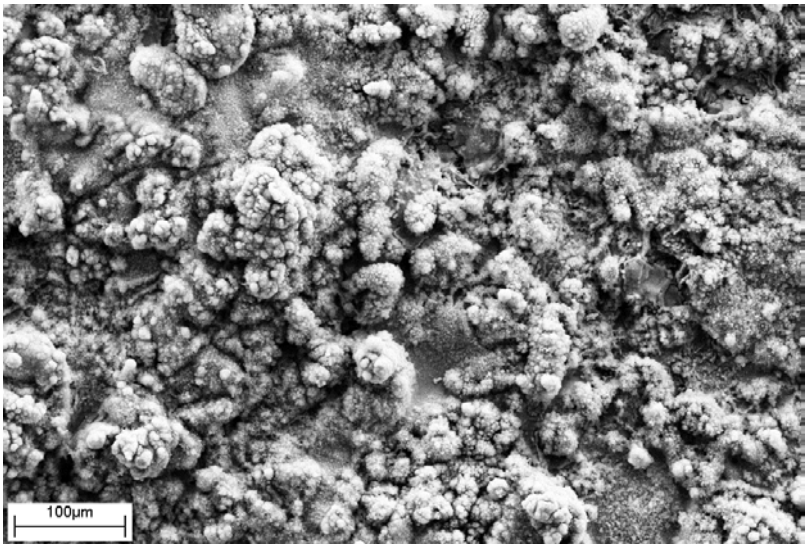

Element (at.%)	O	Al	Si	Mn
Surface	51.6	42.1	1.3	5.0

Figure 70. SEM secondary electron micrograph of the surface of the FSAl coating after porosity testing together with an elemental compositional analysis using EDX below

As noted previously, the trivalent Cr conversion coating had some cracks whilst the underlying EDAl coating was dense and had an absence of any cracks or pores. It presented a good barrier protection property. Figure 71 shows an SEM secondary electron micrograph of an EDAl coating after the porosity test. The morphology of the surface of the coating remained similar to that of the coating before the test. Moreover,

there was no significant increase in Mn or O on the surface of the coating. It can be suggested that cracks observed on the surface of the conversion coating did not go down to the substrate.

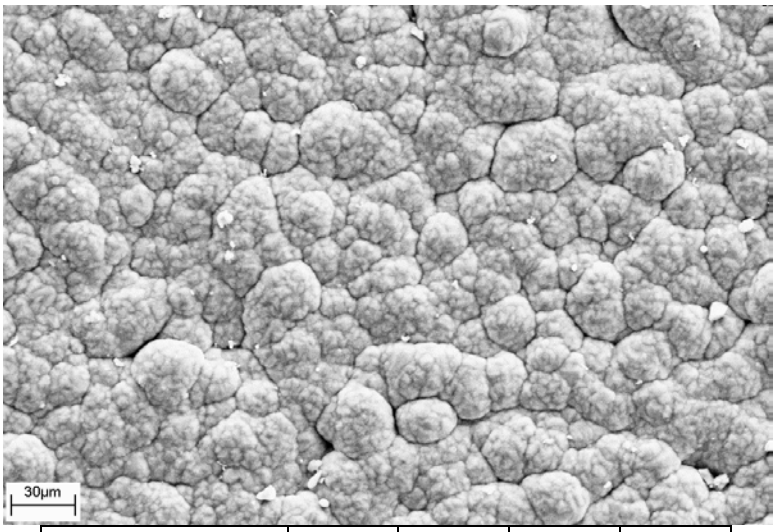

Element (at.%)	O	Al	Cr	Zr
Surface	9.6	89.5	0.6	0.3

Figure 71. SEM secondary electron micrograph of the surface of the EDAl coating after the porosity test with an elemental compositional analysis using EDX below

As Figure 72 shows, the untreated SermeTel 962 coating did not show significant difference in morphology after the porosity test. From the previous morphology characterisation, pores present in the SermeTel were observed to be discrete rather than interconnected. From porosity test results, it was found that untreated SermeTel 962 coating provided a good barrier protection. So it can be suggested that the discrete pores between Al particles did not reduce the barrier protection properties of the coatings.

Post-treated SermeTel 962 coating also presented significant porosity because the post-treatment abrasion resulted in deformation of the Al particles in the coating and loss of the binder, which subsequently resulted in increased porosity. This agrees with a previous observation of the post-treated SermeTel coating, which suggested that interconnected pores were present in the coating. Mn and O were also observed on the specimen surface as shown in Figure 73, further confirming porosity.

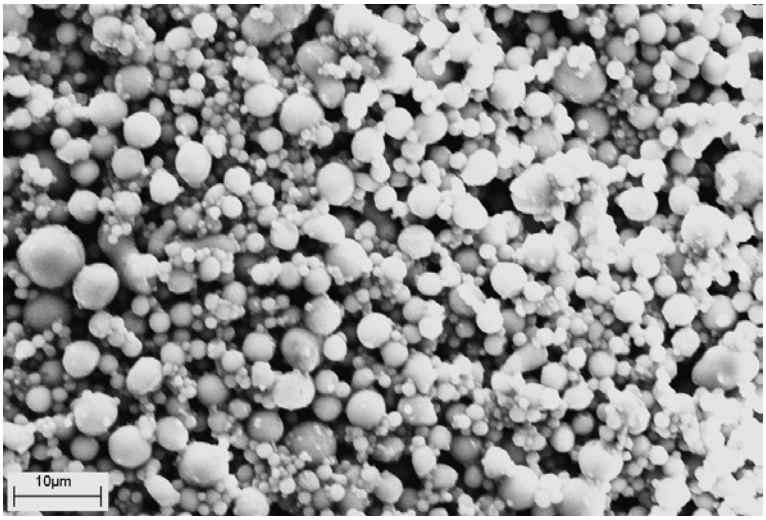

Element (at.%)	O	Al	Mg	P	Cr
Surface	14.8	79.2	1.2	3.3	1.5

Figure 72. SEM secondary electron micrograph of the surface of the untreated SermeTel 962 after porosity testing

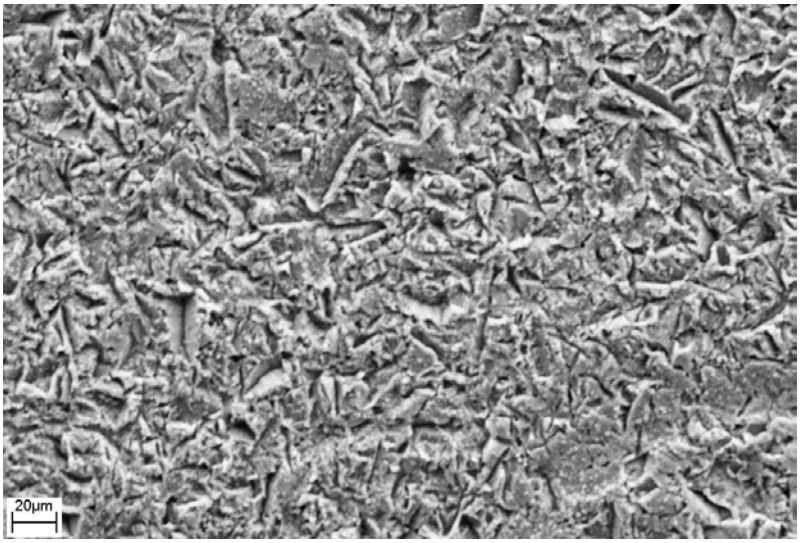

Element (at.%)	O	Al	P	Mn
Surface	29.3	67.0	2.3	1.4

Figure 73. SEM secondary electron micrograph of the surface of the post-treated SermeTel 962 coating after porosity testing together with an elemental compositional analysis using EDX below

As shown in Figure 74, after the porosity testing of the EHC coating, both O and Mn were detected on the surface. As observed in the cross-section of the EHC coating, cracks were observed dispersed in the coating. The $KMnO_4$ solution appears to have penetrated these and formed MnO_2 with the exposed steel substrate. However, no significant changes were observed in the morphology of the EHC coating after the

porosity testing.

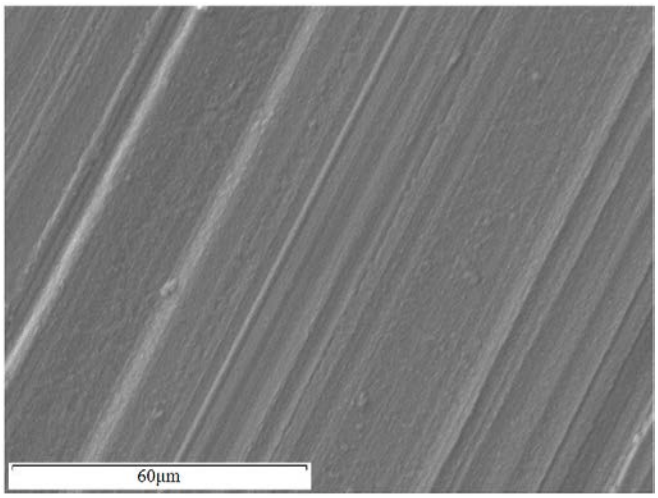

Element (at.%)	O	Cr	Mn
Surface	18.7	77.4	3.9

Figure 74. SEM secondary electron micrograph of the surface of the EHC coating after porosity testing together with an elemental compositional analysis using EDX below

For the HVOF WC/Cr/Co coating, pores were observed in the metallic binder, Co-Cr, where WC phases were dispersed. After the porosity test, significant increase in both O and Mn content was observed in the HVOF WC/Cr/Co coating as Figure 75 shows, which implies that the penetration of the $KMnO_4$ solution to steel substrate through the pores in the coating. The absence of C was also noted on the surface of the HVOF WC/Cr/Co coating after the porosity test.

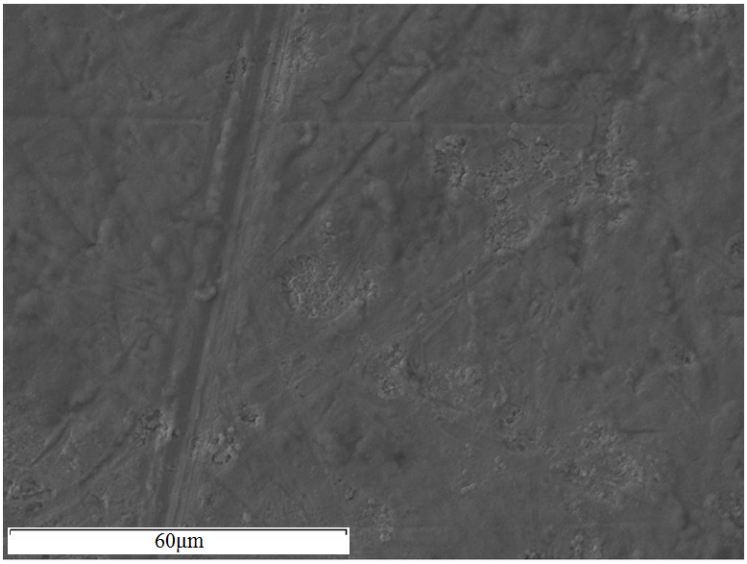

Element (at.%)	O	Cr	Mn	Co	W
Surface	66.9	3.1	7.3	8.4	14.3

Figure 75. SEM secondary electron micrograph of the surface of the HVOF WC/Cr/Co coating after porosity testing together with an elemental compositional analysis using EDX below

4.1.4 XPS of EDAl and SermeTel 962 Coatings

Airbus required confirmation as to whether hexavalent Cr existed in the EDAl and SermeTel 962 coatings. X-ray photoelectron spectroscopy was carried out to investigate the oxidation state of the Cr in the SermeTel 962 and EDAl coatings.

Figure 76 shows the XPS Cr spectra for the two coatings. It was clear that both these two Cr XPS spectra consisted of peaks at about 577.7 and 587.3 eV. According to the database for XPS spectra, the range of the peaks for trivalent Cr is from 575.9-576.8 eV and 586-588 eV whilst for hexavalent Cr it is from 578.3-580.1 eV[108]. So the presence of the peaks at 586.94 and 587.56 eV showed that there was trivalent Cr in these two coating. However, the other peaks at about 577.7 eV, are between the ranges for trivalent and hexavalent Cr. It was suggested that these are the combination of the peaks for trivalent and hexavalent Cr. From the area ratio of the peak for trivalent Cr and the mixed peak for trivalent and hexavalent Cr, it can be concluded that the Cr in both coatings was mainly composed of trivalent Cr but a low concentration of hexavalent Cr was also believed to be present.

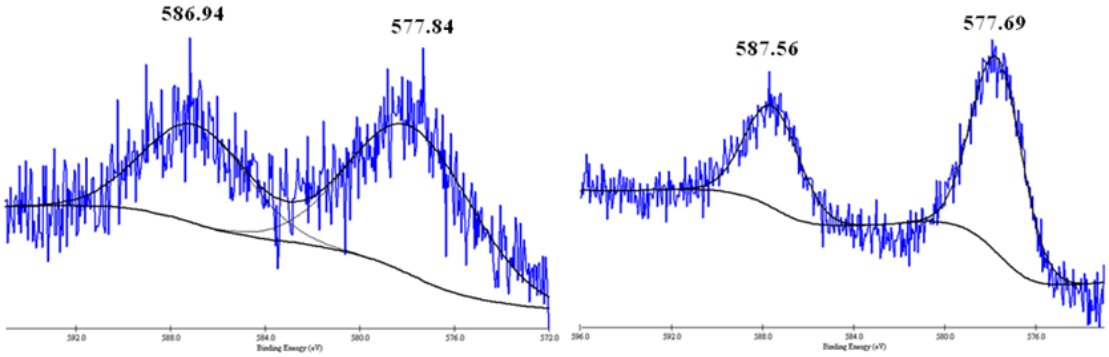

Element (at.%)	Al	P	Mg	Cr	Zr
SermeTel 962 coating	81.0	12.3	4.4	2.3	-
EDAl Al coating (passivation coating)	38.1	-	-	29.9	32.0

Figure 76. XPS Cr spectra from the surface of the untreated SermeTel coating and EDAl coatings with general composition below

4.1.5 Free Corrosion Potential Measurements

The free corrosion potentials of all the coatings were investigated to illustrate their subsequent potential for galvanic corrosion resistance. The greater difference in the free corrosion potential there was between the sacrificial and the hard coatings, the poorer galvanic compatibility they may have, which has a significant effect on possible galvanic corrosion. From Figure 77, the hard coatings, EHC and HVOF WC/Cr/Co, had similar potentials at approximately -500 mV. For the sacrificial coatings, the EC coating presented the lowest potential (-738 mV). The EDAl coating, post-treated SermeTel coating and FSAl coating all had similar potentials of about -715 mV. With the SermeTel coating, the light abrasion deformed the Al particles and increased the coating conductivity, which resulted in a decrease in the potential. The as-deposited SermeTel coating presented a much higher potential than the other sacrificial coatings. From the results of the free corrosion potential of the coatings, the as-deposited SermeTel coating was suggested to have the best galvanic compatibility with the hard coatings.

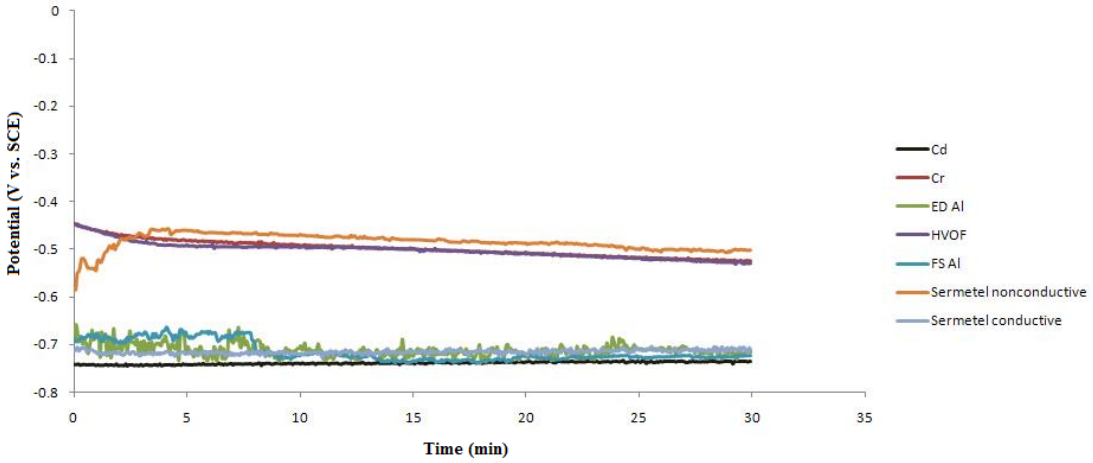

	Cd	Cr	EDAl	HVOF	FSAl	SermeTel	Treated SermeTel
Free Corrosion Potential E_{corr} (V vs. SCE)	**-0.738**	**-0.499**	**-0.712**	**-0.502**	**-0.715**	**-0.484**	**-0.715**

Figure 77. Free corrosion potential of the coatings tested in 3.5 wt.% NaCl solution (vs. SCE)

4.1.6 Galvanic Corrosion Investigation

Galvanic compatibilities of the sacrificial and the hard coatings were identified qualitatively and quantitatively by monitoring their electrode potential and galvanic current during galvanic corrosion. The morphology and composition of the coatings after galvanic corrosion were also shown to illustrate their corrosion mechanisms.

4.1.6.1 EC and EHC Coatings Galvanic Couple

Figure 78 shows the electrode potential and galvanic current of the EHC and EC coatings over 15 days in 3.5 wt.% NaCl. The electrode potential was initially -750 mV and then generally decreased with time. It was noted that with the potential decrease, the current did not increase but also decreased significantly over the first 10 h. It then fluctuated around a value of approximately 5 μA, which implied slight galvanic activity between the two coatings.

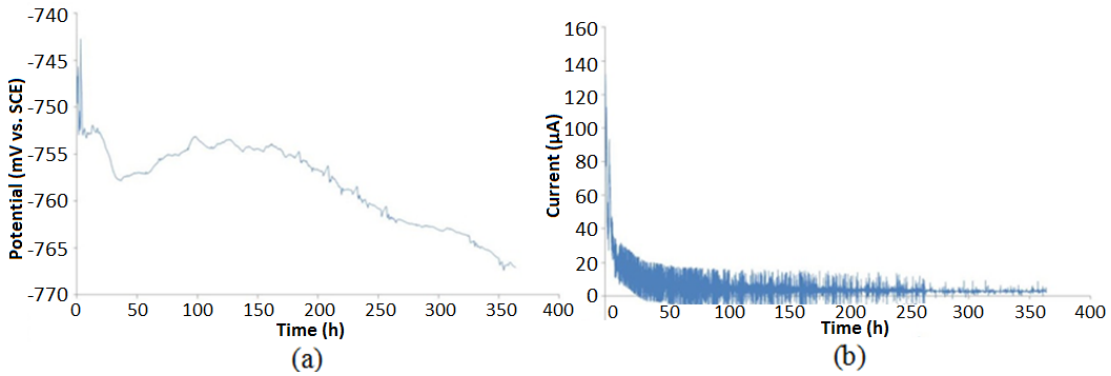

Figure 78. (a) Electrode potential and (b) Galvanic corrosion current, versus time for EHC and EC coatings in 3.5 wt.% NaCl

From Figure 77, the OCP of the uncoupled EC and EHC coatings were approximately -740 and -500 mV respectively. As mentioned previously, a Cr passivation film was present on the EC coating. Therefore, the OCP of the EC was very likely a mixed potential of the chromate passivation layer and underlying EC coating. The EC coating appeared to act as anode when coupled to the EHC coating. The EC coating was examined after galvanic corrosion as shown in Figure 79. Some cracks were observed on the surface of the Cr conversion coating of the EC coating. Compared to the as-received EC coating, a high content of O was evident on the surface of the coating after galvanic corrosion. Moreover, many nodules were also noted. The nodules consisted of O, Cl and Cd. From the OCP of the EC and EHC coatings, the latter was thought to act as the cathode in the galvanic corrosion cell. After the corrosion, there was no significant difference observed in the general underlying coating morphology and composition (Figure 80). However, there were many nodules present on the surface of the EC coating, which consisted of Cl and Cd (see Figure 80).The nodules observed on the surface of the EHC and EC coatings had distinctly different morphologies.

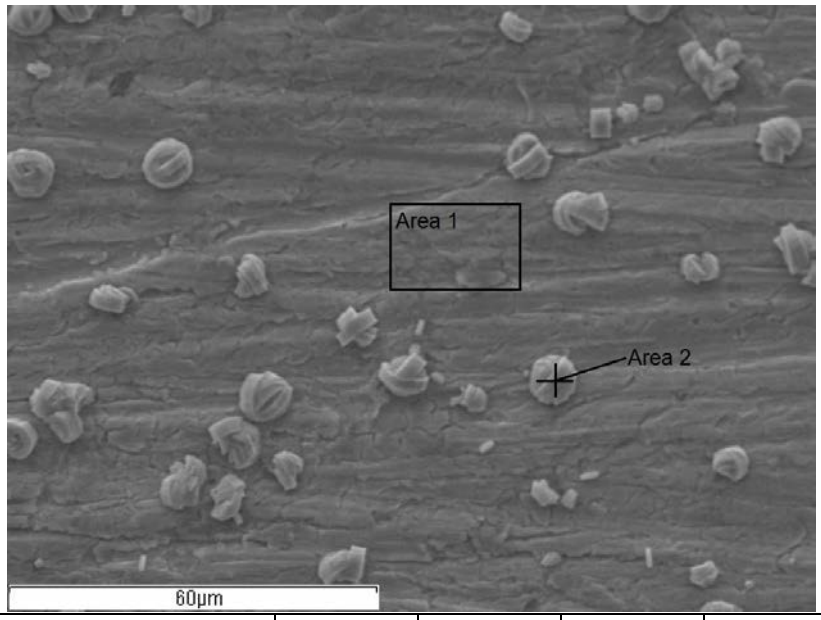

Element (at.%)	Cd	Cr	O	Cl
Area 1	17.0	3.6	77.8	1.6
Area 2	36.4	-	40.2	23.4

Figure 79. SEM secondary electron micrograph of the surface of the EC coating after the galvanic corrosion test coupled with the EHC coating. Also shown is an EDX elemental compositional analysis of (1) the general surrounding region of the coating and (2) a nodule

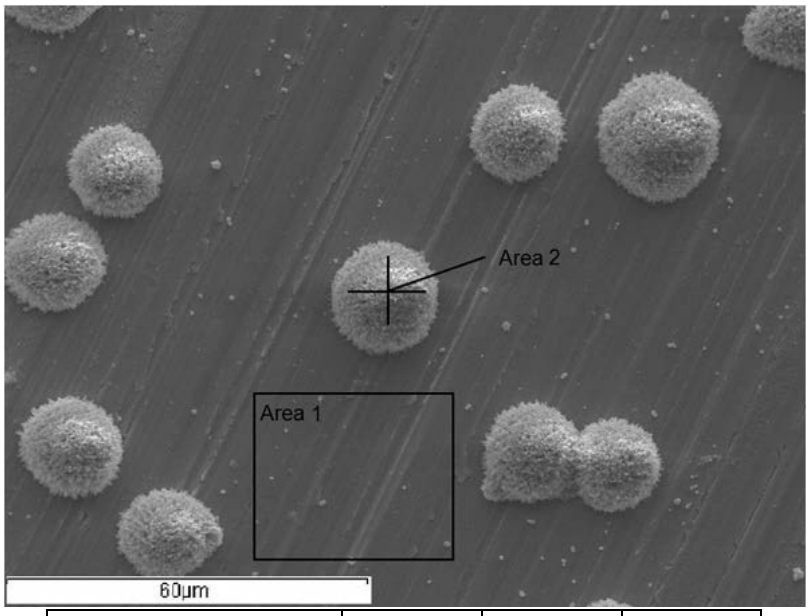

Element (at.%)	Cd	Cr	Cl
Area 1	-	100.0	-
Area 2	59.1	-	40.9

Figure 80. SEM secondary electron micrograph of the surface of the EHC coating after the galvanic corrosion test coupled with EC coating. Also shown is an EDX elemental compositional analysis of (1) a nodule and (2) the general surrounding region of the coating

In order to elucidate the structure of the nodules, FIB-SEM techniques were employed

to produce cross-sections as shown in Figures 81 and 82. The small insets in the figures are the morphology of the nodules before sectioning. Figure 81 shows a section through a nodule on the surface of the EC coating. A dark film between the nodule and substrate was identified as the Cr passivation film. From Figure 81, a physical connection was observed between the nodule and underlying EC coating through the crack in the passivation film (circled on the micrograph). The nodule also appeared to present a dense structure and good adhesion to the EC coating. For the nodules on the EHC coating (Figure 82), a much more porous structure is evident and gaps can also be observed between the nodule and the EHC coating (ellipse circled area in Figure 82). The nodules are suggested to be corrosion products of Cd with Cl^- , that have formed on the cathodic EHC coating.

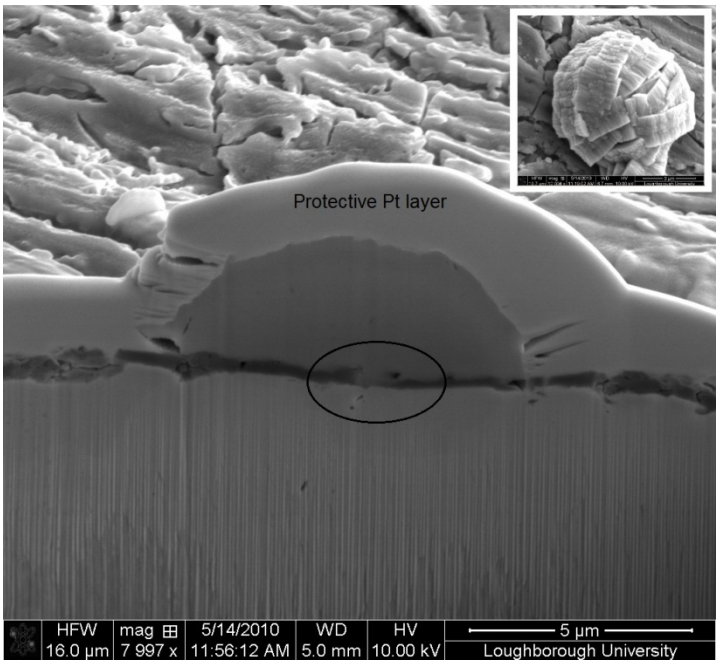

Figure 81. FIBSEM secondary electron micrograph of the cross-section of a nodule on the EC coating after galvanic corrosion testing coupled to the EHC coating (the ellipse circled area illustrates the connection of the nodule and the underlying EC coating). The inset illustrates the nodule before sectioning.

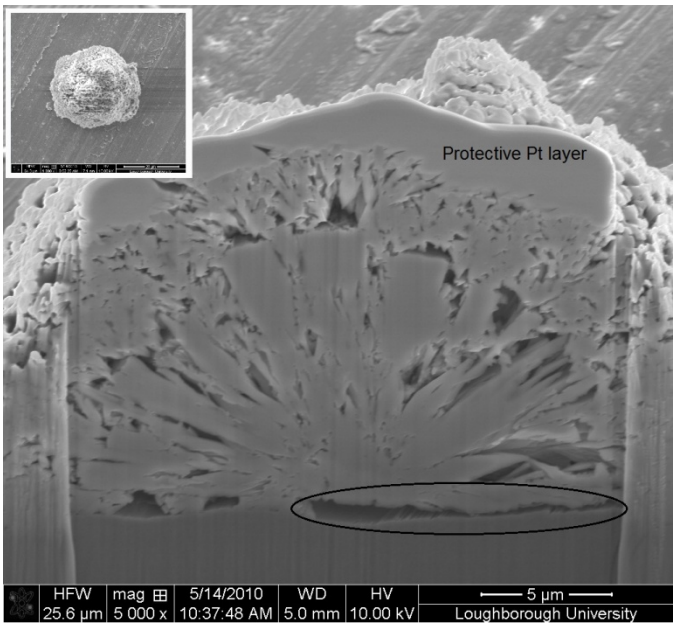

Figure 82. FIBSEM secondary electron micrograph of the cross-section of a nodule on the EHC coating after galvanic corrosion testing coupled to the EC coating (the ellipse circled area illustrates a gap between the nodule and the EHC coating). The inset illustrates the nodule before sectioning.

4.1.6.2 EC and HVOF WC/Cr/Co Coatings Galvanic Couple

Figure 83 illustrates electrode potential and galvanic corrosion current data for EC and HVOF WC/Cr/Co coatings. During the galvanic corrosion test, it was found that the electrode potential increased with time, which was the reverse of the trend for the EC and EHC couple. It was also noted that up to 50 h of testing, negative corrosion currents were observed, which implied that a reversal of the galvanic couple had occurred. After 50 h, the galvanic corrosion current increased to a positive value and tended to be stable at about 25 μA, which was much higher than the corrosion current for the EC and EHC coatings couple.

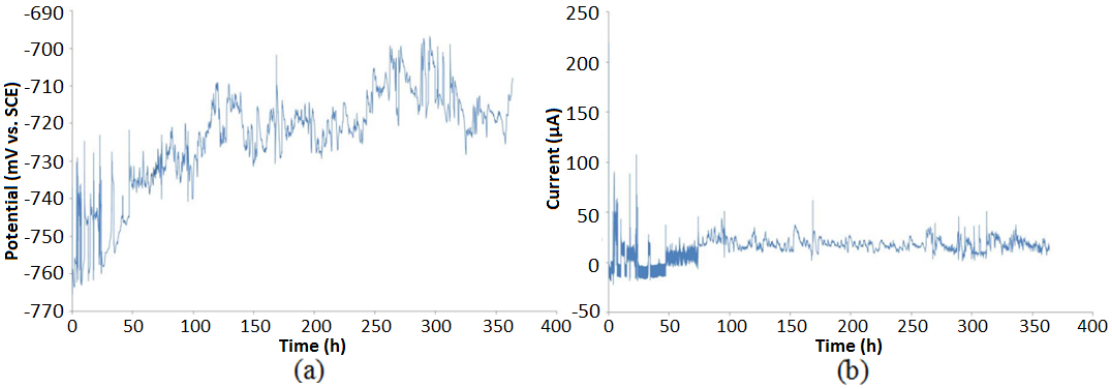

Figure 83. (a) Electrode potential and (b) Galvanic corrosion current, versus time for EC and HVOF WC/Cr/Co coatings

From figure 77, the OCP of the HVOF WC/Cr/Co in 3.5 wt.% NaCl solution was about -500 mV, which was similar to that of the EHC coating. Therefore, the EC coating was expected to be anodic during galvanic corrosion. After the galvanic corrosion test, the general area of the surface of the EC coating presented a similar morphology as observed in EC/EHC coatings galvanic couple. Moreover, two distinct nodule morphologies and composition were observed on the EC surface (Figure 84). As shown in the small inset secondary electron micrograph in Figure 85, these two different morphologies were chosen for further investigation. The structures of these two nodules are illustrated more clearly in Figure 85 through cross-sections obtained by FIBSEM. The whole nodule in Figure 85 (a) had a dense structure whilst for Figure 85 (b) the interior of the nodule presented a dense structure and the exterior a more acicular growth format. Moreover, in Figure 85 (b), a crack was evident in the passivation film on the EC coating. Severe corrosion was observed in the underlying EC coating.

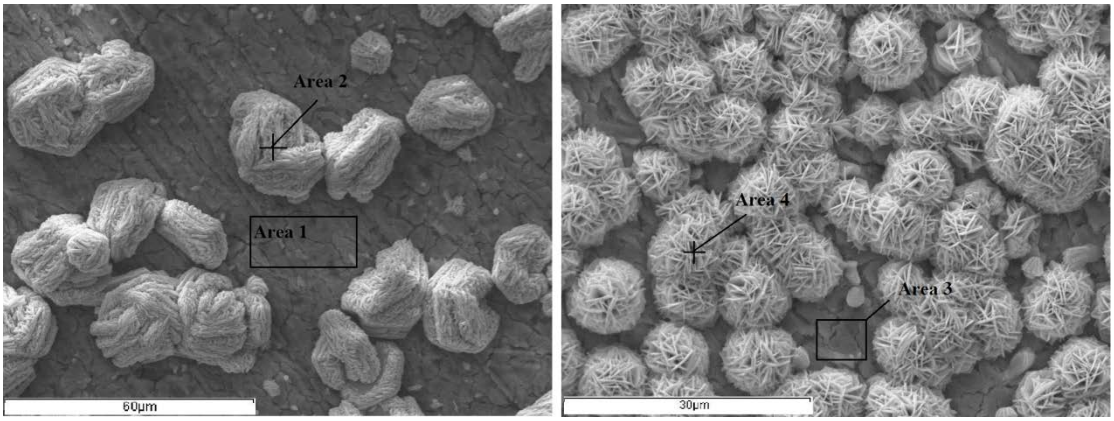

Element (at.%)	Cd	Cr	O	Cl
Area 1	10.0	4.0	83.7	2.3
Area 2	54.2	-	-	45.8
Area 3	12.9	5.1	79.9	2.1
Area 4	36.3	-	50.6	13.1

Figure 84. SEM secondary electron micrographs of the two types of nodules on the surface of the EC coating after the galvanic corrosion test coupled to the HVOF WC/Cr/Co coating

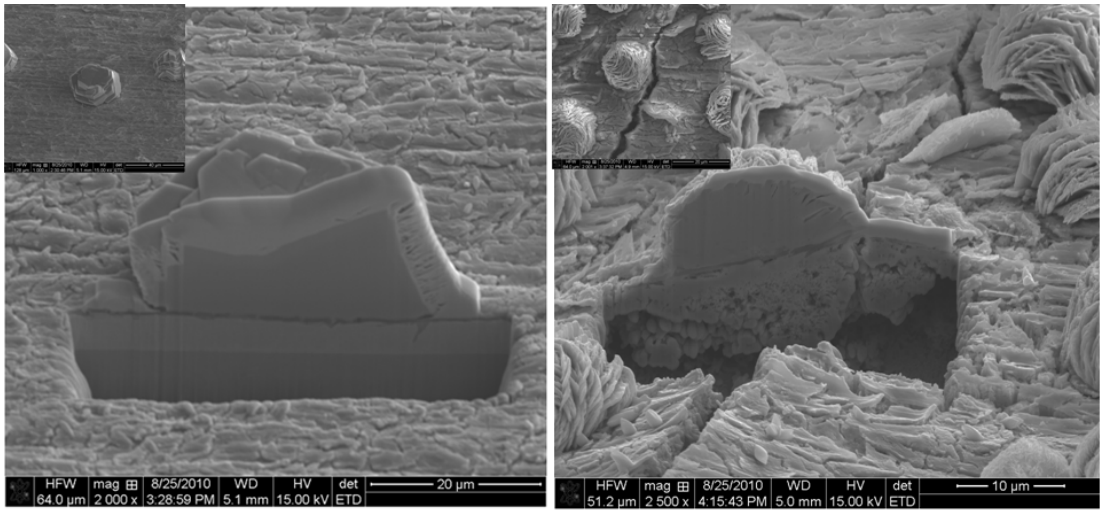

(a) (b)

Figure 85. FIBSEM secondary electron micrographs of the cross-section of (a) a dense structured nodule and (b) an acicular structured nodule on the EC coating after galvanic corrosion coupled to the HVOF WC/Cr/Co coating. The inset secondary electron micrographs show the areas before sectioning.

Thin foils were prepared from these two nodules and observed by TEM with electron diffraction pattern and compositional analysis. The foil from the nodule in Figure 85 (a) is shown in Figure 86 (a). Five areas (circled) were chosen to analyse in terms of microstructure and composition. Figure 86 (b) shows a representative microstructure of

the nodule, which appeared both granular and porous. From compositional analysis using EDX, the nodule was 65.4 at.% Cl, 34.6 at.% Cd, an atom ratio of almost 2:1, probably suggesting $CdCl_2$ corrosion product. A diffraction pattern from the nodule was also obtained by TEM (Figure 87). The d-spacings were calculated and compared to a standard powder diffraction pattern data base by EDAX Orientation Imaging Microscopy v5 software to confirm composition. From Figure 87, it can be seen that the diffraction pattern data from the nodule matched the standard data for $CdCl_2$.

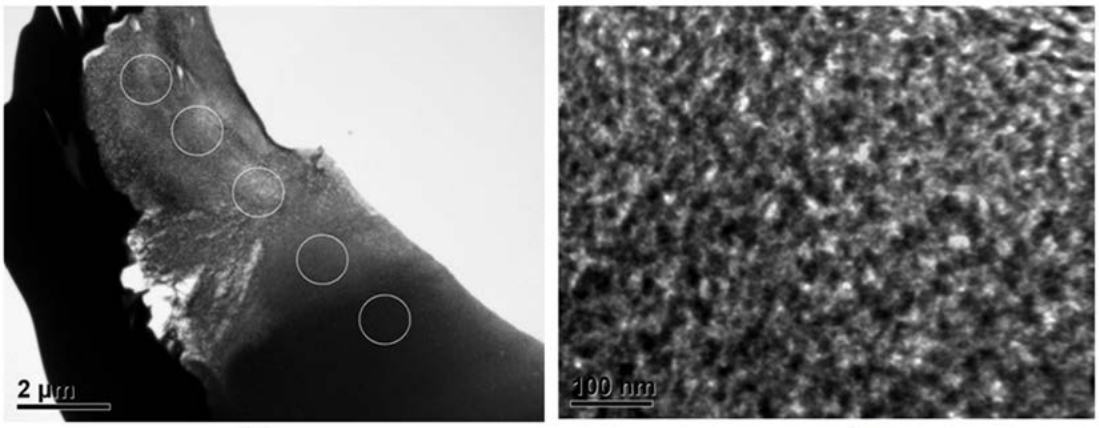

Element (at.%)	Cd	Cl
Circled area	65.4	34.6

Figure 86. TEM micrographs of the nodule presented in Figure 85 (a). (a) lower magnification micrograph, (b) typical nodule microstructure at higher magnification. Circled areas illustrate areas analysed.

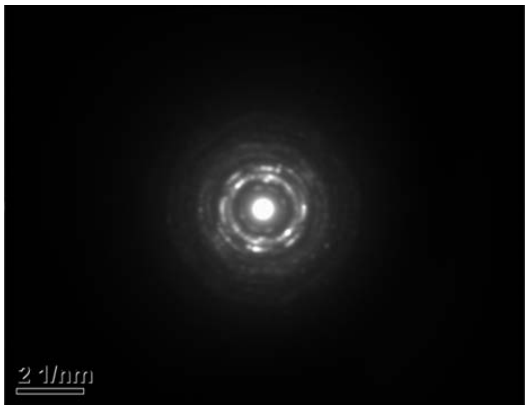

$CdCl_2$ (Trigonal)		
hkl	Sample (d)	Standard (d)
0003	5.81	5.82
1014	3.29	3.27
1120	2.59	2.84

Figure 87. TEM diffraction pattern of the nodule presented in Figure 85 (a) together with d

spacings compared with the standard powder diffraction pattern database

A thin foil was obtained from the acicular nodule in Figure 85 (b) by FIB etching. Figure 88 illustrates that the microstructure of the exterior of the nodule was significantly different to the interior. Compositional (EDX) data suggested that the nodule interior was essentially pure Cd and presented a denser microstructure than the exterior area. The latter was thought to be CdO_2 with a composition of 33.2 at.% Cd and 66.8 at.% O. Following comparison of TEM diffraction patterns with the standard powder diffraction database, agreement was evident with the EDX analysis (see Figure 89). Figure 90 shows that a dense formation of the Cd-based nodular species was noted on the surface of the EC coating after the galvanic corrosion. Some large cracks, which penetrated into the EC coating, were evident on the passivation coating and the 'crystalline' nodules appeared to have been ruptured by the cracks.

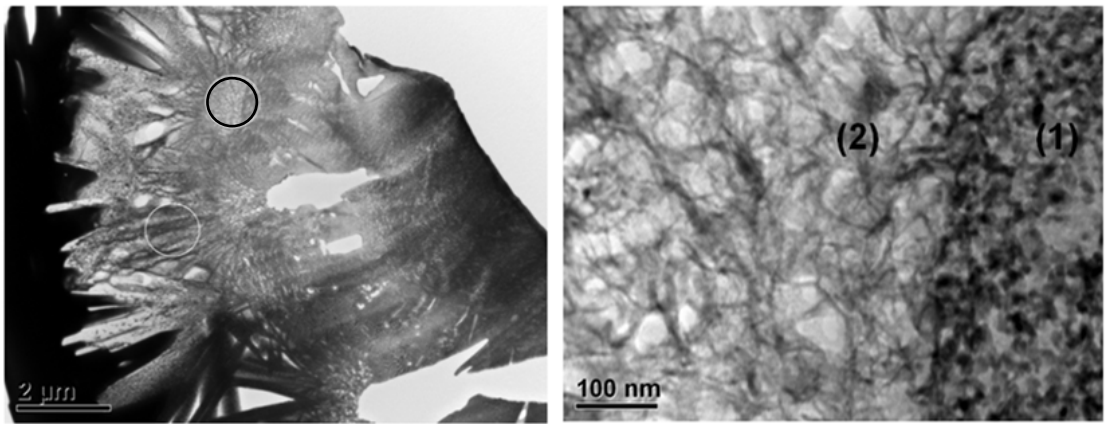

Element (at.%)	Cd	O
Area 1	100.0	-
Area 2	33.2	66.8

Figure 88. TEM micrograph of the nodule presented in figure 84 (b): (a) low magnification micrograph and (b) high magnification micrograph showing (1) interior and (2) exterior microstructure.

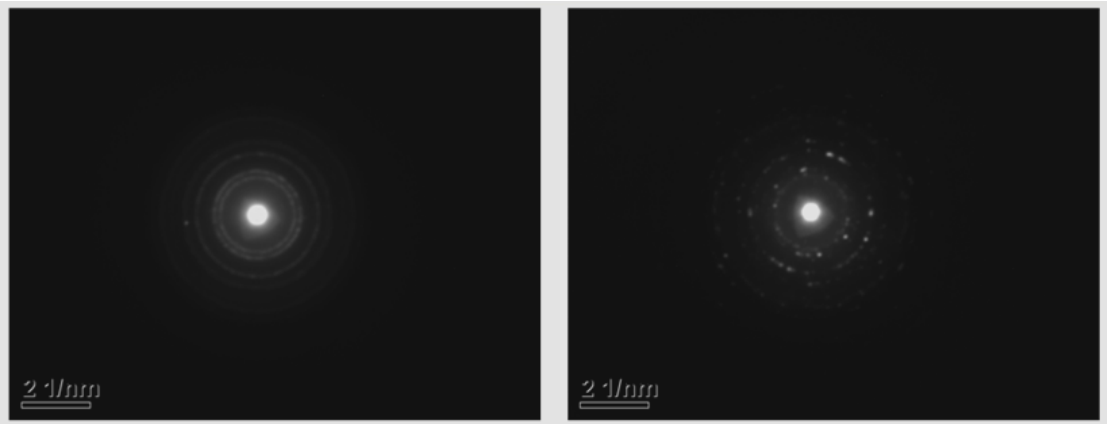

(1) Cd (Hexagonal)		
hkl	Sample (d)	Standard (d)
1011	2.34	2.34
0002	2.801	2.803
1122	1.318	1.313

(2) CdO_2 (Cubic)		
hkl	Sample (d)	Standard (d)
200	2.650	2.657
311	1.605	1.602

Figure 89. TEM diffraction patterns from the two areas of the nodule presented in figure 84 (b) together with d spacings compared with those from the standard powder diffraction pattern database

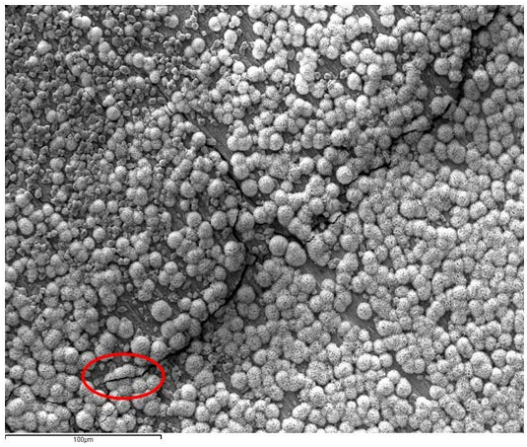

Figure 90. SEM secondary electron micrograph of the cracked area on the surface of the EC coating after the galvanic corrosion test coupled to the HVOF WC/Cr/Co coating

From the OCP of the EC and HVOF WC/Cr/Co coatings, the latter was expected to act as a cathode during galvanic corrosion. After galvanic corrosion trails, many crystalline containing Cd and Cl deposits with an average size of about 30 μm were observed on the HVOF WC/Cr/Co coating as shown in Figure 91. It was also noted that in addition to the crystalline Cd-containing deposits, many similar features also containing Cd and Cl were observed on the surface of the HVOF WC/Cr/Co coating after galvanic

corrosion as Figure 92 shows. These are thought to be semi-dissolved products from the original crystalline Cd-based deposits.

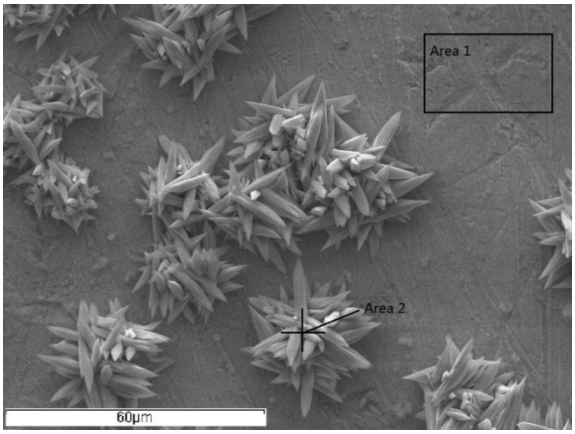

Element (at.%)	O	Cr	Co	W	Cl	Cd
Area 1	48.7	4.5	12.8	34.0	-	-
Area 2	68.1	-	-	-	10.6	21.3

Figure 91. SEM secondary electron micrograph of the surface of the HVOF WC/Cr/Co coating after the galvanic corrosion test coupled to the EC coating together with an elemental compositional analysis of (1) the general background area (2) a nodule, using EDX

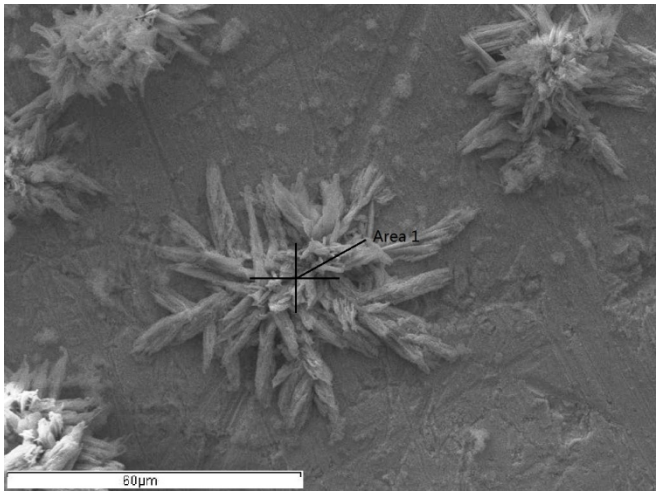

Element (at.%)	Cl	Cd
Area 1	35.3	64.7

Figure 92. SEM secondary electron micrograph of the surface of a HVOF WC/Cr/Co coating after galvanic corrosion from being coupled to a EC coating together with an elemental compositional analysis of partially dissolved nodules using EDX

Severe local corrosion was observed with the HVOF coating coupled to the EC coating (Figure 93). A large area of the HVOF coating was totally removed from the surface (area 2 in Figure 93). The exposed area was presented as a mixture of O, Al, Fe and Cd. The interface between the HVOF WC/Cr/Co and the steel substrate was then

investigated as Figure 94 illustrates. It was noted that there appeared to be good adhesion between the HVOF coating and the substrate, but at some sites, a phase consisting of Al and O was found. These phases are suggested to be Al_2O_3 particles originally trapped on the surface of the substrate from the pre-treatment grit blasting confirmed by the HVOF coating supplier. A local area was ablated by FIBSEM to observe its cross-section as illustrated in Figure 95. A phase different from the HVOF WC/Cr/Co coating was observed under the local corrosion area, which was Al_2O_3.

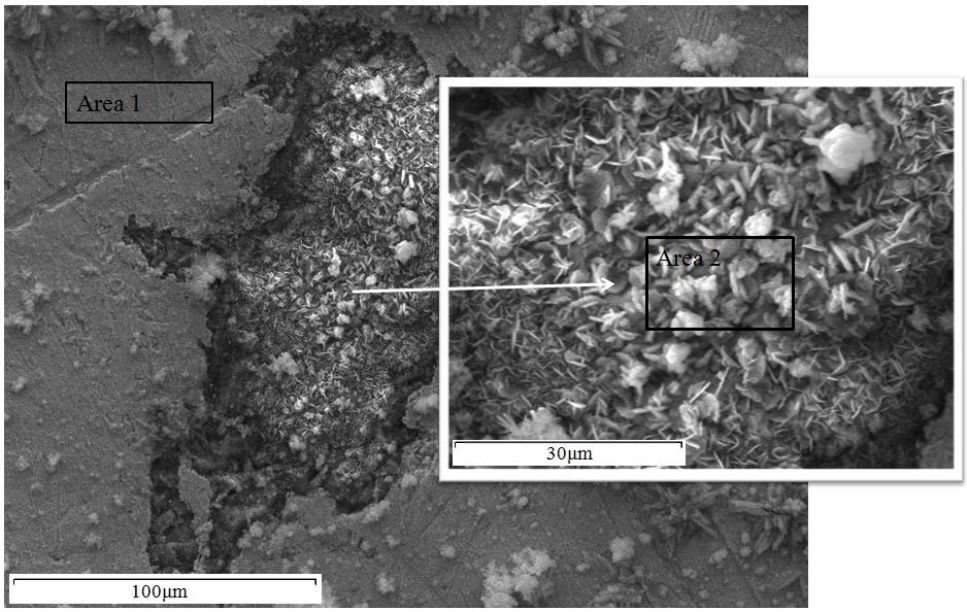

Element (at.%)	Cr	Co	W	O	Al	Fe	Cd
Area 1	20.8	26.5	52.7	-	-	-	-
Area 2	-	-	-	73.3	16.0	10.0	0.7

Figure 93. SEM secondary electron micrograph of the surface of the HVOF WC/Cr/Co coating after the galvanic corrosion test coupled to the Cd coating together with an elemental compositional analysis of (1) general area (2) local corrosion area using EDX

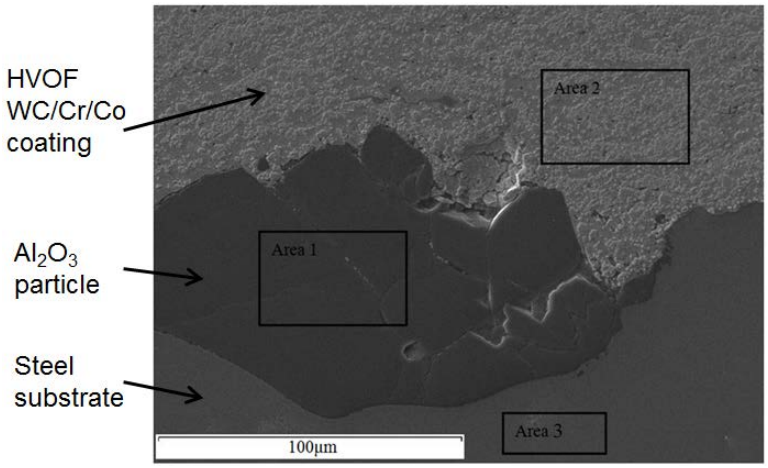

Element (at.%)	O	Al	Fe	C	Cr	Co	W
Area 1	62.3	37.7	-	-	-	-	-
Area 2	-	-	-	56.5	2.3	4.8	36.4
Area 3	-	-	100.0	-	-	-	-

Figure 94. SEM secondary electron micrograph of the cross-section of the interface between the HVOF WC/Cr/Co coating and the steel substrate together with an elemental compositional analysis of (1Al_2O_3 (2) HVOF WC/Cr/Co coating (3) steel substrate using EDX

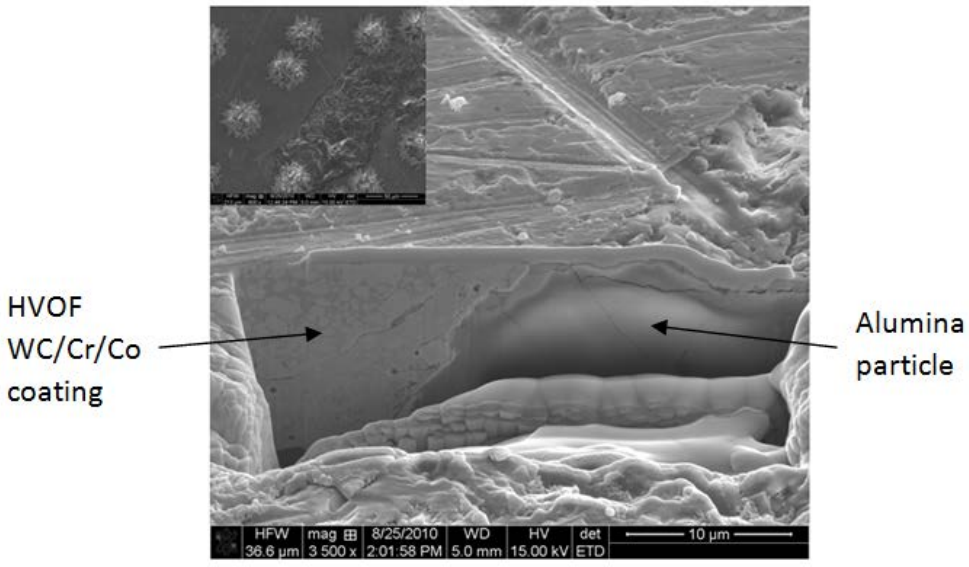

Figure 95. FIBSEM secondary electron micrograph of the cross-section of the local corrosion on the HVOF WC/Cr/Co coating after the galvanic corrosion test coupled to the EC coating. The insert secondary electron micrograph illustrates the area before sectioning

4.1.6.3 FSAl and HVOF WC/Cr/Co Coatings Galvanic Couple

As Figure 96 shows, during the galvanic corrosion test coupled to the HVOF WC/Cr/Co coating, the electrode potential of the FSAl coating was about -650 mV, but

decreased sharply to -1050 mV in the first 10 h and then increased gently to -950 mV. The galvanic current of the couple also presented a much higher value (greater than 50 μA) than the other galvanic couples, which implies a poor galvanic compatibility between the two coatings.

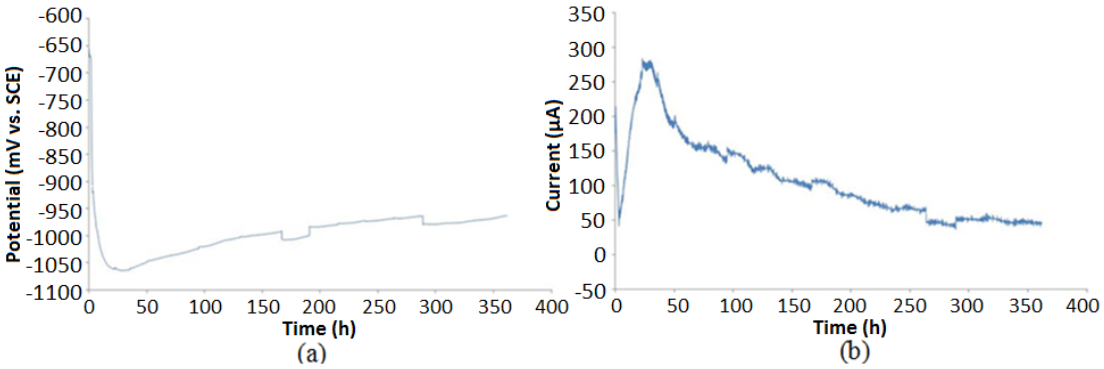

Figure 96. (a) Electrode potential and (b) Galvanic corrosion current versus time for flame sprayed aluminium and HVOF WC/Cr/Co coatings

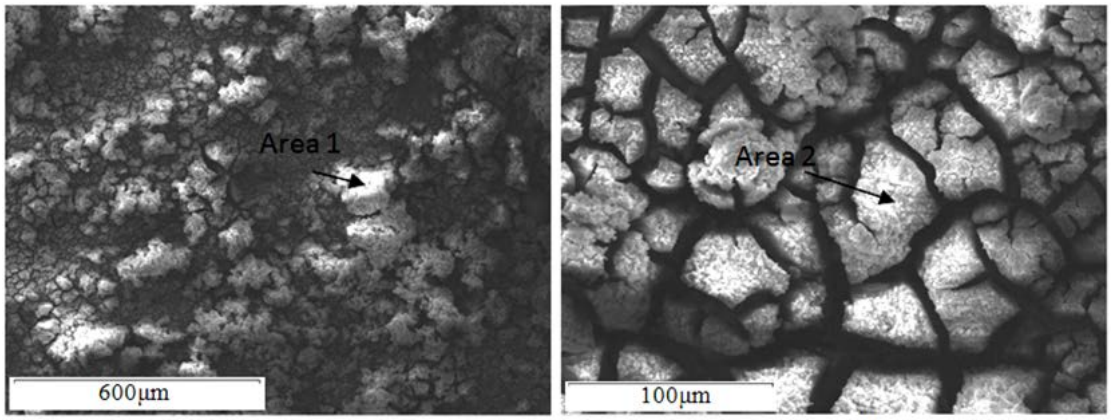

Element (at.%)	O	Al	Cl
Area 1	59.7	28.7	11.6
Area 2	77.9	22.1	-

Figure 97. SEM secondary electron micrographs of (a) the centre and (b) the edge of the surface of the FSAl coating after the galvanic corrosion test coupled to the HVOF WC/Cr/Co coating together with an elemental compositional analysis using EDX

After galvanic corrosion, as Figure 97 shows, severe corrosion of the FSAl coating was observed. In the centre area of the surface of the coating, some powdery Al_2O_3 corrosion products containing Cl presented, which were easily removed from the substrate (Figure 97 (a)). In the edge area of the surface, the coating was transformed into an oxide film with evident large cracks (Figure 97 (b)).

As Figure 98 illustrates, no significant local corrosion, such as that noted previously, was observed on the surface of this HVOF coating. However, it was noted that some depressed features were present on the surface of the HVOF coating. Compare to the as-received HOVF WC/Cr/Co coating (Figure 52 (a)), it was found that a severe decarburisation and oxidation was also observed on the surface of the HVOF coating, which may imply anodic reactions on the coating during galvanic corrosion (table of Figure 98).

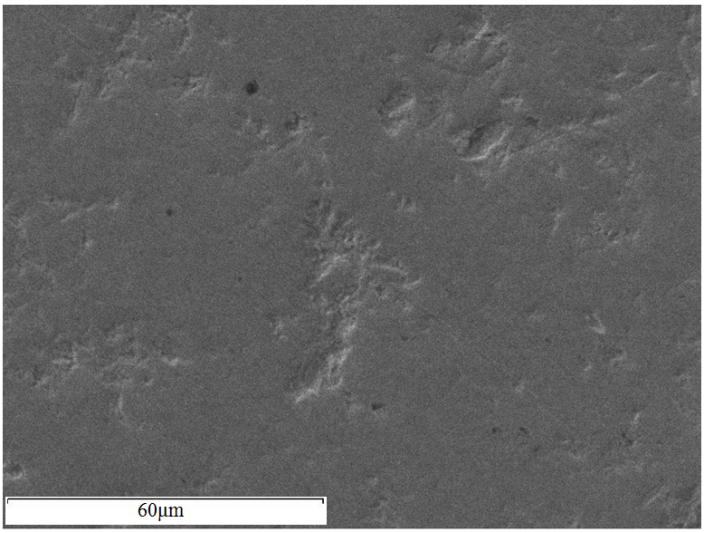

Element (at.%)	O	Cr	Co	W
Surface	27.1	7.6	14.3	51.0

Figure 98. SEM secondary electron micrograph of the surface of the HVOF WC/Cr/Co coating after the galvanic corrosion test coupled to the FSAl coating together with an elemental compositional analysis using EDX

4.1.6.4 EDAl and HVOF WC/Cr/Co Coatings Galvanic Couple

Compared with the galvanic couple of the EC and the EHC coatings, the EDAl and the HVOF WC/Cr/Co coatings presented poorer galvanic compatibility. During the galvanic corrosion test, the electrode potential of the EDAl coating fluctuated around -740 mV for the first 250 h but decreased to about -760 mV between 250 and 350 h, and then increased back to -740 mV (Figure 99). The current decreased initially from 160 µA over the first 5 h, and then tended to be stable at about 17 µA, which was three times the galvanic current from the EC and the EHC coatings galvanic couple.

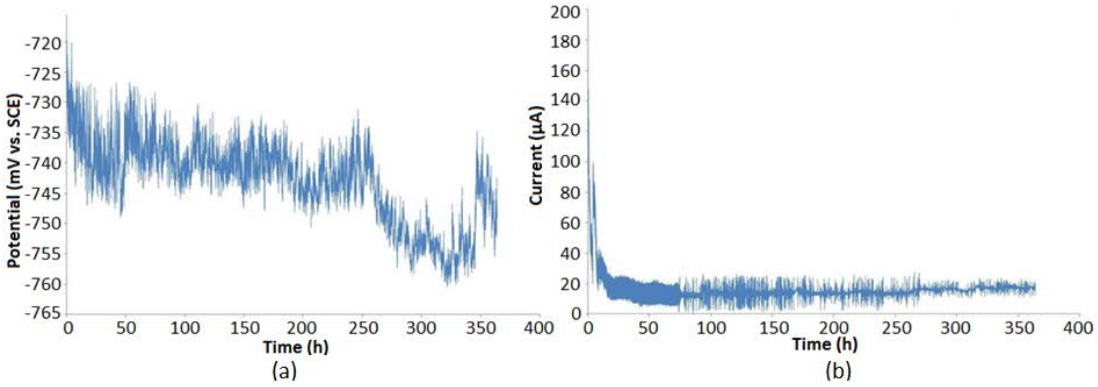

Figure 99. (a) Electrode potential and (b) Galvanic corrosion current versus time for EDAl and HVOF WC/Cr/Co coatings

After the galvanic corrosion, the centre area of the EDAl coating presented less corrosion than the edge area. Compared to the as-received coating (Figure 58), after galvanic corrosion, an absence of the Cr and a significant increase in O at the surface of the coating were observed (Figure 100). In the less corroded areas, an oxide film can be observed to form on the EDAl coating (area 2 in Figure 100). Al_2O_3 was also observed as a corrosion product (area 1 in Figure 100), which was powdery and presented poor adhesion to the coating.

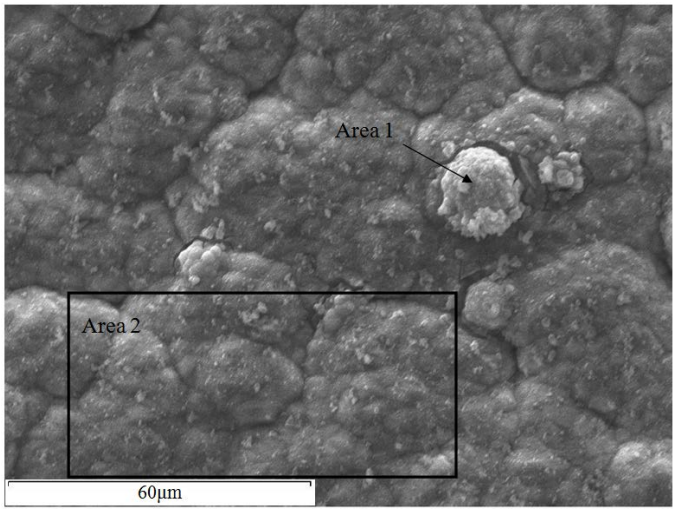

Element (at.%)	O	Al	Cl
Area 1	65.4	31.6	3.0
Area 2	23.3	76.7	-

Figure 100. SEM secondary electron micrograph of the centre of the surface of the EDAl coating after the galvanic corrosion test coupled to the HVOF WC/Cr/Co coating together with an elemental compositional analysis of (Area 1) corrosion product (Area 2) general area using EDX

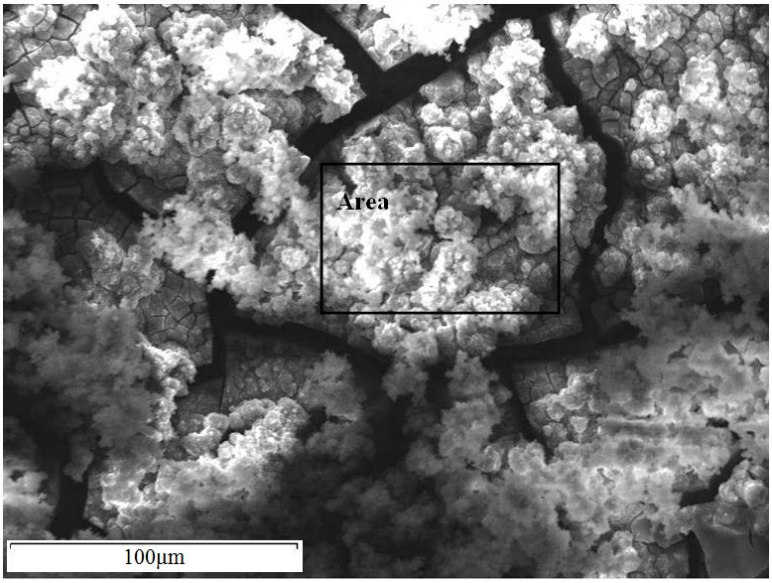

Element (at.%)	O	Al
Area	73.0	26.0

Figure 101. SEM secondary electron micrograph of the edge of the surface of the EDAl coating after the galvanic corrosion test coupled to the HVOF WC/Cr/Co coating together with an elemental compositional analysis using EDX.

As Figure 101 illustrates, much more serious corrosion was observed at the edge of the electrodeposited Al coating after galvanic corrosion. A significant increase in the O content was detected. The Al in the coating was oxidised and formed powdery oxide corrosion products. Cracks were evident in the oxidised Al coating.

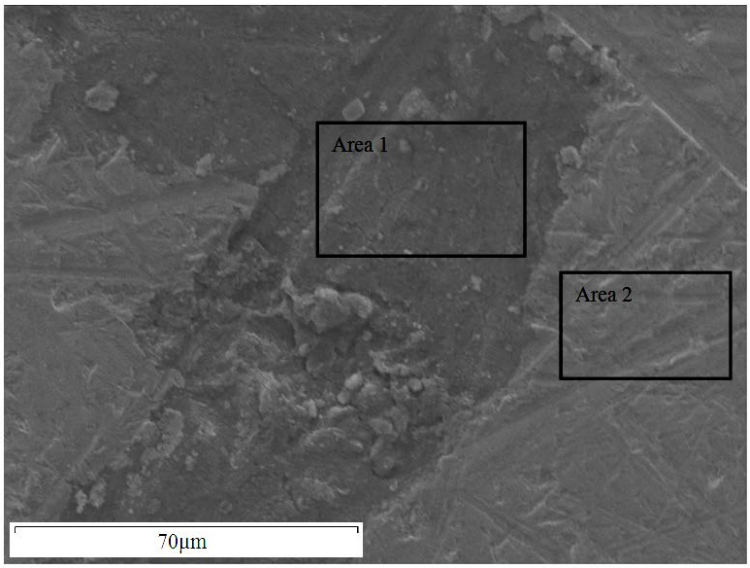

Element (at.%)	O	Al	Fe	Cr	Co	W
Area 1	48.7	4.4	46.9	-	-	-
Area 2	-	-	-	11.2	29.3	59.5

Figure 102. SEM secondary electron micrograph of the surface of the HVOF WC/Cr/Co coating after the galvanic corrosion test coupled to the electrodeposited Al coating together with an elemental compositional analysis of (1) local corrosion area (2) general area using EDX

From Figure 102, severe local corrosion was present on the surface of the HVOF WC/Cr/Co coating again as observed previously (Figure 93). After the galvanic corrosion test, most of the surface area (presented as area 2 in Figure 102) showed no significant change in its morphology, but severe decarburisation in composition as compared to the as-received coating (Figure 52 (a)). Some local corroded areas (shown for example as area 1 in Figure 102) were observed irregularly dispersed across the surface. From EDX analysis, O, Al and Fe were detected, which implied the removal of the HVOF WC/Cr/Co coating, exposing the trapped Al_2O_3 particles and underlying steel substrate.

4.1.6.5 SermeTel 962 and HVOF WC/Cr/Co Coatings Galvanic Couple

From Figure 103, during galvanic corrosion with a HVOF WC/Cr/Co coating, the electrode potential of the SermeTel 962 started at approximately -400 mV, and then

decreased immediately to -610 mV in a short time. After that, the electrode potential decreased much more gradually and tended to be stable at about -670 mV. The galvanic current of the SermeTel/HVOF WC/Cr/Co coatings galvanic couple presented a similar tendency as the electrode potential with time and exhibited stable at about 15 μA.

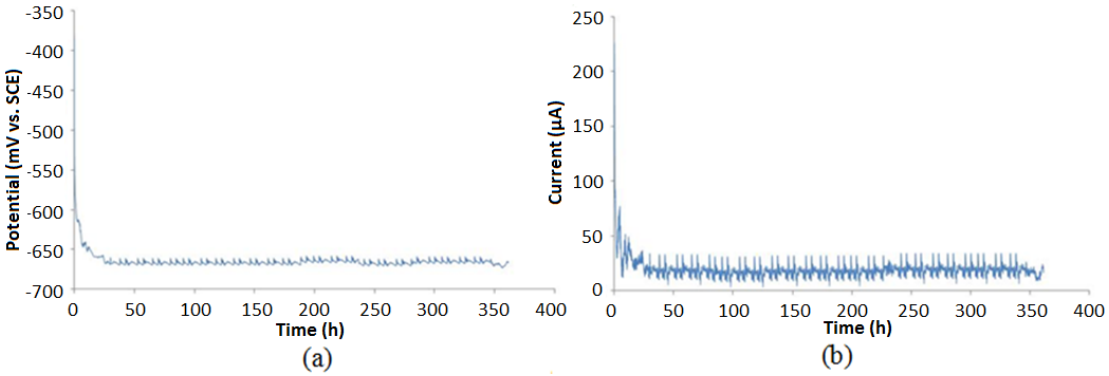

Figure 103. (a) Electrode potential and (b) Galvanic corrosion current, versus time for the SermeTel coating coupled to the HVOF WC/Cr/Co

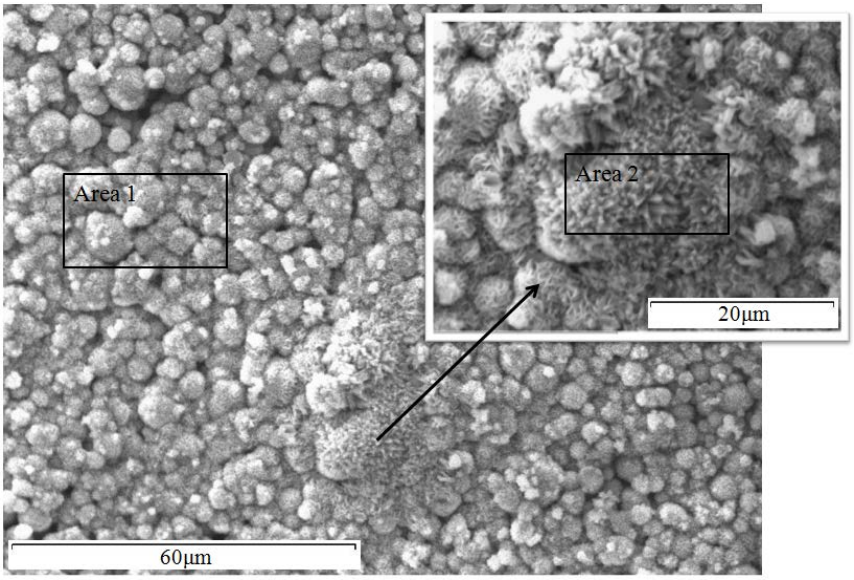

Element (at.%)	O	Fe	Al	P	Cr
Area 1	48.3	13.6	36.0	1.4	0.7
Area 2	36.8	63.2	-	-	-

Figure 104. SEM secondary electron micrographs of the surface of the SermeTel coating after the galvanic corrosion test coupled to the HVOF WC/Cr/Co coating together with an elemental compositional analysis (area 1) general area and (area 2) nodule using EDX

From Figure 104, the Al particles of the SermeTel coating oxidised during galvanic

corrosion by the presence of high level of O content. No significant defect was observed in the coating after the test. The morphology of the SermeTel coating remained with good integrity providing effective barrier and sacrificial protection properties. It was also noted that Fe was detected on the surface of the SermeTel coating after galvanic corrosion, which had never been expected. Moreover, some areas of the coating were covered by Fe oxide like corrosion products after the corrosion (area 2 in Figure 104). The Fe containing area was sectioned and shown in Figure 105. It was found that the SermeTel coating under the Fe containing phase remained intact. So the Fe-based corrosion products observed on the SermeTel coating were presumed to be from the coupled HVOF WC/Cr/Co coated steel substrate rather than the SermeTel coated one.

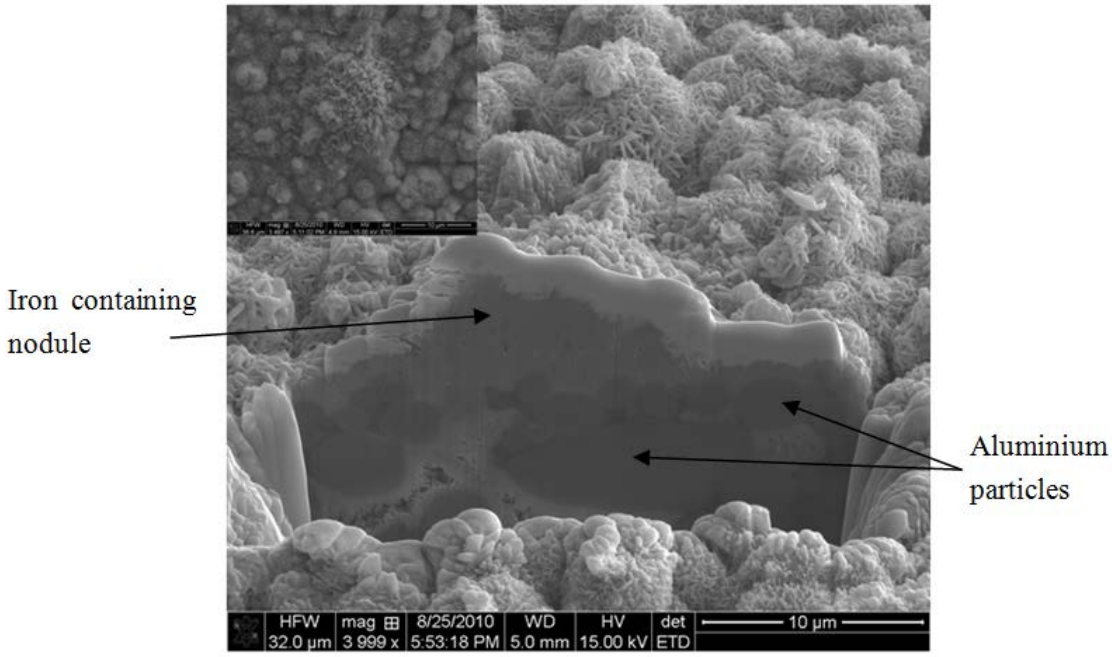

Figure 105. FIBSEM secondary electron micrograph of the Fe containing area on the SermeTel coating after the galvanic corrosion test coupled to the HVOF WC/Cr/Co coating. The insert secondary electron micrograph shows the area before the sectioning

The severe local galvanic corrosion caused by the trapped Al_2O_3 was also observed in the HVOF coating coupled with the SermeTel coating (Figure 106). The exposed area consisted of Al, O and Fe, which caused the local reverse galvanic reaction during the test. That may be the source of the Fe on the surface of the SermeTel coating. Compared

to the as-received coating (Figure 52 (a)), the coating presented severe decarburisation due to the galvanic corrosion test in the other highlighted area of the HVOF coating (Figure 106). The powdery oxide-like corrosion products in the local corrosion areas were observed in the local galvanic corrosion area (Figure 107). From the cross-section of the severe corrosion area (Figure 108), it was noted that the HVOF WC/Cr/Co coating adjacent to the Al_2O_3 presented a much looser structure than the other areas.

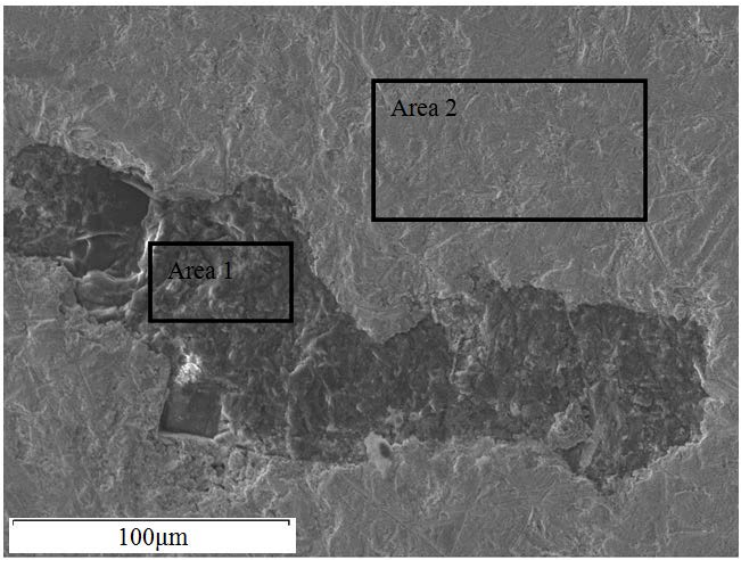

Element (at.%)	O	Fe	Al	Co	Cr	W
Area 1	62.8	2.4	34.8	-	-	-
Area 2	44.9	-	-	10.3	4.9	39.9

Figure 106. SEM secondary electron micrograph of the surface of the HVOF WC/Cr/Co coating after the galvanic corrosion test coupled to the SermeTel coating together with an elemental compositional analysis of (area 1) local corrosion area (area 2) general area using EDX

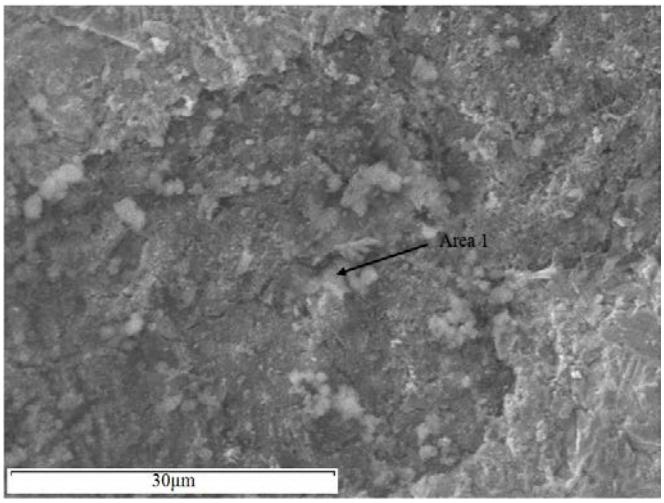

Element (at.%)	O	Fe	Cr
Area 1	54.4	44.0	1.6

Figure 107. SEM secondary electron micrograph of the surface of the HVOF WC/Cr/Co coating after the galvanic corrosion test coupled to the SermeTel coating together with an elemental compositional analysis of corrosion products (area 1) using EDX

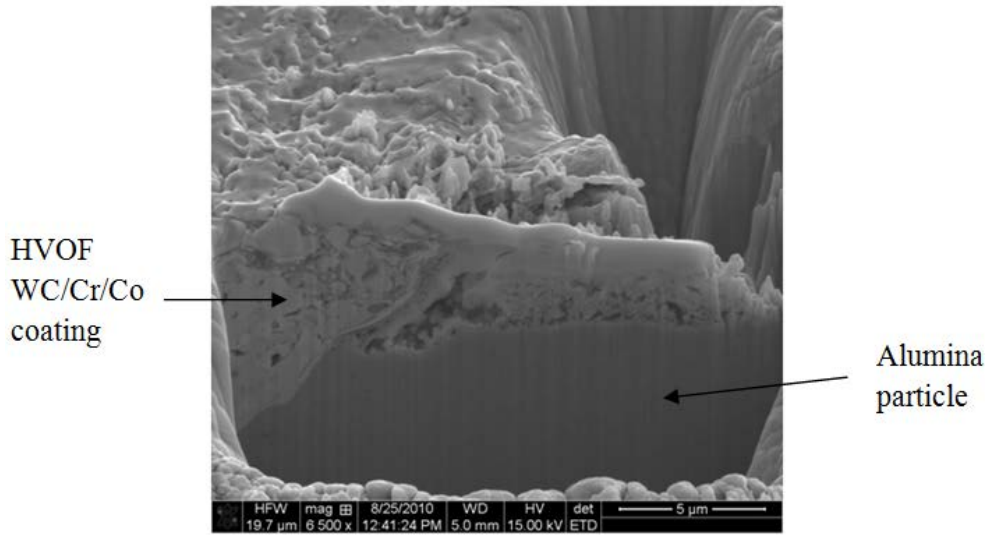

Figure 108. FIBSEM secondary electron micrograph of the local corrosion area on the HVOF WC/Cr/Co coating after the galvanic corrosion test coupled to the SermeTel coating

4.1.6.6 Post-treated SermeTel 962 and HVOF WC/Cr/Co Coatings Galvanic Couple

The lightly abraded post-treatment of the SermeTel coating increased its electrical conductivity and decreased its free corrosion potential significantly, which may have decreased the galvanic compatibility with the HVOF WC/Cr/Co coating. Thus it was

expected that a high corrosion current would be evident between the post-treated SermeTel coating and the HVOF WC/Cr/Co coatings. From Figure 109, the electrode potential of the post-treated SermeTel coating fluctuated over a sizeable range of 100 mV, which implies that severe periodic corrosion behaviour may occur during the corrosion test. The galvanic current of the post-treated SermeTel/HVOF WC/Cr/Co coating was unstable. After approximately 100 h, the current began to fluctuate in a range between positive and negative, which may result from the presence of the reversal galvanic reactions in the galvanic couple.

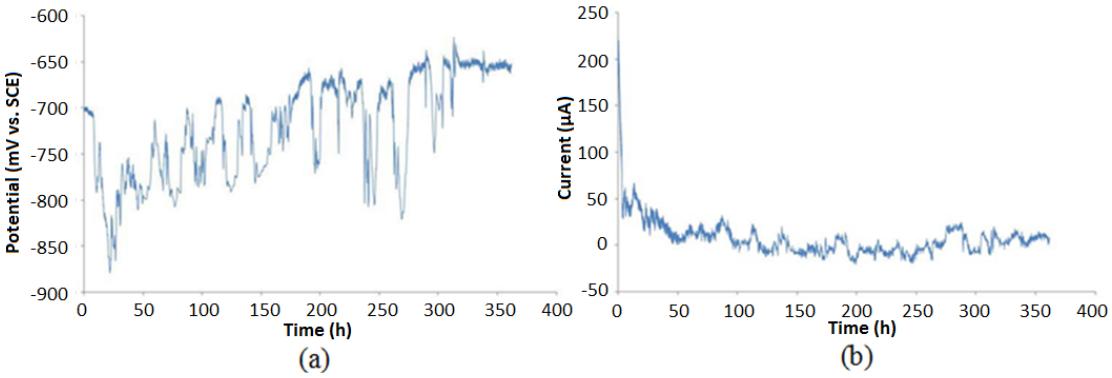

Figure 109. (a) Electrode potential and (b) Galvanic corrosion current versus time for the post-treated SermeTel coating coupled to the HVOF WC/Cr/Co

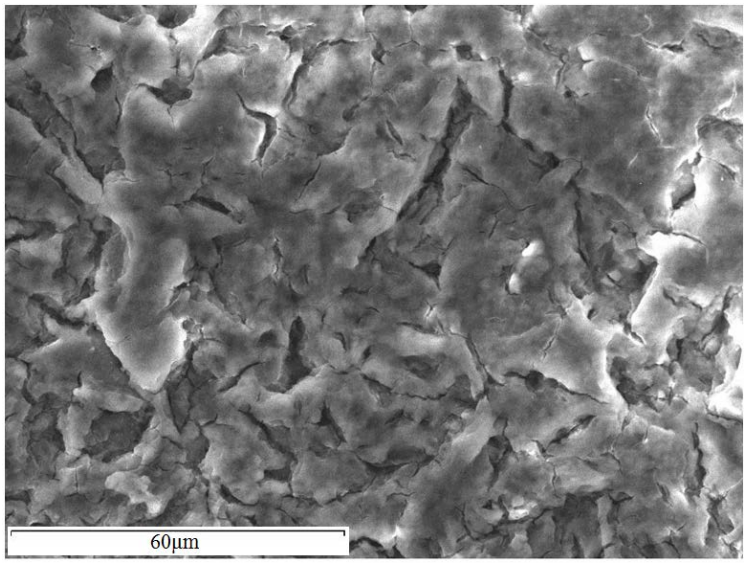

Element (at.%)	O	Al	P	Cr
Surface	58.1	37.1	3.8	1.0

Figure 110. SEM secondary electron micrograph of the centre of the surface of the post-treated SermeTel coating after the galvanic corrosion test coupled to the HVOF WC/Cr/Co coating together with an elemental compositional analysis using EDX

In the central area of the post-treated SermeTel coating, a much lower level of corrosion than the expected was observed (Figure 110). No significant change was observed in the morphology and the Al phases presented a high level of oxidation. However, in the edge area of the post-treated SermeTel coating, severe corrosion was observed. As figure 111 illustrates, the post-treated SermeTel coating was damaged and cracked Al_2O_3 films formed on the surface of the coating. Powdery corrosion products were also evident.

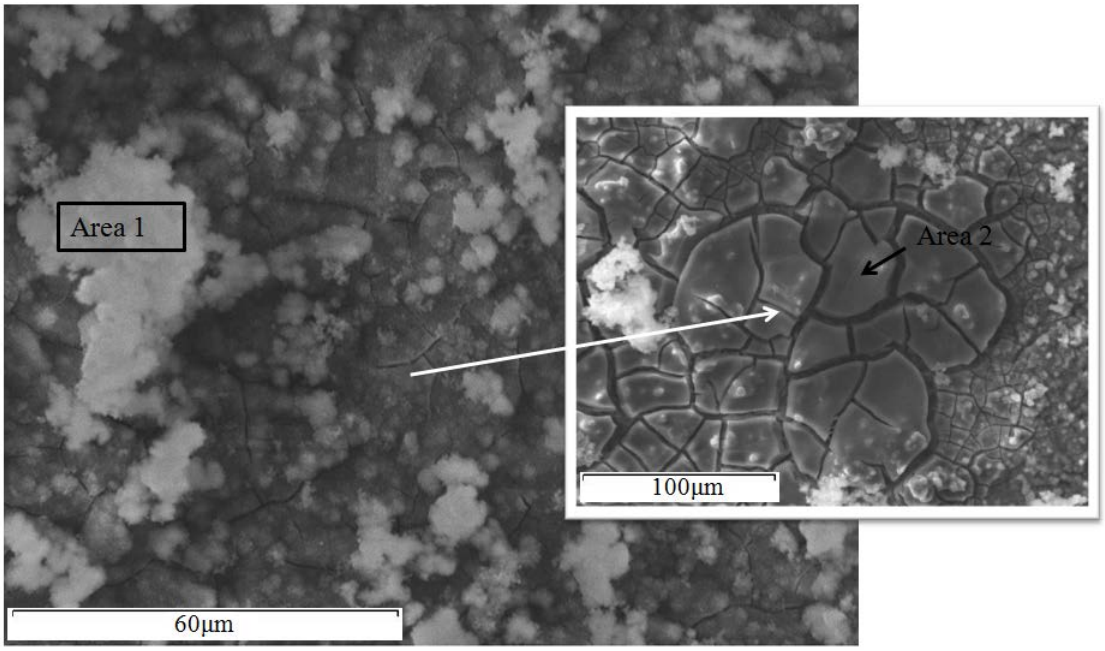

Element (at.%)	O	Al	Cl	W
Area 1	71.2	26.5	2.0	0.3
Area 2	65.6	18.4	16.0	-

Figure 111. SEM secondary electron micrograph of the edge of the surface of the post-treated SermeTel coating after the galvanic corrosion test coupled to the HVOF WC/Cr/Co coating together with an elemental compositional analysis of (area 1) powdery corrosion product (area 2) general area using EDX

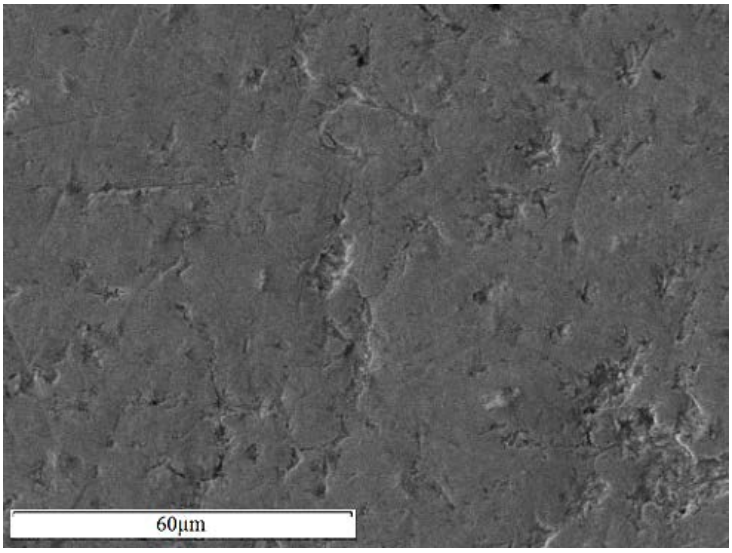

Element (at.%)	O	Cr	Co	W
Surface	43.1	5.6	15.3	36.0

Figure 112. SEM secondary electron micrograph of the surface of the HVOF WC/Cr/Co coating after the galvanic corrosion test coupled to the post-treated SermeTel coating together with an elemental compositional analysis using EDX

Oxidation was also observed on the HVOF WC/Cr/Co coating as expected (Figure 112). Similar changes in the morphology of the HVOF coating were observed to that coupled to the FSAl. Some evident pores were present on the surface of the HVOF WC/Cr/Co coating after corrosion. The serious localised corrosion, which may be caused by trapped alumina particles as shown previously (Figures 93, 102 and 106), was not observed on the surface of the coating after corrosion. Compared to the as-received coating (Figure 52 (a)), a decarburisation was present on the surface of the HVOF WC/Cr/Co coating as galvanic coupled with the post-treated SermeTel coating (Figure 112), which was also observed as galvanic coupled with the other sacrificial coatings (Figures 93, 98, 102 and 106).

4.2 Corrosion of HVOF WC/Cr/Co Coatings

As a EHC coating replacement, HVOF WC/Cr/Co also showed a poorer corrosion resistance than expected when coupled to the sacrificial coatings in the previous investigation. It was also found that Al_2O_3 particles used in the pre-treatment of the

steel, prior to the HVOF WC/Cr/Co coating processes, could be trapped at the interface between the substrate and HVOF WC/Cr/Co coating. This caused severe local corrosion of the HVOF WC/Cr/Co coatings during galvanic compatibility trials with the sacrificial coatings. In this section, the electrochemical corrosion behaviour of HVOF WC/Cr/Co coating is illustrated and the effect of Al_2O_3 particles on the corrosion of HVOF WC/Cr/Co is also investigated.

4.2.1 Corrosion of HVOF WC/Cr/Co Coatings in Solutions Containing Al_2O_3

In the immersion tests, two methods were used to introduce Al_2O_3particles to the HVOF WC/Cr/Co coatings. The first was to add Al_2O_3 particles into the immersion solutions and the other was to utilise Al_2O_3 grit blasted HVOF WC/Cr/Co coatings in immersion tests. The former test was to identify the effect of Al_2O_3 particles from the test environment setting on HVOF WC/Cr/Co coatings. The latter test was to trap Al_2O_3 particles on the HVOF WC/Cr/Co coating surface and observe their possible resultant interactions.

Figure 113 illustrates the surface of a HVOF WC/Cr/Co coating after 7 days of immersion in 3.5 wt.% NaCl solution. After the immersion test, there was no significant change observed in the morphology and composition of the general area of the surface of the coating (area 2 in Figure 113). However, similar local corrosion, which was observed on the surface of the HVOF WC/Cr/Co coating after galvanic tests, presented on the surface of the coating. EDX data show that probable underlying Al_2O_3 particles presented in the corrosion area, and the HVOF WC/Cr/Co coating had been removed.

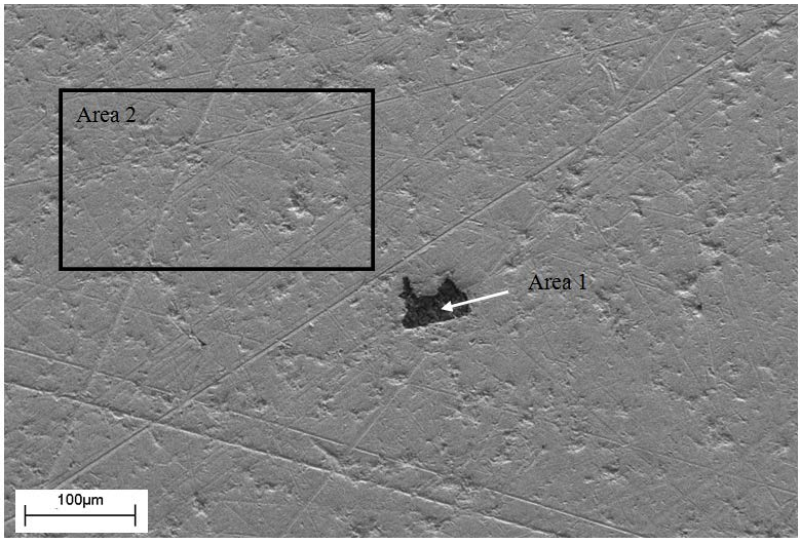

Element (at.%)	O	Al	C	Co	Cr	W
Area 1	48.7	51.3	-	-	-	-
Area 2	-	-	50.4	8.4	3.8	37.4

Figure 113. SEM secondary electron micrograph and elemental compositional analysis of the surface of a HVOF WC/Cr/Co coating after 7 days of immersion in 3.5 wt.% NaCl solution

For investigating the effects of Al_2O_3 particles on the corrosion of HVOF WC/Cr/Co coatings, they were added to a 3.5 wt.% NaCl solution. After 7 days of immersion in 3.5 wt.% NaCl solution with 20 wt. % Al_2O_3 particles, the surface of the HVOF WC/Cr/Co coating was as shown in Figure 114. Due to the low solubility of Al_2O_3in NaCl solution, the immersion solution showed turbidity and most Al_2O_3 particles were observed to precipitate at the bottom of the beaker. After immersion, some pitted areas were evident on the surface of the HVOF WC/Cr/Co coating. From compositional analysis of the pitted areas, a high percentage of Cr was evident while Co and W were not present in the pitted areas. After 7 days of immersion in the solution with a lower percentage of Al_2O_3 particles, as shown in Figure 115, similar areas of pitting were also observed. Both Co and W were absent from the pitted areas.

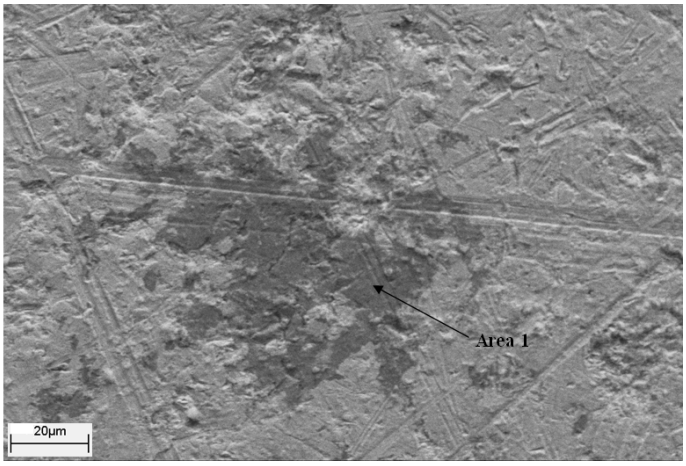

Element (at.%)	C	O	Cr
Area 1	29.8	12.3	57.9

Figure 114. SEM secondary electron micrograph and elemental compositional analysis of the surface of a HVOF WC/Cr/Co coating after 7 days of immersion in 3.5 wt.% NaCl solution with 20 wt. % Al_2O_3 particles

A steric dispersant (Dispex A40: solution of an ammonium salt of an acrylic polymer) was added to the solution containing Al_2O_3 particles to avoid aggregation. Particles were observed to be well dispersed in the solution during immersion tests. From Figures 116 and 117, it was found that the dispersant did not have any significant effects on the corrosion of the HVOF WC/Cr/Co coatings. Some pitted areas were also observed with an absence of Co and W and a high percentage of Cr (figure 116). Severe local corrosion of the HVOF WC/Cr/Co coating also occurred during immersion. In all the local corroded area, underlying Al_2O_3 particles trapped at the interface between the substrate and HVOF WC/Cr/Co coatings were thought be present (figure 117).

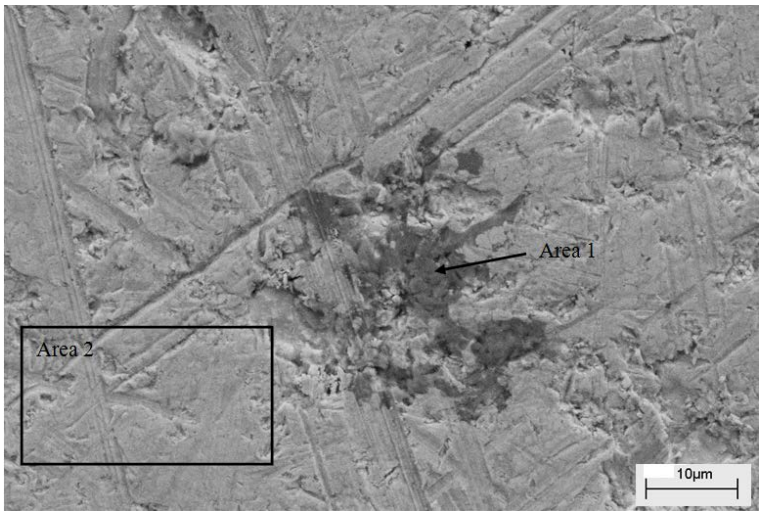

Element (at.%)	C	Cr	Co	W
Area 1	-	100.0	-	-
Area 2	19.1	8.3	19.7	52.9

Figure 115. SEM secondary electron micrograph and elemental compositional analysis of the surface of a HVOF WC/Cr/Co coating after 7 days of immersion in 3.5 wt.% NaCl solution with 1wt.% Al_2O_3 particles

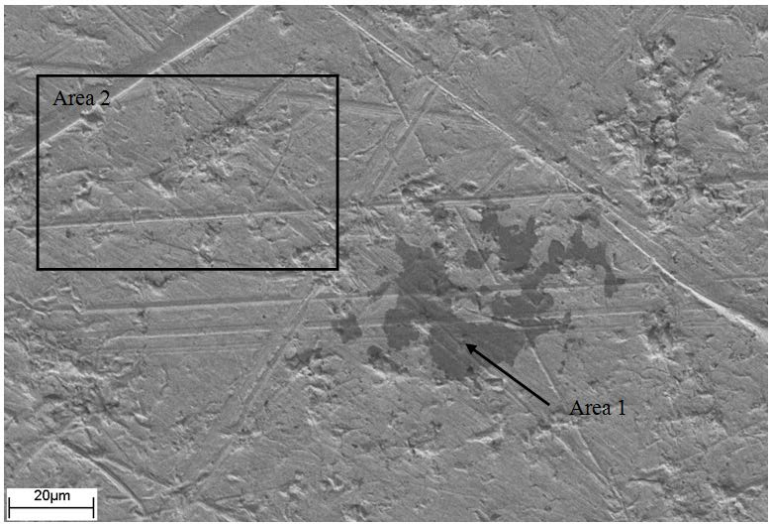

Element (at.%)	C	O	W	Cr	Co
Area 1	42.9	10.4	-	46.7	-
Area 2	47.5	-	33.9	5.4	13.2

Figure 116. SEM secondary electron micrograph and elemental compositional analysis of the surface of a HVOF WC/Cr/Co coating after 7 days of immersion in 3.5 wt.% NaCl solution with 20 wt.% Al_2O_3 particles and 1.5 wt.% steric dispersant (Dispex A40)

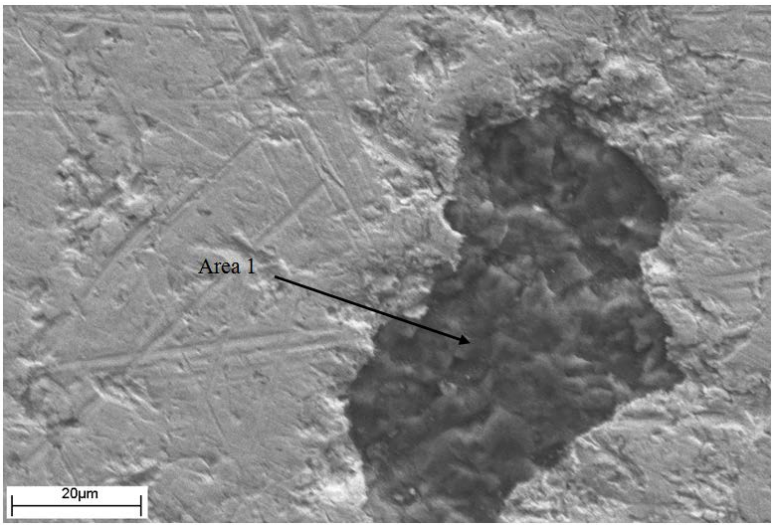

Element (at.%)	Al	O
Area 1	61.1	38.9

Figure 117. SEM secondary electron micrograph and elemental compositional analysis of the local corrosion on the surface of a HVOF WC/Cr/Co coating after 7 days of immersion in 3.5 wt.% NaCl solution with 20 wt.% Al_2O_3 particles and 1.5 wt.% steric dispersant (Dispex A40)

4.2.2 Corrosion of Al_2O_3 Grit Blasted HVOF WC/Cr/Co Coatings

Al_2O_3 particles were also introduced onto the surface of HVOF WC/Cr/Co coating by using such particles in a grit blasting treatment. Figure 118 shows the surface of a HVOF WC/Cr/Co coating after a light grit blasting. It can be seen that there was no significant change to the morphology of the surface of the coating. However, shallow depressions and some trapped particles identified as Al_2O_3 through EDX measurement were observed on the surface after light grit blasting (Figure 118).

After 7 days of immersion in 3.5 wt. % NaCl solution, the Al_2O_3 grit blasted HVOF WC/Cr/Co coating also presented local pitting corrosion as observed previously with the immersion of HVOF WC/Cr/Co coatings in solutions containing Al_2O_3 particles. EDX data showed that in the local pitting corrosion area, trapped Al_2O_3 particles were detected (Figure 119). Moreover, a high percentage of Cr and low levels of Co and W were evident. Many similar local pitting corrosion areas (Figure 120) were observed

across the surface of the Al_2O_3 grit blasted HVOF WC/Cr/Co coatings after immersion. All of these local pitting corrosion areas presented similar EDX results to those from Figure 119.

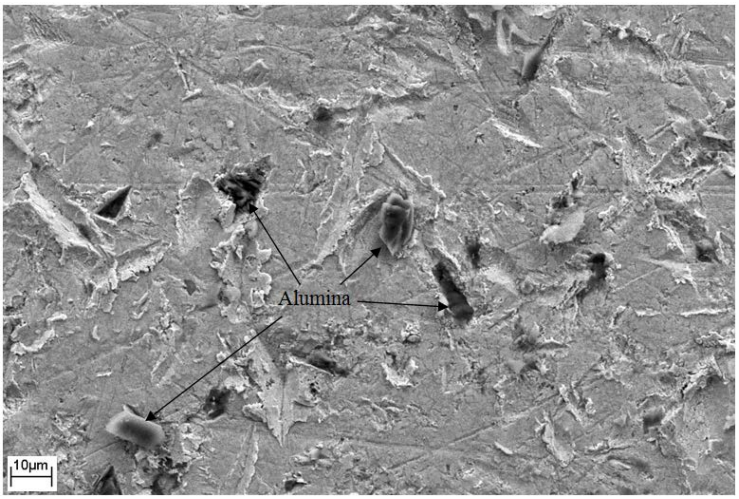

Element (at.%)	Al	O
Alumina	42.3	57.7

Figure 118. SEM secondary electron micrograph of the surface of an Al_2O_3 grit blasted HVOF WC/Cr/Co coating

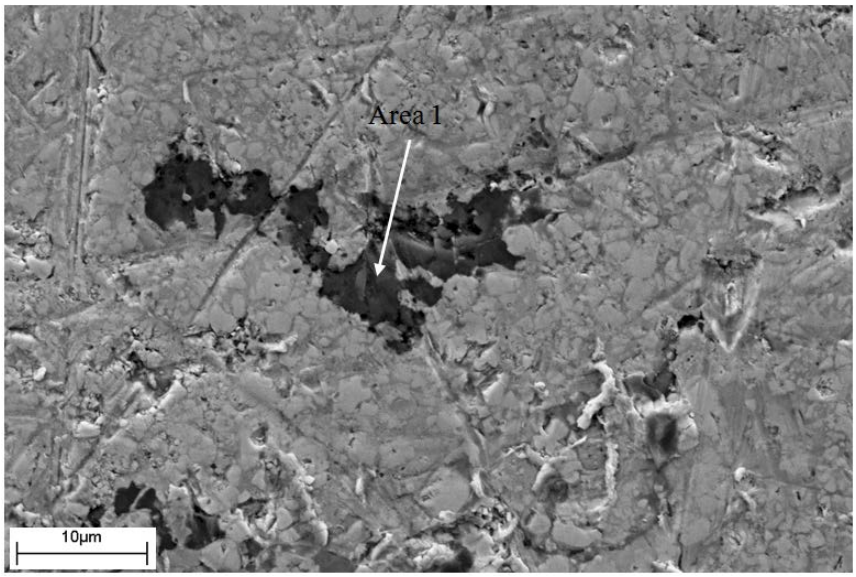

Element (at.%)	Al	O	W	Cr	Co
Area 1	15.8	24.0	1.0	52.2	7.0

Figure 119. SEM secondary electron micrograph and elemental compositional analysis of local corrosion on the surface of the lightly grit blasted HVOF WC/Cr/Co coating after 7 days of immersion in 3.5 wt.% NaCl solution

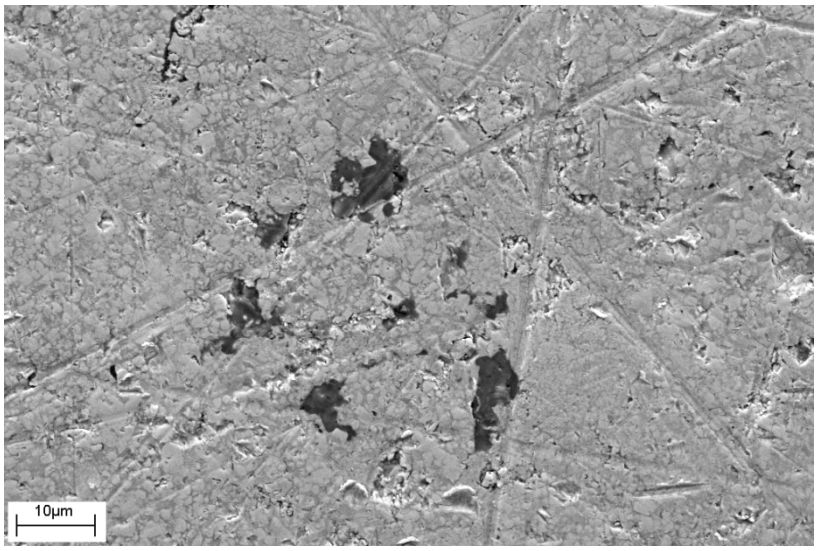

Figure 120. SEM secondary electron micrograph of the surface of the lightly grit blasted HVOF WC/Cr/Co coatings after 7 days of immersion in 3.5 wt.% NaCl solution showing general area of pitting corrosion

4.2.3 Anodic Polarisation Behaviour of HVOF WC/Cr/Co Coatings

Anodic polarisation tests were used to investigate the corrosion of HVOF WC/Cr/Co coatings. From the anodic polarisation curve of a HVOF WC/Cr/Co coating in 3.5 wt.% NaCl (Figure 121), the first breakdown point (P1) was observed at about 250 mV, where the current exhibited a marked increase with increasing anodic potential. It is suggested that corrosion may occur initially in the HVOF WC/Cr/Co coating. The second breakdown point (P2) was observed at about 700 mV. After that the current increased significantly. This may result from the initial loss of WC particles from the coating due to the corrosion of the metallic binder. Two more breakdown points (P3 and P4) at about 850 and 1100 mV may imply further corrosion of the HVOF WC/Cr/Co coating. The mechanisms responsible for P1 ~ P4 were investigated and confirmed by the following morphological observation and further electrochemical analysis.

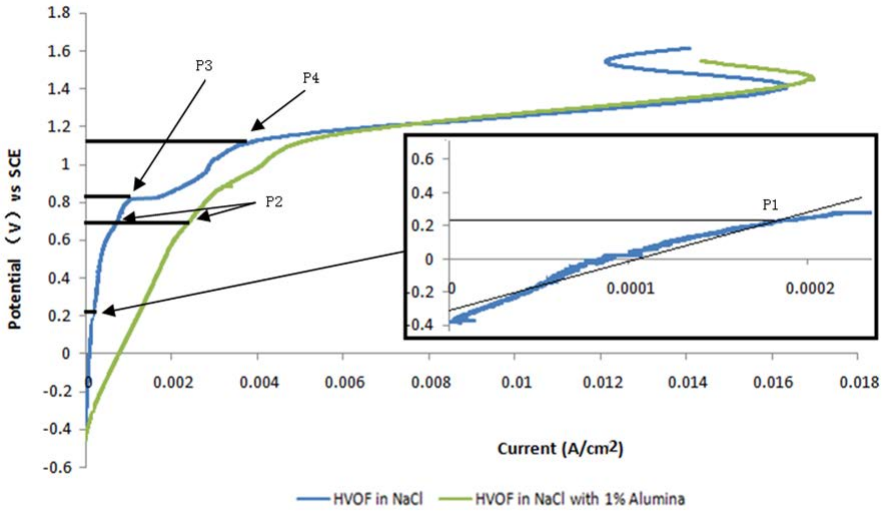

Figure 121. The anodic polarisation curves for the HVOF WC/Cr/Co coatings in a 3.5 wt.% NaCl solution with and without 1 wt.% Al_2O_3 particles

Moreover, the effect of Al_2O_3 particles was also investigated by adding the particles to the electrolyte used for the anodic polarisation test. Due to their low solubility, most particles precipitated at the bottom of the electrolyte and a few Al_2O_3 particles were dispersed in the electrolyte, which produced a cloudy solution. From the anodic polarisation curve of a HVOF WC/Cr/Co coating in the electrolyte containing 1 wt.% Al_2O_3 particles, it was observed that the corrosion of the metallic binder occurred from -400 mV, much more negative than that from in the electrolyte without Al_2O_3 particles. A much higher corrosion current also presented during the first stage of corrosion of the metallic binder in the electrolyte. The second stage of corrosion, the detaching of the WC particles from the HVOF WC/Cr/Co coating, occurred at a similar potential for both solutions.

After the anodic polarisation test, both the cross section and surface of the HVOF WC/Cr/Co coatings were observed by SEM to identify changes in the morphology and composition. From Figure 122, it was found that many defects were present on the surface of the coatings. Dissolution through corrosion was observed on the surface of the coatings after the anodic polarisation in 3.5 wt.% NaCl solution. Underlying WC particles were exposed after the corrosion of the upper layers of the HVOF WC/Cr/Co coating. Some cracks can also be seen around WC particles, which implies that the

corrosion initially occurred at the WC/metallic binder interfaces.

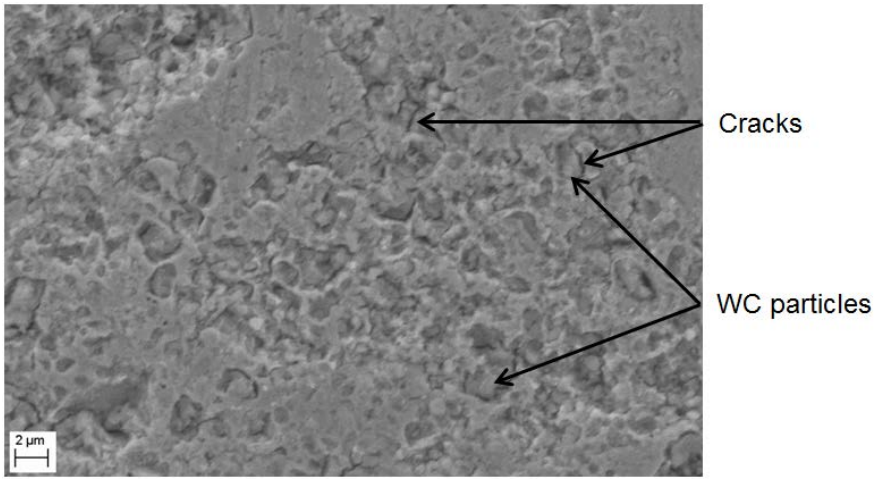

Figure 122. SEM secondary electron micrograph of the surface of the HVOF WC/Cr/Co coating after anodic polarisation in 3.5 wt.% NaCl solution

For the HVOF WC/Cr/Co coating after anodic polarisation test in the solution containing Al_2O_3 particles, severe corrosion was observed. From the circled area of Figure 123, pores left by the loss of the WC particles were observed at the surface of the HVOF WC/Cr/Co coating. More severe corrosion of the HVOF WC/Cr/Co coatings can be observed in Figure 124 due to the higher corrosion current in the anodic polarisation in the solution with Al_2O_3 particles. Removal of the metallic binder and the occurrence of the remaining WC particles were evident on the surface of the coating. Only a small amount of Cr was detected in the remaining metallic binder.

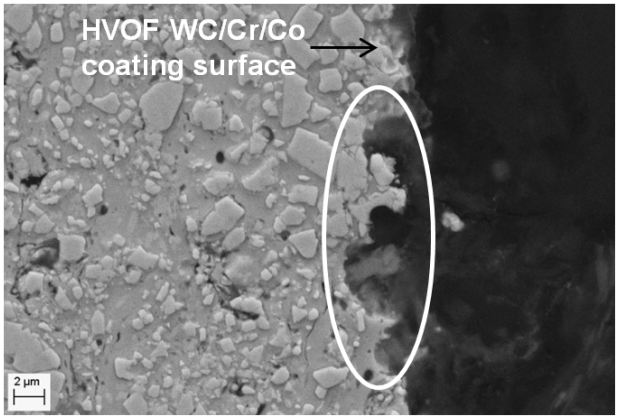

Figure 123. SEM secondary electron micrograph of the cross section of the HVOF WC/Cr/Co coating after anodic polarisation in 3.5 wt.% NaCl containing Al_2O_3

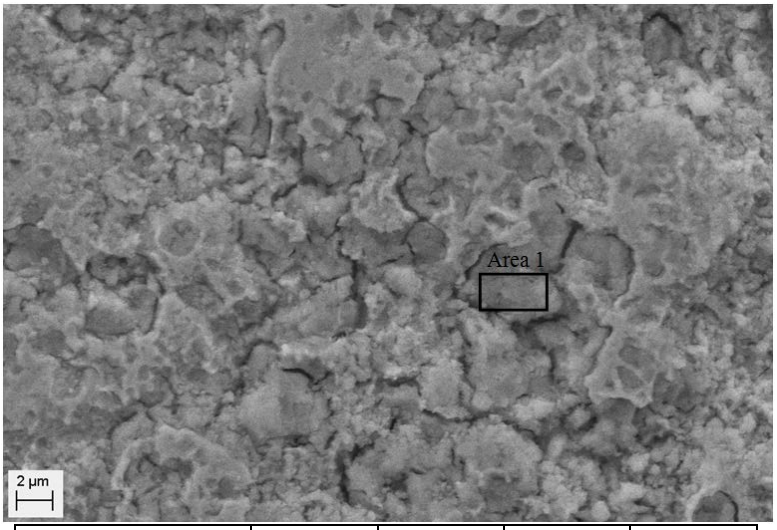

Element (at.%)	C	O	Cr	W
Area 1	21.5	33.7	1.6	43.2

Figure 124. SEM secondary electron micrograph of the severe corrosion on the surface of the HVOF WC/Cr/Co coating after anodic polarisation in 3.5 wt.% NaCl containing Al_2O_3 particles

4.2.4 Potentiostatic Anodic Corrosion of HVOF WC/Cr/Co Coatings

From previous investigations, it was thought that the corrosion of HVOF WC/Cr/Co coating may occur initially in the metallic binder and be followed by the loss of WC particles. Therefore, potentiostatic tests of the HVOF WC/Cr/Co coatings at the potential of the two breakdown points from the anodic polarisation, namely 250 and 700 mV, were carried out to confirm the corrosion mechanisms of the coating further. From the potentiostatic test at 250 mV (Figure 125), the corrosion current remained stable at about 30 $\mu A/cm^2$ from 100 s to 5000 s after this it increased slightly. From the potentiostatic test at 700 mV, a higher stable corrosion current was evident for the first 1000 s, which may result from the corrosion of the metallic binder in the coating. The metallic binder corroded at a higher corrosion rate at the potential of 700 mV and the loss of the WC particles probably occurred after 1000 s, which resulted in a sharp increase in the corrosion current to about 400 $\mu A/cm^2$ and then decreased gradually to a stable corrosion current at approximately 300 $\mu A/cm^2$.

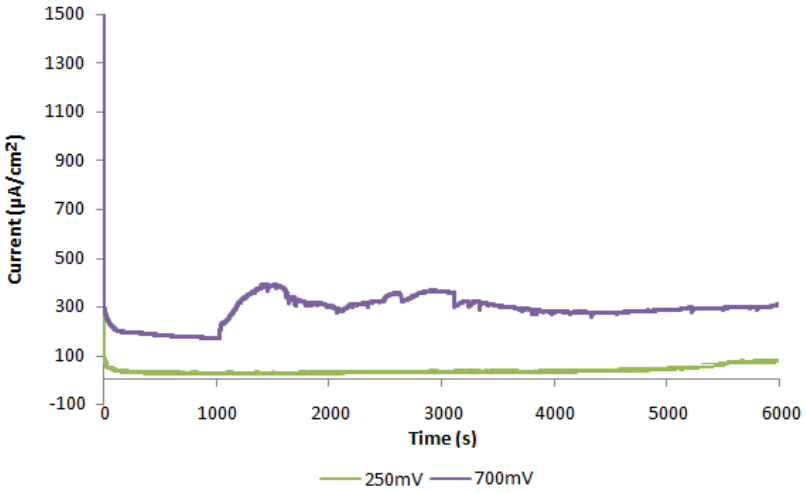

Figure 125. Current versus time plots for potentiostatic tests of the HVOF WC/Cr/Co coatings performed in 3.5 wt.% NaCl solution at 250 and 700 mV.

The potential of 250 mV was suggested as the start of the corrosion of the metallic binder in the HVOF WC/Cr/Co coating from the anodic polarisation tests. After the potentiostatic test at 250 mV, cracks and pores were observed around the WC phase on the surface of the HVOF WC/Cr/Co coating (Figure 126).

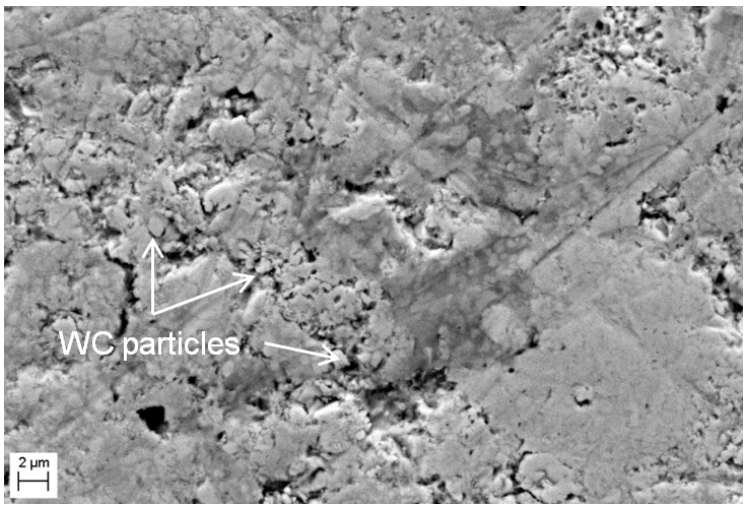

Figure 126. SEM secondary electron micrograph of the surface of the HVOF WC/Cr/Co coating after potentiostatic test at 250 mV in 3.5 wt.% NaCl

At some of the more severe corrosion areas, a porous underlying coating was observed due to the loss of the top layer of the HVOF WC/Cr/Co coating during the potentiostatic test (Figure 127). At 250 mV, the corrosion was in the form of localised etching around the WC/metallic binder interfaces in discrete regions of the surface of

the coating. Due to the low corrosion current, a lot of areas of the coating were still intact after the potentiostatic test.

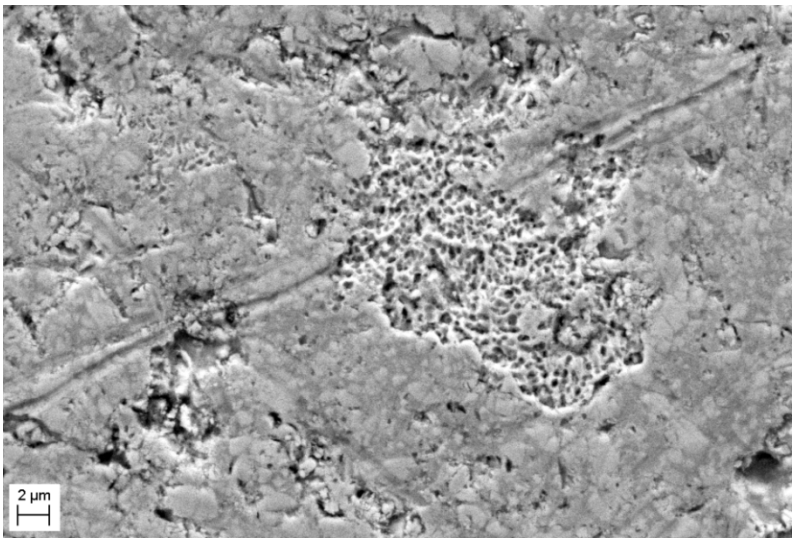

Figure 127. SEM secondary electron micrograph of the surface of the HVOF WC/Cr/Co coating after the potentiostatic test at 250 mV in 3.5 wt.% NaCl solution

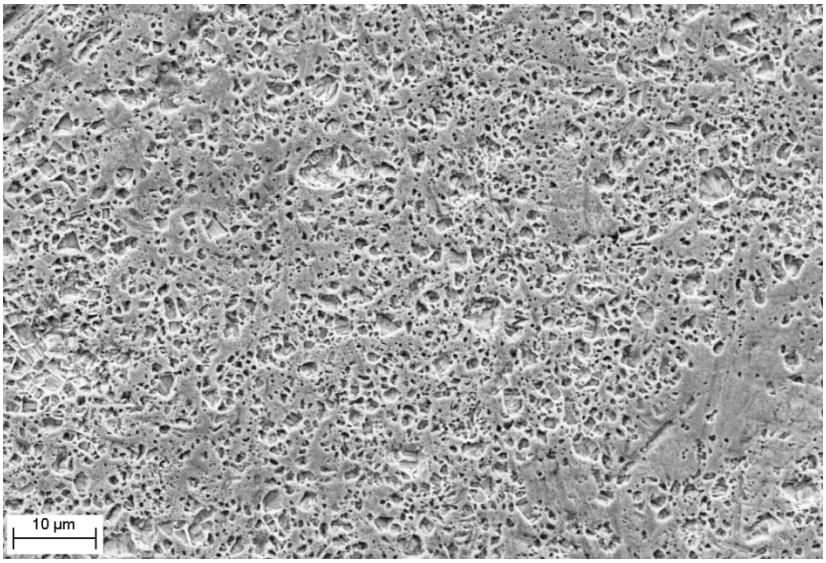

Figure 128. SEM secondary electron micrograph of the surface of the HVOF WC/Cr/Co coating after the potentiostatic test at 700 mV in 3.5 wt.% NaCl solution

In contrast, at the higher potential of 700 mV, the metallic binder had a high corrosion rate and the surface of the coating exhibited a uniformly corroded surface, in which the WC particles were clearly removed due to loss of the surrounding binder (Figure 128). From the cross section of the HVOF WC/Cr/Co coating after the test at 700 mV, a rough surface and several pores left by the loss of WC particles can be clearly seen (Figure

129). Moreover, compared to the underlying coating, the top area of the coating also exhibited significantly more porosity.

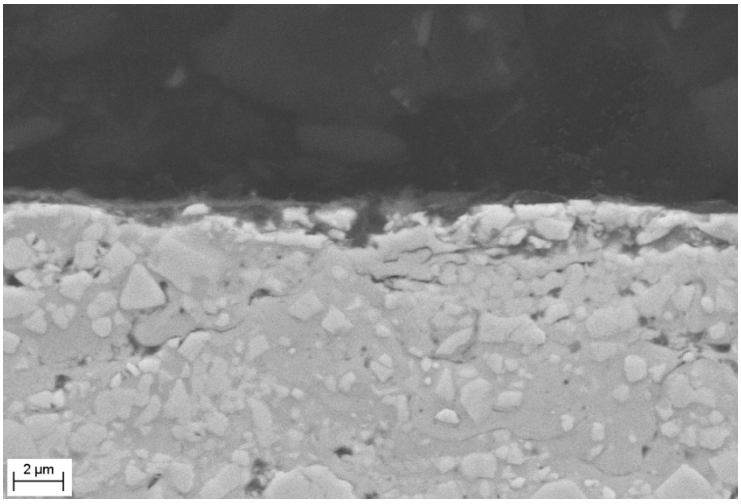

Figure 129. SEM secondary electron micrograph of the cross section of the HVOF WC/Cr/Co coating after the potentiostatic test at 700 mV in 3.5 wt.% NaCl

4.2.5 Galvanic Corrosion of HVOF WC/Cr/Co Coating Coupled to EC Coating

In Section 4.1.6.2, the galvanic corrosion between EC and HVOF WC/Cr/Co coatings was investigated. As Figure 93 shows, after galvanic corrosion, some severe local corroded areas were observed on the surface of the HVOF WC/Cr/Co coating due to underlying Al_2O_3 particles as discussed previously. In this chapter, the HVOF WC/Cr/Co coating was further investigated in terms of cross-section after galvanic corrosion with the EC coating.

From Figure 130, after galvanic corrosion, the HVOF WC/Cr/Co coating around the Al_2O_3 particles remaining at the steel/coating interface, presented a very porous microstructure. Loss of WC particles and pores were observed, which agreed with previous observation of some of the local severe corrosion areas caused by Al_2O_3 particles on the surface of the HVOF WC/Cr/Co coating. Moreover, from Figure 131, it was found that after the galvanic corrosion, the thickness of the HVOF WC/Cr/Co coating was reduced significantly. The thickness of the HVOF WC/Cr/Co coating was

about 170 μm as deposited. After the galvanic corrosion with the EC coating over a period of 15 days, the maximum thickness of the HVOF WC/Cr/Co coating was less than 50 μm and the minimum thickness was only about 7 μm. The significantly reduced thickness of the HVOF WC/Cr/Co coating indicated that severe corrosion had occurred over the surface of the coating. From the cross-section of the HVOF WC/Cr/Co coating, the general surface of the galvanic corroded coating was uniform (Figure 131).

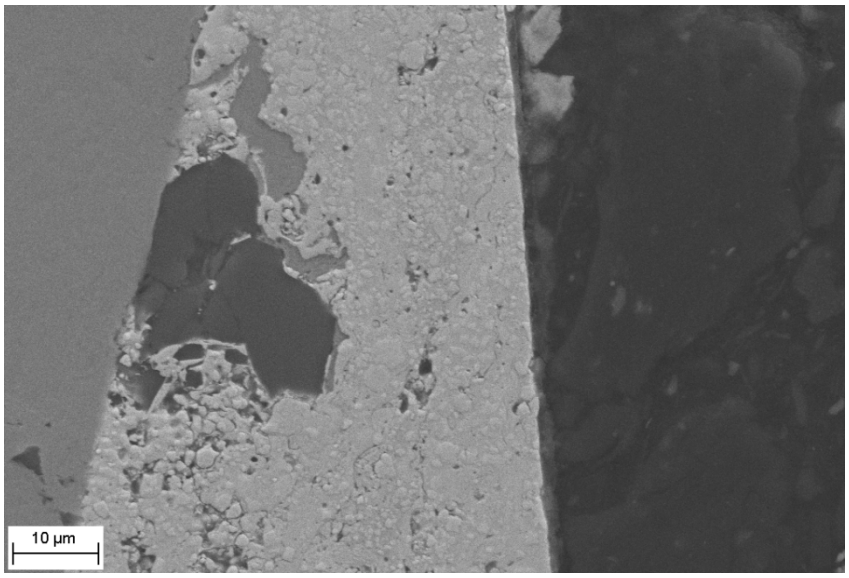

Figure 130. SEM secondary electron micrograph of the cross-section of the HVOF WC/Cr/Co coating after galvanic corrosion with the EC coating

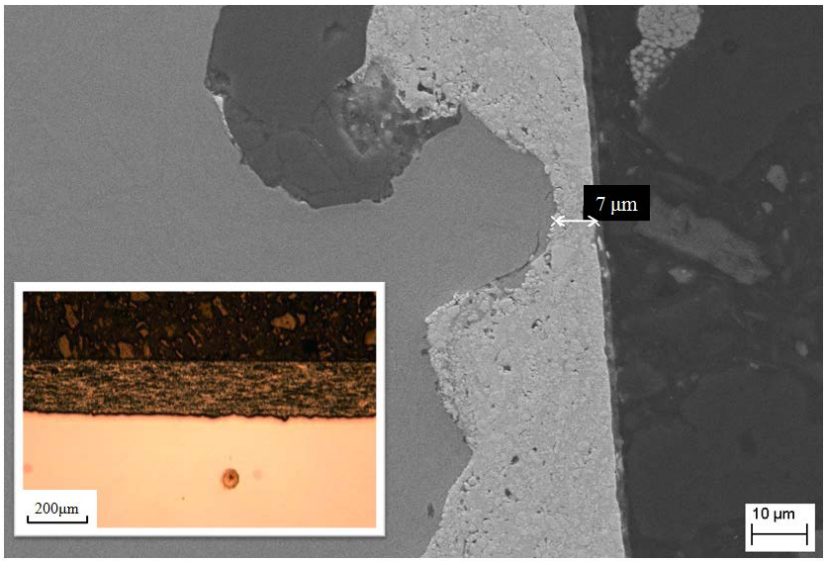

Figure 131. SEM secondary electron micrograph of the cross section of the HVOF WC/Cr/Co coating after galvanic corrosion with the EC coating and an optical secondary electron micrograph of the cross section of the as-received HVOF WC/Cr/Co coating

4.3 Investigation into the Deposition of Al_2O_3 Coatings on HVOF WC/Cr/Co Coatings

It was suggested by Airbus (from past trials) to apply Al_2O_3 layers to HVOF WC/Cr/Co coatings to improve their galvanic compatibility with sacrificial coatings. Two Al_2O_3 deposition methods, electrolytic and sol-gel, which were thought to promote less damage on the substrates, were investigated. Both treatment methods were initially examined on steel substrates to identify their feasibility and were then used to apply Al_2O_3 coatings on HVOF WC/Cr/Co coatings. However, investigations mentioned in Section 4.2 imply that Al_2O_3 may indeed accelerate the corrosion of HVOF WC/Cr/Co coatings, so accordingly only preliminary investigations of the deposition of Al_2O_3 were carried out and are reported.

4.3.1 Electrolytic Deposition of Al_2O_3 Coating

Electrolytic deposition of an Al_2O_3 coating can be divided into two parts, the formation of deposits containing hydrated Al_2O_3 and $Al(OH)_3$, named semi-alumina, on substrates by electrochemical processes and the formation of Al_2O_3 layers by dehydration of the semi-alumina deposits. Investigations of electrolytic formation of the semi-alumina from $Al_2(SO_4)_3$ and $Al(NO_3)_3$ electrolytes on mild steel were undertaken. The electrochemical analyses of all the deposition processes are presented to identify reactions involved during the depositions. The effects of the pre-treatments of substrates on Al_2O_3 coatings were also illustrated, as well as the morphology of deposited Al_2O_3 coatings.

4.3.1.1 Electrochemical Study of the Deposition of Al_2O_3 on Mild Steel

In order to improve the adhesion of electrolytically deposited semi-alumina barriers, a

functional conversion coating pre-treatment has been suggested for application on steel substrates by chemical oxidation in a H_2SO_4 solution with thiosulphates and propargyl alcohol. Morphology of the surfaces of the steel substrates with and without the conversion coating treatment are shown in Figure 132. The conversion coating was evidently porous, which may contribute to improve the adhesion of the subsequent semi-alumina layers and facilitate the interfacial reactions.

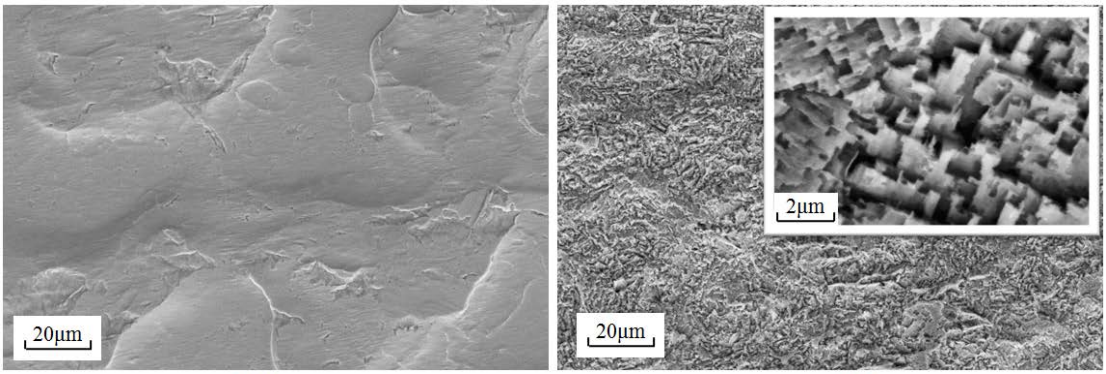

Figure 132. SEM secondary electron micrographs of the surface of (a) steel substrate as received and (b) steel substrate with conversion coating pre-treatment

Cathodic polarization curves for the formation of semi-alumina on 'conversion' pre-treated steels from aqueous solutions of $Al_2(SO_4)_3$, $Al_2(SO_4)_3/YCl_3$ and $Al(NO_3)_3$ are shown in Figure 133. In the case of deposition from the $Al_2(SO_4)_3$ based solution, the current density increased slowly with more negative potentials up to approximately -1.0 V and then increased significantly. The current density of deposition from the $Al_2(SO_4)_3/YCl_3$ solution up to -3.2 V increased slightly faster with more negative potential than that observed for the $Al_2(SO_4)_3$ solution. This may be caused by additional precipitation of $Y(OH)_3$. A plateau observed on the curve after -3.2 V implies that semi-alumina precipitation rate decreased due perhaps to the addition of Y^{3+}.

The cathodic polarisation for semi-alumina precipitation from $Al(NO_3)_3$ solution presented a higher current density up to -2.0 V and two plateaux at around -0.9 V and -2.0 V respectively. Following -2.0 V, a sharp increase in current density occurred with

more negative potentials, which may imply the precipitation of semi-alumina. The current density for deposition from the $Al(NO_3)_3$ based solution increased from a more negative potential than that observed for the $Al_2(SO_4)_3$ based solution.

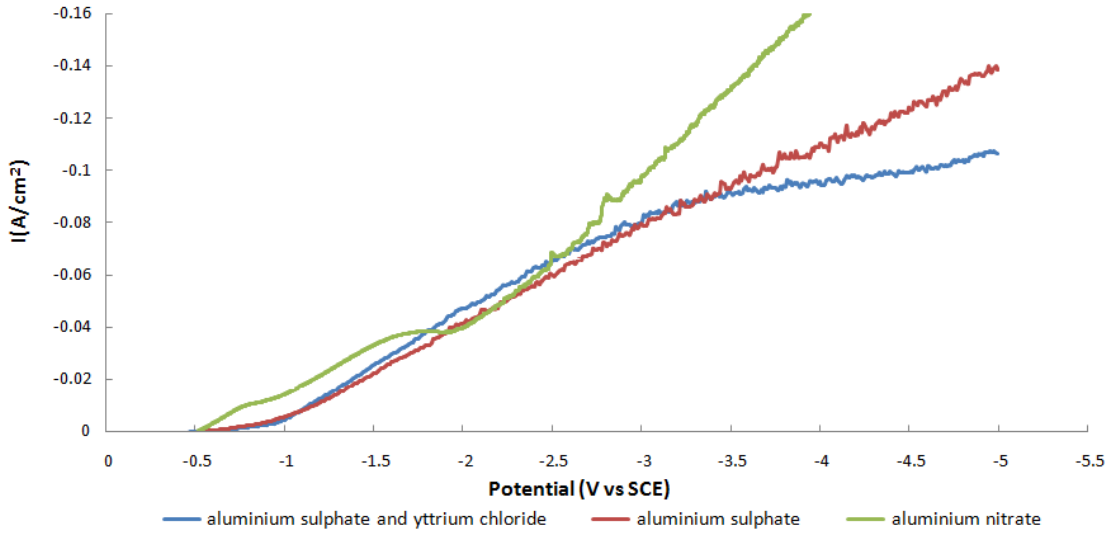

Figure 133.Cathodic polarisation curves for the deposition of semi-alumina on 'conversion' pre-treated steels from three electrolytes

4.3.1.1.1 Electrolytic Deposition of Semi-alumina from the $Al_2(SO_4)_3$ Based Solutions

Evolution of the electrode potentials of the steel substrates with deposition time with different process parameters are illustrated in Figures 134 to 137. In Figure 134, different treatments times for deposition of semi-alumina from $Al_2(SO_4)_3$ solution of 15 and 30 min, were investigated. The electrode potential decreased significantly with time for the first 100 s and then stablised at about -3.7 V. The longer treatment time did not show appreciably different effects on the electrode potential during deposition and presented a similar format. The as-deposited semi-alumina layer on the surface of the steel was grey and uniform.

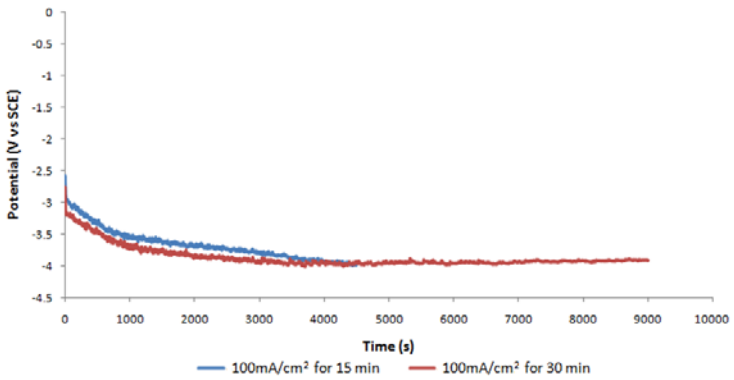

Figure 134. Electrode potential versus deposition time curves of galvanostatic deposition of semi-alumina on conversion pre-treated steel substrates at 100 mA/cm^2 for 15 and 30 min respectively from $Al_2(SO_4)_3$ solutions

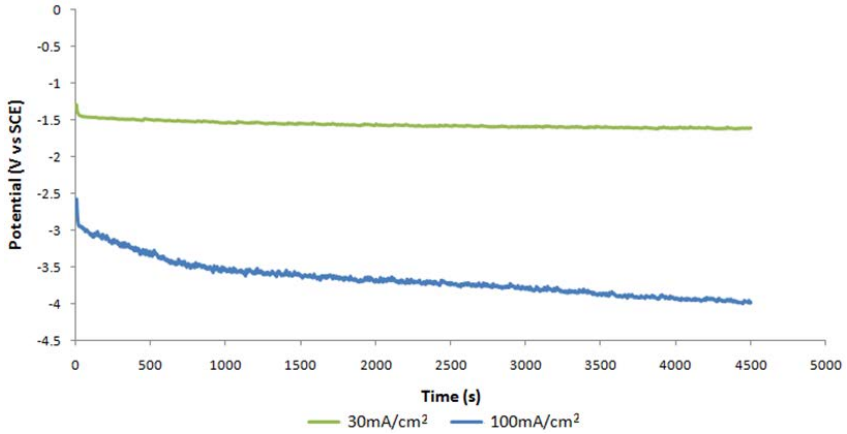

Figure 135. Electrode potential versus deposition time curves for galvanostatic deposition of semi-alumina from $Al_2(SO_4)_3$ solutions on conversion coated pre-treated steel substrates at 30and 100 mA/cm^2 for 15 min

The deposition of semi-alumina from $Al_2(SO_4)_3$ solution is shown in Figure 135. The electrode potential of deposition at 30 mA/cm^2 achieved stability as soon as the deposition began and maintained a value of approximately -1.5 V, which was much higher than that observed at 100 mA/cm^2. It was suggested that only H_2 evolution occurred when depositing at 30 mA/cm^2 and no evident precipitation of semi-alumina was observed. An addition of YCl_3 to the $Al_2(SO_4)_3$ solution caused an evident decrease in the electrode potential during deposition (Figure 136).

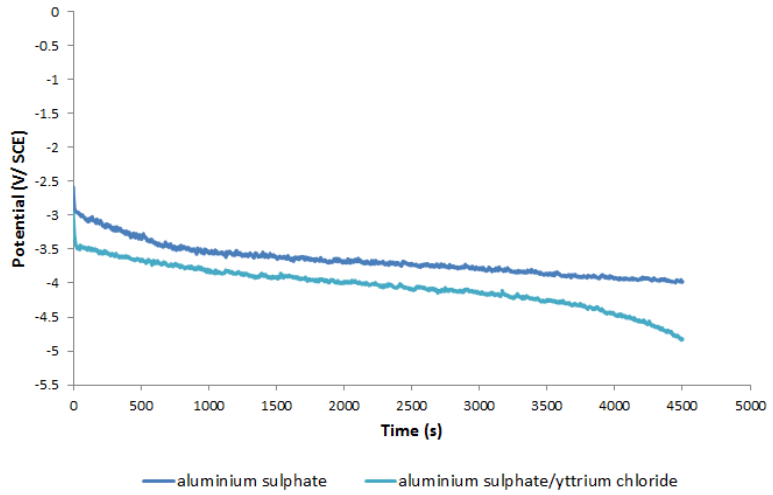

Figure 136. Electrode potential versus deposition time curves for galvanostatic deposition of semi-alumina from $Al_2(SO_4)_3$ and $Al_2(SO_4)_3/YCl_3$ solutions on conversion coated pre-treated steel substrates at100 mA/cm^2 for 15 min

The effect of stirring during the process was also investigated as Figure 137 shows. Stirring during the process did not present an evident effect on the electrode potential during deposition. However, the electrode potential was more stable than that observed without stirring.

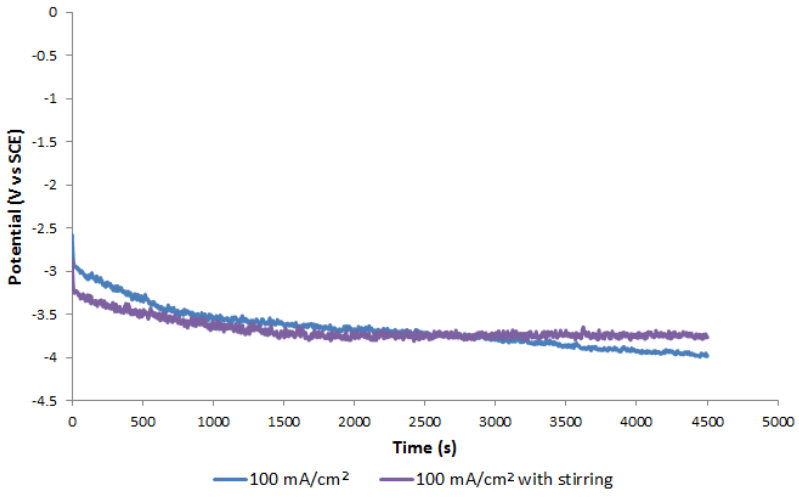

Figure 137. Electrode potential versus deposition time curves for galvanostatic deposition of semi-alumina from $Al_2(SO_4)_3$ solutions on conversion coated pre-treated steel substrates at 100 mA/cm^2 for 15 min with and without stirring

4.3.1.1.2 Electrolytic Deposition of Semi-alumina from $Al(NO_3)_3$ Based Solution

Three current densities at 30, 60 and 100 mA/cm^2 were applied for deposition of Al_2O_3 coatings from $Al(NO_3)_3$ based solution as shown in Figure 138. When applying a

current density of 30 mA/cm^2, the electrode potential presented a similar trend to that from the $Al_2(SO_4)_3$ solution. No evident deposition of semi-alumina was observed. For a current density of 60 mA/cm^2, a uniform Al_2O_3 coating was observed. On applying a current density of 100 mA/cm^2, the evolution of electrode potential was more stable and positive than that observed from the $Al_2(SO_4)_3$ solution. The high electrode potential may have resulted from reduction of NO_3^- and a high precipitation rate of semi-alumina.

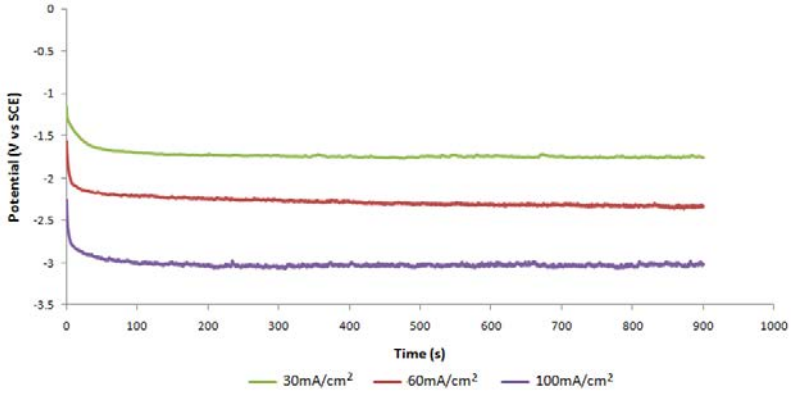

Figure 138. Electrode potential versus deposition time curves for galvanostatic deposition of semi-alumina from $Al(NO_3)_3$ solutions on conversion coated pre-treated steel substrates at 30, 60 and 100 mA/cm^2 for 15 min

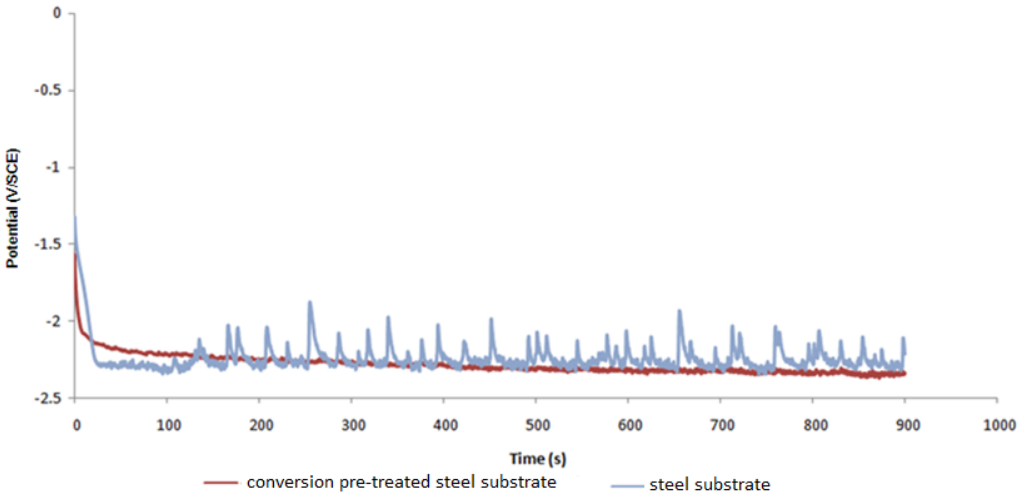

Figure 139. Electrode potential versus deposition time for galvanostatic deposition of semi-alumina from $Al(NO_3)_3$ solutions on steel substrates with and without conversion coating pre-treatment at 60 mA/cm^2 for 15 min

The effects of the conversion coatings were also investigated and are shown in Figure 139. The electrode potential during deposition on steel without a conversion coating presented a significant fluctuation with time. During the process, it was observed that

semi-alumina precipitated and detached, and this repeated with time, which resulted in the fluctuations observed.

4.3.1.2 Morphology and Composition of Al_2O_3 Deposits on Steels

All the semi-alumina layers were dehydrated in air at 20 ℃. All the dehydrated semi-alumina layers displayed an atomic ratio of Al and O of approximately 2:3 by compositional analysis, which was thought to imply the formation of Al_2O_3 coating. The Al_2O_3 coating deposited at 100 mA/cm^2 for both 15 and 30 minutes from an $Al_2(SO_4)_3$ bath are shown in Figure 140. An uneven coating with poor adhesion was observed. Some powdery Al_2O_3 was also present on the surface. From Figure 140 (a), it can be seen that the conversion coating appears to be not completely covered by the Al_2O_3 coating.

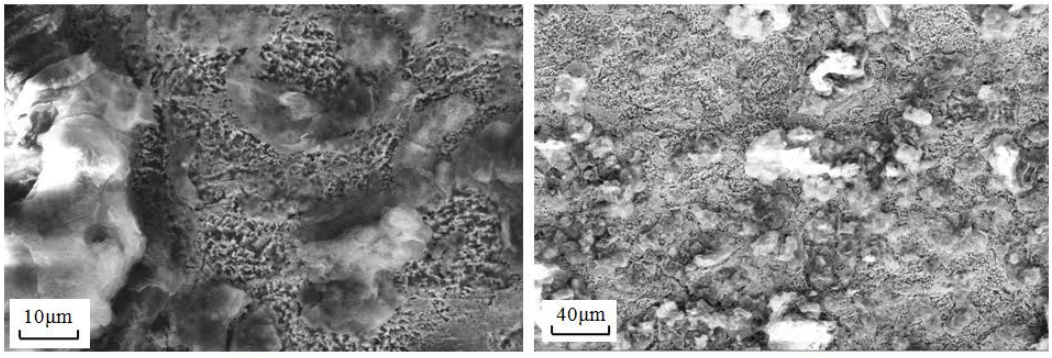

Figure 140. SEM secondary electron micrograph of the surface of the Al_2O_3 deposited from $Al_2(SO_4)_3$ solution at 100 mA/cm^2 for (a) 15 min and (b) 30 min

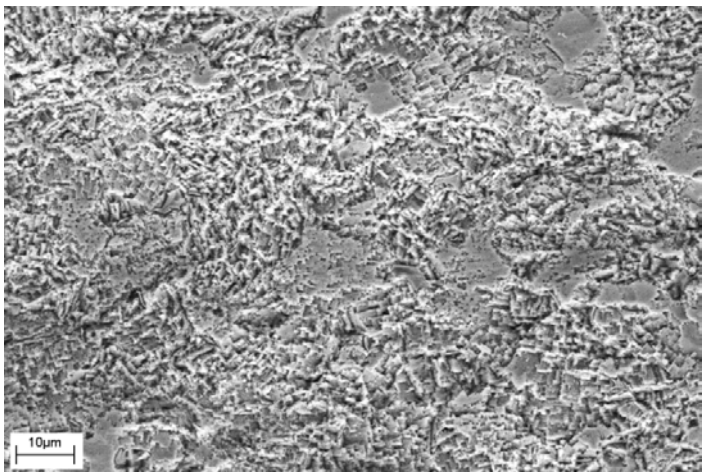

Figure 141. SEM secondary electron micrograph of the surface of the Al_2O_3 deposited from $Al_2(SO_4)_3$ solution at 30 mA/cm^2 for 15 min

From the evolution of the electrode potential, it is suggested that during deposition at low current density, no evident deposition of semi-alumina occurred. From Figure 141, no apparent Al_2O_3 coating can be observed on the steel substrate after deposition at 30 mA/cm^2. This agrees with the previous suggestion that only H_2 evolution occurred.

The addition of YCl_3 to the $Al_2(SO_4)_3$ solution was suggested to decrease the precipitation rate of semi-alumina on the surface. A more uniform Al_2O_3 coating was observed to deposit from the $Al_2(SO_4)_3$ bath with YCl_3 as Figure 142 shows. Stirring during the process resulted in a more stable electrode potential, but it did not appear to improve the quality of the coating significantly as shown by Figure 143 when compared to Figure 140 (a).

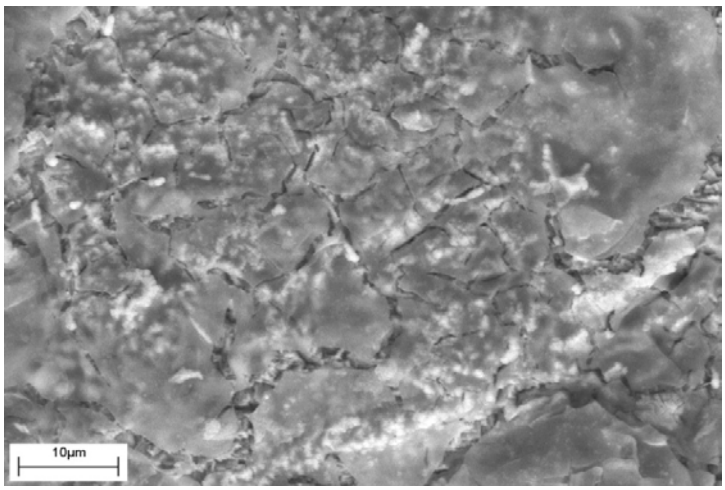

Figure 142. SEM secondary electron micrograph of the surface of the Al_2O_3 deposited from $Al_2(SO_4)_3/YCl_3$ solution at 100 mA/cm^2 for 15 min

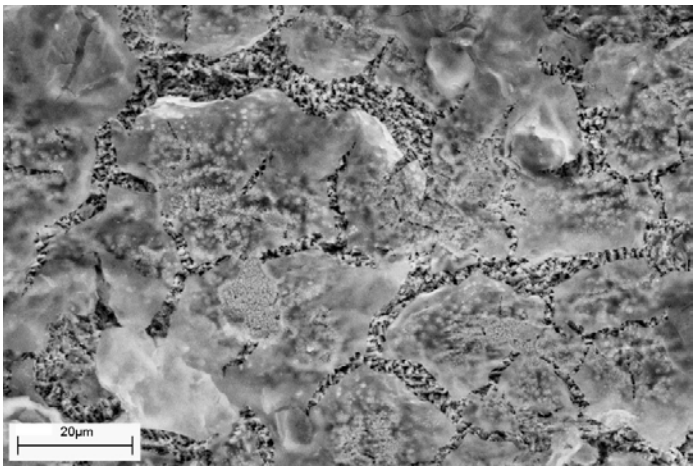

Figure 143. SEM secondary electron micrograph of the surface of the Al_2O_3 deposited from $Al_2(SO_4)_3$ solution at 100 mA/cm^2 for 15 min with stirring

Al_2O_3 deposited from $Al(NO_3)_3$ solution presented a much better morphology than that from $Al_2(SO_4)_3$ solution. As shown in Figure 144, the Al_2O_3 coating produced from $Al(NO_3)_3$ solution showed uniform integrity and good adhesion to the surface after abrasion using a lab wipe with moderate pressure. Heat-treatment at 150℃ for 2 h was suggested to convert $Al(OH)_3$ of semi-alumina layer to Al_2O_3. Compared to Al_2O_3 coatings dried at 20 ℃, the heat-treated Al_2O_3 coating presented denser and had good adhesion to the steel surface (Figure 145).

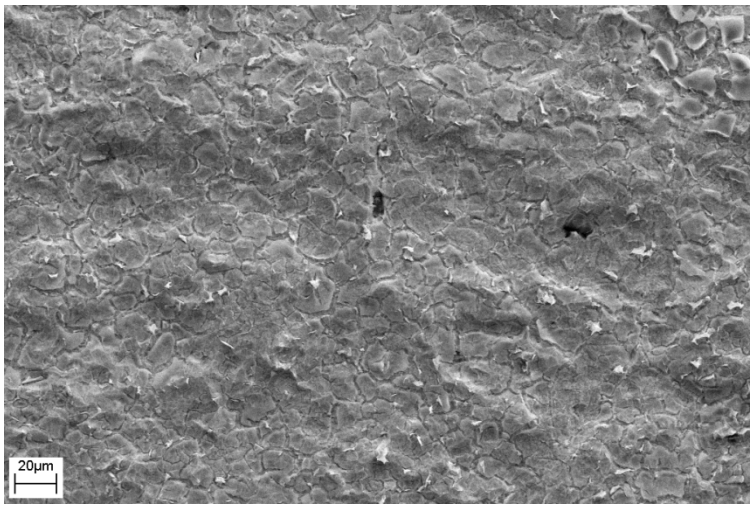

Figure 144. SEM secondary electron micrograph of the surface of the Al_2O_3 deposited from $Al(NO_3)_3$ solution at 60 mA/cm^2 for 15 min

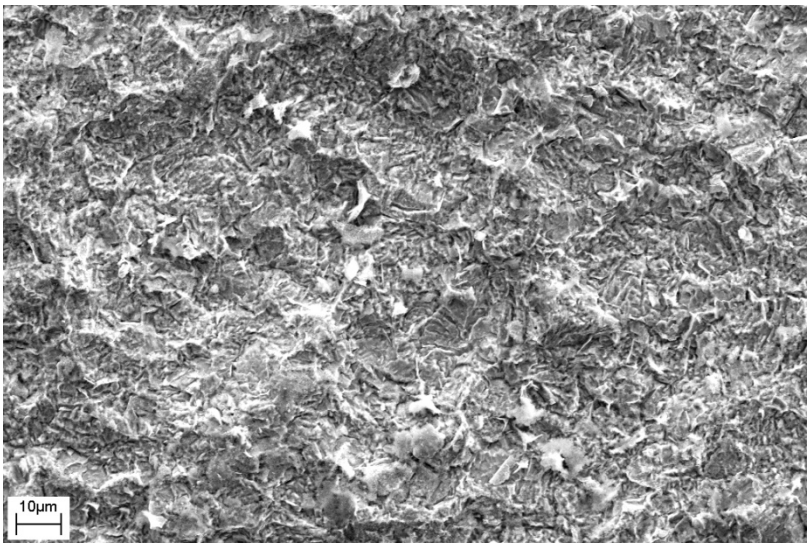

Figure 145. SEM secondary electron micrograph of the surface of the Al_2O_3 deposited from $Al(NO_3)_3$ solution at 60 mA/cm^2 for 15 min and heat-treated at 150 ℃ for 2 h

4.3.1.3 Electrolytic Deposition of Al_2O_3 on HVOF WC/Cr/Co Coated Steels

Both the conversion treatment and grit blasting were applied to the HVOF WC/Cr/Co coating. The conversion treatment showed no significant effect on the HVOF WC/Cr/Co coating. No difference was detected in morphology and composition after the conversion treatment. The electrolytic deposition process for semi-alumina was applied to the as-received, the conversion treated and the grit blasted HVOF WC/Cr/Co coatings. From Figure 146, the galvanostatic formation curves for the precipitation of semi-alumina on the three HVOF WC/Cr/Co coatings with different pre-treatments presented stable potentials with time. However, only hydrogen evolution was observed at HVOF WC/Cr/Co coatings and no precipitate of semi-alumina formed. After the electrolytic deposition, no Al_2O_3 coating was detected on any of the three HVOF WC/Cr/Co coatings.

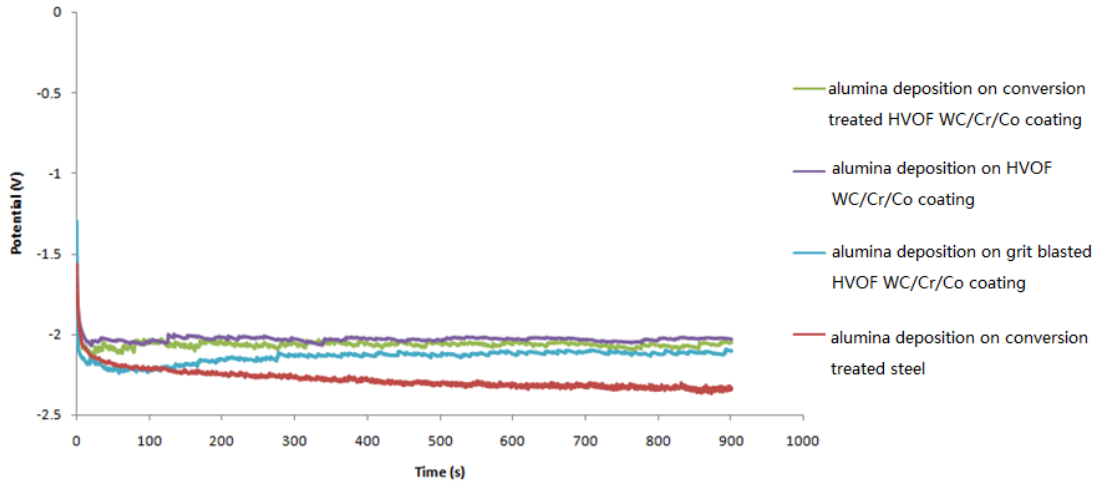

Figure 146. Electrode potential vs. time of galvanostatic deposition of semi-alumina from $Al(NO_3)_3$ solutions onto the conversion treated steel and HVOF WC/Cr/Co surfaces with different pre-treatments at 60 mA/cm^2

4.3.2 Sol-gel Deposition of Al_2O_3 Coatings

The feasibility of forming Al_2O_3 coatings by sol-gel techniques was also investigated and is presented in this section. Sol-gel deposition of Al_2O_3 coatings was examined on

steel substrates initially and then further investigated on HVOF WC/Cr/Co coatings.

4.3.2.1 Sol-gel Deposition of Al_2O_3 on Steels

The effects of pre-treatments on the Al_2O_3 coating were also investigated. Three surface conditions were prepared by phosphating and grit blasting separately and together. From Figure 147, it can be seen that the phosphating treatment provided a coating of insoluble zinc phosphate crystals, which had precipitated on the surface of steel to form a highly interlocked crystalline structure.

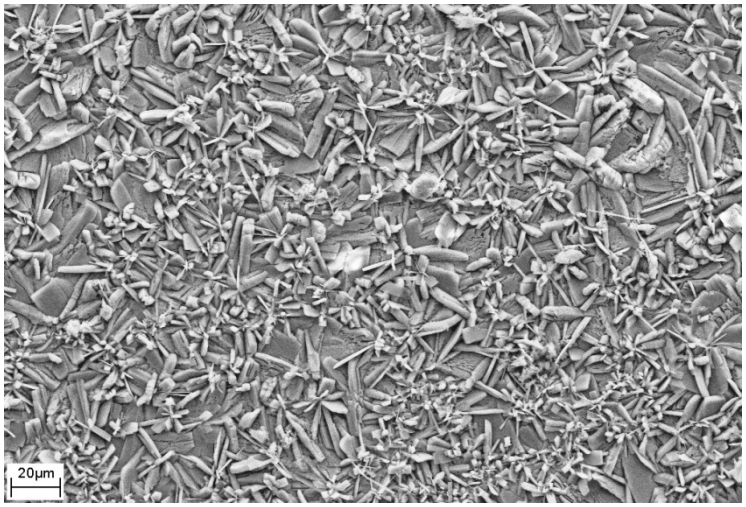

Element (at.%)	O	P	Fe	Zn
Surface	30.4	19.8	18.4	31.4

Figure 147. SEM secondary electron micrograph of the surface of the steel zinc phosphated at 65 ℃ for 20 min with a general compositional analysis by EDX measurement

The sol-gel Al_2O_3 coatings applied to the phosphated steel are shown in Figure 148. Before heat treatment, air-dried sol-gel Al_2O_3 deposits presented a dense morphology with grain sizes of about 100 μm. After heat treatment, a reduction of grain size of the Al_2O_3 coating with cracks was observed. After heat treatment, a better adhesion of Al_2O_3 deposits to the substrates was observed as indicated by abrasion using a lab wipe with moderate pressure.

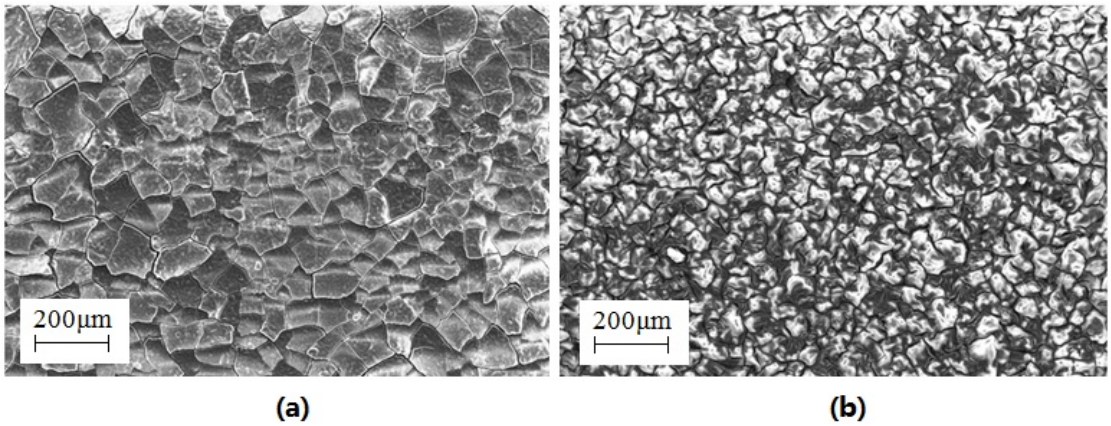

Figure 148. SEM secondary electron micrographs of the sol-gel deposited Al_2O_3 coating on a zinc phosphated steel surface: (a) as-deposited and (b) after heat-treatment at 400 ℃ for 1 h.

Al_2O_3 grit blasting was also considered for activating the surface of steel substrates mechanically, by increasing the reactive surface area. As Figure 149 shows, a similar Al_2O_3 coating morphology was produced on a grit blasted steel as on a phosphated steel. A uniform structure was observed on the surface of the Al_2O_3 coating. The Al_2O_3 coating also exhibited good adhesion.

The phosphating treatment was also applied on a grit blasted steel. Sol-gel deposition of Al_2O_3 on this phosphated and grit blasted steel was then investigated. From Figure 150, no significant difference in morphology and adhesion were observed in the coatings on the three different pre-treated steel substrates.

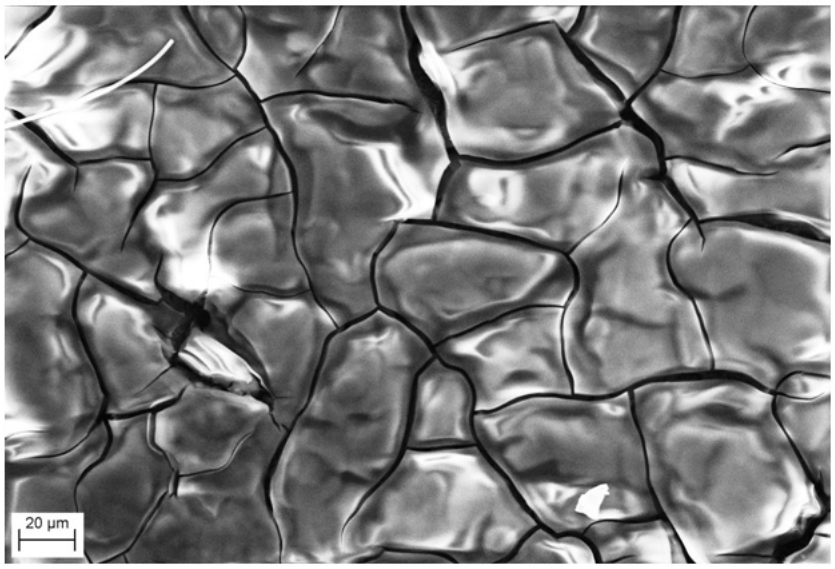

Figure 149. SEM secondary electron micrograph of the sol-gel deposited Al_2O_3 coating on a grit

blasted steel

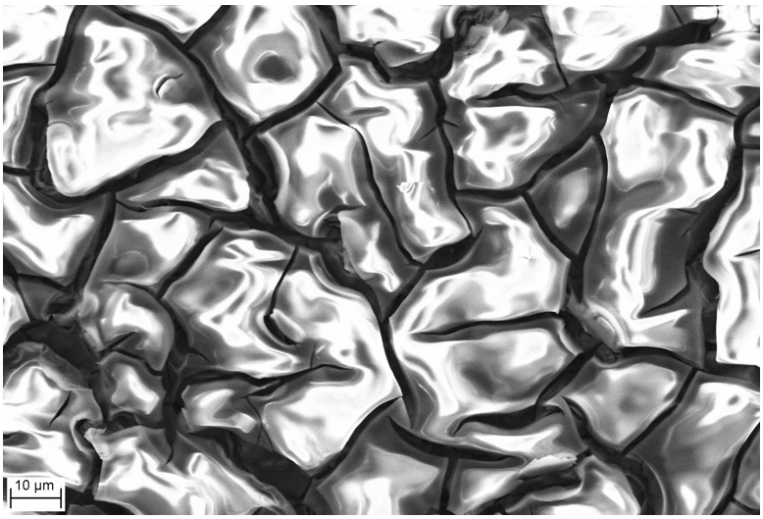

Figure 150. SEM secondary electron micrograph of the sol-gel deposited Al_2O_3 coating on a grit blasted and phosphated steel

4.3.2.2 Sol-gel Deposition of Al_2O_3 on HVOF WC/Cr/Co Coated Steels

Sol-gel Al_2O_3 coatings on steel substrates show a good morphology and adhesion. Both the phosphating and grit blasting pre-treatment on steels appear to help improve the bonding of the sol-gel Al_2O_3 coating with the base steels. Sol-gel deposition of Al_2O_3 coating was also investigated on HVOF WC/Cr/Co coatings. The same pre-treatments as on the steels were applied to the HVOF WC/Cr/Co coatings. The phosphating on the HVOF WC/Cr/Co coating may well have occurred by reaction of the zinc phosphating bath and the metallic binder of the coating (Cr-Co). From Figure 151, the sol-gel Al_2O_3 coating on a phosphated HVOF WC/Cr/Co coating did not present as uniform morphology as on the phosphated steel. The Al_2O_3 coating also exhibited poor adhesion and uncovered areas were also observed. Grit blasting was applied to increase the roughness and porosity of the surface of the HVOF WC/Cr/Co coating. From Figure 152, the Al_2O_3 coating on the grit blasted HVOF WC/Cr/Co coating exhibited a uniform morphology and good adhesion. Phosphating of the grit blasted HVOF WC/Cr/Co coatings was also considered as a pre-treatment. Figure 153 shows that a

much denser and more well adhered Al_2O_3 coating was formed on the phosphated and grit blasted HVOF WC/Cr/Co coating.

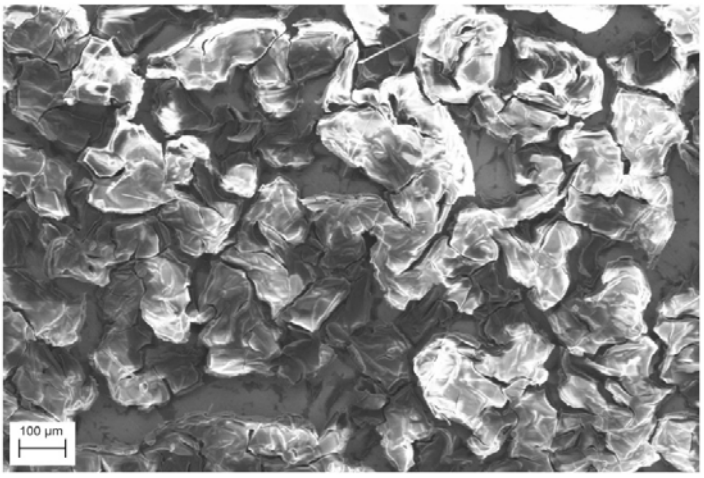

Figure 151. SEM secondary electron micrograph of the sol-gel deposited Al_2O_3 coating on a phosphated HVOF WC/Cr/Co coating

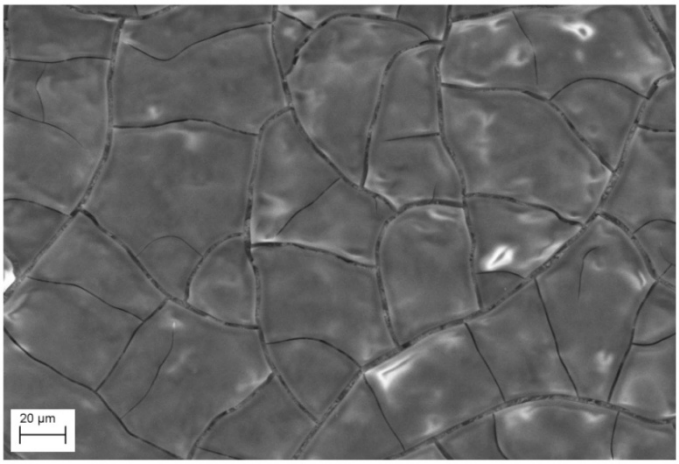

Figure 152. SEM secondary electron micrograph of the sol-gel deposited Al_2O_3 coating on a grit blasted HVOF WC/Cr/Co coating

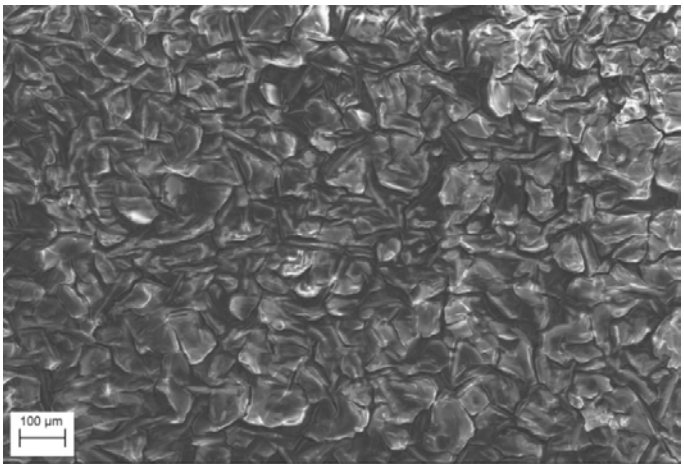

Figure 153. SEM secondary electron micrograph of the sol-gel deposited Al_2O_3 coating on a phosphated and grit blasted HVOF WC/Cr/Co coating

4.4 Investigation of the Electrodeposition of Mn-Cu Coatings

Electrodeposited Mn-Cu coatings were suggested by Airbus as a possible replacement for EC due to their potential sacrificial protection and good mechanical properties. Electrodeposition of Mn-Cu on mild steel was investigated to identify its feasibility in this study. The cathodic reaction mechanisms in the electroplating baths for Mn-Cu coatings were examined to optimise the formulations. Following this, the effects of different electroplating parameters, including current density, deposition time, agitation and electrolyte pH were examined by plotting E vs. T curves. The morphology and composition of all the electroplated Mn-Cu coatings are shown. The corrosion resistance of Mn-Cu coatings produced from the optimised processing are also indicated as the LPR in 3.5 wt.% NaCl solution. Moreover, according to the requirement of Airbus, the corrosion resistance of the Mn-Cu coating was also investigated in an aircraft de-icing fluid.

4.4.1 Cathodic Polarisation Curves for the Electrodeposition of Mn-Cu Coatings

Electrodeposition trials for Mn-Cu coatings began with modification of the electroplating bath by identification of the cathodic polarisation behaviour of baths with different formulae. Gong et al.[73, 74] pointed out two possible pH ranges for Mn-Cu alloy electroplating, one is acidic (pH 2.6-2.8) whilst the other one is near neutral (pH 6.4-6.6). However, in an attempt at electrodeposition of Mn-Cu from the electrolyte at pH 2.7, vigorous H_2 evolution was observed at the cathode during processing and did not produce any favourable results. The coatings deposited at a range of current density from 0.2 – 0.5 A/cm^2 showed a Cu-like colour with very poor adhesion to the substrate, where deposits could easily be removed. No Mn was

detected in the coatings. Therefore, a modification was made to adjust the pH of electrolytes to the near neutral electrolyte (pH 6.4-6.6). During adjusting, it was found that precipitation of Mn compounds was evident in electrolytes without NH_4^+ when the pH of an electrolyte only containing $MnSO_4$ was adjusted to near neutral. Only with the addition of NH_4^+ , did the electrolytes present a clear solution. Therefore, the effects of Mn, Cu and NH_4^+ on electrodeposition of Mn-Cu coatings were electrochemically identified. The cathodic potentiodynamic behaviour of the three ions in the electrolyte are shown in Figures 154-156.

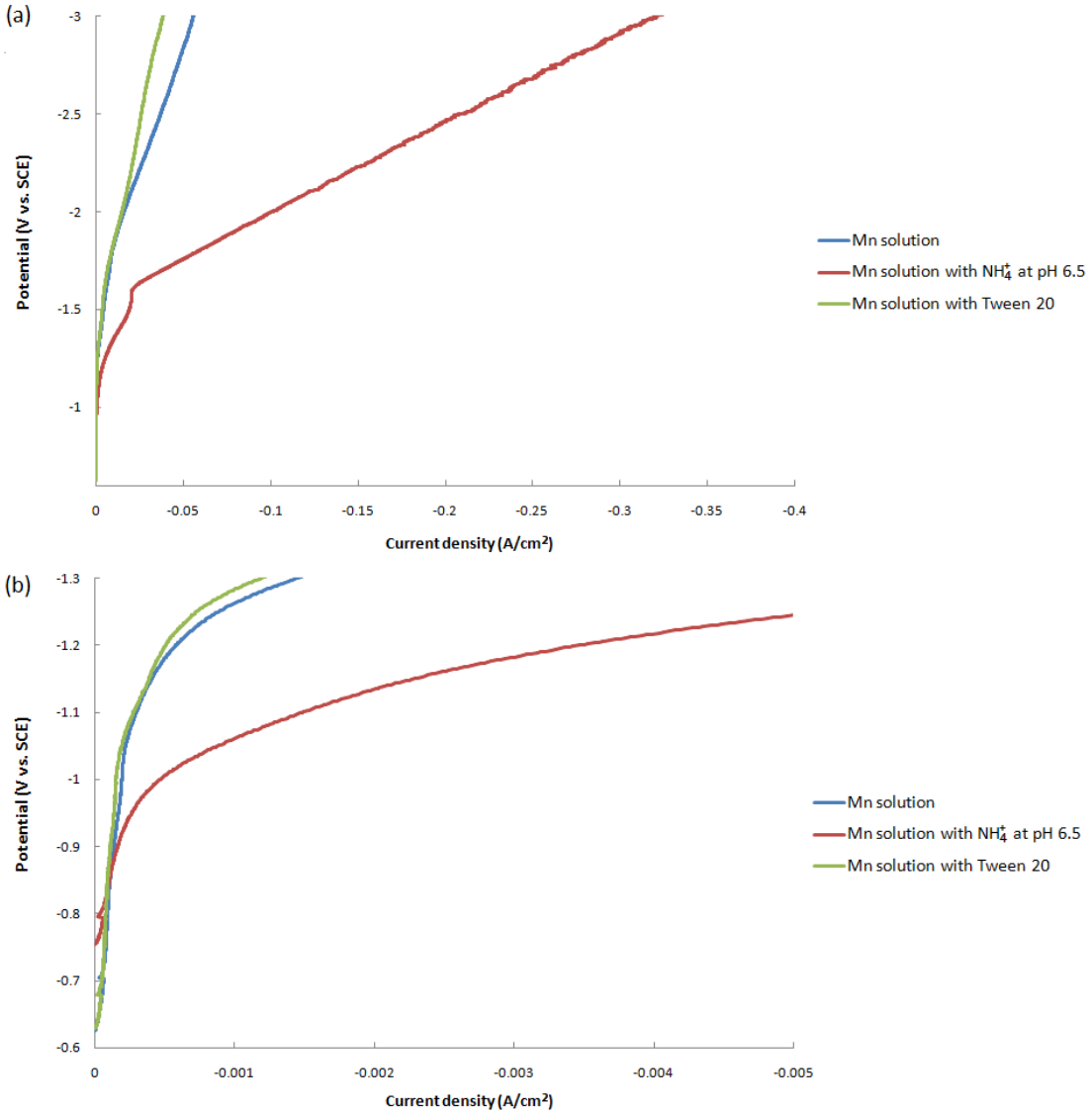

Figure 154. (a) The cathodic polarisation curves for electrolytes (1): 0.59 M $MnSO_4$ (2): 0.59 M $MnSO_4$ /1 M $(NH_4)_2SO_4$ (3): 0.59 M $MnSO_4$/ 5 mL/L Tween 20. (b) A part of the curves of (a) in a potential range of -0.6 ~ -1.3 V

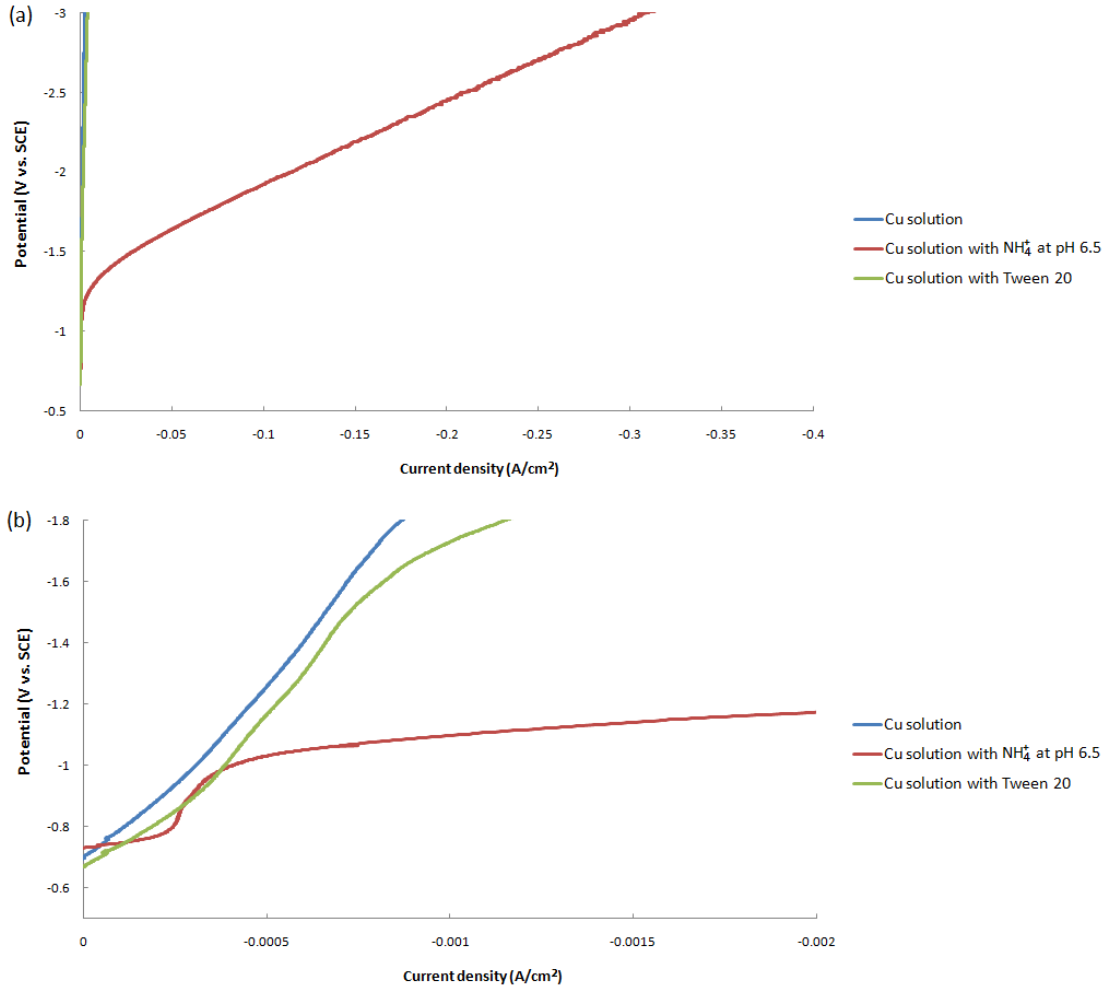

Figure 155. (a) The cathodic polarisation curves for electrolytes (1): 5 mM $CuSO_4$ (2): 5 mM $CuSO_4$/1 M $(NH_4)_2SO_4$ (3): 5 mM $CuSO_4$/5 mL/L Tween 20. (b) A part of the curves of (a) in a potential range of -0.6 ~ -1.8 V

From Figure 154, the effects of NH_4^+ and Tween 20 on the electroplating of Mn were investigated. It was found that in the electrolyte without NH_4^+, a low current density was maintained until the applied potential decreased to approximately -1.0 V. For the electrolyte with NH_4^+, a significant increase in current density was observed at approximately -0.9 V. It was also noticed that Mn^{2+} was reduced at approximately -1.6 V in the electrolyte with NH_4^+, which was slightly higher than the reduction potential of Mn^{2+} (-1.7 V) in the electrolyte without NH_4^+. The cathodic polarisation curves for Mn^{2+} in the electrolyte with and without Tween 20 presented no significant difference. As a surfactant, Tween 20 did not seem to affect the electrochemical properties of Mn^{2+}.

The cathodic polarisation behaviour of Cu^{2+} with addition of NH_4^+ and Tween 20 is shown in Figure 155. In order to eliminate possible immersion coatings of Cu on steel substrates, the cathodic polarisation trials started as soon as the substrates were immersed into the electrolyte containing Cu^{2+}. As a more noble metal, the reduction of Cu occurred at approximately -0.65 V as soon as the cathodic polarisation started. The current density remained low as the applied potential decreased to -3.0 V in the electrolyte without NH_4^+. This may be attributed to the low concentration of mobilized ions in the electrolyte after the reduction of copper. For the Cu electroplating solution with NH_4^+, an evident reduction potential of Cu was noted at about -0.7 V. The pH value of the Cu electroplating solution with NH_4^+ was adjusted to about 6.5 by NH_3 solution. A similar potential of H_2 evolution due to the hydrolysation of NH_4^+ was also observed in the Cu electroplating solution. No evident effect of Tween 20 on the cathodic polarisation behaviour of Cu^{2+} was observed.

From Figure 156, the cathodic polarisation behaviour for the electrodeposition of Mn-Cu alloy coating is shown, including from solutions containing NH_4^+ and Tween 20. In the Mn-Cu electroplating solution without NH_4^+, the cathodic polarisation curve commences with reduction of Cu^{2+} at approximately -0.65 V and is followed by H_2 evolution. The presence of NH_4^+ in the Mn-Cu electroplating solution accelerated H_2 evolution and decreased the reduction potential of Cu^{2+} in the electrolyte, which agreed with previous observations. An evident difference in the reduction potential of Mn^{2+} in the Mn-Cu electroplating solution was observed due to the addition of NH_4^+. The reduction potential of Mn^{2+} increased from approximately -1.7 to -1.5 V due to the addition of NH_4^+.

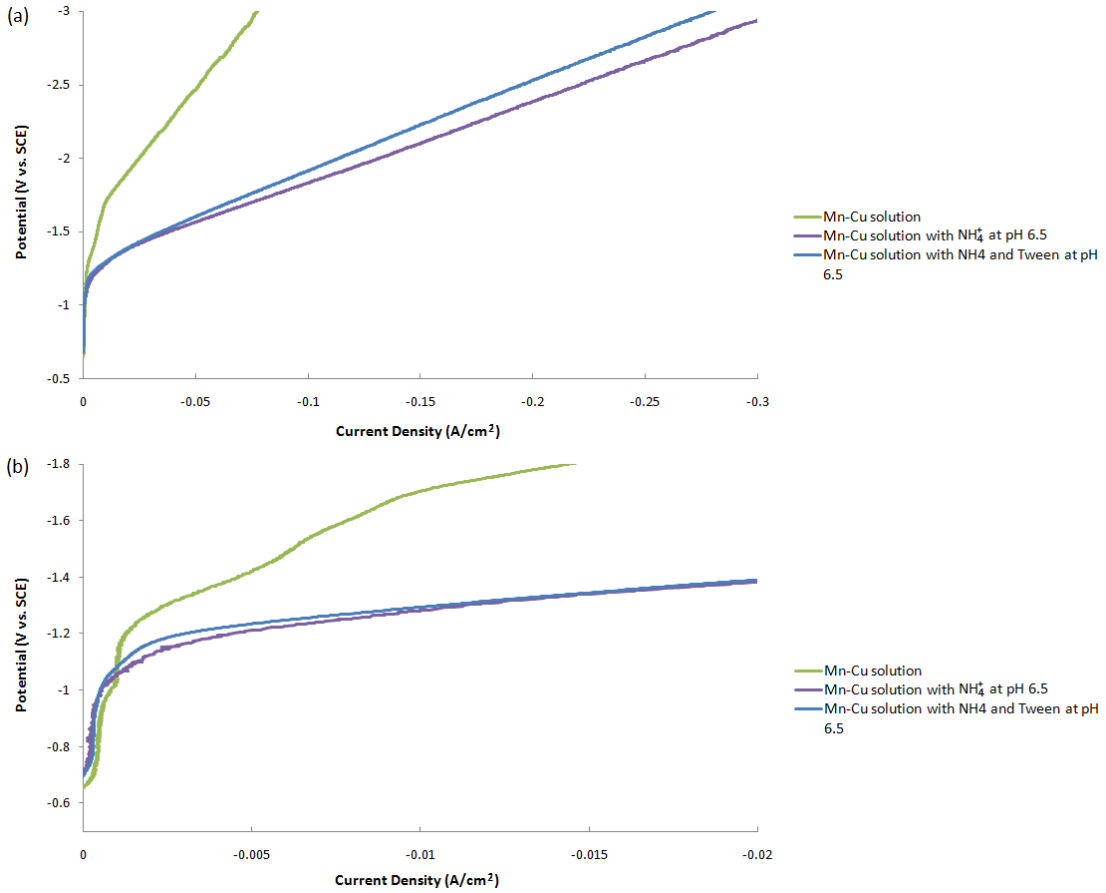

Figure 156. (a) The cathodic polarisation curves for electrolytes (1): 0.59 M $MnSO_4$/5 mM $CuSO_4$ (2): 0.59 M $MnSO_4$/5 mM $CuSO_4$/1 M $(NH_4)_2SO_4$ (3): 0.59 M $MnSO_4$/5 mM $CuSO_4$/1 M $(NH_4)_2SO_4$/ 5 mL/L Tween 20. (b) A part of the curves of (a) in a potential range of -0.6 ~ -1.8 V

4.4.2 Potential vs. Time Curves for the Electrodeposition of Mn-Cu Coatings

The effects of applied current density, agitation, electroplating time and electrolyte composition on the galvanostatic electroplating of Mn-Cu coatings were investigated and the potential vs. time curves for all the electroplating processes are shown in Figures 157-160.

From Figure 157, two attempts to electroplate Mn-Cu from an electrolyte without NH_4^+ are shown. During the processes, the electrode potential of the steel substrate decreased sharply with time, which implied a low current efficiency. No significant reduction of Mn was observed and a powdery Cu colour and film was noted to form

during the process.

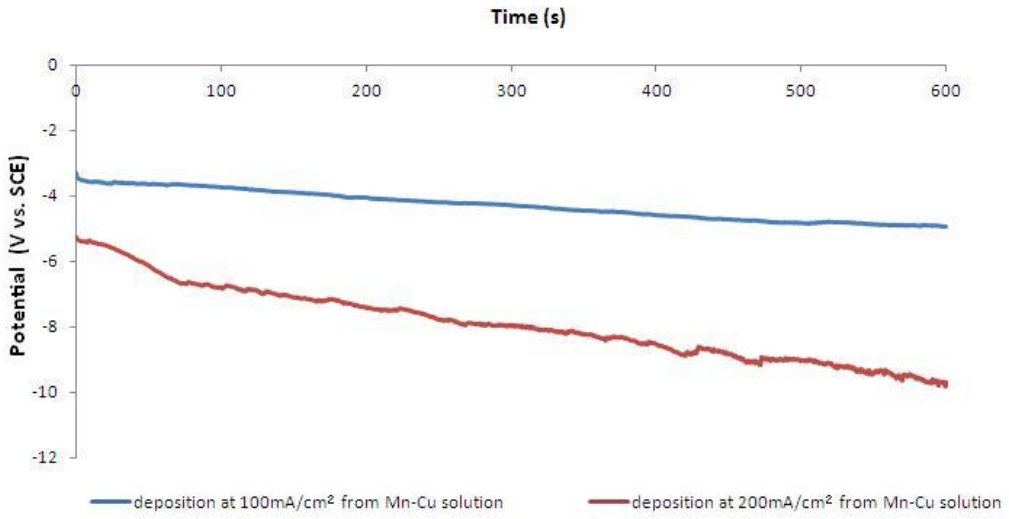

Figure 157. Potential vs. time curves for the galvanostatic electroplating of Mn-Cu coating at current densities of 100 and 200 mA/cm^2 from a 0.59 M $MnSO_4$/5 mM $CuSO_4$ solution for 10 min

With the addition of NH_4^+ to the electrolyte, more stable potential vs. time curves for the processes are observed in Figure 158. Compared to the electroplating from electrolyte without NH_4^+, the electrode potential of steel maintained a much higher value (-2.6 V) during the electroplating at 200 mA/cm^2 from the electrolyte with NH_4^+. From the curves of electrodeposition at 300, 400 and 500 mA/cm^2, it was noted that the working electrode potential increased slightly with time, which may result from the reduction of Mn. Therefore, it is possible that Mn coatings with good quality could be produced at current densities over 300 mA/cm^2.

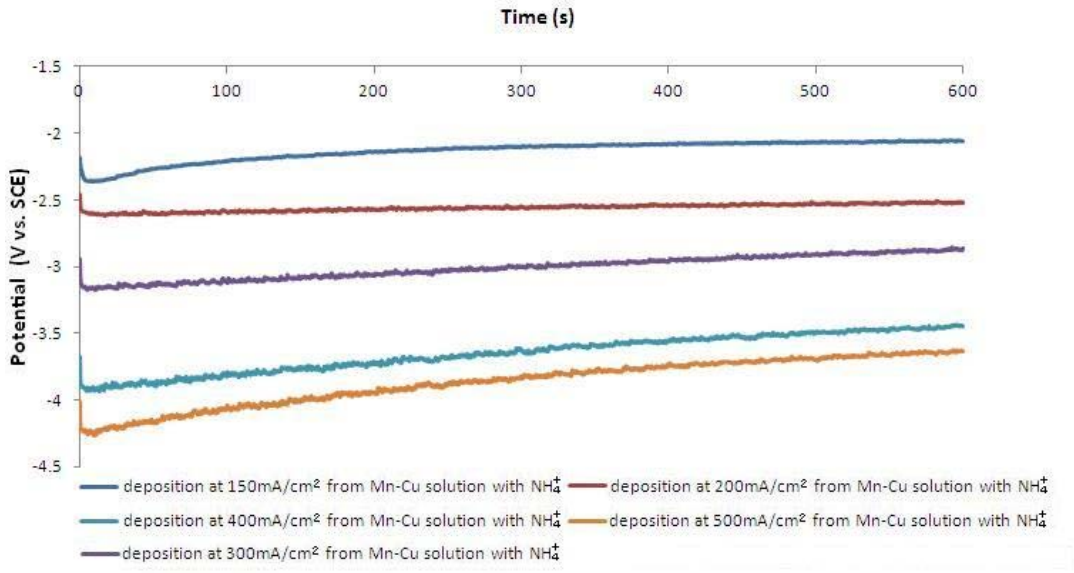

Figure 158. Potential vs. time curves for galvanostatic electroplating of Mn-Cu coatings at current densities of 150 – 500 mA/cm^2 from a 0.59 M $MnSO_4$/5 mM $CuSO_4$/1 M $(NH_4)_2SO_4$ solution for 10 min

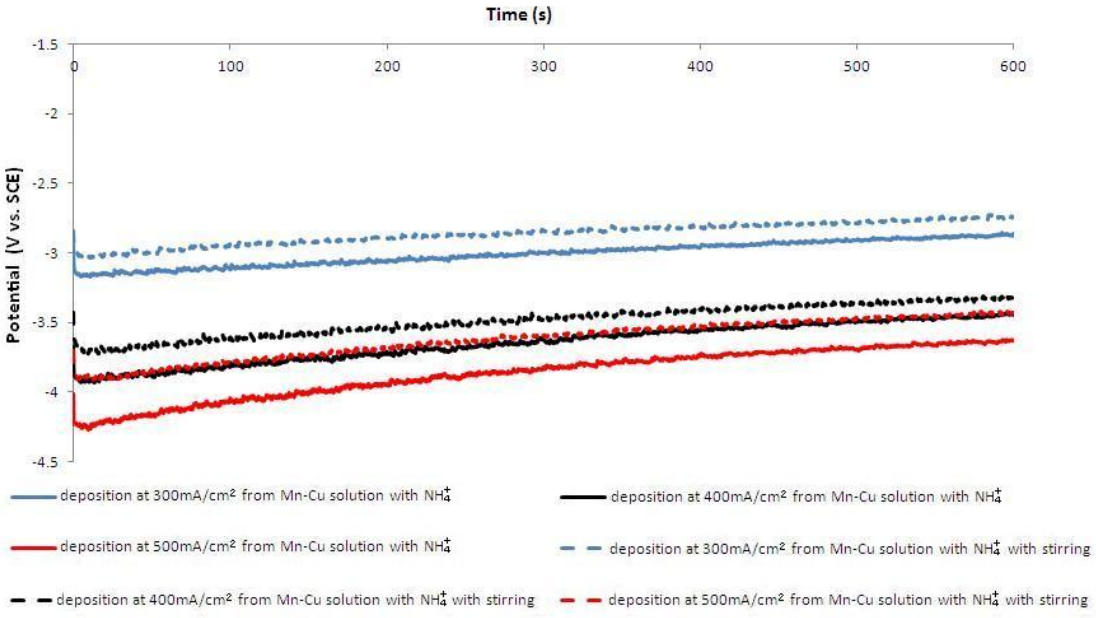

Figure 159. Potential vs. time curves for galvanostatic electroplating of Mn-Cu coatings at current densities from 300 – 500 mA/cm^2 from a 0.59 M $MnSO_4$/5 mM $CuSO_4$/1 M $(NH_4)_2SO_4$ solution for 10 min with and without stirring

The effects of agitation on the electroplating of Mn-Cu were investigated and are shown in Figure 159. It can be seen that agitation did not affect the trend of the potential vs. time curves for the electroplating of Mn-Cu, but resulted in a significant increase in the potentials.

The effects of the addition of Tween 20 in the electrolyte on the electroplating processes were also identified by forming Mn-Cu coatings using the same charge at different current densities and their potential vs. time curves are shown in Figure 160. From Figure 158 and 160, it was found that at the same current density, the working electrode potential for the electroplating processes with short electroplating time presented similar values and trends as those processes with long electroplating times. It was also found that with increased applied current density, the working electrode potential difference caused by the addition of Tween 20 also increased. That implied that the addition of Tween 20 decreased the deposition potential of Mn-Cu with increase in the applied current density, which was thought to result from the more nucleation during electrodeposition of Mn-Cu.

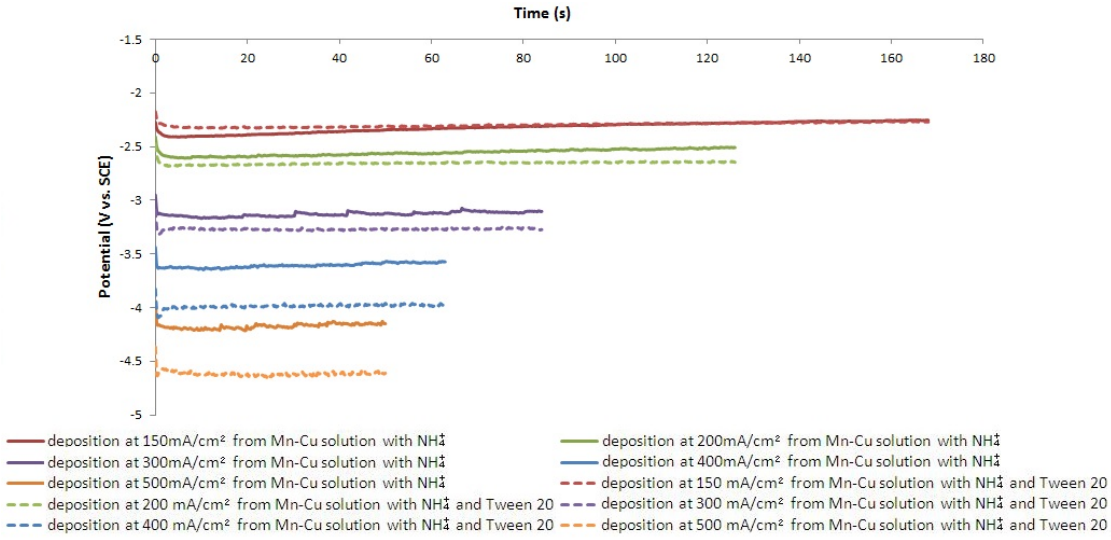

Figure 160. Potential vs. time curves for galvanostatic electroplating of Mn-Cu coatings from a 0.59 M $MnSO_4$/5 mM $CuSO_4$/1 M $(NH_4)_2SO_4$ solution with and without 5 mL/L Tween 20 at current densities from 100 – 500 mA/cm^2 using the same electrochemical charge.

4.4.3 Morphology and Composition of Electroplated Mn-Cu Coatings

The morphology and composition of Mn-Cu coatings electroplated using different parameters were presented in this section. From the observations in Figure 157, it was expected that no Mn-Cu alloy coating was produced by electroplating from an

electrolyte without NH_4^+. From Figure 161, it was observed that the absence of NH_4^+ in the Mn-Cu electroplating solution resulted in a powdery coating and no manganese was detected in the coating by EDX. The coating presented a Cu-like colour and poor adhesion to substrates. With applied current density increased, no significant improvement in coatings was observed.

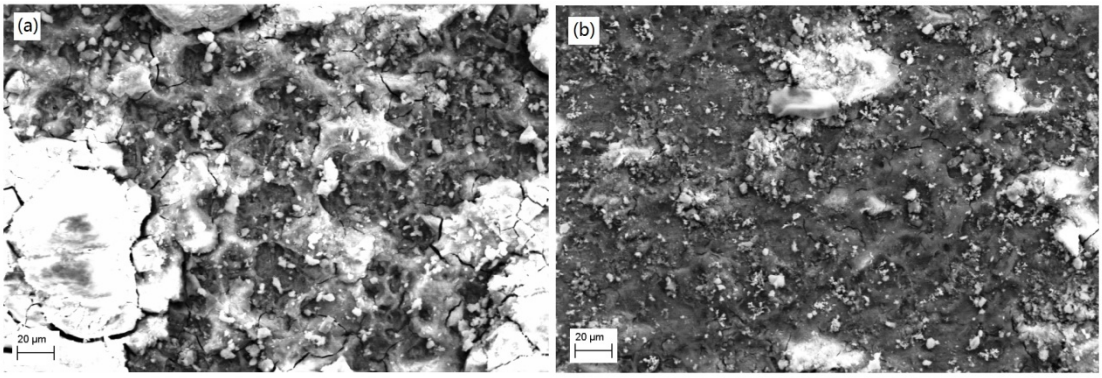

Figure 161. SEM secondary electron micrographs of Mn-Cu coatings produced from 0.59 M $MnSO_4$/5 mM $CuSO_4$ for 10 min at (a) 100 mA/cm^2; (b) 200 mA/cm^2

From previous electrochemical investigation of the Mn-Cu electroplating solution, NH_4^+ was found to stabilize the electroplating processes and reduce the difference of reduction potential of Mn and Cu. In this way, the addition of NH_4^+ was expected to help to produce Mn-Cu alloy coatings with good qualities. The morphology and composition of Mn-Cu coatings produced from the electrolyte with NH_4^+ at different current density is shown in Figures 162 and 163. From Figure 162 (a), it was found that the reduction of Cu occurred and a Cu coating formed at 150 mA/cm^2, but the current density was too low to provide a driving force to reduce Mn^{2+}. Therefore, Cu rich deposits (90.5 wt.% Cu; 2.6 wt.% Mn; 6.9 wt.% O) were formed in a powdery pattern. As the applied current density increased to 200 mA/cm^2, both the quality and quantity of reduction of Mn^{2+} increased. From Figure 162 (b), Cu rich deposits (69.2 wt.% Cu; 24.5 wt.% Mn; 6.3 wt.% O) displayed a porous structure in the centre area of the Mn-Cu coating. Moreover, a sharp increase in Mn content (3.3 wt.% Cu; 94.5 wt.% Mn; 2.2 wt.% O) was observed in the edge area of the Mn-Cu coating produced at 200 mA/cm^2 (Figure 163). It was suggested that due to the current density

distribution on substrates, there was a significant difference in Mn content from centre to edge areas on the surface of substrates.

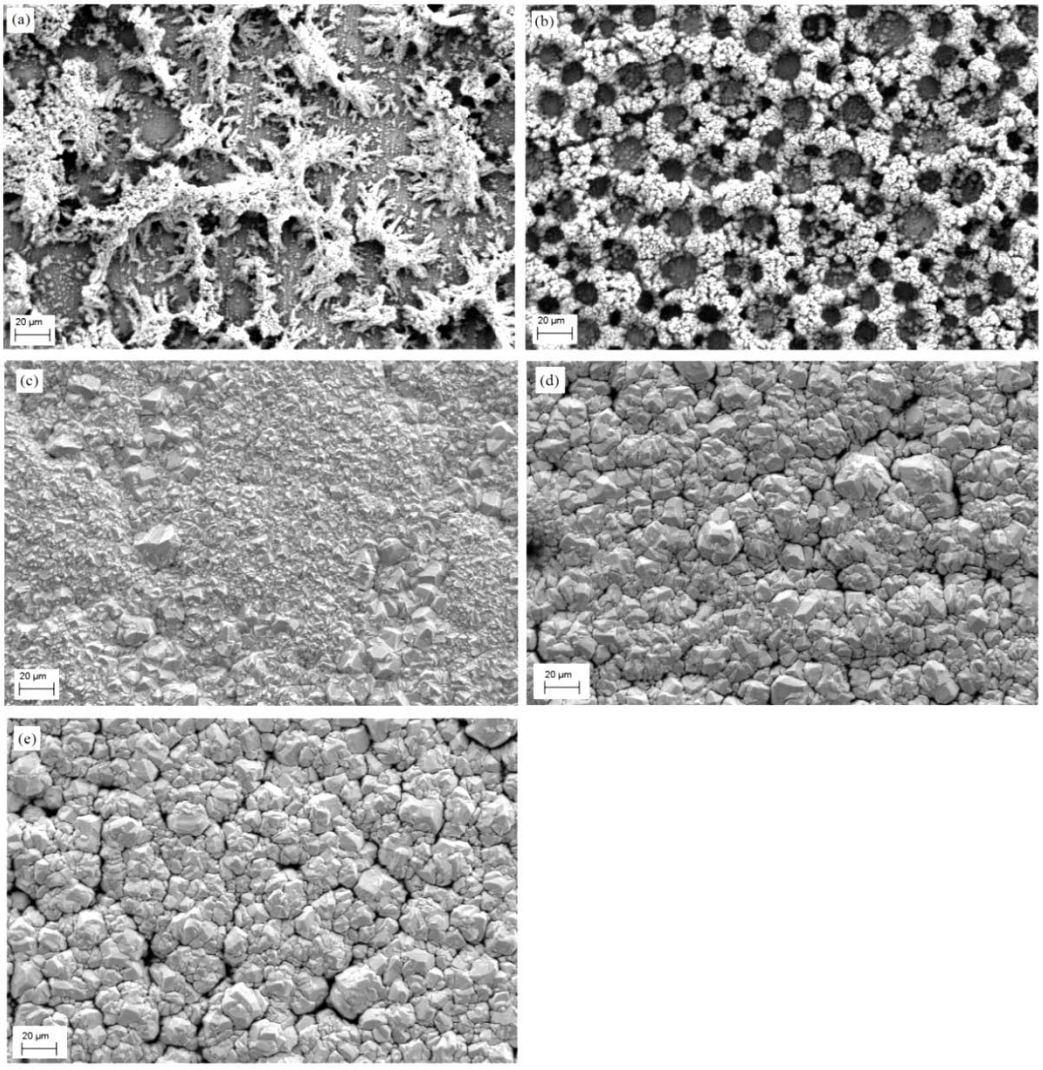

Figure 162. SEM secondary electron micrographs of Mn-Cu coatings produced from 0.59 M $MnSO_4$/5 mM $CuSO_4$/1 M $(NH_4)_2SO_4$ for 10 min at (a) 150 mA/cm^2; (b) 200 mA/cm^2; (c) 300 mA/cm^2; (d) 400 mA/cm^2; (e) 500 mA/cm^2

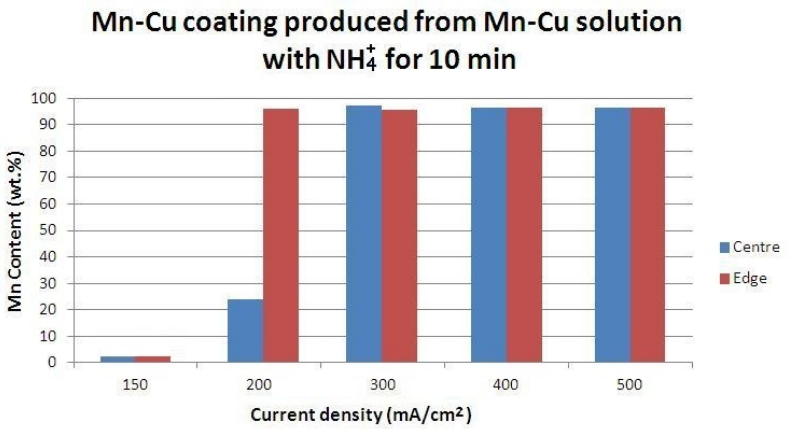

Figure 163. Mn content in the centre and edge areas of Mn-Cu coatings electrodeposited from 0.59 M $MnSO_4$/5 mM $CuSO_4$/1 M $(NH_4)_2SO_4$ at current densities from 150 to 500 mA/cm^2 for 10 min

From Figure 162 (c), an evident improvement was observed in both morphology and composition of Mn-Cu coatings produced at 300 mA/cm^2. The Mn-Cu coating showed a dense and uniform structure, but some grains with relative larger sizes were also observed. As the applied current density increased to 400 and 500 mA/cm^2 (Figure 162 (d) and (e)), a significant increase in grain size of the Mn-Cu coating was observed. Moreover, some defects were seen at the grain boundaries of the Mn-Cu coating. The possible mechanism for that is discussed in the discussion section From the compositional analyse (Figure 163), the Mn-Cu coatings produced at more than 300 mA/cm^2 produced a high Mn content and uniform composition distribution from centre to edge area.

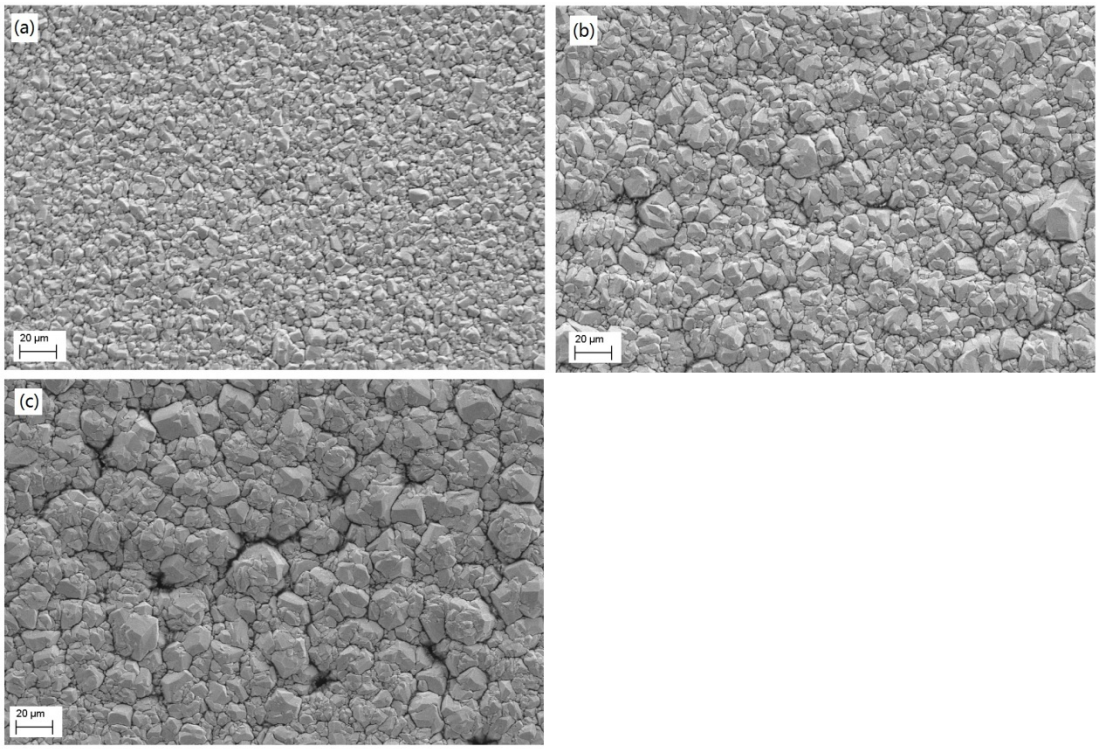

Figure 164. SEM secondary electron micrographs of Mn-Cu coatings produced from 0.59 M $MnSO_4$/5 mM $CuSO_4$/1 M $(NH_4)_2SO_4$ for 10 min with stirring at (a) 300 mA/cm^2; (b) 400 mA/cm^2; (c) 500 mA/cm^2

During the electroplating of Mn-Cu coatings, it was also found that the blue colour of the electrolytes faded around the working electrode obviously due to changes in local pH value. Therefore, magnetic stirring with a speed of 60 rpm was applied to eliminate variation of local pH value around working electrode and improve the mobility of the Cu^{2+} in the electrolytes. The previous electrochemical observations implied that stirring was good for stabilising the Mn-Cu electroplating processes. From Figure 164, the Mn-Cu coatings produced with stirring showed a more uniform morphology. In particular, the Mn-Cu coating produced at 300 mA/cm^2, with stirring, had a crystalline microstructure with uniform grains (Figure 164 (a)). The similar effects of stirring were also observed in the Mn-Cu coatings produced at high current density (Figures 164 (b) and (c)).

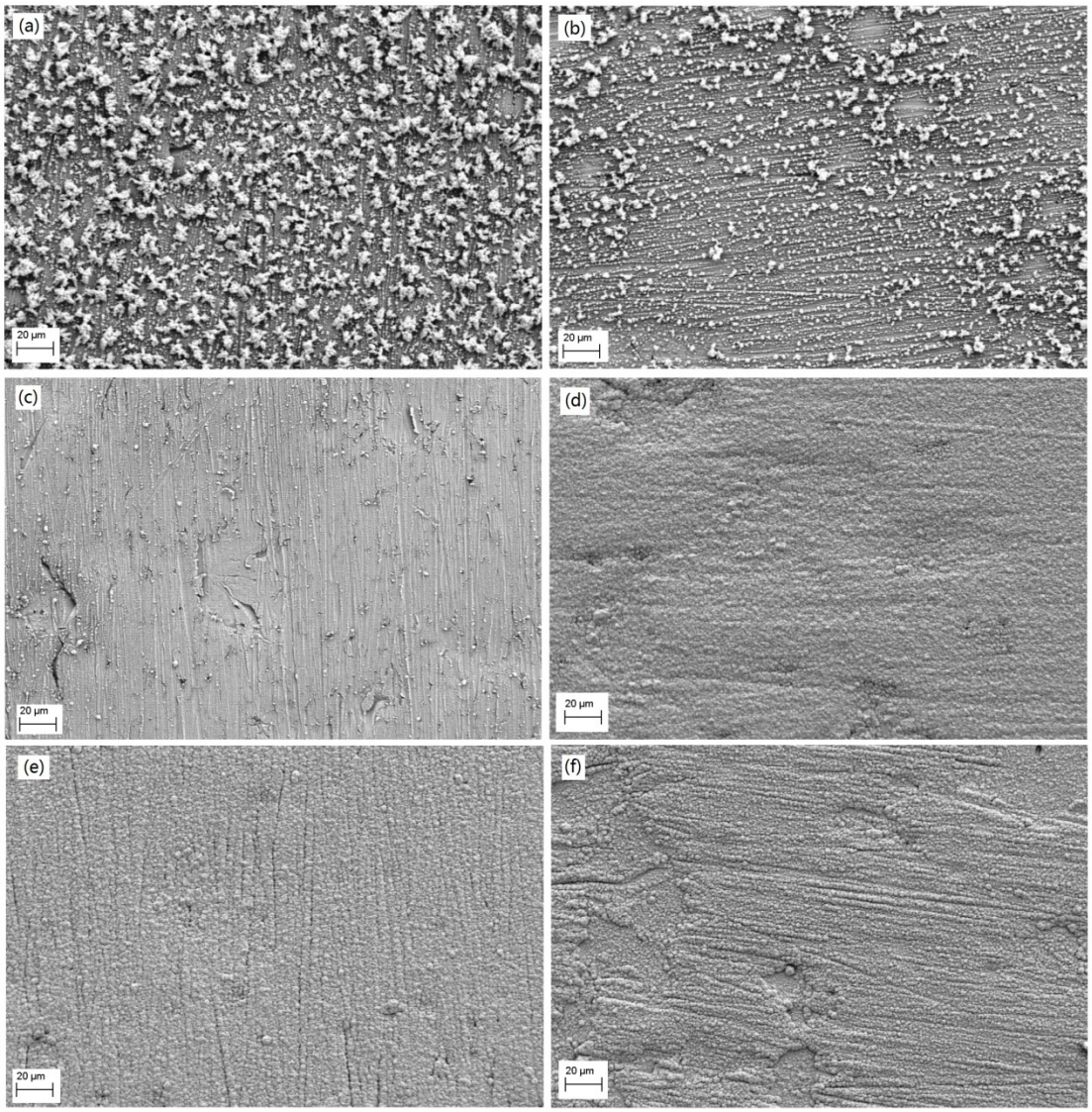

Figure 165. SEM secondary electron micrographs of Mn-Cu coatings produced from 0.59 M $MnSO_4$/5 mM $CuSO_4$/1 M $(NH_4)_2SO_4$using the same charge at (a) 100 mA/cm^2; (b) 150 mA/cm^2; (c) 200 mA/cm^2; (d) 300 mA/cm^2; (e) 400 mA/cm^2; (f) 500 mA/cm^2

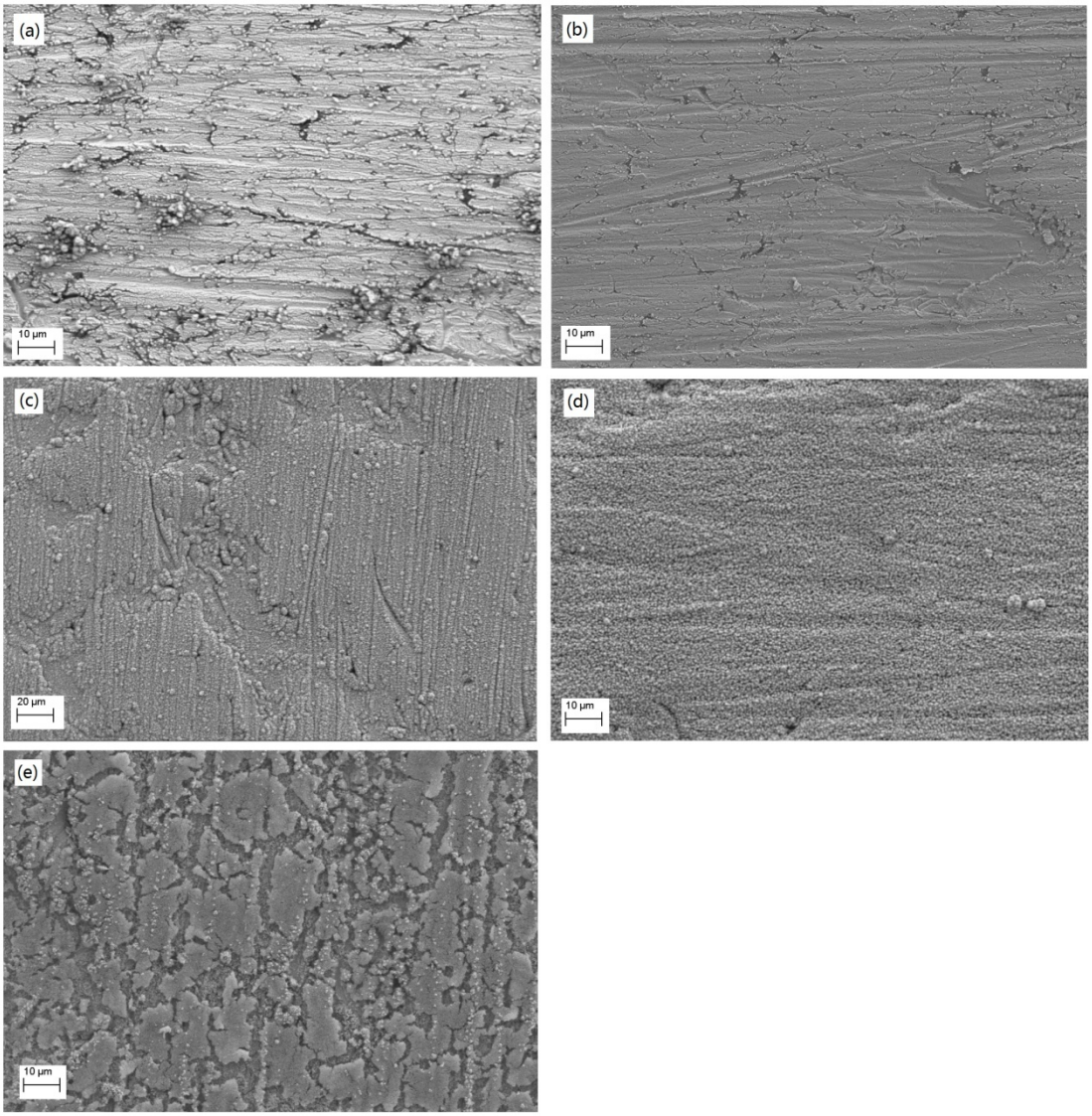

Figure 166. SEM secondary electron micrographs of Mn-Cu coatings produced from 0.59 M $MnSO_4$/5 mM $CuSO_4$/1 M $(NH_4)_2SO_4$/5 mL/L Tween 20 using the same charge at (a) 150 mA/cm^2; (b) 200 mA/cm^2; (c) 300 mA/cm^2; (d) 400 mA/cm^2; (e) 500 mA/cm^2

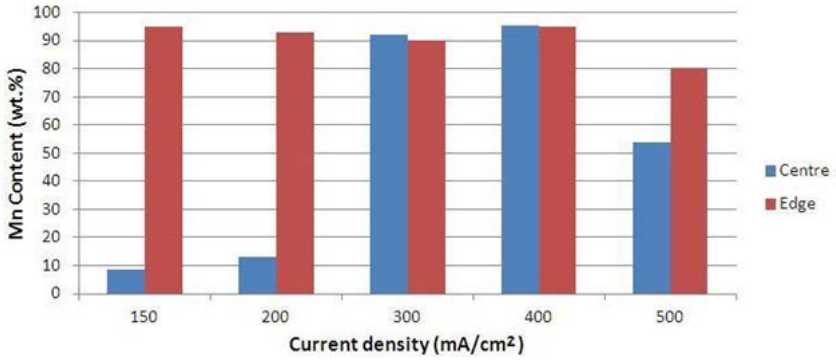

Figure 167. Mn content in the centre and edge areas of Mn-Cu coatings electrodeposited by applying the same electric charge from 0.59 M $MnSO_4$/5 mM $CuSO_4$/1 M $(NH_4)_2SO_4$/5 mL/L Tween 20 at current densities from 150 to 500 mA/cm^2

Figure 165 shows the morphology of the Mn-Cu coatings produced at different current densities but applying the same electric charge. From Figure 165, as using the same electric charge, dense and uniform Mn-Cu coatings were only observed at current density over 300 mA/cm^2 as observed in the coatings produced for 10 min. Compared to the coating shown in Figure 162, a much shorter electroplating time produced a much finer grain size for the coatings (Figure 165). The effects of Tween 20 on the morphology and composition of Mn-Cu coatings is shown in Figures 166-167. From Figure 166, it was found that the effects of current density on Mn-Cu coating were not affected significantly by addition of Tween 20, however, the grain size of the Mn-Cu coating was decreased. In particular, Mn-Cu coating produced from electrolytes with Tween 20 at a high current density of 500 mA/cm^2 presented an amorphous-like structure as Figure 166 (e) shows. From the compositional analysis (Figure 167), the addition of Tween 20 did not help to improve the homogeneity of the coatings, particularly at 150, 200 and 500 mA/cm^2.

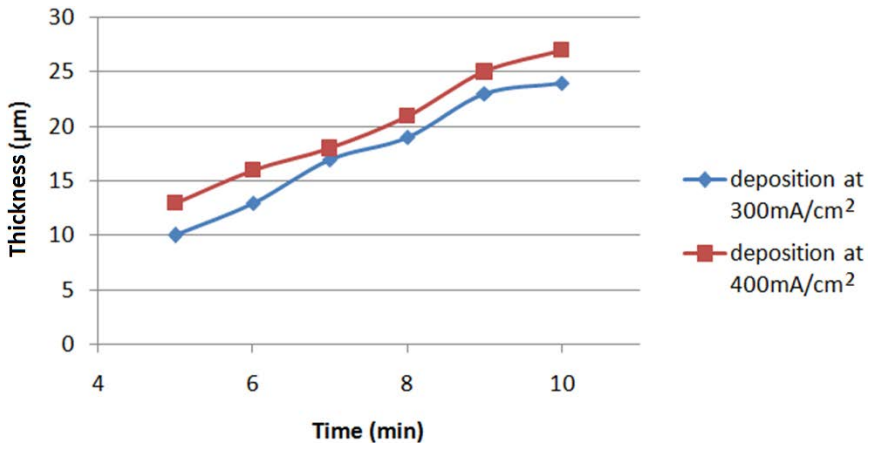

Figure 168. Coating thickness vs. electroplating time curves of Mn-Cu coatings electrodeposited from 0.59 M $MnSO_4$/5 mM $CuSO_4$/1 M $(NH_4)_2SO_4$ at pH 6.5 by applying 300 and 400 mA/cm^2 with magnetic stirring of 60 rpm

After investigating the effect of process parameters on the electroplating Mn-Cu coatings, electroplating from 0.59 M $MnSO_4$/5 mM $CuSO_4$/1 M $(NH_4)_2SO_4$ at pH 6.5 by applying current densities of 300 and 400 mA/cm^2 with magnetic stirring at 60 rpm was suggested to produce a Mn-Cu coating with good quality. A nearly linear relation

of coating thickness and electroplating time is shown in Figure 168.

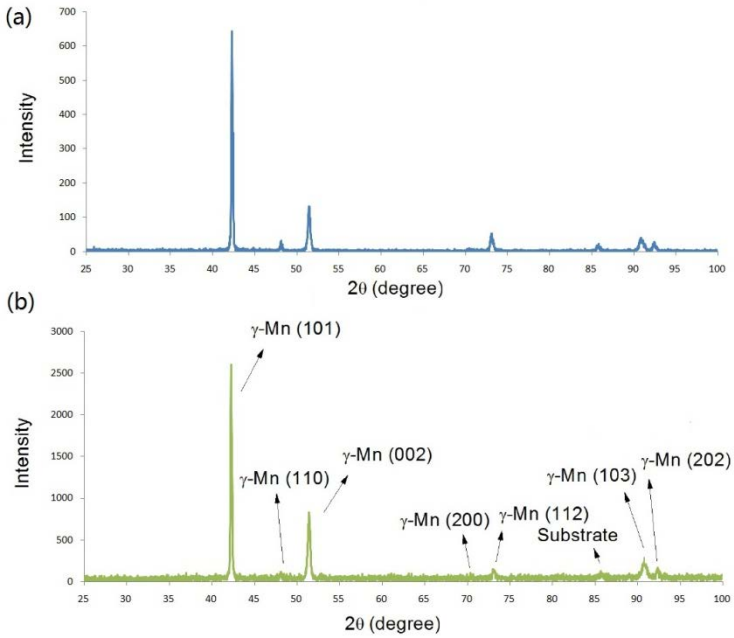

Figure 169. XRD spectra of Mn-Cu coatings obtained from 0.59 M $MnSO_4$/5 mM $CuSO_4$/1 M $(NH_4)_2SO_4$ at current density 300 mA/cm^2 for 10 min (a) as-deposited; (b) After 4-months storage in air at 20 ℃

The crystalline structure of the Mn-Cu coating produced by the optimised electroplating processes was identified as deposited by XRD. The pattern of the as-deposited Mn-Cu coating showed several very narrow peaks, which were found to correspond to the crystalline structure of γ-Mn phase (Figure 169 (a)). From Figure 169 (b), a similar XRD pattern was observed for the 4-month old specimen to the as-deposited Mn-Cu coating and no significant transformation of the Mn phase was evident. That implies that the co-deposition of Cu with Mn inhibits the phase transformation of ductile γ-Mn in as-deposited Mn-Cu coatings to brittle α-Mn.

4.4.4 Potentiodynamic Behaviour of Mn-Cu Coatings

After optimising the process parameters for the electroplating of Mn-Cu coatings, dense and uniform Mn-Cu coatings with high Mn content were produced from 0.59 M $MnSO_4$/5 mM $CuSO_4$/1 M $(NH_4)_2SO_4$ electrolyte by applying 300 mA/cm^2. The Mn-Cu coating with 10μm thickness was investigated in term of sacrificial protection

property by potentiodynamic analysis. The potentiodynamic behaviour of the Mn-Cu coating and its substrate in 3.5 wt.% NaCl are shown in Figure 170. The free corrosion potential of mild steel substrate was decreased from -1.03 V to -1.22 V by applying the Mn-Cu coating and the coating showed a higher corrosion current density (33.3 mA/cm^2).

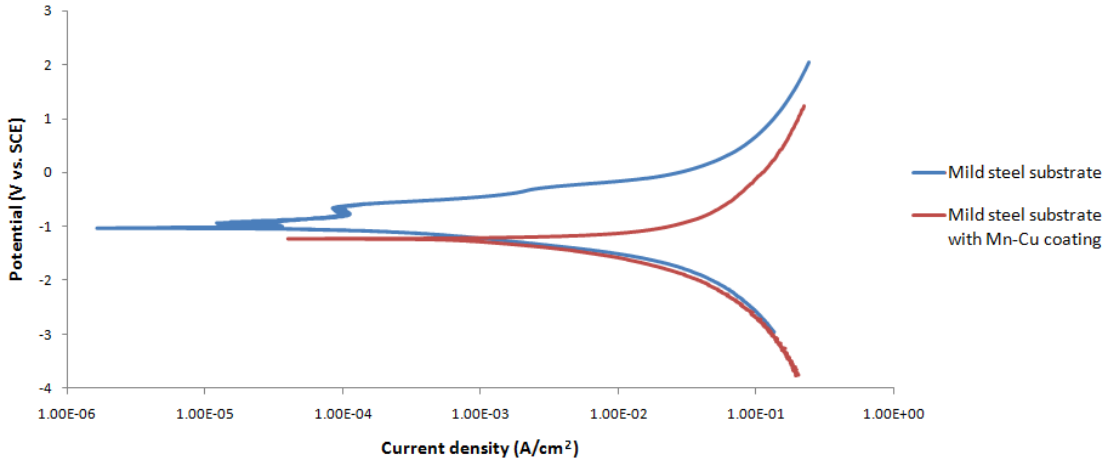

Figure 170. Potentiodynamic behaviour of mild steel substrate and Mn-Cu coating on mild steel substrate in 3.5 wt.% NaCl produced from 0.59 M $MnSO_4$/5 mM $CuSO_4$/1 M $(NH_4)_2SO_4$ at current density 300 mA/cm^2 for 5 min

4.4.5 Corrosion Resistance to an Aircraft De-icing Fluid

According to the requirements of Airbus, the corrosion resistance of electroplated Mn-Cu coating to an aircraft de-icing fluid, which is a glycol-based, water-soluble fluid and named Konsin, was investigated by immersion tests. During the immersion test in Konsin, it was observed that there was no evident change observed in both the immersion bath and on the Mn-Cu coating in the first 10 days of the test. After that, a significant change in colour of the solution occurred and the clear and colourless bath changed to a brown colouration and became turbid, which implied degradation of the coating. Both SEM and visual observation of as-deposited Mn-Cu coating and after immersion tests are shown in Figure 171. It was found that both morphology and composition of the Mn-Cu coating were seriously affected. After the immersion test, the Mn-Cu coating became detached and Mn was completely removed and only a thin Cu film remained on the substrate. In conclusion electroplated Mn-Cu presented a

poor corrosion resistance to Konsin for long-term application.

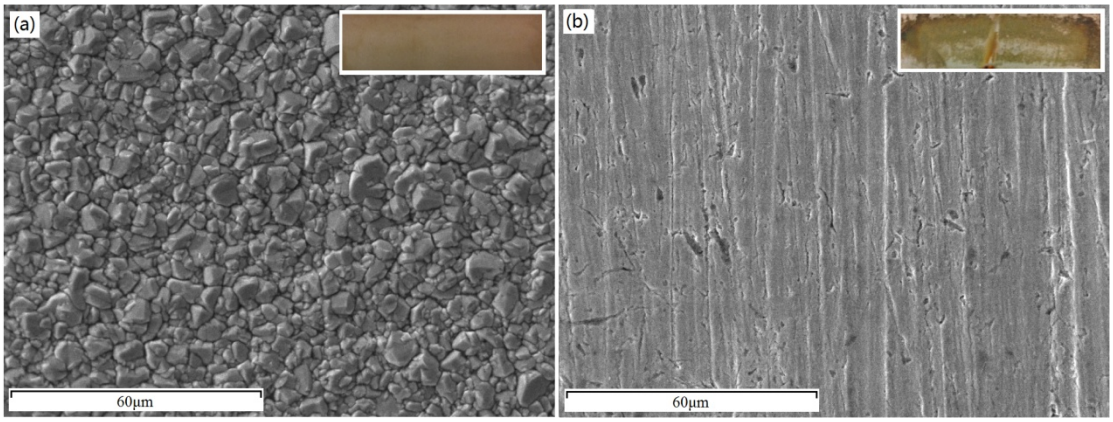

Element (at.%)	O	Fe	Cu	Mn
(a)	12.3	-	3.9	83.8
(b)	18.9	74.2	6.9	-

Figure 171. SEM secondary electron micrographs of Mn-Cu coating produced from from0.59 M $MnSO_4$/5 mM $CuSO_4$/1 M $(NH_4)_2SO_4$ at a current density of 300 mA/cm^2 for 5 min (a) as-deposited; (b) after immersion test in Konsin for 14 days. The inserts illustrates the visual morphology of the coating.

CHAPTER 5: DISCUSSION

5.1 EC and EHC Coatings, and Their Replacements

According to the requirements of Airbus, targeted sacrificial coatings, comprising EDAl, FSAl and SermeTel 962 (Al based composite) coatings, were investigated as EC coating replacements whilst a HVOF WC/Cr/Co coating was investigated as an EHC coating replacement. In order to identify the feasibility of the replacements, they were compared with EC and EHC coatings in terms of morphology, composition, corrosion resistance and porosity. Galvanic compatibility of the sacrificial and the hard coatings was also examined qualitatively and quantitatively due to previous significant galvanic corrosion reported by Airbus.

5.1.1 Characterisation of the Sacrificial Coatings

5.1.1.1 EC Coating

As-deposited EC coatings had an irregular and rough surface and an open and heterogeneous structure in cross section (Figures 48 and 49). The gaps and pores observed in the coating are suggested to result from H_2 evolution during the electroplating process for the EC coating, which is confirmed by the coating supplier. Moreover, the AIPS 02-04-002 specification[96] implies that hydrogen de-embrittlement was performed in forced air furnaces to totally remove the hydrogen absorbed by the material during the electrodeposition process. It has been reported that EC coatings have a low permeability for hydrogen[109]. So inherent porosity can aid hydrogen out-gassing during the post-electroplating de-embrittlement processes. A post-treatment passivation was applied to the EC coating, which was implied by the presence of Cr. No evident O was detected on the surface of the passivated EC coating, but a high O content in the coating cross-section implied the oxidation of the Cd coating.

Cd is oxidised to form CdO and $Cd(OH)_2$ in air, especially in moist environments[110]. Oxidation of the Cd coating was suggested to occur during storage of the cross-sectioned sample. Therefore, the absence of O on the surface of the EC coating implied that the passivation treatment protected the EC coating from oxidation.

From the corrosion resistance characterisation of all the sacrificial coating (Figure 63), the EC coatings presented the most negative E_{corr} (- 796 mV), which may suggest the best sacrificial protection for the steel substrate. The EC coatings had a corrosion current density, I_{corr}, of 26.1 $\mu A/cm^2$, which was thought to indicate good corrosion resistance. From its anodic polarisation behaviour (Figure 63), passivation occurred in a range of potential (from -770 mV to -734 mV). After LPR testing, evident cracking was observed on the surface of the chromate conversion coating of the EC coating (Figure 64). The cracked conversion coating was thought to expose the underlying EC coating during the LPR test, and resulted in oxidation of the Cd, which may be the reason for the passivation occurring in its anodic polarisation test. A significant increase in O content on the surface of the EC coating after the LPR test further suggested this.

Equation (5) indicates that any discontinues in coatings can cause a reaction between steel substrate and permanganate, which results in the formation of MnO_2. The barrier protection property of the EC coating was identified by the Mn and O contents on the surface of the coating after the porosity test. High O content presented on the surface of the EC coating after porosity testing, which was believed to result from the oxidation of Cd due to the cracking of the chromate conversion coating (Figure 69). However, the surface of the EC coating showed no Mn, which implied that there was no reaction between the $KMnO_4$ solution and steel substrate (Figure 69). Therefore, the oxide films were thought to hinder the penetration of $KMnO_4$ solution to the steel substrate. The EC coating was suggested to provide good barrier protection to the steel substrate.

5.1.1.2 FSAl Coating

The FSAl coatings had a splash pattern-like structured surface, which was suggested to be caused by the collapse of the molten coating droplets on the substrate during processing (Figure 53). From the observation of their cross-sections (Figures 54 and 55), some interconnecting pores were present in the coating. From the EDX data for the cross-section, Si from the polishing processes was trapped in the pores of the coating, which further indicated a significant level of porosity in the coating. At the interface between the coating and the substrate, diffusion was thought to have occurred indicated by the presence of a wide range of elements (Figure 56). It is suggested that the surface layers of the steel may recrystallise during thermal spraying due to the high temperature of the molten Al droplets. The rapid cooling rate of the molten Al droplets also resulted in the precipitation of carbides and other alloying elements on the grain boundaries.

In terms of corrosion resistance, compared to the EC coating in LPR data, the FSAl coating presented a higher E_{corr} of -621 mV (Figure 63). The inclusion of Si in the FSAl coating was thought to promote more electronegative Al-Si eutectics which constituted the coating matrix, hence perhaps being the reason for its higher E_{corr}. A similar mechanism has been reported by Qian et al.[111]. As an EC replacement, the FSAl presented a higher corrosion current density, I_{corr} (62.8 $\mu A/cm^2$), than the EC coating. Pores present in the coating were thought to result in the penetration of electrolyte during LPR testing and therefore increased the corrosion current. After the LPR test, there was an evident change in morphology observed on the surface of the FSAl coating due to corrosion (Figure 65).

Porosity observed from the morphology characterisation of the FSAl coating was also confirmed by the porosity test. The penetration of permanganate solution to the steel substrate through the interconnected pores in the FSAl coating was thought to occur

indicated by the presence of a high level of Mn and O content on the surface of the coating after testing (Figure 70). Therefore, the FSAl coating was suggested to offer poorer barrier protection to the steel substrate as an EC replacement.

5.1.1.3 EDAl Coating

The EDAl coating had a Cr-based conversion layer on its surface. This layer contained cracks. The conversion coating was identified to be mainly composed of trivalent Cr, however, a low content of hexavalent Cr was also detected. The EDAl coating itself was a dense and uniform coating with a marked absence of cracking or pores from its cross-sectional observations (Figures 57 and 58). The cracks presented on the surface of the chromium conversion coating were not expected to decrease the barrier protection of the EDAl coating. The dense underlying EDAl was thought to protect substrates from any environmental penetration through the cracked conversion coating.

Compared to the EC coating, the EDAl exhibited a more noble E_{corr} (-699 mV) and a much lower corrosion current I_{corr} (5.36 $\mu A/cm^2$) as shown in Figure 63. After LPR testing, no significant change occurred in the morphology and composition of the surface of the EDAl coating (Figure 66). However, some pitting-like attack was noticed along the cracks of the trivalent Cr conversion coating, where underlying EDAl coating was exposed. No evident oxidation of the aluminium presented in these pitted areas, it was therefore believed that the dense EDAl coating could prevent the coating from further corrosion by penetration through the cracks of the conversion coating. The dense and uniform EDAl coating was thought to provide good sacrificial protection and have high corrosion resistance as an EC replacement.

The EDAl coating exhibited a structure with an absence of defect, which was further illustrated by its porosity test. After immersion in the $KMnO_4$ solution for 3.5 h, there was no MnO_2 formed on the surface of the coating (Figure 71). Though the cracks

were evident in the Cr conversion coating, $KMnO_4$ solution did not penetrate through the EDAl down to the substrate. This suggests good barrier protection provided by the EDAl coating.

5.1.1.4 As-deposited SermeTel 962 Coating

As-deposited SermeTel 962 coatings exhibited a structure consisting of Al particles dispersed in a phosphate/chromate binder (Figure 59). Marked diffusion was thought to occur between the binder and the Al particles, which suggested good bonding strength between the particles. From its cross-section (Figure 60), it was found that the Al particles were in an agglomerated form and no significant interconnected pores were observed in the coating. Therefore, pores in the coating were not expected to decrease the barrier protection property of the coating. Concerning the environmental issue, according to the requirement of Airbus, a chemical valence for Cr in the SermeTel coating was identified by XPS (Figure76). It was suggested that the Cr in the binder of the SermeTel coating was mainly composed of trivalent Cr and a low concentration of hexavalent Cr.

Compared to the EC coatings, with respect to corrosion resistance, LPR data indicated that the as-deposited SermeTel coating exhibited a lower corrosion current density of 9.99 $\mu A/cm^2$ (Figure 63). After the LPR test, only an increase in O content was observed on the surface of the SermeTel coating (Figure 67). The coating morphology seemed to remain the same after the LPR test, no evident corrosion was therefore thought to occur during LPR testing. The SermeTel coating also had the most positive E_{corr} (-487 mV) of all the sacrificial coatings used in this study. The coating may, therefore, have a less sacrificial protection to steel substrates, but it was also expected to have good galvanic compatibility with hard coatings (EHC and HVOF WC/Cr/Co coatings) due to the small difference in their free corrosion potential.

The SermeTel coating was not affected significantly in both morphology and

composition by the porosity test (Figure 72). From its original surface observation, the coating exhibited a porous structure. However, as discussed previously, the pores in the coating were discretely dispersed and good diffusion between the Al particles and binder was evident. Therefore, during porosity testing, the permanganate solution did not penetrate through these discrete pores easily. As an EC replacement, the SermeTel was suggested to provide a good barrier protection to the steel substrate.

5.1.1.5 Post-treated SermeTel 962 Coating

After a lightly abrading post-treatment, it was found that the Al particles were smeared and deformed, and the contact between each other appeared to increase (Figure 61). In this way, the electrical conductivity of SermeTel 962 coating was thought to be improved. Moreover, compared to the as-deposited SermeTel coating, in addition to the surface of the post-treated coating, Al particles were also dispersed in a more discrete manner in the coatings, which resulted in more interconnected pores (Figure 62). Therefore, the barrier protection properties of the SermeTel coating were expected to be decreased by the post-treatment.

In addition to the effects on the morphology, light abrading also affected the electrochemical properties of the SermeTel coating significantly. The abrading post-treatment deformed the spherical Al particles into a flat format. In this way, the Al occupied area on surface of the post-treated SermeTel coating increased considerably. Therefore, the post-treated SermeTel coating exhibited a more negative E_{corr} (- 672 mV) than the untreated one (Figure 63). Moreover, from the LPR test, its corrosion current also increased significantly to 72.6 $\mu A/cm^2$, which implied a reduced corrosion resistance. After the LPR test, some local seriously corroded areas were noted on the surface of the post-treated SermeTel coating (Figure 68). In these areas, more binder was exposed suggested by the presence of increased P and Cr content, and a significant increase in O content was also observed, which implied that

a serious oxidation occurred during the LPR test.

As observed in the morphological characterisations of the post-treated SermeTel coating, a light abrading post-treatment deformed the Al particles, which transformed the discrete pores in the SermeTel coating into interconnected forms. From the porosity test, these interconnected pores in the post-treated SermeTel coating made the penetration of $KMnO_4$ easier and an increased Mn and O content was detected (Figure 73). Therefore, the post-treatment was thought to reduce the barrier protection property of the SermeTel coating.

5.1.2 Characterisation of the Hard Coatings

5.1.2.1 EHC Coating

The EHC coating exhibited a dense, homogeneous structure containing 100 % Cr with a good adhesion to the substrate (Figures 50 and 51). Some cracks were present in the coating, and the longest one traversed the whole coating. A similar structure for an EHC coating was also observed by Aguero et al.[112]. The formation of the micro-cracks was suggested to result from the EHC forming in a highly stressed state during the electroplating process. From the porosity test, an evident increase in Mn and O content was observed on the surface of the EHC coating, which resulted from the reaction between the $KMnO_4$ solution and steel substrate (Figure 74). The cracks in the coating were thought to cause the penetration of $KMnO_4$ solution to steel substrate. Therefore, these cracks were suggested to reduce the barrier protection property of the EHC coating.

5.1.2.2 HVOF WC/Cr/Co coating

The HVOF WC/Cr/Co coating presented a structure with a range of size of WC particles dispersed in the Cr-Co metallic binder (Figure 52). This structure probably

results from the collapse of the molten droplets on the substrate during the thermal spraying process when metallic particles and the external surface of WC particles are thought to melt[53]. From the observation of the surface of the coating, the greatest area was occupied by WC phases and the spaces between them exposed the Cr-Co metallic binder. The metallic binder was thought to have a high activity and oxidised easily by showing a high level of O content (area 2 in Figure 52). Diffusion between the WC particle and the Cr-Co metallic binder was observed by the presence of W, C, Cr and Co in the binder area of the coating (area 4 in Figure 52). During the HVOF spraying process, the external part of the carbide particles melts along with molten metallic binder droplets when travelling through the flame. The impacting droplets are flattened on the surface of substrates and then rapidly cool to pile up and form the coatings. This results in the diffusion of W and C into the metallic binder and improves the binding strength between the two. The porosity of the HVOF WC/Cr/Co coating was identified in the porosity test (Figure 75). A serious penetration of $KMnO_4$ solution through the HVOF WC/Cr/Co coating to steel substrate was thought to occur shown by the presence of a high level of Mn and O content after the porosity test. Therefore, the HVOF WC/Cr/Co coating was thought to provide a relatively poor barrier protection to a steel substrate.

5.1.3 Galvanic Compatibilities of the Sacrificial and the Hard Coatings

The replacement of EC and EHC coatings for aircraft application has produced a modern problem concerning accelerated rates of galvanic corrosion between alternative coating materials. Airbus suggested HVOF coatings in the form of WC/Cr/Co to be used to replace EHC coatings. Al-based coatings, including FSAl, EDAl and SermeTel 962, were thought to be qualified instead of EC coating to provide sacrificial protection on non-wearing surfaces. However, in some cases when both coatings were applied to the same part and in contact, severe galvanic corrosion

between them was observed. Therefore, the severity of galvanic corrosion in EC/EHC coatings and their replacements was identified by quantitative electrochemical methods and the corrosion mechanisms are discussed in this section.

5.1.3.1 EC/EHC Coatings Galvanic Couple

The free corrosion potentials of the EC and EHC coatings were -738 and -499 mV respectively (Figure 77). A free corrosion potential difference of 239 mV presented in the EC/EHC coatings galvanic couple, where the sacrificial coating (EC) was expected to act as the anode and the hard coating (EHC) acted as cathode.

During galvanic corrosion testing for 15 days, the electrode potential of the EC coating was monitored (Figure 78 (a)). The electrode potential was initially approximately -750 mV, which was a mixed potential of the Cr conversion coating and the underlying EC coating. From Figure 78 (a), a plateau presented at the first 10 h in the curve, which may be attributed to the barrier protection of the chromate conversion coating. After that, a sharp decrease in the electrode potential occurred, when the cracking of the conversion coating was thought to appear and expose the underlying EC coating. As discussed previously, Cd was oxidised to form an oxide film which could provide barrier protection. Therefore, it may result in a gradual increase in the electrode potential after the sharp decrease. After galvanic corrosion of approximate 160 h, the electrode potential decreased gradually, this may be caused by the breakdown of the oxide film with time. The galvanic current of the EC/EHC couple decreased significantly over the first 10 h and tended to be stable at 5 μA (Figure 78 (b)). Slight galvanic corrosion was expected to occur in an EC/EHC couple.

After galvanic corrosion, a cracking Cr conversion coating and high O content was generally evident on the EC coating surface, which was similar to the observation after the LPR test (Figure 79). Moreover, many nodules consisting of Cd, O and Cl

were formed on the surface of the EC coating. It is possible that the Cd electrochemically reduced dissolved O from the electrolyte. The subsequent OH^- production may be responsible for the high O content on both the general areas and nodules on the surface of the EC coating. From the EDX results, it was also noted that Cr was absent from the nodules observed on the EC coating. The formation of Cd-based nodules upon the passivation film was speculated as a possible form of Cd whisker growth as these features have been known to form on EC coatings[113]. These Cd-based nodules were thought to then react with Cl^- in the electrolyte to form chloride-based corrosion products.

The EHC coating was thought to be cathode as galvanic coupled to the EC coating, so there was no significant change in morphology and composition expected on the surface of the EHC coating after galvanic corrosion, which was proved by observation (Figure 80). However, many nodules containing Cd and Cl also presented on the surface of the EHC coating, but in a different morphology from the nodules on the surface of the EC coating. General anodic oxidation of the EC coating in the coupled state would have released Cd^{2+} into solution. These may have precipitated onto the EHC cathode during galvanic corrosion. It has been reported that Cd^{2+} may react with Cl^- in aqueous solution[114], it is therefore suggested that in the present investigations this has resulted in the corrosion product containing Cd and Cl on the cathode.

Further observations of these nodules in their cross-sections are shown in Figures 80 and 81. The nodule on the surface of the EC coating showed a physical connection to the underlying EC coating through a crack on the top of the conversion coating. Therefore, the nodules observed on the EC coating could be a form of corrosion product or the spontaneous growth of a form of nodular ‘whisker’ from the EC coating through the cracks in the passivation film. It has been reported that Cl can accelerate whisker growth from hot dipped coatings of Zn[115]. It could be construed that the presence of the Cl in the nodules may have a similar effect in this instance. It might be suggested that

the corrosive chloride solution promoted cracking of the top passivation layer of the EC coating and exposed the crystalline Cd beneath, thus providing the initiation of Cd whisker-like growth. The nodule on the EHC coating had a porous structure and an evident gap between it and the EHC coating implied a poor adhesion to the EHC coating. That was thought to be a $CdCl_2$ -like corrosion product attached on the EHC coating. From Figure 80, which was representative of the surface of the EHC coating after galvanic corrosion, it can be suggested that almost 20% of the surface area was covered by this type of Cd-based deposits. Thus it may be construed that during galvanic corrosion, the EHC coated electrode surface became predominantly a surface of Cd and Cr, which decreased the galvanic potential difference and corrosion current as evident in Figure 78 (b).

5.1.3.2 EC/HVOF WC/Cr/Co Coatings Galvanic Couple

The free corrosion potentials of the EC and HVOF WC/Cr/Co coatings were -738 and -502 mV respectively (Figure 77). A free corrosion potential difference of 236 mV presented in the EC/HVOF WC/Cr/Co coatings galvanic couple, where the sacrificial coating (EC) was expected to act as anode and the hard coating (HVOF WC/Cr/Co) as cathode.

During the galvanic corrosion test, it was found that the electrode potential of the EC coating fluctuated in a wide range of approximately 30 mV and increased with time, which was the reverse of the trend for the EC and EHC couple (Figure 83 (a)). The serious fluctuation of the electrode potential implied some significant changes in the morphology and composition of the surface of the EC coating during galvanic corrosion. Therefore, multi-reactions were expected to occur on the surface of the EC coating due to galvanic corrosion. From the galvanic current of the EC/HVOF WC/Cr/Co coatings galvanic couple (Figure 83 (b)), it was also noted that negative corrosion currents were observed in the first 50 h of testing, which indicated that a

reversal of the galvanic couple had occurred. After 50 h, the galvanic corrosion current increased to a positive value and tended to be stable at about 25 μA, which was much higher than the corrosion current for the EC/EHC coatings couple. Compared to its coupling to the EHC coating, the EC coating presented poor galvanic compatibility with the HVOF WC/Cr/Co coating.

After the galvanic corrosion test, the general surface area of the EC coating exhibited a similar morphology to that observed in the EC/EHC coatings galvanic couple (Figure 84). The similar corrosion mechanism for it was as suggested and discussed previously. With respect to composition, Cl was also detected on the surface of the galvanic corroded EC coating after galvanic corrosion, which was thought to be from the electrolyte and promote the cracking of the top passivation layer.

Moreover, two distinct nodule morphologies were observed on the EC surface. One exhibited an entangled morphology, named ‘nodule 1’, as area 2 in Figure 84 shows. From its EDX data (Figure 84), nodule 1 appeared to be a $CdCl_2$ product. After sectioning, the nodule 1 had a dense structure as seen in Figure 85 (a). Further investigations in this nodule by TEM/EDX were shown in Figures 86 and 87. From the investigations, it was found that the nodule shows a microstructure, which appeared both granular and porous. From compositional analysis using EDX, the nodule was 65.4 at.% Cl, 34.6 at.% Cd, an atom ratio of almost 2:1, probably suggesting $CdCl_2$ corrosion product. From Figure 87, it can be seen that the diffraction pattern data from nodule 1 matched the standard data for $CdCl_2$, which further supported that the nodule was $CdCl_2$ corrosion product. As discussed previously, a reversal of the galvanic couple was speculated to occur in the EC/HVOF WC/Cr/Co coatings’ couples during galvanic corrosion. Therefore, both anodic and cathodic reactions were expected to occur on the surface of the EC coating. During galvanic corrosion, Cd^{2+} was released into the electrolyte from the EC coating due to general anodic oxidation. As a reversal of the galvanic couple occurred, the EC

coating transformed became cathodic. In this way, Cd^{2+}, which may react with Cl^- in the electrolyte, deposited on the surface of the EC coating again, but as a chloride compound. The presence of $CdCl_2$corrosion products on the EC coating, which were also observed on the surface of the cathodic EHC coating as galvanic coupled with EC coating, further supported that a reversal of the galvanic couple occurred between the EC and the HVOF WC/Cr/Co coatings.

The other nodule showed an acicular morphology, named ‘nodule 2’, as shown in area 4 in Figure 84. From the observations of its cross-section (Figure 85 b), the interior of the nodule 2 presented a dense microstructure and the exterior a more acicular growth format. Compared to nodule 1 in term of composition, more oxide presented in nodule 2 with much less Cl content. From further investigation by TEM/EDX (Figures 88 and 89), it was found that the nodule 2 interior was essentially pure Cd and presented a denser microstructure than the exterior area. The latter was thought to be CdO_2 with a composition of 33.2 at.% Cd and 66.8 at.% O. It is therefore speculated that the nodule 2 growth began with metallic Cd and formed with subsequent oxidation during galvanic corrosion. Figure 89 shows that a dense deposition of the nodular 2-like species on the surface of the EC coating. Some large cracks, which penetrated into the EC coating, were evident on the passivation coating and the ‘crystalline’ nodules appeared to have been ruptured by the cracks. The nodules were therefore thought to form before cracking of the passivation film. The penetration of the crack from the coating into the nodules implied that a strong adherence was exhibited between the nodules and EC coating. This further supports the suggestion that the acicular Cd-based nodules were probably as a result of Cd ‘whisker-like’ growth. The high rate of this growth on the EC coating seemed to promote the cracking of the Cr conversion coating into the underlying EC coating, as observed in Figure 85 (b). The evident crack went through the conversion film into the EC coating and caused the penetration of electrolyte into the underlying EC coating. In this way, in these local cracking regions, the area of anodic Cd was much smaller than the area of cathodic

HVOF WC/Cr/Co coating, which was thought to result in severe galvanic corrosion as Figure 85 (b) shows.

Compared to the EC coating, the HVOFWC/Cr/Co coating presented a more negative free corrosion potential (Figure 77) and was expected to act as the cathode during galvanic corrosion. After galvanic corrosion trials, many crystalline Cd-containing deposits with an average size of about 30 μm were observed on the HVOF WC/Cr/Co coating as shown in Figure 91. These were thought to result from the precipitation of Cd^{2+} and Cl^{-} on the cathode as happened on the EHC coating galvanic coupled with the EC coating. A higher galvanic corrosion current occurred with the Cd and HVOF WC/Cr/Co coating couple than the Cd and EHC coating couple, so a greater reduction of dissolved O was expected on the HVOF WC/Cr/Co coating during galvanic corrosion and significant increases in O content (from reaction with generated hydroxyl species) were observed on both the general area and Cd-based deposits. Moreover, it was also noted that in addition to the crystalline Cd-containing deposits, many similar features also containing Cd and Cl were observed on the surface of the HVOF WC/Cr/Co coating after galvanic corrosion, as Figure 92 shows. These are thought to be semi-dissolved products from the original crystalline Cd-based deposits due to anodic reaction on surface of the HVOF WC/Cr/Co coating during the reversal of the galvanic couple of the EC and HVOF WC/Cr/Co coatings as discussed previously.

Being the cathode, no serious corrosion was expected to occur on the HVOF WC/Cr/Co coating during galvanic corrosion. However, in addition to the features shown above, severe local corrosion was observed on the surface of the HVOF coating coupled with the EC coating (Figure 93). The HVOF WC/Cr/Co coating was totally removed from the surface as area 2 in Figure 93. A mixture of O, Al, Fe and Cd remained in the area where the coating detached. In order to identify the source of O and Al, which was not expected to be present, the interface between the HVOF

WC/Cr/Co and the steel substrate was then investigated as Figure 94 illustrates. It was noted that there appeared to be good adhesion between the HVOF coating and the substrate, but at some sites, a phase consisting of Al and O was found. These phases are suggested to be Al_2O_3 particles originally trapped on the surface of the substrate from the pre-treatment grit blasting confirmed by the HVOF coating supplier. A local corrosion area was ablated by FIBSEM to observe its cross-section as illustrated in Figure 95. A phase different from the HVOF WC/Cr/Co coating was observed under the local corrosion area, which was Al_2O_3 as highlighted in Figure 94. It can therefore be concluded that the presence of Al_2O_3 at the interface of the HVOF coating and substrate caused serious local corrosion of the coating and resulted in the detaching of the coating. It was supposed that during the galvanic corrosion test, the electrolyte penetrated the HVOF coating due to its porosity. It was thought that this allowed the trapped Al_2O_3 to form a localised galvanic-like cell with the surrounding HVOF coating, though Al_2O_3 is not expected to be electrochemically active due to its low conductivity. In the local galvanic-like corrosion, the trapped Al_2O_3 probably acted as cathode, while the Co-Cr metallic binder of the HVOF coating became anode, which resulted in corrosion and removal of the HVOF coating. The hypothesis of the corrosion mechanism between HVOF WC/Cr/Co coating and Al_2O_3 particles are investigated and discussed in Section 5.2.

5.1.3.3 FSAl/HVOF WC/Cr/Co Coatings Galvanic Couple

In the characterisation of the FSAl, the coating presented the poorest perceived barrier protection property and LPR of all the sacrificial coatings tested. Additionally, due to an evident difference in the free corrosion potential of FSAl and HVOF WC/Cr/Co coatings, a poor galvanic compatibility was expected. During galvanic corrosion, the electrode potential of the FSAl coating decreased sharply to -1050 mV in the first 10 h. During the initial stage of the galvanic corrosion, the Al of the coating was thought to be oxidized quickly and to form an oxide film. The high level of interconnected

pores in the coating may promote the penetration of electrolyte into the coating, which may cause the underlying Al to be activated and resulted in a significant decrease in the electrode potential. After that, with galvanic corrosion time, more and more Al_2O_3 corrosion products were expected to form on the surface of the coating. In this way, the electrode potential then increased gently to -950 mV, which was much more negative compared to the EC coating as galvanically coupled with a HVOF WC/Cr/Co coating. The galvanic current of the galvanic couple also increased to its maximum (~270 μA) in the initial stage of the corrosion, which followed the tendency of the electrode potential vs. time. After that, it decreased gradually, but even its minimum value was still much higher (greater than 50 μA) than the EC/HVOF WC/Cr/Co coatings galvanic couple. This implies that as an EC replacement, the FSAl may have a poor galvanic compatibility with HVOF WC/Cr/Co coating.

After galvanic corrosion, as Figure 97 shows, severe corrosion of the FSAl coating was observed. In the central area of the surface of the coating, relatively less corrosion was evident in the underlying area and the Al in the top area of the coating was oxidized into powdery corrosion products, which were easily removed (Figure 97 (a)). The presence of Cl in the corrosion products may imply attack from corrosive Cl^- in electrolyte. In the edge area of the surface, the FSAl coating was transformed into essentially an oxide film with large cracks (Figure 97 (b)). The different corrosion severity from the centre to the edge of the surface of the coating was thought to be caused by galvanic corrosion current distribution on the surface. A possible mechanism for it was suggested according to Faraday's law[116]. During galvanic corrosion, a current presented in a galvanic couple may generate a time varying magnetic field and this kind of magnetic field could induce an electric field in opposite direction of the galvanic current on the surface of anode. This electric field is proportional to the magnetic field, which is stronger in the centre than the edge. Therefore, in the centre area on the surface of anode, the decrease in corrosion current by the electric field is greater than in the edge area. In this way, the edge of the

surface of FSAl coating exhibited more serious corrosion than the centre. A similar galvanic corrosion current distribution on a flat surface has also been reported by Song[117]. The severe corroded FSAl coating was not expected to provide sufficient sacrificial and barrier protection to steel substrate.

With respect to the HVOF WC/Cr/Co coating, as Figure 98 illustrates, no significant local corrosion, such as that noted previously, was observed on the surface of this HVOF coating. This may result from the absence of any Al_2O_3 trapped at the interface from the pre-treatment. However, it was noted that some evident depressed features were present on the surface of the HVOF coating. From the EDX results (Figure 98), the significant oxidation and decarburisation presented on the surface of the coating implied the overall oxidation of C, which diffused in the binder and in the carbides. A similar corrosion mechanism of HVOF WC/Cr/Co coatings has also been reported[118,119, 120]. Corrosion in the metallic binder was also thought to occur during galvanic corrosion. As discussed previously, the Cr-Co metallic binder exhibited significant corrosion and caused the detaching of the coating when coupled to any underlying trapped Al_2O_3 particles. It was speculated that the Al was oxidised in the FSAl coating due to galvanic corrosion and the oxidised Al content increased with time, which was thought to decrease the electrochemical activity of the FSAl coating. Meanwhile, the active metallic binder in the HVOF WC/Cr/Co coating presented an anodic behaviour and was oxidised into ions dissolved in the electrolyte. The corrosion of the metallic binder decreased the cohesive strength of WC particles and resulted in the formation of the pores in the coating.

5.1.3.4 EDAl/HVOF WC/Cr/Co Coatings Galvanic Couple

During galvanic corrosion testing, the electrode potential of the anodic EDAl coating fluctuated over a sizeable range of about 15 mV and decreased slowly from approximately -730 to - 740 mV in the first 250 h (Figure 99 (a)). This could be

attributed to the oxidation of trivalent-Cr-based conversion coating on the EDAl coating. The dissolution of the conversion coating decreased its barrier protection to the underlying Al and promoted the penetration of electrolyte to the Al. In this way, the Al was oxidised to form dense oxide, which was thought to prevent further penetration by electrolyte whilst intact. The repetitive 'making and breaking' of the Al_2O_3 on the surface of the EDAl coating during galvanic corrosion may result in the fluctuation of the electrode potential. A significant decrease in the electrode potential to approximately -760 mV occurred between 250 and 350 h during the corrosion (Figure 99 (a)), which may imply more marked damage, such as the detaching of a large area of the oxide films, in the coating. The galvanic current of the EDAl/HVOF WC/Cr/Co coating decreased sharply from 160 μA over the first 5 h and tended to stabilise at about 17 μA, which was three times the galvanic current from the EC and the EHC coatings galvanic couple. The formation of the Al_2O_3 film was thought to decrease and stabilise the galvanic current in a short time, but compared with the galvanic couple of the EC and the EHC coatings, the EDAl and the HVOF WC/Cr/Co coatings were expected to have a poorer galvanic compatibility as suggested by the presence of the relatively high galvanic current.

After the galvanic corrosion, a difference in the level of corrosion between the centre and edge areas was also observed on the surface of the EDAl coating as had been on the FSAl coating. The centre area of the EDAl coating presented less corrosion than the edge area. An absence of Cr and a significant increase in O at the surface of the coating implied that the removal of the Cr passivation coating from the EDAl coating. As previously mentioned, the thin Cr passivation coating on the EDAl coating was mainly made up of trivalent Cr, which acted as an anode initially and dissolved. The underlying Al coating was also oxidised after the detaching of the conversion coating. In the 'less corrosion' areas, the oxidation of the EDAl coating was evident, but the morphology of the general area of coating was not affected significantly (area 2 in Figure 100). Some Al_2O_3 was also observed as a corrosion product (area 1 in Figure

100), which was powdery and presented poor adhesion to the coating. As discussed previously, the galvanic current density exhibited higher at the edge than the centre of a flat surface. As Figure 101 illustrates, much more serious corrosion was observed at the edge of the EDAl coating after the galvanic corrosion. A significant increase in the powdery Al_2O_3 corrosion product content was observed on the surface of the coating. The severe oxidation of the Al also caused cracking of the coating. The sacrificial and barrier protection properties of the EDAl coating were suggested to be weakened after galvanic corrosion.

The HVOF WC/Cr/Co coating acted as the cathode in the galvanic cell coupled to the EDAl coating. However, from Figure 102, severe local corrosion was observed on the HVOF WC/Cr/Co coating. In the general areas of the surface (presented as area 2 in Figure 102), severe decarburisation was also observed, which implied that general corrosion may occur on the HVOF WC/Cr/Co coating as discussed for the FSAl/HVOF WC/Cr/Co coatings galvanic couple. The local corrosion areas (shown for example as area 1 in Figure 102) were observed to be irregularly dispersed across the surface. From EDX analysis, the severe corrosion only exhibited in the areas of the coating, where Al_2O_3 particles presented at the interface. This further supported the assumption that the alumina accelerated the corrosion of the HVOF WC/Cr/Co coating.

5.1.3.5 SermeTel 962/HVOF WC/Cr/Co Coatings Galvanic Couple

From the characterisation, the SermeTel coating presented a high LPR value, low porosity and a small difference in the free corrosion potential compared to the HVOF WC/Cr/Co coatings. A good galvanic compatibility for the SermeTel 962 and the HOVF WC/Cr/Co coatings was expected. From Figure 103, during galvanic corrosion with a HVOF WC/Cr/Co coating, the electrode potential of the SermeTel 962 started

at approximately -400 mV, which was closest to the free corrosion potential of the HVOF WC/Cr/Co coating. The electrode potential then decreased immediately to -610 mV in a short time. The penetration of electrolyte into the SermeTel coating resulted in more Al particles being exposed, which increased the activity of the coating. After that, the electrode potential decreased much more gradually and tended to stabilise at about -670 mV. The significant oxidation of Al particles and Cr in the coating was expected, and this hindered the further corrosion of the coating. The galvanic current of the SermeTel/HVOF WC/Cr/Co coatings galvanic couple presented a similar tendency as the electrode potential with time and exhibited stability at about 15 μA, which may imply that the SermeTel coating had a better compatibility than the EC coating with the HVOF WC/Cr/Co coating.

After galvanic corrosion, it was found that Al particles in the SermeTel coating were covered by crystalline structured oxide films (Figure 104). The oxide films were thought to be from the oxidation of Al particles and binder in the coating. Moreover, the oxide films increased the average size of the Al particles. In this way, the spaces between the particles were occupied by the dense oxide corrosion products. Therefore, the porosity of the coating was reduced significantly (Figure 105). The formation of the oxide films did not show any evident effects on the morphology of the coating. Compared to the other sacrificial coating, no evident defects, such as cracks or pores, were observed in the coating after galvanic corrosion with the HVOF WC/Cr/Co coating. Therefore, the SermeTel coating presented good galvanic corrosion resistance with the hard coating as an EC replacement.

It was also noted that some iron oxide like corrosion products were detected in the SermeTel coating after the test. This was not expected due to there being no evident damage presented in the coating (area 2 in Figure 104). The Fe containing area was sectioned to identify its source (Figure 105). It was found that the SermeTel coating under the Fe containing phase remained intact. Therefore, the Fe-based corrosion

products observed on the SermeTel coating were presumed to be from the coupled HVOF WC/Cr/Co coated steel substrate rather than the SermeTel itself.

The severe local galvanic corrosion caused by the trapped Al_2O_3 was also observed in the HVOF coating coupled with the SermeTel coating (Figure 106). The exposed area consisted of Al, O and Fe. These serious corroded areas were thought to present anodic behaviour during galvanic corrosion. In this way, exposed steel substrate was oxidised into Fe ions, dissolved in the electrolyte. This may be the source of the Fe on the surface of the SermeTel coating. The similar morphology and decarburisation were also observed in the other highlighted area of the HVOF coating as discussed previously. It is suggested that the increased oxidised Al content in the sacrificial coating may cause the reverse galvanic reaction of the Cr-Co metallic binder in the HOVF WC/Cr/Co coating, which resulted in the overall corrosion. The corrosion products from the Cr-Co metallic binder were observed in the local galvanic corrosion area as Figure 107 illustrates. The powdery oxide-like corrosion products were thought to result from the oxidation of exposed steel substrate. There was also some Cr-based metallic binder in the local corrosion area, which may imply that the Cr in the binder had higher corrosion resistance than the Co. From the cross-section of the local corrosion area, it was noted that the HVOF WC/Cr/Co coating adjacent to the Al_2O_3 presented higher porosity than the other areas which agrees with the suggestion.

5.1.3.6 Post-treated SermeTel 962/HVOF WC/Cr/Co Coatings Galvanic Couple

The light abrasion post-treatment of the SermeTel coating decreased its free corrosion potential significantly, which may have decreased the galvanic compatibility with the HVOF WC/Cr/Co coating. Thus it was expected that a high corrosion current would be evident between the post-treated SermeTel coating and the HVOF WC/Cr/Co

coatings. From Figure 109, the electrode potential of the post-treated SermeTel coating was initially about -700 mV, which was much more negative than the value for the untreated SermeTel coating. As discussed previously, the light abrasion flattens the Al particles in the coating, which increases the presented area of Al on the surface of the coating. The surface of the post-treated SermeTel coating was thought to exhibit high anodic activity. During galvanic corrosion, the electrode potential increased to approximately -650 mV in a fluctuating manner over a sizeable range of 100 mV, which may be caused by the repetitive formation and breakdown of Al_2O_3 films on the surface of the coating during the corrosion test. The results for the corrosion current showed that it fluctuated in a range between positive and negative, which also agreed with the presence of the reverse galvanic reaction in the galvanic couple.

After the galvanic corrosion, a significant difference presented between the corrosion of the centre and the edge areas of the surface of the post-treated SermeTel coating. In the central area of the coating, a low level of corrosion was observed (Figure 110). The Al phases presented a high level of oxidation, but did not cause any evident defects on the surface of the coating. However, in the edge area of the coating, severe corrosion was observed. As Figure 111 illustrates, the coating was damaged by the absence of the phosphate/chromate binder, and the Al phases were transformed into cracked Al_2O_3 films. The corrosive Cl^- also presented an evident attack into the coating by the presence of Cl in the oxidised coating. The light abrasion post-treatment decreased the galvanic corrosion resistance of the SermeTel coating with HVOF WC/Cr/Co coating by two possible mechanisms. Firstly it was possible that there was an increased content of interconnected pores in the coating caused by the post-treatment. As discussed previously, the isolated pores in the as-deposited SermeTel coating could be occupied by the oxide corrosion products and provided a further barrier protection. However, the pores were interconnected in the post-treated coating and promoted the penetration of electrolyte through the whole coating. The

formation of the oxide corrosion products in the post-treated coating did not provide evident barrier protection due to the large size of the interconnected pores. Secondly, the other possible mechanism was thought to be the decreased area of anodic Al phases by the post-treatment. Although the abrasion treatment flattened the Al particles and increased the connection of each other, the flattened Al area are much smaller than the overall surface area of the spherical Al particles presented on the surface of the SermeTel coating. Therefore, the decreased area ratio of anode to cathode in the post-treated SermeTel/HVOF WC/Cr/Co coatings galvanic couple accelerated the corrosion of the anodic Al phases of the post-treated SermeTel coating. The light abrasion post-treatment resulted in a poor galvanic corrosion resistance of the SermeTel coating with the hard coating, which was not suitable for the coating as an EC replacement.

Due to the reverse galvanic reaction, oxidation was observed on the HVOF WC/Cr/Co coating (Figure 112). Similar changes in the morphology of the HVOF coating were observed to that coupled to the FSAl coating. A similar corrosion mechanism to that responsible for the formation of the Al_2O_3 on the sacrificial coating causing the corrosion of the exposed Cr-Co metallic binder on the surface of the coating, may be responsible for the changes in the HVOF coating. Similar decarburisation occurred on the surface of the coating after galvanic corrosion, which indicated the overall corrosion of the C from both carbide and binder in the coating as discussed previously.

5.2 Corrosion Resistance of HVOF WC/Cr/Co Coating

From the free corrosion potential investigations, the HVOF WC/Cr/Co coating was more noble than the sacrificial coatings, so it was expected to present cathodic in galvanic corrosion. However, the HVOF WC/Cr/Co produced unexpected anodic

corrosion behaviour when coupled to the sacrificial coatings. It was also found, in particularly, that severe local corrosion of the HVOF WC/Cr/Co coatings occurred through the presence of the underlying alumina particles, used for the pre-treatment of the steel substrate. Therefore, in this chapter, the corrosion mechanisms of HVOF WC/Cr/Co are discussed and the effects of Al_2O_3 particles on the corrosion of the coating are also elucidated.

5.2.1 Effects of Al_2O_3 on the Corrosion of HVOF WC/Cr/Co Coating

Through the comparison between the corrosion behaviour of the HVOF WC/Cr/Co coating during immersion in NaCl solution with and without the addition of Al_2O_3, the effects of the latter on the corrosion of the coating were identified.

5.2.1.1 Immersion Test in 3.5 wt.% NaCl with Al_2O_3 Particles

The possible effects of Al_2O_3 in the environment on the corrosion of the HVOF WC/Cr/Co coating were investigated by immersion testing in NaCl solution containing Al_2O_3 particles. After the normal immersion test in 3.5 wt. % NaCl solution, the severe local corrosion, initially observed in the galvanic corrosion tests, also occurred on the surface of the HVOF WC/Cr/Co coating (Figure 113). The removal of the coating exposed the underlying Al_2O_3 particles. Compared to the galvanically corroded HVOF WC/Cr/Co coating, most areas on the surface of the coating presented good corrosion resistance during immersion illustrated by the absence of evident changes in the morphology and composition of the coating. Moreover, the severe decarburisation, which occurred on the coating due to galvanic corrosion, was not evident the coating after immersion. This indicated that the severe local corrosion was mainly caused by the trapped Al_2O_3 particles rather than the galvanic corrosion with the sacrificial coatings. The HVOF WC/Cr/Co coatings

presented poor corrosion resistance and adhesion to the steel substrate when underlying Al_2O_3 particles were present. It was suggested that the electrochemically stable Al_2O_3 particles present under HVOF WC/Cr/Co coatings, may promote the anodic behaviour of the active Cr-Co metallic binder to form a micro-galvanic cell. In this way, the oxidation rate of the metallic binder was accelerated, which resulted in the dissolution of the metallic binder into electrolyte and the detaching of HVOF WC/Cr/Co coatings.

Al_2O_3 particles were added into the immersion solution (3.5 wt.% NaCl) used for the immersion test of the HVOF WC/Cr/Co coating. After immersion, some pitted areas were evident on the surface of the HVOF WC/Cr/Co coating (Figure 114). From compositional analysis, the pitting area was thought to be the metallic binder with carbon diffused from WC particles during thermal spraying. The absence of cobalt in the binder area indicated its selective oxidation during immersion. It has been reported[118,119] that in a HVOF WC/Co coating, WC phases and Co binder could form micro-galvanic cells to accelerate the corrosion of Co. There was no evident pitting corrosion observed on the coating after immersion in the solution without Al_2O_3 particles. Therefore, it can be suggested that Al_2O_3 particles presented a more effective driving force to promote the corrosion of Co in the binder. A high content of Cr remained in the pitting area, which may indicate better galvanic compatibility than Co with Al_2O_3 particles and WC phases. The addition of Cr into the Co binder in a HVOF WC/Cr/Co coating to improve the galvanic compatibility of the metallic binder has also been reported[118]. The content of Al_2O_3 particles and the presence of dispersant in the immersion solution did not present any significant effects on the corrosion of the coating and the similar areas of pitting were also observed on the coating as long as Al_2O_3 particles presented in solution. All the pitting areas presented a high level of Cr content and the absence of Co. They further supported the idea that Co in the metallic binder was prone to corrode during immersion due to the presence of Al_2O_3 particles in solution.

5.2.1.2 Immersion Test of Al_2O_3 Grit Blasted HVOF WC/Cr/Co Coatings in 3.5 wt.% NaCl Solution

Al_2O_3 particles were also introduced onto the surface of HVOF WC/Cr/Co coating by using such particles in a grit blasting treatment. Shallow depressions and some trapped Al_2O_3 particles were observed on the surface after light grit blasting (Figure 118). After 7 days of immersion in 3.5 wt.% NaCl solution, the Al_2O_3 trapped on the surface of the HVOF WC/Cr/Co coating by grit blasting, also resulted in the pitting corrosion as observed previously on the HVOF WC/Cr/Co coatings after immersion in solutions containing Al_2O_3 particles. The pitting corrosion mainly occurred around the trapped Al_2O_3 particles on the surface of the coating (Figure 119). EDX data shows that in the local pitting corrosion area, a high level of the metallic binder presented and no underlying steel substrate was evident, which indicated that the detected Al_2O_3 were from grit blasting post-treatment rather than that trapped at the interface. Moreover, the binder remaining in the pitting areas exhibited a much higher Cr content than the binder of the as-deposited coating, which implied a significant corrosion of cobalt in the binder. Many similar local pitting corrosion areas (Figure 120) were observed on the surface of the Al_2O_3 grit blasted HVOF WC/Cr/Co coatings after immersion. Therefore, it was suggested that Al_2O_3 particles, present in the HVOF WC/Cr/Co coating or its environment, may form micro-galvanic cell with the active metallic binder in the coating and accelerate the corrosion of the binder. Moreover, compared to the Cr, the Co in the binder presented poorer corrosion resistance in the micro-galvanic corrosion. The Al_2O_3 in particular trapped at the interface caused serious galvanic corrosion of the binder close to it when connected by electrolyte. In this way, the corrosion of the binder decreased the adhesion of the coating to the substrate, which resulted in a detachment of the coating.

5.2.1.3 Electrochemical Properties of the HVOF WC/Cr/Co Coating

From the anodic polarisation curve of a HVOF WC/Cr/Co coating in 3.5 wt.% NaCl (Figure 121), the anodic corrosion of the coating was thought to be divided into the following stages: The first stage started at approximately 250 mV, at which the oxidation of the active metallic binder in the coating occurred. With the dissolution of the binder into the electrolyte, the second stage was thought to happen at about 700 mV. At this point, there was an initial loss of WC particles from the coating due to the increased loss of the metallic binder, which reduced the bonding strength between the WC phase and the metallic binder. The dissolved binder and the detachment of the WC particles may increase the porosity of the coating and promote the penetration of electrolyte into the coating. Therefore, the overall corrosion occurred in the coating as P3 and P4 (850 and 1100 mV) in Figure 121 imply. A passivation-like behaviour was also observed at a high anodic potential, higher than 1.4 V. The passivation-like behaviour has also been reported by other researches[121, 122, 123] and has been suggested to be related to the oxidation of W and C dissolved in the binder and in the carbide phases. The corrosive dissolution was observed on the surface of the coatings after anodic polarisation in 3.5 wt.% NaCl solution (Figure 122). Underlying WC particles were exposed after the corrosion of the top layers of the HVOF WC/Cr/Co coating (Figure 123). Some cracks can also be seen around WC particles, which implied that the corrosion initially occurred at the WC/metallic binder interfaces (Figure 122). These observations concerning the morphology agreed with the assumption of the anodic corrosion mechanism of the HVOF WC/Cr/Co coating.

Moreover, the anodic polarisation behaviour of the HVOF WC/Cr/Co coating in an electrolyte with Al_2O_3 particles was also investigated. It was observed that the presence of the Al_2O_3 particle in the electrolyte resulted in a significant decrease from 250 mV to -400 mV in the potential, at which the corrosion of the metallic binder in

the coating initially occurred. The corrosion rate of the metallic binder also increased due to the Al_2O_3 particles as shown by much higher corrosion current during anodic polarisation. This further supported the micro-galvanic cell mechanism as discussed previously between Al_2O_3 particles and the metallic binder in the coating. As the higher corrosion current indicated, more severe corrosion was also observed on the surface of the HVOF WC/Cr/Co coating after the anodic polarisation tests in the electrolyte containing Al_2O_3 particles. Removal of the metallic binder and the occurrence of the remaining WC particles were evident on the surface of the coating. Only a little Co was detected in the remaining metallic binder, which agreed with the previous observation that Co presented poorer corrosion resistance in the Co-Cr metallic binder.

Potentiostatic tests of the HVOF WC/Cr/Co coatings at the potentials of 250 and 700 mV, were carried out to investigate the corrosion mechanism of the coating further. During the potentiostatic test at 250 mV (Figure 125), the current presented stable and increased slightly after 5000 s. This was attributed to the metallic binder corroding initially and with time the loss of metallic binder resulted in the detaching of the WC particles causing the corrosion current to increase. The potential of 250 mV was suggested as the start of the corrosion of the metallic binder in the HVOF WC/Cr/Co coating from the anodic polarisation tests. After the potentiostatic test at 250 mV, cracks and pores were observed to be evident around the WC phases and also some severe corrosion was evident, where the top layer of the coating had detached (Figures 126 and 127). At the low anodic potential, the corrosion was in a localised aggressive form around the WC/metallic binder interfaces on the surface of the coating.

From the potentiostatic test at 700 mV, a higher stable corrosion current presented and a sharp increase was observed just after 1000 s. The metallic binder was thought to corrode at a higher corrosion rate at the high anodic potential, which caused the more premature loss of the WC particles. After the potentiostatic tests at the high anodic

potential, the WC particles detached from the coating due to the loss of the surrounding binder (Figure 128). From its cross section, the top area of the coating exhibited a looser structure with several pores left by the loss of WC particles (Figure 129). Therefore, at a high anodic potential, the corrosion of the HVOF WC/Cr/Co coating starts with dissolution of the metallic binder at the interface of WC particles and binder and then the WC particles become detached.

5.2.2 Galvanic Corrosion of HVOF WC/Cr/Co Coating

In the galvanic corrosion investigations between the sacrificial and the HVOF WC/Cr/Co coatings, some severe local corrosion areas were observed due to underlying Al_2O_3 particles as discussed previously (Figure 93). However, for most areas on the surface of the HVOF WC/Cr/Co, oxidation of the coating was observed, but there was no significant damage presented after galvanic corrosion. The HVOF WC/Cr/Co coating was regarded as a hard coating and cathodic during galvanic corrosion with the sacrificial coatings. Therefore, no overall severe corrosion was expected to occur on the HVOF WC/Cr/Co coating, though some potential reversal reaction and anodic behaviour were observed on the coating during galvanic corrosion tests.

However, from the electrochemical investigations into the corrosion of the HVOF WC/Cr/Co coatings, the Co-Cr metallic binder in the coating exhibited evident anodic corrosion through the micro-galvanic cell with the WC phase or Al_2O_3 particles. Moreover, particularly during the galvanic corrosion of the HVOF WC/Cr/Co and EC coating, a negative galvanic current implied that a potential reversal in the galvanic reaction had taken place and overall corrosion occurred on the HVOF WC/Cr/Co coating (Figure 83 (b)). So the HVOF WC/Cr/Co coating was further investigated in term of cross section after galvanic corrosion with the EC coating.

From Figure 130, after the galvanic corrosion, the HVOF WC/Cr/Co coating around

the Al_2O_3 particles remaining at the steel/coating interface, presented a very porous structure. Loss of WC particles and pores were observed, which agreed with previous observation of some of the local severe corrosion areas caused by Al_2O_3 particles on the surface of the HVOF WC/Cr/Co coating. Moreover, a significant reduction in the thickness of the HVOF WC/Cr/Co coating from 170 to < 50 μm was observed after the galvanic corrosion with the EC coating over a period of 15 days. However, from its cross section, the surface of the coating was thought to corrode uniformly during the galvanic corrosion (Figure 131). That was the reason why the coating presented a smooth surface after the galvanic corrosion. From the evident change in thickness, a very significant loss of HVOF WC/Cr/Co coating was believed to occur during galvanic corrosion with the EC coating. The galvanic corrosion of the HVOF WC/Cr/Co coating was suggested to occur by a mechanism similar to that occurring during low overpotential anodic polarisation was applied as discussed previously. In this mechanism, the anodic metallic binder corroded slowly and uniformly over all the surface of the HVOF WC/Cr/Co coating and then the loss of metallic binder resulted in the detaching of unsupported WC particles from the coating. Therefore, the HVOF WC/Cr/Co coating corroded layer by layer from the top surface. Moreover, underlying Al_2O_3 particles accelerated the corrosion rate of the surrounding metallic binder and in these cases, the corrosion from both the top and bottom area of the coating caused the absolute removal of the HVOF WC/Cr/Co coating during the galvanic corrosion.

From all the corrosion investigations of the HVOF WC/Cr/Co coating, it can be summarized that the metallic binder of the coating, in particular Co, presented significant anodic corrosion behaviour when galvanically coupled with the sacrificial coatings. Al_2O_3 present in the coating or environment could accelerate the corrosion rate of the metallic binder through the micro-galvanic mechanism.

5.3 Deposition of Al_2O_3

According to the requirement of Airbus, the deposition of Al_2O_3 coatings was investigated on HVOF WC/Cr/Co for improving its galvanic compatibility by decreasing its electrical conductivity. Electrolytic and sol-gel depositions were investigated due to their low level of damage to the HVOF WC/Cr/Co coating. The feasibility of the two methods was initially identified on steel substrate and then on the HVOF WC/Cr/Co coating. However, the unexpected corrosion behaviour between Al_2O_3 and HVOF WC/Cr/Co coatings was later found in this study as discussed previously, so only the feasibility and the primary mechanism of deposition of Al_2O_3 by the two methods were examined.

5.3.1 Electrolytic Deposition of Al_2O_3 Coating

In order to improve the adhesion of electrolytic deposited Al_2O_3 barriers, a functional conversion pre-treatment has been reported to apply on steel substrates by chemical oxidation in sulphate based acid solution[66]. The conversion coating was evidently porous, which may contribute to improve the adhesion of the Al_2O_3 layers and facilitate the interfacial reactions (Figure 132). The effects of the conversion coating are proved in the following discussion. Both $Al_2(SO_4)_3$ based and $Al(NO_3)_3$ based solutions was investigated as electrolytic deposition baths.

5.3.1.1 Electrolytic Deposition of Al_2O_3 Coatings from $Al_2(SO_4)_3$ Based Solution on Steel

The electrolytic deposition of Al_2O_3 coatings on conversion pre-treated steel substrates was performed cathodically from aqueous solutions, and involved both electrochemical and chemical reactions. The process using $Al_2(SO_4)_3$ solution is said to be the following[60]:

(1) Dissociation of the $Al_2(SO_4)_3$ salt:

$$Al_2(SO_4)_3 \rightarrow 2Al^{3+} + 3SO_4^{2-}$$ Equation (6)

(2) Interaction of the Al^{3+} with OH^- to form a mixture of hydrated aluminium oxide ($Al_2O_3 \cdot xH_2O$) and hydroxide ($Al(OH)_3$), named 'semi-alumina' deposits.

The OH^- may be formed in two successive reactions:

H_2 evolution:

$$2H_2O + 2e^- \rightarrow H_2 + 2OH^-$$ Equation (7)

Reduction of dissolved O_2 according:

$$O_2 + 2H_2O + 4e^- \rightarrow 4OH^-$$ Equation (8)

The pre-treated surfaces of the steel substrates were porous and the generation of OH^- may have occurred at the bottom of the pores with a resulting rise in local pH. The pH increase induced precipitation of semi-alumina deposits with varying degrees of hydration in the pores and at the surface.

(3) Dehydration of the semi-alumina deposits was carried out to form Al_2O_3 coatings.

The cathodic polarisation curve for deposition from the $Al_2(SO_4)_3$ based solution (Figure 133) implies that the deposition process commenced with H_2 evolution and precipitation of semi-alumina deposits in the pores and surface of the conversion coating after a potential of -1.0 V was reached. The addition of YCl_3 into the $Al_2(SO_4)_3$ solution caused the cathodic current density of deposition to increase slightly up to -3.2 V. This may be caused by precipitation of $Y(OH)_3$, which have been reported to improve adhesion and morphology of Al_2O_3 films[66]. The addition of Y^{3+} also decreased the semi-alumina deposits precipitation rate as suggested by the presence of a plateau after -3.2 V.

The effects of processing parameters on the electrochemical deposition of semi-alumina deposits are illustrated by their potential vs. time curves. The deposition time did not have appreciable effects on the deposition of Al_2O_3 coating as Figure 134 shows. After deposition and dehydration in air at 20 ℃, a powdery Al_2O_3 coating was

present on the surface of the steel (Figure 140). It can be seen that the substrate was not completely covered by the Al_2O_3 coating. Increased deposition time did not promote a positive effect on the deposition of the Al_2O_3 coating. In fact it only increased the amount of Al_2O_3 deposits on the surface presumably without improving the morphology and adhesion.

With respect to the applied current density, a sufficient current was necessary to produce an adequate generation rate of OH^-. In this way, a high concentration of OH^- on the steel substrate resulted in the precipitation of semi-alumina deposits. The electrolytic deposition at 30 mA/cm^2 produced a stable potential (-1.5 V) (Figure 135), at which only slight H_2 evolution occurred on the steel substrate. No Al_2O_3 coating was observed on the steel substrate after deposition at 30 mA/cm^2 as expected (Figure 141).

An evident decrease in the electrode potential during deposition by the addition of YCl_3 to the $Al_2(SO_4)_3$ solution, further supported the suggestion that the presence of Y^{3+} in the solution decreased the precipitation rate of semi-alumina deposits by co-deposition of $Y(OH)_3$ during the process (Figure 136). In this way, a low and uniform growth rate of semi-alumina deposits on the conversion coated steel substrate occurred, which produced a more uniform Al_2O_3 coating (Figure 142).

Effects of stirring during the process only stabilised the precipitation of semi-alumina deposits slightly as noted from electrochemical observations (Figure 137). However, it did not improve the quality of the coating significantly (Figure 143). Stirring increased the flow rate of ions in the deposition bath, but it also increased the risk of precipitated semi-alumina deposits detaching from the surface.

5.3.1.2 Electrolytic Deposition of Al_2O_3 Coatings from $Al(NO_3)_3$ Based Solution on Steel

The reactions involved in the deposition of Al_2O_3 from $Al(NO_3)_3$ electrolyte are presented as follows:

(1) Dissociation of the $Al(NO_3)_3$ salt:

$$Al(NO_3)_3 \rightarrow Al^{3+} + 3NO_3^- \quad \text{Equation (9)}$$

(2) Interaction of the Al^{3+} with OH^- to form a mixture of hydrated aluminium oxide ($Al_2O_3 \cdot xH_2O$) and hydroxide ($Al(OH)_3$), named 'semi-alumina' deposits.

The OH^- may be formed in two more successive reactions in addition to those as illustrated with the $Al_2(SO_4)_3$ solution:

H_2 evolution:

$$2H_2O + 2e^- \rightarrow H_2 + 2OH^- \quad \text{Equation (10)}$$

Reduction of dissolved O_2 according:

$$O_2 + 2H_2O + 4e^- \rightarrow 4OH^- \quad \text{Equation (11)}$$

Reduction of NO_3^- according to:

$$NO_3^- + H_2O + 2e^- \rightarrow NO_2^- + 2OH^- \quad \text{Equation (12)}$$

$$NO_3^- + 6H_2O + 8e^- \rightarrow NH_3 + 9OH^- \quad \text{Equation (13)}$$

In this way, the presence of NO_3^- was expected to increase the generation rate of OH^- and precipitation rate of semi-alumina deposits.

(3) A simple dehydration, as illustrated with the $Al_2(SO_4)_3$ solution, was also applied to produce Al_2O_3 coatings.

In the case of deposition from $Al(NO_3)_3$ (Figure 133), it is suggested that the first stage of reduction of NO_3^- occurred at about -0.9 V (the cathodic reduction of NO_3^- is thermodynamically feasible at a potential of -0.94 to -0.96 V[124]) and then further reduced to the final product $-NH_3$. During the reduction of NO_3^- , H^+ were simultaneously reduced. H atoms formed at the cathode helped to reduce

NO_3^- chemically[124] to NH_3 molecules through the following route:

$$HNO_3 \xrightarrow{2H} HNO_2 \xrightarrow{2H} NO \xrightarrow{2H} NH_2OH \xrightarrow{2H} N_2H_4 \xrightarrow{2H} NH_3 \qquad \text{Equation (14)}$$

In this manner, reduction of NO_3^- inhibited H_2 evolution, which improved adhesion of the precipitated semi-alumina deposits to the conversion coating surface. Addition of NH_4^+ in the $Al(NO_3)_3$ based bath accelerated NH_3 evolution. A wet pH indicator paper was held close to the steel substrate electrode (cathode) and suggested alkali, which agreed that NH_3 evolution occurred at the cathode to generate OH^-. After reaching the cathodic potential of -2.0 V, the current density for deposition from the $Al(NO_3)_3$ based solution increased this was occurring from a more negative potential than that observed for the $Al_2(SO_4)_3$ based solution (Figure 133). This was thought to be attributed to the higher precipitation rate for semi-alumina deposits occurring at the interface in the $Al(NO_3)_3$ based solution.

From the investigation of the effects of applied current in the deposition of Al_2O_3 coating from $Al(NO_3)_3$ based solution (Figure 138), it was found that a low current density (30 mA/cm^2) did not produce any evident precipitation of semi-alumina deposits. The current density of 60 mA/cm^2 produced a uniform Al_2O_3 coating due to the presence of NO_3^- in the solution increasing the generation rate of OH^- and precipitation of semi-alumina deposits on the substrate. The electrode potential was more stable and higher for a current density of 100 mA/cm^2 applied from the $Al(NO_3)_3$ solution as opposed to the $Al_2(SO_4)_3$ solution, which further supported the occurrence of reduction of NO_3^- and a high precipitation rate of semi-alumina deposits during deposition.

The Al_2O_3 coating produced from $Al(NO_3)_3$ solution presented uniform integrity and good adhesion to the surface (Figure 144), which was much better than that produced from $Al_2(SO_4)_3$ solution (Figure 143). The presence of NO_3^- increased the generation rate of OH^- at the cathode and reduction of NO_3^- also inhibited H_2 evolution, which improved adhesion of the Al_2O_3 coating to the surface. Dehydration at 150 ℃ was

more effective than at 20 ℃ for transforming semi-alumina deposits into oxide. In this manner, the Al_2O_3 coating exhibited denser and better adhesion to the substrate (Figure 145).

The prior conversion coating treatment was found to significantly stabilise the precipitation process of semi-alumina deposits on steel substrate (Figure 139). During the deposition on a steel substrate without the conversion coating, it was observed that semi-alumina deposits precipitated and detached, and this repeated with time, which was further supported by the fluctuations in its electrode potential. No Al_2O_3 deposit was observed on the untreated steel (no conversion coating) after deposition.

5.3.1.3 Electrolytic Deposition of Al_2O_3 Coatings from $Al(NO_3)_3$ Based Solution on HVOF WC/Cr/Co Coating

Both the conversion treatment and grit blasting were applied to the HVOF WC/Cr/Co coating. The conversion treatment showed no significant effect on the HVOF WC/Cr/Co coating. No difference was detected in morphology and composition after the conversion treatment, which was thought to result from the relative low content of the metallic binder and its higher corrosion resistance in the treatment solution. From all the electrolytic deposition of Al_2O_3 applied on as-received, conversion treated and grit blasted HVOF WC/Cr/Co coatings, only H_2 evolution was observed at HVOF WC/Cr/Co coatings and no precipitation of semi-alumina deposits occurred (Figure 146). This was suggested to result from that the surface of the three HVOF WC/Cr/Co coatings not exhibiting porosity, which could not support a local area of high concentration of OH^- to form the semi-alumina deposits during deposition. After the electrolytic deposition, no Al_2O_3 coating was detected on all three HVOF WC/Cr/Co coatings. It can be concluded that a porous and conversion treated surface on the substrate was necessary for electrolytic deposition of Al_2O_3. So electrolytic deposition was not practical for the application of Al_2O_3 coatings on HVOF WC/Cr/Co coated

steel substrates.

5.3.2 Sol-gel Deposition of Al_2O_3 Coatings

5.3.2.1 Sol-gel Deposition of Al_2O_3 Coating on Steel

The surface condition of the substrate played an important role in the deposition of Al_2O_3 coatings. The effects of pre-treatment of the steel substrate on the sol-gel deposition of Al_2O_3 coating were examined. Three surface conditions were prepared by phosphating and grit blasting separately and together. The phosphating treatment was reported to improve bonding of the Al_2O_3 layer to the steel substrate[104]. In this study, zinc phosphating was used with ZnO_2 in the phosphating bath. The reaction on the steel surface can be expressed as follows[104]:

$$3Zn(H_2PO_4)_2 + Fe + 4H_2O \rightarrow Zn_3(PO_4)_2 \cdot 4H_2O + FeHPO_4 + 3H_3PO_4 + H_2$$

Equation (15)

The phosphating treatment provided an interlocked crystalline structured coating of insoluble zinc phosphate crystals (Figure 147). This agrees with Kirk et al.'s observations[125] and has been reported to provide an excellent base for an Al_2O_3 layer and helped to improve the bonding of the sol-gel Al_2O_3 coating to the steel substrate. The sol-gel Al_2O_3 coating applied to the phosphated steel presented a dense morphology with grain sizes of about 100 μm as expected (Figure 148). After heat treatment at 400 ℃, the shrinking of the Al_2O_3 coating was observed to reduce the grain size and cause the cracking due to the loss of organic function group (isopropyl) and water in the Al_2O_3 deposits. After heat treatment, a better adhesion of Al_2O_3 deposits to the substrates was observed. The sol-gel Al_2O_3 coating was applied by repeating dipping, air-drying and heat treatment to form a multilayer structure. In this way, cracks in the Al_2O_3 coating were thought to be reduced.

Al_2O_3 grit blasting was also considered for activating the surface of steel substrates mechanically, by increasing the reactive surface area. A uniform microstructure was observed on the surface of the Al_2O_3 coating and it also exhibited good adhesion (Figure 149). Grit blasting treatment was suggested to help in attaining better adherence of the Al_2O_3 coating to the substrate due to strong mechanical interlocking, which has also been reported by Zhou et al.[126].

The phosphating treatment was also applied on a grit blasted steel, being a combined treatment. No significant improvement in morphology was observed in the coating on this combined pre-treated steel substrate. It can be summarised that sol-gel Al_2O_3 coating on both the phosphating and grit blasting pre-treated steel substrates presented a good morphology and adhesion.

5.3.2.2 Sol-gel Deposition of Al_2O_3 Coating on HVOF WC/Cr/Co Coating

The same pre-treatments as used on the steels were applied to the HVOF WC/Cr/Co coatings. The phosphating on the HVOF WC/Cr/Co coating may well have occurred by reaction of the zinc phosphating bath and the metallic binder of the coating. The phosphating layer was not expected to be as dense as that on the steels due to the low content of the metallic binder. Therefore, the sol-gel Al_2O_3 coating on a phosphated HVOF WC/Cr/Co coating did not present a uniform morphology as on the phosphated steel (Figure 151). This loose and thin phosphating layer on the HVOF WC/Cr/Co coating did not provide a highly interlocking crystalline structure for the deposition of the Al_2O_3 coating. Grit blasting was applied to increase the roughness and porosity of the surface of the HVOF WC/Cr/Co coating. In this way, the morphology and adhesion of the Al_2O_3 coating on the grit blasted HVOF WC/Cr/Co coating was improved significantly by a mechanical interlocking mechanism (Figure 152).

A further improvement of the sol-gel coating on the HVOF WC/Cr/Co coating was thought to be provided by phosphating on the grit blasted HVOF WC/Cr/Co coatings as a combined pre-treatment. A much denser and well adhered Al_2O_3 coating presented on the combined treated HVOF WC/Cr/Co coating (Figure 153). Compared to the phosphating layer on a smooth HVOF WC/Cr/Co coating, a denser and more porous phosphating layer was expected on the grit blasted HVOF WC/Cr/Co coating. Zhou et al.'s[126] suggested that the grit blasting treatment helped to form a more porous phosphating layer. Grit blasting increased the porosity of the surface of the HVOF WC/Cr/Co coating, which helped the penetration of the phosphating solution into the HVOF WC/Cr/Co coating and more metallic binder areas reacted during the phosphating treatment. In this way, a dense and porous phosphating binder formed, which was suggested to improve the adhesion of the sol-gel Al_2O_3 coating..

5.4 Electroplating of Mn-Cu Coatings

The feasibility of electroplating Mn-Cu coatings on steel is discussed in this Section. The optimisation of Mn-Cu electroplating bath formulae was elucidated. Moreover, the effects of different electroplating parameters, including current density, electroplating time and stirring rate on electrodeposited Mn-Cu coatings were also indicated by their morphology and compositional characterisation. The corrosion resistance of optimised Mn-Cu coatings was also discussed by their electrochemical observation and corrosion behaviour in an aircraft de-icing fluid.

In this study, all the steel substrates were mechanically polished prior to electroplating Mn-Cu. This pretreatment was thought to affect the grain size of the coating formed, which may even determine the possibility of electrodeposition. The mechanical polishing increased the smoothness of the substrates greatly and helped to remove some of the metal oxides on the surface, which was believed to contribute immensely to the uniform nucleation upon substrates.

5.4.1 Effects of Electroplating Parameters on Mn-Cu Coating

5.4.1.1 Electroplating Bath Formulae

The electroplating bath used in this study mainly consisted of Mn^{2+}, Cu^{2+}, NH_4^+ and Tween 20. It was believed that the cathodic behaviour of these ions in the bath may have significant effects on the electrodeposited Mn-Cu coating. Two possible pH ranges for Mn-Cu alloy electroplating, namely pH 2.6-2.8 and pH 6.4-6.6, has been reported by Gong et al.[73, 74]. However, vigorous hydrogen evolution was evident in the electroplating of Mn-Cu coating from the electrolyte at pH 2.7, which only produced poorly adhered Co-like deposits with no manganese. Therefore, the electroplating bath in acid conditions was not thought to be suitable for Mn-Cu electroplating.

In order to inhibit hydrogen evolution, the pH value of the Mn-Cu electroplating bath was adjusted to near neutrality (pH 6.4-6.6). It was found that in the bath, NH_4^+ stablised Mn^{2+} and Cu^{2+} by complexing mechanism, which prevented Mn^{2+} and Cu^{2+} from forming hydroxides and precipitating in the bath at near pH neutrality. From the effects of NH_4^+ on the cathodic polarisation behaviour of $MnSO_4$ electrolyte (Figure 154), it was found that NH_4^+ increased the reduction potential of H^+ from -1.0 to -0.9 V. The hydrolysation of NH_4^+ increased the concentration of H^+ in the electrolyte whilst hydrogen evolution accelerated hydrolysation of NH_4^+, so a high potential and current density of hydrogen evolution were observed in the electrolyte with NH_4^+ (Equations (16) and (17))

$$NH_4^+ + H_2O \leftrightarrow NH_3 + H_3O^+ \quad \text{Equation(16)}$$

$$2H_3O^+ + 2e \rightarrow H_2 + 2OH^- \quad \text{Equation(17)}$$

It was also noticed that the reduction potential of Mn^{2+} also increased from approximately -1.7 to -1.6 V due to the addition of NH_4^+. Mn^{2+} in an electrolyte at a low

pH value forms a hexaaqua-manganese (II) ion ($[Mn(H_2O)_6]^{2+}$). In this way, the six water molecules are attached to central Mn^{2+} via a co-ordinate bond using one of the lone pairs on the O. The 2+ charge locating on the Mn^{2+} pulls the electron pairs away from the O atoms toward the Mn^{2+}. In this way, the charge is no longer located entirely on the Mn, but spread out over the whole complex ion. The H atoms attached to the water ligands of the complex ion are sufficiently positive to be pulled off in a reaction involving water molecules in the solution as Equation (18) shows. With increase in the pH value of electrolyte, the position of the equilibrium in Equation (18) moves to right. In this way, the mobility of the Mn complex ions toward the cathode was thought to decrease during electroplating. The presence of NH_4^+ in electrolyte could inhibit Equation (18) by its hydrolysation (Equation (16)), which was thought to improve the mobility of the Mn complex ions. That could possibly increase the reduction potential of Mn^{2+} as observed.

$$[Mn(H_2O)_6]^{2+} + H_2O \leftrightarrow [Mn(H_2O)_5(OH)]^{+} + H_3O^{+} \quad \text{Equation (18)}$$

The cathodic polarisation behaviour of Cu^{2+} with addition of NH_4^+ indicated a decrease in the reduction potential of copper from approximately -0.65 to -0.7 V (Figure 155). The pH value of the Cu electroplating solution with NH_4^+ was adjusted to about 6.5 by NH_3 solution, so it was expected that complexing Cu ions $[Cu[NH_3]_4(H_2O)_2]^{2+}$ formed in the electrolyte (Equation (19)). The low mobility of complexing Cu ions was suggested to hinder the reduction of Cu and decreased its reduction potential.

$$[Cu(H_2O)_6]^{2+} + 4NH_3 \leftrightarrow [Cu(NH_3)_4(H_2O)_2]^{2+} + 4H_2O \quad \text{Equation (19)}$$

NH_4^+ also presented similar effects on co-deposition of Mn-Cu as discussed above, which further supported the previous observation, which moved the reduction potential of Mn and Cu closer and was expected to make the co-deposition of Mn-Cu easier. The effects of NH_4^+ on electroplating of Mn-Cu were also confirmed by galvanostatic deposition experiments. From the comparison of Figures 157 and 158, at the same current density of 200 mA/cm^2, the addition of NH_4^+ in the electrolytes resulted in a

more stable and positive electrode potential of the substrates. That implies that more reduction of Mn^{2+} and Cu^{2+} occurs at the cathode in the electrolyte with NH_4^+. In this way, it was thought that the absence of NH_4^+ in the Mn-Cu electroplating solution resulted in a low current efficiency and a powdery Cu-like coating with no Mn (Figure 161).

With addition of NH_4^+ in the electrolyte, more stable co-deposition of Mn-Cu presented (Figure 158). During Mn-Cu electroplating at 200 mA/cm^2, the presence of NH_4^+ also resulted in a much higher electrode potential (-2.6 V) for the substrate. It was suggested that the hydrolysation of NH_4^+ accelerated hydrogen evolution and prevented the working electrode potential from decreasing too far during electroplating. Therefore, it can be summarised that NH_4^+could stabilize the Mn-Cu electroplating processes and reduce the difference of reduction potential between Mn and Cu, which helps to produce Mn-Cu coatings with good qualities.

5.4.1.2 Current Density

From the galvanostatic electroplating from optimised Mn-Cu electroplating baths at a range of current densities (150-500 mA/cm^2), the evident reduction of Mn on steel substrates occurred when current densities over 300 mA/cm^2 were applied (Figures 158, 162 and 163). Only powdery Cu rich deposits were produced on the substrate at 150 mA/cm^2 due to lack of a driving force to reduce Mn^{2+}. Moreover, Cu displacement coatings were also believed to form as soon as the substrates were immersed into the electrolytes. At 200 mA/cm^2, the crystallized Mn appeared but in a porous pattern on the substrate, whilst in the edge area of the substrate, a sharp increase in Mn content presented. It was suggested that uneven current density distribution on substrates caused a significant difference in Mn content from centre to edge areas on the surface of substrates. As expected from the electrochemical observations, at current densities over 300 mA/cm^2, the Mn-Cu coatings showed a dense and uniform structure. The

co-deposition system of Mn-Cu has been reported[73] with the noble metal, Cu, deposited preferentially at low current density and the active metal, Mn, deposited only under diffusion-limiting condition for Cu reduction. At low current density, the crystalline features of the coating was dominated by the nucleation rate, which mainly depended on the concentration of Cu^{2+} in electrolyte. In this study, due to the low concentration of Cu^{2+} in the bath, the nucleation rate of Cu in the coating was thought to be limited and the growth rate following reduction of Mn increased significantly as the current density increased to more than 300 mA/cm^2. This resulted in a great increase in the grain size of the coating produced at 400 mA/cm^2 (Figure 162 (d)). No significant change in the crystal features by further increasing the current density to 500 mA/cm^2 were evident (Figure 162 (e)) due to the limiting current for the reduction of Mn being reached. Moreover, the increased growth rate of the coating also resulted in some defects at the grain boundary. Therefore, it was suggested that current density of more than 300 mA/cm^2 can supply a sufficient driving force to deposit Mn-Cu alloy coatings with good quality (Figures 162 and 163).

5.4.1.3 Agitation

Agitation was suggested to improve the mobility of the Mn^{2+} and Cu^{2+} in electrolytes and eliminate the local pH value change around the working electrode during electroplating. These were thought to accelerate and stabilise the Mn-Cu electroplating processes through a significant increase in the electrode potential of the substrate during the processes (Figure 159). These effects were also supported by the morphology of the Mn-Cu coatings produced with and without stirring the former showing a more uniform structure (Figure 164).

5.4.1.4 Surfactant (Tween 20)

The effects of the nonionic surfactant, Tween 20 [polyoxyethylene (20)

sorbitanmonolaurate], on the electroplating of Mn-Cu coating was investigated because it has been reported that it can suppress the preferential deposition of more noble metal to improve the co-deposition with Mn[68]. From the effects of Tween 20 on the cathodic polarisation behaviour of Mn^{2+} and Cu^{2+} s (Figures 154 -156), it was found that the deposition of Cu was slightly suppressed. However, the effect was thought to be negligible compared to the effect of NH_4^+ and Tween 20 did not provide a further suppression in an electroplating bath containing NH_4^+. With respect to the deposition of Mn, Tween 20 did not show any evident effects on the reduction potential of Mn, but retarded slightly the deposition rate. It can be summarised that Tween 20 presented negligible effects on the cathodic polarisation behaviour of Mn^{2+} and Cu^{2+}.

From the observations of galvanostatic deposition of Mn-Cu coatings, as applied current density increased, the cathodic polarisation on the surface of substrates increased with the presence of Tween 20 in baths (Figure 160). The surfactant attached to the surface of cathode (substrate) and formed a complex film, which was thought to make the discharge of metal ions more difficult. In this way, a more significant cathodic polarisation exhibited on the cathode and the nucleation rate of the Mn-Cu coating was expected to increase. This was also supported by the greatly reduced grain size of Mn-Cu coating produced from the baths containing Tween 20 as Figures 165 and 166 show. In particular, at a high current density of 500 mA/cm^2, an amorphous-like Mn-Cu coating presented. However, the addition of Tween 20 resulted in poor uniformity of the coatings.

5.4.2 Characterisation of Electroplated Mn-Cu Coating

After optimizing the process parameters for the electroplating of Mn-Cu coatings, dense and uniform Mn-Cu coatings with a high Mn content were produced from 0.59 M $MnSO_4$/5 mM $CuSO_4$/1 M $(NH_4)_2SO_4$ electrolyte by applying 300 mA/cm^2, which exhibited stability by the presence of a nearly linear relation of coating thickness and

electroplating time using this process (Figure 168). The effect of Cu to prevent γ-Mn phase from transforming to α-Mn phase was also proven by XRD analysis of the same Mn-Cu coating after 4-months storage in air at 20 ℃ (Figure 169 (b)). From the linear polarisation resistance test of the coating, the electroplated Mn-Cu coating presented a more negative free corrosion potential (-1.22 V) compared to the EC coating and its alternatives mentioned previously (Figure 63). Therefore, electrodeposited Mn-Cu was believed to provide sacrificial protection to steels. However, it was also noted that due to the high activity of Mn, the Mn-Cu coating with high Mn content showed a higher corrosion current of approximately 33.3 mA/cm^2 in anodic polarisation, which was thought to limit its application as an EC replacement.

As a possible EC replacement, electrodeposited Mn-Cu coatings have a lot of opportunities to come into with contact aircraft de-icing fluids. According to the requirement of Airbus, the corrosion resistance of electrodeposited Mn-Cu coating in Konsin, which is a glycol-based, water-soluble, de-icing fluid, was investigated by immersion tests. The corrosion of Mn-Cu coating in Konsin appeared to take place two stages. In the first 10 days of immersion, no evident corrosion occurred on the surface of the coating. It has been reported that glycol could be absorbed on the surface of steel and to form a protective layer[127]. A similar mechanism may have occurred in this case. After 10 days of immersion, corrosion occurred and caused the detaching of the coating (figure 171). The possible mechanism was the oxidation of glycol kept at 70 ℃ for a long time through Equations (20) and (21) and glycol was transformed into glycolic acid and oxalic acid, which decreased the pH value of the immersion solution greatly. In this way, severe corrosion attack took place. Therefore electroplated Mn-Cu presented a poor corrosion resistance to Konsin for long-term application particular at high temperature.

$$[HO - CH_2 - CH_2 - OH] + O_2 \rightarrow [HO - CH_2 - COOH] + H_2O \quad \text{Equation (20)}$$

$$[HO - CH_2 - COOH] + O_2 \rightarrow [HOOC - COOH] + H_2O \quad \text{Equation (21)}$$

5.5 Summary

In all the EC alternatives, FSAl had a porous structure and poor properties in both barrier protection and corrosion resistance. Therefore, it was not thought to be suitable to replace EC coatings. Both EDAl and SermeTel 962 coatings exhibited a uniform structure and good corrosion resistance. They also showed both good barrier and sacrificial protection properties compared to EC coatings. However, SermeTel 962 coatings had much better galvanic compatibility with the hard coatings, including EHC and HVOF WC/Cr/Co coatings, than EDAl coatings. Moreover, it was also noted that a light abrasion can be utilised to modify the surface morphology of SermeTel coatings, which has significant effects on the electrochemical properties. This may make SermeTel 962 coating to be capable to adjust its electrochemical properties easily. Therefore, it was suggested that SermeTel 962 coatings showed the largest potential as an EC alternative.

As an EHC alternative, an HVOF WC/Cr/Co coating exhibited poor barrier protection to a steel substrate. It is also concerning that the active metallic binder in HVOF WC/Cr/Co coating showed some several corrosion problems. Al_2O_3 particles trapped at the interface between HVOF WC/Cr/Co coatings and substrates caused the coatings to be absolutely removed in a short time when immersed in 3.5 wt.% NaCl solution. Moreover, as galvanically coupled to EC and its alternatives, HVOF WC/Cr/Co coatings exhibited a significant reduction in thickness in 15 days. Therefore, an HVOF WC/Cr/Co coating was not suggested to be an EHC alterative for a long-term application.

The project sponsor, Airbus, suggested to deposit Al_2O_3 coatings on HVOF WC/Cr/Co coatings for improve its galvanic compatibility. From the investigations of deposition of Al_2O_3, electrochemical deposition did not work on HVOF WC/Cr/Co due to its unsatisfied surface condition. Sol-gel deposition applied Al_2O_3 coatings on

HVOF WC/Cr/Co coatings successfully by using zinc phosphating and grit blasting pre-treatment. However, Al_2O_3 was found later in this project to have an unexpected negative effect on the corrosion of HVOF WC/Cr/Co coatings. Therefore, applying Al_2O_3 coatings was not thought to be a suitable method to improve the galvanic corrosion resistance of HVOF WC/Cr/Co coatings.

A Mn-Cu coating was investigated as a possible EC alternative in this project. Mn has an active electrochemical property, which make it difficult to co-deposit with other noble metals to produce uniform coatings by electroplating. In this project, uniform and dense Mn-Cu coatings containing >90 wt.% Mn were electrodeposited on mild steels by an optimised electroplating process. The coatings did not exhibit any evident phase transformation in Mn during a long-term observation, which may make it to have a good mechanical property. However, as a possible EC alternative, the Mn-Cu coating showed a too active electrochemical property, which was thought to limit its long-term application in a corrosive environment. Therefore, it was thought that further investigations need to do to make Mn-Cu coating practical as an EC alternative.

CHAPTER 6: CONCLUSIONS

From the characterisation of the coatings:

- The EC coating presented an irregular and rough surface and an open and heterogeneous structure with a Cr conversion coating present. The passivation treatment protected the EC coating from oxidation. The EC coatings may provide the best sacrificial protection for the steel substrate by presenting the most negative E_{corr} (- 796 mV). The EC coatings had good corrosion resistance with a LPR value of 1570 $\Omega \cdot cm^2$ and provided good barrier protection to the steel substrate.
- The FSAl had a splash-pattern structure and high porosity, with some interconnecting pores present. The inclusion of Si in the FSAl coating increased its electronegativity. The FSAl presented a poor corrosion resistance with a LPR value of 256 $\Omega \cdot cm^2$. The FSAl coating was suggested to offer poor barrier protection to the steel substrate.
- The EDAl coating had a dense and uniform structure with a trivalent chromium based conversion coating. It provided a sacrificial protection with a comparable E_{corr} (-699 mV) to EC and good corrosion resistance with a LPR value of 6510 $\Omega \cdot cm^2$. It also provided good barrier protection to the steel substrate.
- The SermeTel 962 coating had a structure with packed Al particles in a phosphate and trivalent Cr based binder. It still provided good barrier protection to steel substrate because the pores present in the coating were isolated. It also had good corrosion resistance with a LPR value of 2990 $\Omega \cdot cm^2$.
- A lightly abrading post-treatment decreased the barrier protection property of the SermeTel 962 coating by increasing interconnected pores. It also reduced the corrosion resistance of the coating with a LPR value of 175 $\Omega \cdot cm^2$.
- The EHC coating had a dense and homogeneous structure, but with some cracks dispersed in the coating, which reduced its barrier protection property.
- The HVOF WC/Cr/Co coating consisted of WC phases dispersed in the Cr-Co

metallic binder with a poor barrier protection property.

From the galvanic corrosion investigations between the coatings:

- The EHC/EC coatings couple presented good galvanic compatibility with a galvanic current at 5 μA. Cd nodular 'whiskers' grew through the cracks of the passivation layer on the EC coating during the galvanic corrosion.
- EDAl, FSAl and post-treated SermeTel coatings presented poor galvanic compatibility with the HVOF WC/Cr/Co coating. After galvanic corrosion, Al phases transformed into powdery Al_2O_3 corrosion products and oxide films with evident cracks on all the three coatings.
- The SermeTel coating presented the best galvanic corrosion resistance with the HVOF WC/Cr/Co coating with a galvanic current of 15 μA.

From the corrosion investigation of the HVOF WC/Cr/Co coating:

- The corrosion of HVOF WC/Cr/Co coating initially occurred in the metallic binder at the interface of WC particles and Co-Cr metallic binder, and then resulted in the detaching of WC particles.
- Al_2O_3 particles in electrolytes increased the corrosion rate of the anodic metallic binder of HVOF WC/Cr/Co coating by a microgalvanic mechanism. Al_2O_3 particles trapped at the interface of HVOF WC/Cr/Co coating and substrate caused severe corrosion of the coating.
- The metallic binder of the HVOF WC/Cr/Co coating produced anodic dissolution behaviour during galvanic coupling with the sacrificial coatings and resulted in a large loss of the HVOF WC/Cr/Co coating illustrated by a significant reduction in its thickness.

From the investigations of electrolytic deposition of Al_2O_3:

- A uniform and well adhered Al_2O_3 film can be applied by electrolytic deposition on steel substrate following the initial formation of a porous conversion coating.
- Electrolytic deposition cannot apply an Al_2O_3 film on the HVOF WC/Cr/Co coating.

From the investigations of sol-gel deposition of Al_2O_3:

- A uniform and well adhered Al_2O_3 film can be applied on steel substrates, which have been pre-treated by grit blasting or zinc phosphating
- A uniform and well adhered Al_2O_3 film can be applied on HVOF WC/Cr/Co, which had been grit blasted and then zinc phosphated prior to deposition.
- Zinc phosphating pre-treatment formed a highly interlocked crystalline structured base for the Al_2O_3 layer and helped to improve the bonding of the sol-gel Al_2O_3 films to the steel substrate, but it presented a negligible effect on the HVOF WC/Cr/Co coating.
- Al_2O_3 grit blasting pre-treatment activated the surface of the steel substrate and HVOF WC/Cr/Co coating mechanically, and improved the adhesion of the sol-gel Al_2O_3 film to substrate due to strong mechanical interlocking.
- A grit blasting pre-treatment helped to form a porous and well adhered phosphate layer on HVOF WC/Cr/Co coating, which also helped to subsequently form a uniform sol-gel Al_2O_3 film with good adhesion.

From the investigation of the electrodeposition of Mn-Cu:

- NH_4^+ prevents Mn^{2+} and Cu^{2+} from precipitating as hydroxides as the pH value of the electrolyte increased to nearly neutral by hydrolysis and complexing mechanisms. It also suppresses the discharge of Cu^{2+} and moves the reduction potential of Mn^{2+} and Cu^{2+} closer to improve their co-deposition. In addition, it makes the electrodeposition of Mn-Cu electrochemically stable.
- Dense and uniform Mn-Cu coatings with more than 90 at.% Mn can be produced at 300 mA/cm^2 from a bath (0.59 M $MnSO_4$/5 mM $CuSO_4$/1 M $(NH_4)_2SO_4$) with agitation (60 rpm).
- The electrodeposited Mn-Cu coating can provide sacrificial protection to steel substrate, but presented a high corrosion density (33.3 mA/cm^2). The coating also presented abrupt corrosion behaviour after 10-days immersion in a glycol-based aircraft de-icing fluid.

CHAPTER 7: FURTHER INVESTIGATIONS

Some subject areas are listed below, in which further investigation work could be carried out.

- A further investigation into the galvanic corrosion of a part, where both sacrificial and hard coatings are applied and are in contact, could be carried out to calculate galvanic corrosion rate by SVET and immersion technology. That could be useful to estimate the lifetimes of sacrificial coatings when galvanic coupled with hard coatings. A further study could also be done to improve the galvanic corrosion resistance of these coatings. A possible method is to apply a polymer topcoat on the cathodic coating, which decreases the cathodic area and reduces possible anodic corrosion.

- In this project, it was found that Al_2O_3 grit blasting pre-treatment of steel substrates for the deposition of HVOF WC/Cr/Co coatings could trap Al_2O_3 particles at the interface between steels and the coatings. The trapped Al_2O_3 particles cause severe local corrosion of HVOF WC/Cr/Co coatings. Therefore, pre-treatment alternatives should be investigated to replace grit blasting. Moreover, grit blasting by using other grit rather than Al_2O_3 could also be studied as a possible replacement.

- A further investigation into the effects of Al_2O_3 coatings on HVOF WC/Cr/Co coating on the galvanic corrosion with Al-based coatings needed to be carried out. Moreover, the possible galvanic corrosion between the Al_2O_3 layer and the underlying HVOF WC/Cr/Co coating is thought to be necessary to be investigated.

- Though Mn-Cu coatings have been successfully electroplated with regular morphology from aqueous electrolytes onto mild steel substrates, the composition

of the coating could still be optimised and be made nobler by increasing the Cu content or co-deposition a second noble metal to improve the corrosion resistance of the Mn-Cu coatings. The significant sacrificial protection property of Mn-Cu coating also possibly implies poor galvanic compatibility with other hard (cathodic) coating. This should be examined.

- Mn-based coatings were found to be sensitive to the current density distribution on the substrate surface. In order to obtain a homogeneous Mn-Cu coating on a complex-shaped substrate, techniques such as the use of electroplating additives needs to be examined. Moreover, a method to decrease the applied current density of Mn based coatings is also necessary for their industrial application.

REFERENCES

1. Brooktronics Engineering Corporation. *http://www.brooktronics.com/Aerospace%20(Aircraft).htm [Accessed 20/09/2013]*.

2. Perry, J. M.; Neville, A.; Wilson, V. A.; Hodgkiess, T., Assessment of the corrosion rates and mechanisms of a WC-Co-Cr HVOF coating in static and liquid-solid impingement saline environments. *Surface and Coatings Technology* **2001,** *137*, 43-51.

3. Gong, J.; Zana, I.; Zangari, G., Electrochemical synthesis of crystalline and amorphous manganese coatings. *Journal of Materials Science Letters* **2001,** *20*, 1921-1923.

4. Gong, J.; Zangari, G., Electrodeposition and Characterization of Manganese Coatings. *Journal of The Electrochemical Society* **2002,** *149*, C209-C217.

5. Schlain, D.; Prater, J. D., Electrodeposition of Gamma Manganese. *Journal of The Electrochemical Society* **1948,** *94*, 58-73.

6. Brenner, A., Electrodeposition of alloys: principles and practice / Vol.2, Practical and specific information. *Adacemic* **1963**.

7. Hayes, A. W., Principles and Methods of Toxicology. *Philadelphia: CRC Press* **2007**.

8. Piscator, M., Role of Cadmium in Carcinogenisis with Special Reference to Cancer of the Prostate. *Environmental Health Perspectives* **1981,** *40*, 107-120.

9. Her Majesty's Inspectorate of Pollution, Chief Inspector's Guidance to Inspectors, Environmental Protecion Act 1990, Process Guidance Note IPR 4/23. 'Process Involving the Use or Release of Cadmium or Any Compound of Cadmium. HMSO publication: 1993.

10. Abda, M.; Oren, Y., Removal of cadmium and associated contaminants from aqueous wastes by fibrous carbon electrodes. *Water Research* **1993,** *27* (10), 1535-1544.

11. Baldwin, K. R.; Smith, C. J. E., Advances In Replacements For Cadmium Plating in Aerospace Application. *Transactions of the Institute of Metal Finishing* **1996,** *74*, 202-209.

12. Hotta, S.; Itou, Y.; Saruki, K.; Arai, T., Fatigue-Strength at a Number of Cycles of Thin Hard Coated Steels with Quench-Hardened Substrates. *Surf Coat Tech* **1995,** *73*, 5-13.

13. EEC COMMISSION DIRECTIVE 2012/7/EU of 2 March 2012.

14. Wilcox, G. D.; Gabe, D. R., Electrodeposited Zinc Alloy Coatings. *Corrosion Science* **1993,** *35*, 1251-1258.

15. Watson, S. A., Electrodeposited coatings of zinc-nickel. *Trans. Inst. Metal Finish* **1992,** *70*, 28-31.

16. EEC COMMISSION DIRECTIVE 2004/96/EC of 27 September 2004.

17. Lodhi, Z. F.; Tichelaar, F. D.; Kwakernaak, C.; Mol, J. M. C.; Terryn, H.; de Wit, J. H. W., A combined composition and morphology study of electrodeposited Zn–Co and Zn–Co–Fe alloy coatings. *Surface and Coatings Technology* **2008,** *202*, 2755-2764.

18. Eliaz, N.; Venkatakrishna, K.; Hegde, A. C., Electroplating and characterization of Zn–Ni, Zn–Co and Zn–Ni–Co alloys. *Surface and Coatings Technology* **2010,** *205*, 1969-1978.

19. Kautek, W.; Birkle, S., Aluminum-electrocrystallization from metal--organic electrolytes. *Electrochimica Acta* **1989,** *34*, 1213-1218.

20. Chang, J.-K.; Chen, S.-Y.; Tsai, W.-T.; Deng, M.-J.; Sun, I. W., Electrodeposition of aluminum on magnesium alloy in aluminum chloride (AlCl3)-1-ethyl-3-methylimidazolium chloride (EMIC) ionic

liquid and its corrosion behavior. *Electrochemistry Communications* **2007,** *9*, 1602-1606.

21. Hurley, F. H.; Wier, J. T. P., Electrodeposition of Metals from Fused Quaternary Ammonium Salts. *Journal of The Electrochemical Society* **1951,** *98*, 203-206.

22. Bardi, U.; Caporali, S.; Craig, M.; Giorgetti, A.; Perissi, I.; Nicholls, J. R., Electrodeposition of aluminium film on P90 Li-Al alloy as protective coating against corrosion. *Surf Coat Tech* **2009,** *203*, 1373-1378.

23. Martin, F. J.; Cheek, G. T.; O'Grady, W. E.; Natishan, P. M., Impedance studies of the passive film on aluminium. *Corrosion Science* **2005,** *47*, 3187-3201.

24. Zhang, B.; Li, Y.; Wang, F., Electrochemical corrosion behaviour of microcrystalline aluminium in acidic solutions. *Corrosion Science* **2007,** *49*, 2071-2082.

25. Liu, Q. X.; El Abedin, S. Z.; Endres, F., Electroplating of mild steel by aluminium in a first generation ionic liquid: A green alternative to commercial Al-plating in organic solvents. *Surface and Coatings Technology* **2006,** *201*, 1352-1356.

26. Pardo, A.; Casajús, P.; Mohedano, M.; Coy, A. E.; Viejo, F.; Torres, B.; Matykina, E., Corrosion protection of Mg/Al alloys by thermal sprayed aluminium coatings. *Appl Surf Sci* **2009,** *255*, 6968-6977.

27. Pardo, A.; Merino, M. C.; Coy, A. E.; Arrabal, R.; Viejo, F.; Matykina, E., Corrosion behaviour of magnesium/aluminium alloys in 3.5 wt.% NaCl. *Corrosion Science* **2008,** *50*, 823-834.

28. Brooman, E. W., Corrosion Behavior of Environmentally Acceptable Alternatives to Cadmium and Chromium Coatings: Cadmium, Part I. *Metal Finishing* **2000,** *98*, 42-50.

29. Figueroa, D.; Robinson, M. J., The effects of sacrificial coatings on hydrogen embrittlement and re-embrittlement of ultra high strength steels. *Corrosion Science* **2008,** *50*, 1066-1079.

30. Emsley, J., Chromium. *Nature's Building Blocks: An A-Z Guide to the Elements, Oxford, England, UK: Oxford University Press* **2001**.

31. Eastmond, D. A.; MacGregor, J. T.; Slesinski, R. S., Trivalent Chromium: Assessing the Genotoxic Risk of an Essential Trace Element and Widely Used Human and Animal Nutritional Supplement. *Criticial Reviews In Toxicity* **2008,** *28*, 173-190.

32. DeGarmo, E. P.; Black, J. T.; Kohser, R. A., Materials and Processes in Manufacturing (9th ed.). *Wiley* **2003**.

33. Sahraoui, T.; Guessasma, S.; Fenineche, N. E.; Montavon, G.; Coddet, C., Friction and wear behaviour prediction of HVOF coatings and electroplated hard chromium using neural computation. *Materials Letters* **2004,** *58*, 654-660.

34. Brooman, E. W., Corrosion performance off environmentally acceptable alternatives to cadmium and chromium coatings: Chromium--Part I. *Metal Finishing* **2000,** *98*, 38-43.

35. Wang, S.; Li, Y.; Yao, M.; Wang, R., Compressive Residual Stress Introduced by Shot Peening. *J Mater Process Tech* **1998,** *73*, 64-73.

36. Schario, D. S.; Viszlay, D. S.; Moyer, H.; Brooman, E. W., Overview of Important Characteristics and Properties of Chromium Coatings. *Proceedings of the 83rd AESF annual technical conference SUR/FIN* **1996,** *83*, 389-400.

37. ASTM Standard B117-11 Standard Practive for Operating Salt Spray (Fog) Apparatus. *ASTM International, West Conshohocken, PA, 2011*.

38. ASTM Standard B368-09 Standard Test Method for Copper-Asselerated Acetic Acid-Salt Spray

(Fog) Testing (CASS Test). *AstM International, West Conshohocken, PA, 2009*.

39. ASTM standard B380-97 Standard Test Method for Corrosion Testing of Decorative Electrodeposited Coatings by the Corrodkote Procedure. *ASTM International, West Conshohocken, PA, 2008*.

40. Armini, A. J., Replacement of Chromium Electroplating Using a Cathodic Arc Process. *Proc. 2nd Annual Advanced Techniques for Replacing Chromium: An Information Exchange, Concurrent Technologies Corp., Johnstown, Pa* **1995**, 44.

41. Almeida, A.; Anjos, M.; Vilar, R.; Li, R.; Ferreira, M. G. S.; Steen, W. M.; Watkins, K. G., Laser alloying of aluminium alloys with chromium. *Surface and Coatings Technology* **1995,** *70*, 221-229.

42. Bayer, G. T., Chromium-Silicon Codiffusion Coating. *Advanced Materials & Processes* **1998,** *153*, 25-30.

43. Yun, H. J.; Dulal, S. M. S. I.; Shin, C. B.; Kim, C.-K., Characterisation of electrodeposited Co–W–P amorphous coatings on carbon steel. *Electrochimica Acta* **2008,** *54*, 370-375.

44. Bielewski, M., Replacing Cadmium and Chromium. *Corrosion Fatigure and Environmentally Assisted Cracking in Aging Military Vehicles, NATO Science and Technology Organization* **2011,** *23*, 1-17.

45. Brandl, W.; Gendig, C., Corrosion behaviour of hybrid coatings. *Thin Solid Films* **1996,** *290-291*, 343-347.

46. Stepanova, L. I.; Purovskaya, O. G., Electrodeposition of Nickel-Based alloys with tungsten and molybdenum. *Metal Finishing* **1998,** *96*, 50-53.

47. Ghahin, G. E., Alloys are Promising as Chromium or Cadmium Substitutes. *Plating and Surface Finishing* **1998,** *85*, 8-11.

48. Dykhouse, R. J., Vitrinite Protective Finish-An Inorganic Polymer. *Proc. Advanced Techniques for Replacing Chromium: An Information Exchange, Concurrent Technologies Corp., Johnstown, Pa* **1996**.

49. Brooman, E. W., Corrosion performance of environmentally acceptable alternatives to cadmium and chromium coatings: Chromium--Part II. *Metal Finishing* **2000,** *98*, 39-45.

50. Ruggiero, P. F., Tungsten Carbide Coatings Replace Chromium. *Advanced Materials & Processes* **2005**, 163, 39-41.

51. Nascimento, M. P.; Souza, R. C.; Miguel, I. M.; Pigatin, W. L.; Voorwald, H. J. C., Effects of tungsten carbide thermal spray coating by HP/HVOF and hard chromium electroplating on AISI 4340 high strength steel. *Surface and Coatings Technology* **2001,** *138*, 113-124.

52. Schwetzke, R.; Kreye, H., Microstructure and properties of tungsten carbide coatings sprayed with various high-velocity oxygen fuel spray systems. *Journal of Thermal Spray Technology* **1999,** *8*, 433-439.

53. Picas, J. A.; Forn, A.; Rilla, R.; Martín, E., HVOF thermal sprayed coatings on aluminium alloys and aluminium matrix composites. *Surface and Coatings Technology* **2005,** *200*, 1178-1181.

54. Kim, H.; Chen, M.; Yang, Q.; Troczynski, T., Sol-gel alumina environmental barrier coatings for SiC grit. *Materials Science and Engineering: A* **2006,** *420*, 150-154.

55. Sundararajan, G.; Rama Krishna, L., Mechanisms underlying the formation of thick alumina coatings through the MAO coating technology. *Surface and Coatings Technology* **2003,** *167*, 269-277.

56. Jianming, X.; Weijiang, Z.; Wolf, G. K., The corrosion properties of Al/Al2O3 multilayered coatings on CK45 steel deposited by IBAD. *Surface and Coatings Technology* **2004,** *187*, 194-198.

57. Xue, J.; Zhao, W., Properties of IBAD alumina coatings of different thicknesses. *Surface and Coatings Technology* **1998,** *103-104*, 74-77.

58. Wituschek, H.; Barth, M.; Ensinger, W.; Frech, G.; Ruck, D. M.; Leible, K. D.; Wolf, G. K., ALLIGATOR - An apparatus for ion beam assisted deposition with a broad-beam ion source. *Review of Scientific Instruments* **1992,** *63*, 2411-2413.

59. Gal-Or, L.; Silberman, I.; Chaim, R., Electrolytic ZrO_2 Coatings. *Journal of The Electrochemical Society* **1991,** *138*, 1939-1942.

60. Lgamri, A.; Guenbour, A.; Ben Bachir, A.; El Hajjaji, S.; Aries, L., Characterisation of electrolytically deposited alumina and yttrium modified alumina coatings on steel. *Surface and Coatings Technology* **2003,** *162*, 154-160.

61. Lima, R.; Marple, B., Thermal Spray Coatings Engineered from Nanostructured Ceramic Agglomerated Powders for Structural, Thermal Barrier and Biomedical Applications: A Review. *Journal of Thermal Spray Technology* **2007,** *16*, 40-63.

62. Lin, X.; Zeng, Y.; Zhou, X.; Ding, C., Microstructure of alumina-3wt.% titania coatings by plasma spraying with nanostructured powders. *Materials Science and Engineering A* **2003,** *357*, 228-234.

63. Turunen, E.; Varis, T.; Gustafsson, T. E.; Keskinen, J.; Fält, T.; Hannula, S.-P., Parameter optimization of HVOF sprayed nanostructured alumina and alumina-nickel composite coatings. *Surface and Coatings Technology* **2006,** *200*, 4987-4994.

64. Toma, F. L.; Berger, L. M.; Naumann, T.; Langner, S., Microstructures of nanostructured ceramic coatings obtained by suspension thermal spraying. *Surface and Coatings Technology* **2008,** *202*, 4343-4348.

65. Sully, A. H., Manganese. *Butterworths* **1955**.

66. Ortiz, Z. I.; Díaz-Arista, P.; Meas, Y.; Ortega-Borges, R.; Trejo, G., Characterization of the corrosion products of electrodeposited Zn, Zn–Co and Zn–Mn alloys coatings. *Corrosion Science* **2009,** *51*, 2703-2715.

67. Díaz-Arista, P.; Ortiz, Z. I.; Ruiz, H.; Ortega, R.; Meas, Y.; Trejo, G., Electrodeposition and characterization of Zn–Mn alloy coatings obtained from a chloride-based acidic bath containing ammonium thiocyanate as an additive. *Surface and Coatings Technology* **2009,** *203*, 1167-1175.

68. Chen, K.; Wilcox, G. D., Tin-Manganese Alloy Electrodeposits: I. Electrodeposition and Microstructural Characterisation. *Journal of The Electrochemical Society* **2006,** *153*, C634-C640.

69. Chen, K.; Wilcox, G. D., Tin–Manganese Alloy Electrodeposits: II. Corrosion Performance Studies. *Journal of The Electrochemical Society* **2008,** *155*, C53-C61.

70. Stephen, A.; Ananth, M. V.; Ravichandran, V., Corrosion behaviour of electrodeposited Ni-Mn alloys - electrochemical impedance measurements. *Anti-Corrosion Methods and Materials* **1999,** *46*, 117-121.

71. Yang, N. Y. C.; Headley, T. J.; Kelly, J. J.; Hruby, J. M., Metallurgy of high strength Ni–Mn microsystems fabricated by electrodeposition. *Scripta Materialia* **2004,** *51*, 761-766.

72. Ananth, M. V.; Parthasaradhy, N. V., Magnetic susceptibility of the electrodeposited Fe-Mn system. *Materials Science and Engineering: B* **1990,** *7*, 103-106.

73. Gong, J.; Zangari, G., Electrodeposition and Characterization of Sacrificial Copper-Manganese Alloy Coatings: Part I. Electrochemical and Morphological Characterisation. *Journal of The Electrochemical Society* **2004,** *151*, C297-C306.

74. Gong, J.; Wei, G.; Barnard, J.; Zangari, G., Electrodeposition and characterization of sacrificial copper-manganese alloy coatings: Part II. Structural, mechanical, and corrosion-resistance properties. *Metallurgical and Materials Transactions A* **2005,** *36*, 2705-2715.

75. Gong, J.; Zangari, G., Increased Metallic Character of Electrodeposited Mn Coatings Using Metal Ion Additives. *Electrochemical and Solid-State Letters* **2004,** *7*, C91-C94.

76. Mangolini, F.; Magagnin, L.; Cavallotti, P. L., Pulse plating of sacrificial Mn-Cu alloys from sulphate bath. *Transactions of the Institute of Metal Finishing* **2007,** *85*, 27-33.

77. Mangolini, F.; Magagnin, L.; Cavallotti, P. L., Pulse Plating of Mn–Cu Alloys on Steel. *Journal of The Electrochemical Society* **2006,** *153*, C623-C628.

78. Chung, P. P.; Cantwell, P. A.; Wilcox, G. D.; Critchlow, G. W., Electrodeposition of zinc-manganese alloy coatings from ionic liquid electrolytes. *Transactions of the Institute of Metal Finishing* **2008,** *86*, 211-219.

79. Tsuchiya, Y.; Hashimoto, S.; Ishibashi, Y.; Urakawa, T.; Sagiyama, M.; Fukuda, Y., Structure of Electrodeposited Zn-Mn Alloy Coatings. *ISIJ International* **2000,** *40*, 1024-1029.

80. Gong, J.; Zangari, G., Electrodeposition of sacrificial tin–manganese alloy coatings. *Materials Science and Engineering: A* **2003,** *344*, 268-278.

81. Chen, K.; Wilcox, G. D., Observations of the Spontaneous Growth of Tin Whiskers on Tin-Manganese Alloy Electrodeposits. *Physical Review Letters* **2005,** *94*, 66-104.

82. Joslin, D. L.; Oliver, W. C., A new method for analyzing data from continuous depth-sensing microindentation tests. *Journal of Materials Research* **1990,** *5*, 123-126.

83. Shreir, L. L., Corrosion Vol 1 Metal/Environment Reaction (second edition). *Newnes-Butterworths* **1976**.

84. Devaraj, G.; Guruviah, S.; Seshadri, S. K., Pulse plating. *Materials Chemistry and Physics* **1990,** *25*, 439-461.

85. Viswanathan, M.; Raub, C. J., Pulse plating of nickel-gold alloys. *Surface Technology* **1976,** *4*, 339-342.

86. Deng, M.-J.; Chen, P.-Y.; Sun, I. W., Electrochemical study and electrodeposition of manganese in the hydrophobic butylmethylpyrrolidinium bis((trifluoromethyl)sulfonyl)imide room-temperature ionic liquid. *Electrochimica Acta* **2007,** *53*, 1931-1938.

87. Chen, P.-Y.; Hussey, C. L., The electrodeposition of Mn and Zn–Mn alloys from the room-temperature tri-1-butylmethylammonium bis((trifluoromethane)sulfonyl)imide ionic liquid. *Electrochimica Acta* **2007,** *52*, 1857-1864.

88. Chen, P.-Y.; Deng, M.-J.; Zhuang, D.-X., Electrochemical codeposition of copper and manganese from room-temperature N-butyl-N-methylpyrrolidinium bis(trifluoromethylsulfonyl)imide ionic liquid. *Electrochimica Acta* **2009,** *54*, 6935-6940.

89. Francis, R., Galvanic corrosion - A practical guide for engineers. *NACE International* **2001**.

90. Schwermer, C. U.; Lavik, G.; Abed, R. M. M.; Dunsmore, B.; Ferdelman, T. G.; Stoodley, P.; Gieseke, A.; Beer, D. d., Impact of Nitrate on the Structure and Function of Bacterial Biofilm Communities in Pipelines Used for Injection of Seawater into Oil Fields. *Applied and Environmental Microbiology* **2008,** *74*, 2841-2851.

91. Jia, J.; Song, G.; Atrens, A., Experimental Measurement and Computer Simulation of Galvanic Corrosion of Magnesium Coupled to Steel. *Advanced Engineering Materials* **2007,** *9*, 65-74.

92. Deshpande, K. B., Experimental investigation of galvanic corrosion: Comparison between SVET and immersion techniques. *Corrosion Science* **2010,** *52*, 2819-2826.

93. Battocchi, D.; He, J.; Bierwagen, G. P.; Tallman, D. E., Emulation and study of the corrosion behavior of Al alloy 2024-T3 using a wire beam electrode (WBE) in conjunction with scanning vibrating electrode technique (SVET). *Corrosion Science* **2005,** *47*, 1165-1176.

94. ASTM Standard G102-89, Calculation of Corrosion Rates and Related Information from Electrochemical Measurement. *Annual Book of ASTM Standards, ASTM International, Philadelphia. 2004*.

95. Aerospace Material Specification (AMS) 6419F. *The Engineering Society For Advancing Mobility Land Sea Air and Space. SAE International* **2002**.

96. Airbus Process Specification (AIPS) 02-04-002 Electrolytic Cadmium Plating. *AIRBUS S.A.S Engineering Directorate, Blagnac Cedex, France* **Jan 2009**.

97. PCS-2550 Heat Resistant Metallic-Ceramic Anti-Corrosion Coating. *Messier-Dowty Snecma Group* **May 2004**.

98. MIL-DTL-83488D Coating, Aluminium, High Purity. *Department of Defense Index of Specifications and Standards (DoDISS)* **Apr 1999**.

99. Airbus Process Specificiation (AIPS) 02-03-004 Deposition of Aluminium by the Thermal Spray Process. *AIRBUS S.A.S Engineering Directorate, Blagnac Cedex, France* **Feb 2007**.

100. Airbus Process Specification (ABP) 1-4042 Hard Chromium Plating. *AIRBUS UK Limited* **Feb 2004**.

101. Messier-Dowty Process Specification (MD PCS) 2560. *Messier-Dowty DAFRAN Group* **Jan 2006**.

102. ASTM Standard G71-81 (2009) Standard Guide for Conducting and Evaluating Galvanic Corrosion Tests in Electrolytes. *ASTM International, West Conshohocken, PA, 2003* **2009**.

103. British Standard BS EN ISO 10308: 1997, Metallic Coatings-Review Of Porosity Test. **1997**.

104. Ruhi, G.; Modi, O. P.; Singh, I. B.; Jha, A. K.; Yegneswaran, A. H., Wear and electrochemical characterization of sol-gel alumina coating on chemically pre-treated mild steel substrate. *Surface and Coatings Technology* **2006,** *201*, 1866-1872.

105. Aries, L., Preparation of electrolytic ceramic films on stainless steel conversion coatings. *Journal of Applied Electrochemistry* **1994,** *24*, 554-558.

106. International Standard ISO 2812-1: Paints and varnishes - Determination of resistance to liquids Part 1: Immersion in liquids other than water (2nd edition). **2007**.

107. Uhlig, H. H.; Revie, R. W., CORROSION AND CORROSION CONTROL: An Introduction to Corrosion Science and Engineering fourth edition. *A JOHN WILEY & SONS, INC., PUBLICATION* **2008**.

108. Wagner, C. D.; Naumkin, A. V.; Vass, A. K.; Allison, J. W.; Powell, C. J.; Rumble, J. R., NIST X-ray Photoelectron Spectroscopy Database. **2007**.

109. Zamanzadeh, M.; Allam, A.; Kato, C.; Ateya, B.; Pickering, H. W., Hydrogen Absorption during Electrodeposition and Hydrogen Charging of Sn and Cd Coatings on Iron. *J. Electrochem. Soc* **1982,** *129*, 284-289.

110. Ciampi, S.; di Castro, V.; Polzonetti, G., XPS study of cadmium oxidation in air. *Journal of Electron Spectroscopy and Related Phenomena* **1991,** *56*, R1-R6.

111. Qian, M.; Li, D.; Liu, S. B.; Gong, S. L., Corrosion performance of laser-remelted Al–Si coating on magnesium alloy AZ91D. *Corrosion Science* **2010,** *52*, 3554-3560.

112. Aguero, A.; Camon, F.; Garcia de Blas, J.; del Hoyo, J. C.; Muelas, A.; Santaballa, A.; Ulargui, S.;

Valles, P., HVOF-Deposited WCCoCr as Replacement for Hard Cr in Landing Gear Actuators. *Journal of Thermal Spray Technology* **2011,** *20*, 1292-1309.

113. U, L., A model for the spontaneous growth of zinc, cadmium and tin whiskers. *Acta Metallurgica* **1976,** *24*, 181-186.

114. Nicholls, D., Complexes and First-row transition elements. *London: Macmillan* **1974**.

115. Lahtinen, R.; Gustafsson, T. E., SEM Investigation of Zinc Whiskers on Hot-dip Glavanized Coatings and Bright Electroplated Coatings. *Journal of Applied Surface Finishing* **2007,** *2*, 15-19.

116. Griffiths, D. J., Introduction to electrodynamics 3rd Edition. *Upper Saddle River, N.J: Prentice Hall* **1999**.

117. Song, G.-L., Potential and current distributions of one-dimensional galvanic corrosion systems. *Corrosion Science* **2010,** *52*, 455-480.

118. Lekatou, A.; Zois, D.; Grimanelis, D., Corrosion properties of HVOF cermet coatings with bond coats in an aqueous chloride environment. *Thin Solid Films* **2008,** *516*, 5700-5705.

119. Monticelli, C.; Frignani, A.; Zucchi, F., Investigation on the corrosion process of carbon steel coated by HVOF WC/Co cermets in neutral solution. *Corrosion Science* **2004,** *46*, 1225-1237.

120. Wang, Q.; Zhang, S.; Cheng, Y.; Xiang, J.; Zhao, X.; Yang, G., Wear and corrosion performance of WC-10Co4Cr coatings deposited by different HVOF and HVAF spraying processes. *Surface and Coatings Technology* **2013,** *218*, 127-136.

121. Sutthiruangwong, S.; Mori, G., Corrosion properties of Co-based cemented carbides in acidic solutions. *International Journal of Refractory Metals and Hard Materials* **2003,** *21*, 135-145.

122. Cho, J. E.; Hwang, S. Y.; Kim, K. Y., Corrosion behavior of thermal sprayed WC cermet coatings having various metallic binders in strong acidic environment. *Surface and Coatings Technology* **2006,** *200*, 2653-2662.

123. Human, A. M.; Exner, H. E., Electrochemical behaviour of tungsten-carbide hardmetals. *Materials Science and Engineering: A* **1996,** *209*, 180-191.

124. Filimonov, E. V.; Shcherbakov, A. I., The Effect of Products of Nitrate Ion Reduction on the Kinetics of Electrode Reactions on Stainless Steel. *Protection of Metals* **2001,** *37*, 539-542.

125. Kirk, R. E.; Othmer, D. F., Encyclopedia of chemical technology 4th edition. **1996,** *15*.

126. Zhou, M.; Yang, Q.; Troczynski, T., Effect of substrate surface modification on alumina composite sol–gel coatings. *Surface and Coatings Technology* **2006,** *200*, 2800-2804.

127. Guilminot, E.; Dalard, F.; Degrigny, C., Mechanism of iron corrosion in water–polyethylene glycol (PEG 400) mixtures. *Corrosion Science* **2002,** *44*, 2199-2208.